

INFORMATION TO USERS

This manuscript has been reproduced from the microfilm master. UMI films the text directly from the original or copy submitted. Thus, some thesis and dissertation copies are in typewriter face, while others may be from any type of computer printer.

The quality of this reproduction is dependent upon the quality of the copy submitted. Broken or indistinct print, colored or poor quality illustrations and photographs, print bleedthrough, substandard margins, and improper alignment can adversely affect reproduction.

In the unlikely event that the author did not send UMI a complete manuscript and there are missing pages, these will be noted. Also, if unauthorized copyright material had to be removed, a note will indicate the deletion.

Oversize materials (e.g., maps, drawings, charts) are reproduced by sectioning the original, beginning at the upper left-hand corner and continuing from left to right in equal sections with small overlaps.

Photographs included in the original manuscript have been reproduced xerographically in this copy. Higher quality 6" x 9" black and white photographic prints are available for any photographs or illustrations appearing in this copy for an additional charge. Contact UMI directly to order.

Bell & Howell Information and Learning
300 North Zeeb Road, Ann Arbor, MI 48106-1346 USA
800-521-0600

UMI[®]

University of Alberta

Switches and Filters for Wavelength Division Optical Networks

By

Alan Julian Paul Hnatiw



A thesis submitted to the Faculty of Graduate Studies and Research in partial fulfilment of the requirements for the degree of **Doctor of Philosophy**

Department of Electrical and Computer Engineering

Edmonton, Alberta

Fall 1999



National Library
of Canada

Acquisitions and
Bibliographic Services

395 Wellington Street
Ottawa ON K1A 0N4
Canada

Bibliothèque nationale
du Canada

Acquisitions et
services bibliographiques

395, rue Wellington
Ottawa ON K1A 0N4
Canada

Your file Votre référence

Our file Notre référence

The author has granted a non-exclusive licence allowing the National Library of Canada to reproduce, loan, distribute or sell copies of this thesis in microform, paper or electronic formats.

The author retains ownership of the copyright in this thesis. Neither the thesis nor substantial extracts from it may be printed or otherwise reproduced without the author's permission.

L'auteur a accordé une licence non exclusive permettant à la Bibliothèque nationale du Canada de reproduire, prêter, distribuer ou vendre des copies de cette thèse sous la forme de microfiche/film, de reproduction sur papier ou sur format électronique.

L'auteur conserve la propriété du droit d'auteur qui protège cette thèse. Ni la thèse ni des extraits substantiels de celle-ci ne doivent être imprimés ou autrement reproduits sans son autorisation.

0-612-46852-6

UNIVERSITY OF ALBERTA

LIBRARY RELEASE FORM

NAME OF AUTHOR: **Alan Julian Paul Hnatiw**

TITLE OF THESIS: **Switches and Filters for
Wavelength Division Optical
Networks**

DEGREE: **Doctor of Philosophy**

YEAR THIS DEGREE GRANTED: **1999**

Permission is hereby granted to the University of Alberta Library to reproduce single copies of this thesis and to lend or sell such copies for private, scholarly or scientific research purposes only.

The author reserves all other publication and other rights in association with the copyright in the thesis, and except as hereinbefore provided, neither the thesis nor any substantial portion thereof may be printed or otherwise reproduced in any material form whatever without the author's prior permission.

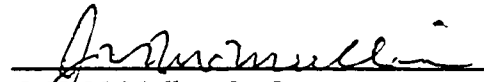
DATE: May 25, 1999


Alan Hnatiw
39 Hartin Street
Stittsville, Ontario, Canada
K2S 1B9


UNIVERSITY OF ALBERTA

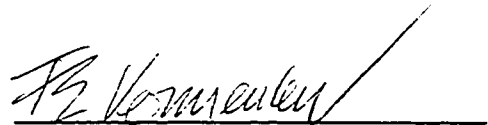
FACULTY OF GRADUATE STUDIES AND RESEARCH

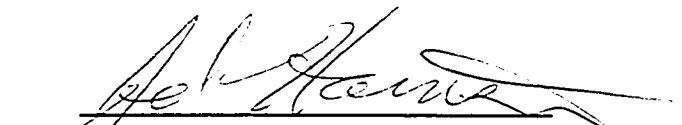
The undersigned certify that they have read, and recommend to the Faculty of Graduate Studies and Research for acceptance, a thesis entitled **Switches and Filters for Wavelength Division Optical Networks** submitted by **Alan Julian Paul Hnatiw** in partial fulfillment of the requirements for the degree of **Doctor of Philosophy**.


J. N. McMullin, Co-Supervisor

for 
R. I. MacDonald, Co-Supervisor


A.M. Robinson


F. E. Vermeulen


D. J. Harrison


K. McGreer, External Examiner

DATE: May 21, 1999.

*For my wife Christine and daughter Ariel
Their support and love have made this work possible.*

Abstract

This thesis is concerned with the development of optical filters and switches which are essential components for implementing wavelength division multiplexed fibre optic networks. Optical and optoelectronic switches are used to route signals through a network from source to destination. Optical filters are used to construct wavelength sensitive components, such as wavelength multiplexers, wavelength demultiplexers, and bandpass filters.

A novel evaporation technique, called Glancing Angle Deposition, was used to fabricate multilayer thin-film interference filters. By concurrently rotating and tilting a substrate, a variable porosity thin film may be grown. This in turn results in a variable effective refractive index that can be used to fabricate thin-film interference filters. A Win95/NT filter synthesis program incorporating a simulated annealing optimization algorithm was written to allow the index profile of a thin-film filter to be optimized. Using glancing angle deposition, an optical bandpass filter having a bandwidth of 50 nm centered about 460 nm was fabricated.

A 1x4 multimoded thermo-optic polymer switch based on a generalized Mach-Zehnder interferometer was designed and fabricated. The device uses multimode interference couplers to perform the necessary passive power splitting and combining operations. Electrically controlled chromium heaters are then used to perform the switching operation by altering the refractive index of the Mach-Zehnder arms. The polymer switch was fabricated from liquid ultraviolet-curable adhesives using a modified photolithography process. A switching time of 3 ms and contrast ratio of 5 dB were measured.

Finally, a 4x4 hybrid integrated optoelectronic matrix switch was constructed using polymer waveguides, linear arrays of broadband metal-semiconductor-metal photodetectors, and directly modulated distributed feedback lasers. This resulted in a low-cost broadband switch matrix with a channel bandwidth greater than 6 GHz and a switching time of approximately 1 μ s. An important application of such a switch may be wavelength rearrangement in wavelength division multiplexed optical fibre networks.

Acknowledgements

I thank my supervisors Dr. James McMullin and Dr. R. Ian MacDonald. These gentlemen have been superb mentors and their constant tutelage has helped to guide me through this thesis. Many valuable lessons, both academic and professional, will be of great assistance throughout my career.

I am indebted to Dr. Ray DeCorby and Dino Corrazza for investing their time and effort in proof-reading this thesis. Also, I have gleaned much knowledge from both of these individuals and value greatly their experience and friendship.

I would also like to thank TRLabs and NSERC for their financial assistance. In addition, the staff and students at TRLabs have been very helpful throughout my work. Special thanks to Dave Boertjes, Reza Paim, John Doucette, Cibby Pulikkaseril, Dave Morley and Demetrios Stamatelakis.

Also, the Communication Research Centre (CRC) was crucial in the fabrication of both the MSM photodetectors and thermo-optic polymer switches. I would like to thank Dr. Claire Callender for her assistance and discussions, and Julian Noad for taking SEM photographs.

Finally, I thank my wife for her continual support, encouragement and love over the years.

Table of Contents

1. INTRODUCTION	1
1.1 OVERVIEW OF LIGHTWAVE TRANSMISSION SYSTEMS	1
1.2 ENABLING TECHNOLOGIES FOR WDM SYSTEMS	3
1.3 SIGNAL TRANSPARENT NETWORKS.....	5
1.3.1. <i>Wavelength Cross-connects</i>	7
1.4 THESIS ORGANIZATION	8
2. INHOMOGENEOUS THIN FILM OPTICAL FILTERS FABRICATED USING GLANCING ANGLE DEPOSITION	10
2.1 INTRODUCTION.....	10
2.2 RUGATE FILTERS.....	11
2.2.1. <i>Index Profile of a Rugate Filter</i>	12
2.3 METHODS OF CALCULATING A REFLECTION SPECTRUM	14
2.3.1. <i>Characteristic Matrix Method</i>	14
2.3.2. <i>Coupled-Wave Theory</i>	19
2.3.3. <i>Derivation of Integral Calculation of Reflectance</i>	21
2.4 RUGATE FILTER SYNTHESIS	22
2.4.1. <i>Fourier Transform Synthesis Method</i>	23
2.4.2. <i>Simulated Annealing Optimization Algorithm</i>	27
2.4.3. <i>Windows95 Based Filter Synthesis and Optimization Program</i>	29
2.5 FILTER FABRICATION METHODS	33
2.6 EXPERIMENTAL RESULTS	35
2.7 APPLICATIONS.....	38
2.7.1. <i>Telecommunications Applications</i>	38
2.7.2. <i>Other Areas</i>	39
2.8 SUMMARY	40
3. MULTIMODE THERMO-OPTIC POLYMER SWITCH	42
3.1 BACKGROUND	42
3.2 OPTICAL SWITCHING APPLICATIONS	44
3.2.1. <i>SONET Ring Protection Switching</i>	44
3.2.2. <i>Local Area Networks</i>	49
3.2.3. <i>Incorporation of an Optical Switch in an Optoelectronic Switch Matrix</i>	50
3.3 THEORY OF OPERATION	50
3.4 MATERIAL SELECTION	55
3.5 DESIGN AND SIMULATION	57
3.5.1. <i>Waveguide Structure</i>	57
3.5.2. <i>Multimode Interference Couplers</i>	64
3.5.3. <i>Effects of Multiple Modes on the Performance of a Generalized Mach-Zehnder Interferometer</i>	70
3.5.4. <i>Thermal Design Considerations and Modeling Results</i>	73
3.5.5. <i>Beam Propagation Simulations of the Overall Device</i>	77
3.6 DEVICE FABRICATION	79
3.6.1. <i>Metal Deposition</i>	81
3.6.2. <i>Polymer Waveguide Fabrication</i>	82
3.7 EXPERIMENTAL RESULTS	86
3.7.1. <i>Passive Optical Performance</i>	86
3.7.2. <i>Switching Action</i>	89
3.7.3. <i>Transient Response</i>	92

3.7.4.	<i>Comparison of Simulated and Experimental Results</i>	93
3.8	SUMMARY	95
4.	HYBRID INTEGRATED OPTOELECTRONIC MATRIX SWITCH	96
4.1	INTRODUCTION.....	96
4.2	APPLICATIONS.....	97
4.2.1.	<i>Wavelength Cross-connect and Reassignment in Optical Networks</i>	98
4.2.2.	<i>Broadband Analogue Switch for CATV Networks</i>	100
4.2.3.	<i>High Speed Broadband Signal Processor</i>	101
4.3	IMPLEMENTATION	103
4.3.1.	<i>Overview of the 4x4 Hybrid Integrated Optoelectronic Switch</i>	104
4.4	METAL-SEMICONDUCTOR-METAL PHOTODETECTORS AND PHOTODETECTOR ARRAYS.....	110
4.4.1.	<i>Theory of Operation</i>	110
4.4.2.	<i>Linear Arrays of MSM Photodetectors</i>	113
4.5	CROSSPOINT MODULE.....	118
4.5.1.	<i>Optical Distribution</i>	118
4.5.2.	<i>Power and Dispersion Budget</i>	120
4.5.3.	<i>Substrate Design and Layout</i>	122
4.5.4.	<i>Experimental Results</i>	124
4.6	TRANSMITTER MODULE	126
4.7	PERFORMANCE OF THE ENTIRE SWITCH (PROTOTYPE II ONLY).....	133
4.8	FUTURE DESIGN RECOMMENDATIONS AND CONCLUSIONS	134
5.	CONCLUSIONS	136
5.1	FUTURE WORK.....	139
6.	REFERENCES	140
7.	APPENDIX I: THERMAL MODELING SOURCE CODE	146
7.1	STEADY STATE SOLUTION.....	146
7.2	TIME-DEPENDENT SOLUTION	149

List of Tables

Table 2.1. Properties and characteristics of optical filters. A filter design must address each issue concurrently, while still allowing for an optimum design.	11
Table 3.1. Performance summary of JDS Fitel's commercially available polymer thermo-optic switches. Specifications are valid in the optical bandwidth range from 1530-1565 nm [78].	44
Table 3.2. Commonly used SONET bit (line) rates for optical fibre networks. The bit rate or line rate is the total number of bits transmitted per second, while the data rate is the bit rate minus the amount of SONET overhead information.	45
Table 3.3. Effect of splitter imbalance on a 1x2 or 2x2 Mach-Zehnder optical switch. Control of the splitter imbalance is crucial in achieving good switching performance.	54
Table 3.4. Summary of the properties and characteristics of glass, semiconductors, and polymers for use in thermo-optic switches.	56
Table 3.5. Summary of the phase relationship between any input and output of a 4x4 MMI coupler. A constant phase factor of $47/32 \pi$ was added so that the phase factors were multiples of $1/4 \pi$	70
Table 3.6. Calculated propagation constants normalized to the free-space wavenumber k_0 for the first four modes of a $10 \times 10 \times 3518 \mu\text{m}$ waveguide. The phase change, $\Delta\phi$, should be $\pi/2$ or 1.5708.	72
Table 3.7. Summary of the constants used in the thermal models (source [57]-[58]).	75
Table 4.1. Performance summary of the 10x10 optoelectronic matrix switch. Cross-talk and contrast measurements were made at 1 GHz [63].	104
Table 4.2. Summary of the loss budget for the hybrid integrated OES.	121

List of Figures

- Figure 1.1. Schematic diagram of a three channel WDM system. Electrical signals S_i are converted to optical signals each having a unique wavelength. A WDM MUX combines the three separate wavelengths from three fibres onto a single optical fibre. At the receiving end, a DMUX is used to separate the wavelengths and receivers convert the optical signals to electrical ones. 3
- Figure 1.2. Schematic drawing of an arrayed-waveguide grating. Slab waveguide power splitter/combiners are used. Increasing the number of waveguides between the power splitter and combiner reduces the insertion loss and increases resolution of the device. 4
- Figure 1.3. Implementation of a four-channel wavelength demultiplexer with thin-film interference filters. Each filter transmits only a single wavelength and reflects the rest. 5
- Figure 1.4. (a) Individual rings may be administered and provisioned as all-optical rings. When two ring intersect, an opaque wavelength cross-connect (WXC) may be used to avoid wavelength contention and perform 3R regeneration. (b) Complex networks with multiple rings will require sophisticated management if the entire network is all-optical. 7
- Figure 1.5. A wavelength cross-connect using an electronic or optoelectronic space switch, MUXs/DMUXs, receivers (photodetectors) and transmitters (lasers and modulators). An all-optical WXC may be constructed by replacing the electronic space switch with an optical switch, eliminating the transmitters and replacing the receivers with optical wavelength converters. Note, S_i are the electrical information signals. 8
- Figure 2.1. Refractive index profile for a rugate filter with a single reflection peak. The refractive index profile is shown in (a) and the corresponding reflection spectrum in (b). Note that the glass ($n=1.5$) and air ($n=1$) interfaces have been included in the refractive index profile in (a). 12
- Figure 2.2. Refractive index profile corresponding to a rugate filter with two peaks centred at 460 nm and 560 nm. Shown on the right is the corresponding reflection spectrum. 13
- Figure 2.3. Refractive index profile corresponding to a rugate filter with two peaks centred at 460 nm and 470 nm. This configuration may be used to create a reflection peak that is broader than those obtained by using a single line filter for a given filter thickness. 13
- Figure 2.4. The three intermediate matrices, P_i , R_U and P_h are multiplied together to get the characteristic matrix for a single layer. The horizontal axis represents thickness and the vertical axis represents refractive index. 15
- Figure 2.5. Example of how an inhomogeneous (continuously graded) index profile is discretised into many homogeneous layers. The characteristic matrix method can then be used to calculate the reflection spectrum. 16

- Figure 2.6. The index profile given in (a) was used to calculate the reflection spectrum in (b) using the CMM. The index variation in (a) is $\Delta n=0.8$. The index of the substrate was taken to be $n=1.5$ (glass) and the index of the incident medium was taken to be $n=1.0$ (air). The 3-dB bandwidth and reflectance of (b) are, $BW=103$ nm and $R=100\%$, respectively. 17
- Figure 2.7. The index profile in (a) with $\Delta n=0.1$. Note that the bandwidth of the reflection peak has narrowed as compared with Figure 2.6. The 3-dB bandwidth of the reflection peak in (b) is $BW=16$ nm and a peak reflectance of $R=98.8\%$ 17
- Figure 2.8. Reflection spectrum of a single line rugate neglecting the effect of the substrate and air interfaces, but otherwise identical to the index profile of Figure 2.6. 18
- Figure 2.9. Reflection corresponding to the index profile given in Figure 2.7 with the exception that the substrate and air interfaces have been neglected. Note that the broad bandwidth reflections are almost completely eliminated. 19
- Figure 2.10. Calculated reflection spectra corresponding to the index profiles given in Figure 2.6 and Figure 2.7, respectively. The 3-dB bandwidth for (a) and (b) is 158 nm and 16 nm, respectively. Note that the reflection spectrum of (a) is quite different from Figure 2.6 due to the large index difference. In contrast, the coupled-wave approach gives good results for (b) where the index difference is a factor of eight less. 21
- Figure 2.11. Comparison of Q-functions Q_1 through Q_3 , respectively. The left column shows the index profile corresponding to the reflection spectrum on the right. The same filter design parameters were used. The design/prototype filter was a rectangular shaped filter having a bandwidth of 100 nm centred at 550 nm and a peak reflectance of 90%. The 3-dB bandwidth for b), d), and f) are 145 nm, 102 nm, and 193 nm. The reflection peak at 250 nm corresponds to the second harmonic. Note that the three different Q-functions produce different spectral responses, therefore the filter design will need optimized. 25
- Figure 2.12. Comparison of Q-functions Q_1 to Q_3 , when the prototype brickwall filter bandwidth is reduced to 10 nm. The 3-dB bandwidth for b), d), and f) are 18.7 nm, 11.7 nm and 23.2 nm, respectively. 26
- Figure 2.13. Two-dimensional plots of (a) the generating function and (b) the acceptance function. In (a), as the temperature T tends towards zero, the deviation, dX , of a new value from the previous value decreases. In (b), when the temperature is high, the probability of accepting a worse solution is approximately 0.5. As the temperature is lowered, the probability of selecting a worse solution also decreases. 28

Figure 2.14. Schematic illustration of how the temperature parameter influences how the SA algorithm explores the solution space. The numbers in (a) and (b) represent consecutive iterations. When the temperature is high (a), each new parameter of the solution vector is likely to be fairly distant, i.e. a large Δx , from the previous value. Also, the probability of accepting a worse value of the function to be minimized, $f(x)$, is high (~50%). As the temperature is lowered, it is more probable that newly generated points will be close to the previous point. Furthermore, as shown by the transition from iteration 2 to 3 in (b), uphill or worse solutions are less likely to be accepted..... 29

Figure 2.15. The refractive index profile was altered to optimize the reflection spectrum. The circles represent the desired reflection spectrum and the continuous line is the calculated reflection spectrum. The reflection spectrum is calculated as a function of wavelength. The target spectrum is specified as a series of ranges with constant wavelength spacing and reflection coefficient. Therefore, in regions where the spectrum is changing slowly, fewer calculations are performed, thus reducing the computation time. 31

Figure 2.16. Screen capture of the custom written Win95 based filter optimization program. The red circles in the top plot indicate the target reflection spectrum and the solid line represents the calculated reflection spectrum. The second graph illustrates the current refractive index profile as a function of depth. The dialog box shown at the bottom is where most of the program data/parameters are entered. 32

Figure 2.17. Conceptual drawing of a GLAD system. The substrate holder rotates about one axis and tilts about the other. As the vapour flux is deposited onto the substrate, various processes combine to produce sculpted films..... 34

Figure 2.18. Effects of tilt and rotation on film growth. A fully dense MgF_2 (a) results from normal incident film growth, (b) MgF_2 grown with the substrate tilted, (c) SiO_2 grown by rotating the substrate slowly and with a constant tilt (helix pitch ~2 μm) and (d) MgF_2 grown with fast rotation and constant tilt (helix pitch ~60nm) [26]... 35

Figure 2.19. SEM micrograph of a rugate filter that has a sinusoidal refractive index profile. The refractive index has been estimated to vary from 1.11 to 1.34. The boundaries between the high and low index layers can just be discerned as dark lines. The film was deposited by rotating the substrate rapidly and by varying the substrate tilt sinusoidally. 37

Figure 2.20. Reflection spectrum of a rugate filter fabricated using GLAD. The bandwidth is approximately 50 nm and the peak reflectance is 82%. The characteristic matrix method was used to calculate the reflection spectrum. The vertical offset between the two curves is believed to be the result of scattering within the film. 38

Figure 2.21. Calculated reflection spectra for a glass-air interface that has been treated with different AR-coatings. The reflection coefficient from an air-glass interface is typically 4%. The spectrum when a fully dense layer of MgF_2 ($n=1.38$) is used as an AR-coating on glass is shown in (a). In (b) the effect of GLAD deposited MgF_2 film ($n=1.225$) with no capping layer is shown. In (c), a GLAD MgF_2 film ($n=1.225$) and a 10 nm MgF_2 ($n=1.38$) cap layer is used..... 40

- Figure 3.1. Top view (a) and cross-section view (b) of a Y-junction 1x2 thermo-optic polymer switch. Switching is achieved by applying current to one heater. The refractive index of the polymer is lowered due to the thermo-optic effect inherent in the polymer. The result is that an optical signal travelling through the polymer waveguide will experience a shift to the opposite side of the splitter (c) (effect is exaggerated and simplified for clarity). 43
- Figure 3.2. An example of a four node SONET ring with one-for-one fibre protection. Each heavy line represents a pair of fibres. For BLSRs, data can flow in both directions around the ring, while for UPSRs, data is always routed either clockwise or counter clockwise around the ring. 46
- Figure 3.3. When a fibre cut occurs between nodes 1 and 2, the working capacity (heavy line) of the ring can be restored by using the spare link (dotted line). (a) represents the shortest path restoration route and (b) is the longest route. Both routes can be used to restore the working capacity, although the shortest one is preferred. Note, the actual switching function takes place inside nodes 1 and 2. but is illustrated outside the nodes for clarity..... 47
- Figure 3.4. Example of how an optical layer (top) may be used in conjunction with the SONET layer (bottom). With such an architecture, the optical layer may be used for link protection and to more efficiently route traffic. 48
- Figure 3.5. (a) In a path switched ring, the protection switch is normally configured in the bar-state (dotted lines) and is switched to the cross-state (solid lines) for protection. (b) In a bi-directional line switched ring, the protection switch is normally configured in the bar-state (dashed lines) and is switched to the cross-state (solid line) for protection. 49
- Figure 3.6. Conceptual drawing of a 1x4 thermo-optic switch. Multimode polymer waveguides and multimode interference couplers are used to construct a four-arm generalized Mach-Zehnder interferometer. Phase shifters are used to switch the input optical signal to any output. 51
- Figure 3.7. A single-port integrated optic Mach-Zehnder (a) actually has two outputs: a guided port and a radiation (lossy) port. A true integrated two-port Mach-Zehnder (b) can be designed using directional couplers, where both outputs are guided. .. 52
- Figure 3.8. Dependence of the output intensity on the phase difference for a Mach-Zehnder interferometer. When the signals are completely out-of-phase, $\Delta\phi=\pi$, destructive interference results in zero light intensity at that particular output.... 53
- Figure 3.9. Geometry of the polymer waveguide used in the MTOPS. The refractive indices of the core and cladding layers are 1.5367 and 1.5145, respectively. Both glass and silicon substrates were used. The heating elements are made by depositing a very thin layer of chromium between the cladding and substrate..... 58

- Figure 3.11. The twelve largest eigenvalues and eigenvectors for the waveguide structure shown in Figure 3.9. The effective refractive index for each mode, which is equal to the propagation constant divided by the free space wavenumber, is indicated at the top of each figure. Due to the limited size of the solution space, i.e. finite computer memory, modes 10-12 are numerical artifacts and are not guided. It can also be seen that mode 9 is probably not a guided mode since the effective index is lower than the cladding index. 60
- Figure 3.12. Cross-sectional intensity plots of the fundamental waveguide mode. The vertical lines indicate the boundaries between the core, cladding, and substrate regions. The ratio of the field intensity at the cladding-substrate interface to the peak intensity was -30 dB..... 61
- Figure 3.13. Calculations of the normalized power distribution for the first nine modes supported in a 10 μm x 10 μm polymer waveguide. The coupling efficiency and offset of the input fibre were: (a) 94.7 % (-0.24 dB) for the geometric centre of the waveguide, (b) 95.6 % (-0.2 dB) for a vertical offset of 1.2 μm , (c) 76.1 % (-1.2 dB) for 3 μm offset in both directions, and (d) 38.5 % (-4.1 dB) for a 5 μm offset in both directions. 62
- Figure 3.14. 3D BPM simulations illustrating the effect of input offset on coupling loss and switch contrast ratio. In (a), the input field was located at the geometric centre, and resulted in a total loss of 0.5 dB and a contrast ratio of 23.4 dB. In (c), the input was located at $\Delta y = -3 \mu\text{m}$, $\Delta x = 3 \mu\text{m}$, and resulted in 1 dB of loss and a contrast ratio of 20 dB. For a -5 μm offset in y and 5 μm offset in x (e), the loss and the contrast ratio were 6.7 dB and 5.4 dB, respectively. Figures (b), (d) and (f) are cross-sectional plots of the intensity profile at the output of the switch..... 63
- Figure 3.15. Perspective drawing of a 1x2 multimode interference coupler. The input field excites multiple modes in the MMI. The propagating modes have a phase relationship that results in multiple images along the z -direction. The length and width of a MMI are critical design parameters and have a direct bearing on the relative intensities at the output ports..... 64
- Figure 3.16. The input and output waveguides must be located at specific transverse locations as indicated in the drawing. N is the number of input/output waveguides. 65
- Figure 3.17. The field (a) and intensity (b) of the first four modes in a metal walled waveguide (note: the plots for each mode are offset for clarity). 65
- Figure 3.18. The cross-state occurs when the input signal is cross-connected to an output (a). The bar-state occurs when the input signal appears at the same lateral output (b). The equal-split or 3 dB state results when the input signal is split equally among the outputs. The definition of cross and bar states is not well suited for switches larger than 2x2, because there are many cross-states and only one bar-state. Therefore, when stating a switch is in the cross-state, extra information must be provided for switches larger than 2x2 to eliminate ambiguity..... 66

- Figure 3.19. Excess loss of a 1x4 MMI as a function of the sensitivity to length and width variations calculated using 2D BPM simulations. Notice that the MMI coupler is extremely sensitive to width variations, ΔW , resulting in stringent device fabrication tolerances. 68
- Figure 3.20. (a) Intensity plot of a 75 μm wide MMI obtained from a 2D BPM simulation. The vertical line indicates where the input signal splits into four, which corresponds to a 6 dB MMI coupler length of $\sim 5480 \mu\text{m}$. (b) A plot of the intensity at the 6 dB length..... 69
- Figure 3.21. (a) Intensity plot from a 3D BPM simulation of a 75 μm wide MMI coupler. (b) The coupling and insertion losses were 0.27 dB and 0.1 dB, respectively. The relative power in each of the outputs, labelled from top to bottom, were approximately $P_1 = -6.35 \text{ dB}$, $P_2 = -6.40 \text{ dB}$, $P_3 = -6.48 \text{ dB}$, and $P_4 = -6.44 \text{ dB}$ 69
- Figure 3.22. Numbering convention used to describe the phase relationship between inputs and outputs given by equation (3.17)..... 70
- Figure 3.23. Calculated percent deviation of the phase change from the ideal value of 1.5708 for the first four modes of a $10 \times 10 \times 3518 \mu\text{m}$ polymer waveguide. 72
- Figure 3.24. 2D BPM simulations illustrating the effects of input coupling misalignment. Intensity plots in the x-z plane are shown on the left side, while plots of the output intensity are shown on the right. The input excitation is located at the centre of the input guide in (a) and (b) and was offset by $1 \mu\text{m}$ in (c) and (d). The relative power in each of the output waveguides for (b) and (d) are: $P_1 = -0.29 \text{ dB}$, $P_2 = -27.1 \text{ dB}$, $P_3 = -32.6 \text{ dB}$, $P_4 = -20.3 \text{ dB}$, and $P_1 = -0.22 \text{ dB}$, $P_2 = -31.3 \text{ dB}$, $P_3 = -37.3 \text{ dB}$, $P_4 = -21.1 \text{ dB}$, respectively. 73
- Figure 3.25. Waveguide structure used in thermal analysis. The core and cladding polymer layers were combined since their thermal properties were nearly identical. 75
- Figure 3.26. Steady-state thermal modeling results obtained from PDEase. (a) The geometry and refined finite element mesh used to solve the problem. (b) Contour plot of the temperature profile. (c) Cross-sectional temperature profile of a waveguide with the heater turned on. Note the temperature is nearly constant in the waveguide. (d) Temperature profile of a waveguide approximately $20 \mu\text{m}$ from the heater representing the thermal cross-talk or equivalently the thermal isolation. The vertical line shown in the thumbnail plots located in the lower right corner of plots (c) and (d) represent the path used to calculate the cross-sectional temperature plots. 76
- Figure 3.27. Transient thermal modeling results. Temperature profiles were generated as a function of time at four specific points. The arrows indicate the locations on the thumbnail plots where the temperature was monitored. (a) The temperature was measured on the top surface of the heater and waveguide. The switching time estimated from (a) is $\sim 3 \text{ ms}$. (b) The temperature was measured at the SiO_2 -polymer interface and at the top of the waveguide..... 77

- Figure 3.28. 2D BPM simulations of the overall device operating in the unbiased state. Each MMI imparts a phase delay to each signal, and when cascaded results in the intensity plots shown. (a) When the signal is applied to input two, two equal signals are produced at outputs two and three. (b) When the signal is applied to input four, two equal signals are produced at outputs one and four. The remaining two combinations can be obtained by making use of symmetry. The total loss, not including propagation loss, was <0.2 dB. 78
- Figure 3.29. 2D BPM simulations showing the MTOPS connecting input-four to output-one. (a) Intensity plot. (b) Cross-sectional intensity plot at $z=18$ mm. The output power relative to the launched power for each output is: $P_1=-0.22$ dB, $P_2=-31.3$ dB, $P_3=-37.3$ dB, and $P_4=-21.1$ dB. 78
- Figure 3.30. Composite plot of the four layer mask set used in the photolithography fabrication process. Mask layers Metal 1 and Metal 2 were used to pattern the chromium heaters and gold interconnect metal. Mask layers Polymer 1 and Polymer 2 were used to pattern the cladding and core polymer layers. 79
- Figure 3.31. Plots of the individual mask layers. The chromium heaters are patterned with mask layer Metal 1 (a). The electrical interconnections were made using mask layer Metal 2 (b) to pattern gold. Mask layers Polymer 1 (c) and Polymer 2 (d) were used to pattern the cladding and core polymer layers, respectively. Note that during the mask fabrication process, negative images of layers one, two and three were generated. This was due to the use of positive photoresist in the lift-off process and simplified the layout of the cladding mask..... 80
- Figure 3.32. Photographs of the processed metal layers taken through an optical microscope. The vertical gold traces in (a), (c) and (d) are nominally $8\ \mu\text{m}$ wide. Photos (a) and (b) clearly illustrate the two layers misaligned by approximately $1-2\ \mu\text{m}$. Photos (c) and (d) illustrate adjacent heater control lines may become shorted out due to misalignment..... 82
- Figure 3.33. The locations of the five shims are shown in (a). Cross-sectional view of three 1 mil tantalum foil pieces stacked vertically (b). Note the width and length of the shims were different for each layer. Since the lower shim would displace the liquid polymer, the polymer would tend to coat the sides and even the top surface of the middle shim. To prevent the liquid polymer from adhering to the mask the top-most shim was made as narrow as possible. The middle shim was typically 3-5 mm square and the top and bottom shims were approximately 1 mm square..... 83
- Figure 3.34. Electron microscope photographs illustrating the results from the first attempt at processing the polymer (a)-(b) and using a more refined process (c)-(d). The initial process used 4 mil thick shims and because of diffraction, produced poorly defined features (a)-(b). Further process refinements and 3 mil thick shims, resulted in better delineated features. 84
- Figure 3.35. Electron microscope photographs showing waveguide sidewall roughness (a) and waveguide cross-section (b). 85
- Figure 3.36. Photograph of a processed silicon wafer. The white lines are optical waveguides..... 85

- Figure 3.37. Liquid polymer was spun on top of a patterned glass substrate (a). A patterned polymer layer results after exposure to UV light and removal of the unexposed polymer (b). 86
- Figure 3.38. Photograph of a gold patterned glass substrate (a). Resulting polymer waveguides (b) after exposure to UV light and rinsed with acetone. 86
- Figure 3.39. Light from an optical fibre on the left, is focussed by a 40x microscope objective onto the waveguide under test (or device under test, DUT). The light from the output of the waveguide is collected, collimated by a 60x objective, and focussed onto a long wavelength (germanium) photodetector approximately 50 cm from the sample. A calibrated optical power meter displays the optical power incident on the photodetector. 88
- Figure 3.40. Cut-back measurements to determine propagation loss. The trend-lines are linear curve fits to the data. The slope of the line equals the propagation loss in dB/cm. The average propagation loss is approximately 1.6 dB/cm. 89
- Figure 3.41. Photographs of the test setup used to couple light to and from the switches. A multiple lead probe is used to supply current to the heaters. Light is focused by the left microscope objective into an input waveguide. Light from the output waveguide(s) is collected by a high numerical aperture (NA) microscope objective on the right. This objective also is used to image the output light onto a camera or photodetector. 90
- Figure 3.42. The optical power from each output was normalized to the total optical power from all outputs for each of three switch states. State 1 corresponded to no current being applied to the heaters. State 2 is for the following heater currents, $I_1=27$ mA, $I_2=0$, $I_3=14.1$ mA and $I_4=0$. Switch state 3 is for the following currents, $I_1=25$ mA, $I_2=24$, $I_3=12.6$ mA and $I_4=0$. Notice the power in output four rises, while the power in output 1 falls, clearly indicating that switching has occurred. The accuracy of the data is approximately $\pm 5\%$ 90
- Figure 3.43. Pictures of the output waveguides imaged using a long-wavelength camera. The off- and on-state of a single channel are shown in (a) and (b), respectively. The intensity in (a) and (b) was reduced to prevent the camera from saturating. Images of all four output waveguides when channel three is in (c) the off-state and (d) in the on-state. 91
- Figure 3.44. Comparison of the mode structure for (a) 670 nm and (b) 1550 nm light. Predictably, more modes are supported at the shorter wavelength. 92
- Figure 3.45. Switching time measurements of a MTOPS. (a) A 10 V_{pp} 100 Hz square wave signal applied to arms two and three resulted in a rise time of 1.3 ms and a fall time of 1.4 ms. (b) A 10 V_{pp} 200 Hz square wave signal applied to arms one and four resulted in a rise time of 1.3 ms and fall time of 1.3 ms. Note, a 0.5 V_{pp} square is shown for reference instead of the 10 V_{pp} drive signal. 93

- Figure 3.46. 3D BPM simulations of the MTOPSs that have non-optimal coupler length and width. In (a) the width was increased to $76\ \mu\text{m}$. The worst contrast ratio and excess loss were 11.0 dB and 4.4 dB, respectively. In (c) the width was increased to $77\ \mu\text{m}$, and the worst contrast ratio and excess loss were 1.7 dB and 5.5 dB, respectively. Plots (b) and (d) illustrate intensity at the output of the device as a function of x at the output of the switch. 94
- Figure 4.1. Architecture of an optoelectronic switch matrix. The output from each laser on the left is split into N optical signals and broadcast to each photodetector array on the right. At the photodetector (PD) array, one of N optical signals is selected by biasing 'on' one of N photodetectors in the array. 97
- Figure 4.2. A detailed view of an O/E photodetector element. Light from four optical fibres or waveguides (left) illuminates each photodetector. Selection is achieved by biasing on one of the four photodetectors. The photocurrent is then delivered to a common output (right), 97
- Figure 4.3. Comparison of an optical network which does not contain wavelength conversion (a) and one that can reassign wavelengths (b). All spans contain a single fibre. In (a) two rings require the same wavelength in span A-B and therefore conflict with one another, whereas in (b) wavelength reassignment circumvents wavelength blocking. 98
- Figure 4.4. A wavelength cross-connect node in an optical network can be designed using only optical components or a mixture of optical and electronic devices. The all-optical approach shown in (a) requires a WDM demultiplexer/multiplexer, an optical switch and a number of wavelength converters. The second approach (b) uses an optical demultiplexer/multiplexer but replaces the optical switch with an OES and wavelength converters with optical-to-electrical electrical-to-optical transducers. 99
- Figure 4.5. In modern CATV networks, analogue and digital information signals are bi-directionally routed on a combination of optical fibre and coaxial cable. 100
- Figure 4.6. The three basic operations that can be performed by an optoelectronic switch are: summation, delay, and multiplication. The summation operation illustrates how a 1×4 MSM photodetector array is used to add four optical signals and convert the result to an equivalent electrical signal. Note that the multiplication and summation operations may be combined into a single parallel operation. The red (thick) and black (thin) lines correspond to optical and electrical signals, respectively. Delay is achieved by inserting a specific length of fibre having a known propagation delay time between each detector in an array and the splitter. 102
- Figure 4.7. Transversal filter implemented using operations that can be performed by an optoelectronic switch. The weights, V_n , are produced by altering the bias voltage of individual MSM detector. To be most practical, the frequency response of the detectors should be independent of responsivity, i.e. the bias voltage should not significantly reduce the bandwidth of the MSM. 103

- Figure 4.8. The discretely packaged 10x10 OES was a fully assembled non-blocking switch matrix. The front panel (a) illustrates the 10 electrical inputs and outputs that connect to the transmitters and crosspoints, respectively. In (b), the back of the enclosure was removed to reveal the 100 optical fibres used for the optical distribution. The dimension of the switch is 0.53 m x 0.43 m x 0.50 m. 104
- Figure 4.9. Photograph of the transmitter module package in a RF enclosure (a). Schematic of the patterned aluminium nitride substrate (b) illustrating 50 Ω coplanar transmission lines, semiconductor lasers and butt-coupled graded index multimode fibre. 105
- Figure 4.10. Schematic drawing of the 4x4 hybrid integrated optoelectronic switch matrix. Electrical signals applied to the inputs of the transmitter module at the bottom directly modulate semiconductor lasers. The resulting optical signals are transported by graded index multimode fibre to the crosspoint module. Each incoming optical signal is split into four by polymer waveguide splitters and distributed to one of four 1x4 metal-semiconductor-metal photodetector arrays. The desired optical signal selected by biasing 'on' the appropriate photodetector in the array. The resulting electrical signal is amplified and directed to one of four electrical (RF) output ports. 106
- Figure 4.11. Photograph of the packaged crosspoint module. The four rectangular devices in the centre of the substrate are the MSM photodetector arrays. Protruding through the left and right sides of the enclosure are the RF outputs (threaded SMA connectors), and electrical control lines (thin wires). The coplanar transmission lines can be seen leading away from the MSM photodetector arrays. 107
- Figure 4.12. The gold pattern alumina substrate (top) provides physical support and electrical connections to the metal-semiconductor-metal photodetector arrays (bottom)..... 108
- Figure 4.13. Scale drawing of the optical distribution submount (a) illustrating the locations of the 1x2 polymer splitters. The positional information in (a) was used for defining both laser written and photolithographic polymer waveguides. A scanning electron microscope photograph of a laser written polymer waveguide with a 45° cut is shown in (b). A cross-section of the polymer waveguide (c) reveals how light travelling from left to right is redirected vertically out-of-plane by a 45° angle-cut in the polymer via total internal reflection at the polymer-air interface. 109
- Figure 4.14. Cross-sectional view (left) and top view (right) of a typical MSM photodetector. Not shown is a cap or passivation layer that has the dual purpose of reducing surface charge traps and operating as a narrow-band anti-reflection coating. 110
- Figure 4.15. Photograph of a single MSM photodetector. The light coloured area represent the metal fingers and metal interconnect, while the darker areas are semiconductor material. Also visible is the mesa edge used to isolate adjacent devices and reduce surface leakage current..... 111
- Figure 4.16. Measured DC I-V characteristic for a long wavelength MSM photodetector. (source [74]). Note that higher bias voltages are required to saturate the device.. 112

- Figure 4.17. An electron (-) and hole (+) pair generated by an incident photon, that has an energy greater than the bandgap of the semiconductor, are swept to the cathode (+) and anode (-), respectively, due to the internal electrical field created by the bias voltage. If the field is strong enough, the electrons and holes will reach their saturation velocities in a very short distance. 113
- Figure 4.18. Schematic drawing of a 1x4 linear array of independently bias controlled MSM photodetectors connected to a common RF bus. 113
- Figure 4.19. Photograph of a 1x8 linear MSM array. Also shown on the left, right and bottom side of the die are the wire bonds used to provide electrical connections to the RF substrate. For a perspective of size, the bias bond-pads (bias pads) are 100 μm on each side. 114
- Figure 4.20. Frequency response from a first generation 1x4 linear MSM photodetector array. Note that although the 3-dB bandwidth of the device was limited to 2.35 GHz, the detector was still responsive up to >5 GHz, indicating that a better design could substantially improve the operational bandwidth. The lower two curves indicate the isolation when the bias was set to zero under illumination and the noise floor of the test setup. 114
- Figure 4.21. A approximate lumped element model of a linear array of MSM photodetectors attached to a common bus. $C_{i\text{off}}$ is the total capacitance of the i^{th} MSM plus the wirebond pad in the "off" or unbiased state. Similarly, $C_{i\text{on}}$ is the total capacitance of an MSM and its bondpad, in the "on" or biased state. V_{on} indicates a bias voltage present on detector two. 115
- Figure 4.22. Unit cell for the new mask set designed by DeCorby [74]. The unit cell, measuring approximately 21 mm square, is repeated nine times on the mask. A total of 5 masks, one for each layer, are used when fabricating the MSM photodetectors. In addition to the photodetector arrays, there are individual detectors used for comparison testing, and a differential photodetector element. The large red rectangle is an opening in the mask that aids in the alignment process and is used for process calibration and monitoring purposes. 116
- Figure 4.23. Layout for three different second generation MSM photodetector arrays that incorporate the impedance matched bus concept and coplanar transmission lines. (a) Shows a 1x4 array with detectors on 1 mm pitch designed for the 1x4 hybrid integrated OES. In (b) the MSM detectors were attached to both sides of the array to facilitate the larger 1x16 array while maintaining isolation. In (c) a serpentine bus was used so that the detectors are co-linear. MSM detectors are the red squares, the common bus is turquoise, the ground plane metal is purple and green represents where windows will be opened. 117
- Figure 4.24. Scale view of the mask layout designed by the author and used to create the optical distribution in the hybrid integrated OES. On the mask, the dark lines are 50 μm wide and correspond to the absence of chrome. Thus, when UV light is exposed through a mask placed overtop a polymer coated substrate, the exposed polymer cures and forms optical waveguides. The longest waveguide is 78 mm long. 118

- Figure 4.25. Main interface window of the LabView control program, called PC-XYZ. Real-time control and monitoring of three axes can be done from this window. The Module Selection box (located right middle) is used to select pre-written routines, such as S-bends, splitters, calibration routines, etc. The program is highly modularized, and is currently being expanded to allow users to load a CAD layout file into the program. 119
- Figure 4.26. Photograph showing the laser writing station. The two crossed linear translation stages are indicated as the upper and lower stage. Some of the optics used for beam expansion and collimation can also be seen in the background. .. 119
- Figure 4.27. Photographs of the crosspoint substrate use in the first prototype OES. The photo on the left illustrates the bare substrate and the polymer waveguides. The red material is a thin layer of photoresist that was used as a buffer and UV light absorber. Without this layer, the reflected laser light from the rough gold film was diffuse and resulted in distorted waveguide profiles (a lower grade 96% unpolished alumina substrate was used). On the right, one output channel was populated and tested. The horizontal lines barely visible are the laser written polymer waveguides..... 123
- Figure 4.28. Scale view of the RF substrate used in the crosspoint module for the second prototype designed by the author. The yellow areas are evaporated gold. Also, the gold are is a ground plane, with the exception of the centre conductors of the coplanar transmission lines. The coplanar transmission lines were used to minimize cross-talk and only require one side of the substrate to be metalized. Furthermore, vias were not required to connect components, i.e. resistors, capacitor and inductors, because the ground plane is on the same surface..... 123
- Figure 4.29. Circuit schematic for bias decoupling. L_{WB} is the inductance from each wire-bond and L_{FB} is the inductance of the ferrite bead (lossy inductor). The proximity of the first capacitor to the MSM is crucial in achieving high frequency decoupling (the 82 pF capacitor is a parallel plate capacitor measuring $\sim 400 \mu\text{m}$ on each side). A π -circuit is constructed from the 1 nF and 10 nF capacitors and the ferrite bead..... 124
- Figure 4.30. Photograph of a vector network analyzer. The two coaxial cables at the bottom are used to measure the frequency characteristics of an RF device. 125
- Figure 4.31. Frequency response from one MSM detector array in the second switch prototype. The responses for each of the four channels are offset for clarity. 126
- Figure 4.32. Photograph of the laser transmitter used in the first prototype. All the passive and active components were secured to the RF substrate using silver epoxy. 126
- Figure 4.33. Frequency response of the first prototype transmitter module. The 3 dB bandwidth is approximately 2 GHz, which surpassed the targeted 1.2 GHz bandwidth of the 10x10 discretely packed OES. 127
- Figure 4.34. Frequency response plot of one laser transmitter channel from first prototype OES 128

Figure 4.35. Frequency response plots for two different lasers. Not that both transmitters exhibited a low frequency gain, or mid-frequency loss.	128
Figure 4.36. Electrical schematic (a) of the high-pass equalizer circuit used for the lasers in the second prototype OES. The frequency response of the equalizer is shown in (b). The insertion loss of this device was 2.5 dB.	129
Figure 4.37. Light-current plots for seven lasers tested for use in the second prototype transmitter module. The lasers were classified into two groups: Group 1 has a slope efficiency of 0.04 mW/mA and Group 2 has a slope efficiency of 0.017 mW/mA. Only those with the higher slope efficiency were used in the second prototype transmitter module.	130
Figure 4.38. Frequency response plots for two different lasers. The plots were obtained for three different fibre positions: blue was very close to the laser facet (<10 μm), green was about 25-50 μm from the facet and black was about one fibre width or 125 μm from the facet. Note that as the fibre gets closer to the laser facet the amount of light collected increase, i.e. more signal power, however, the relative intensity noise also increases. Also, it can be seen that the effect of back-reflected light affects the two lasers differently.	130
Figure 4.39. Photograph illustrating the BERT and high speed digital oscilloscope (left). Some of the RF components used to increased the data rate beyond the BERT's 3 Gb/s limit are visible on the right.	131
Figure 4.40. Measured transmitter eye-diagrams for the second prototype at the following bit rates: (a) 0.5 Gb/s, (b) 1 Gb/s, (c) 3 Gb/s, (d) 6.7 Gb/s, (e) 8.2 Gb/s and (f) 9.95 Gb/s. Clearly the transmitter module is capable of transmitting data at various rates. The eye closure for data rates greater than 3 Gb/s was partly due to the test setup.	132
Figure 4.41. Eye-diagram for a 9.95 Gb/s binary signal when the test setup is connected electrically back-to-back. Significant signal distortion is imparted by the test setup.	133
Figure 4.42. System (transmitter and crosspoint modules) eye-diagrams for (a) 6 Gb/s and (b) 9.95 Gb/s binary data. Some of the eye closure was attributed to the test setup (see Figure 4.41).....	134

List of Symbols

c	Mode Coupling Factor, speed of light
E	Electric Field
f	Frequency
h	Impulse Response or Interfacial Heat Transfer Coefficient
I	Intensity of Light
I_p	Photo-current
I_d	Dark current
k	Wavenumber in a Material
k_B	Boltzman's Constant
k_o	Wavenumber in free-space
L_π	Beat Length of a Multimode Interference Coupler
M_m	Characteristic Matrix for the m^{th} Layer
M	Characteristic Matrix
N_f	Effective Refractive Index of the Film or Core Layer
N_c	Effective Refractive Index of the Cladding Layer
n	Index of Refractive
Δn	Change in Refractive Index
n_{avg}	Average Index of Refractive
P	Optical Power
P_l	Phase Matrix for the Low Refractive Index Layer
P_h	Phase Matrix for the High Refractive Index Layer
Q	Spectral Reflection Funtion
q	Electron Charge
R_U	Reflection Matrix for a High/Low Index Step
R	Power Reflectance or Electrical Resistance

r	Complex Reflectance
T	Temperature or Time Delay
V_n	Bias Voltage of the n^{th} MSM Photodetector
W_{eff}	Effective Width of a Multimode Interference Coupler
W	Physical Width of a Multimode Interference Coupler

Greek Symbols

β	Propagation Constant
Φ	Complex Scalar Electric Field of a Waveguide Mode
ϕ	Phase Factor
ϕ_h	Phase Delay Encountered in a High Index Layer
ϕ_l	Phase Delay Encountered in a Low Index Layer
Λ	Optical Period of a Rugate Filter
λ	Wavelength of Light
$\Delta\lambda$	Change in Wavelength

List of Abbreviations

ADM	Add Drop Multiplexer
AlN	Aluminum Nitride
AR	Anti-reflection
BERT	Bit Error Rate Tester
BLSR	Bi-directional Line Switched Ring
BPM	Beam Propagation Method
BW	Bandwidth
CAD	Computer Aided Drafting
CATV	Cable Television
CM	Characteristic Matrix
CMM	Characteristic Matrix Method
CVD	Chemical Vapour Deposition
DC	Direct Current
DFB	Distributed Feedback
DS	Digital Signal
E/O	Electrical-to-Optical
FOCSS	Fibre Optic Communication Systems Simulator
GaAs	Gallium Arsenide
GLAD	Glancing Angle Deposition
GRIN	Graded Index
HP-MDS	Hewlett Packard Microwave Device Simulator
InP	Indium Phosphide
LAN	Local Area Network
MgF ₂	Magnesium Fluoride
MMI	Multimode Interference
MSM	Metal-Semiconductor-Metal

MTOPS	Multimode Thermo-optic Polymer Switch
MZI	Mach-Zehnder Interferometer
NOA	Norland Optical Adhesive
OC	Optical Carrier
OES	Optoelectronic Switch
OSI	Open System Interconnection
RF	Radio Frequency
RIN	Relative Intensity Noise
ROP	Relaxation Oscillation Peak
SA	Simulated Annealing
SEM	Scanning Electron Micrograph (or Microscopy)
Si ₃ N ₄	Silicon Nitride
SiO	Silicon Monoxide
SNR	Signal-to-Noise Ratio
SONET	Synchronous Optical Network
STP	Standard Temperature and Pressure
STS	Synchronous Transport Signal
TDM	Time Division Multiplexing (Multiplexed)
TE	Transverse Electric
TM	Transverse Magnetic
TRLabs	Telecommunications Research Laboratories
UPSR	Unidirectional Path Switched Ring
UV	Ultra-violet
VCSEL	Vertical Cavity Surface Emitting Laser
WDM	Wavelength Division Multiplexing (Multiplexed)
WXC	Wavelength Cross-connect

1. Introduction

1.1 Overview of Lightwave Transmission Systems

Demand for information capacity (bandwidth) is growing at an exponential rate. Modern long-haul transport networks use fibre optic cable, rather than coaxial cable or microwave links, to transmit information from source to destination because optical fibre has a number of inherent benefits such as low attenuation, frequency independent attenuation, low cost and large bandwidth. However, the fibre optic backbone networks have nearly reached full utilization. Burying new fibre underground is both expensive and slow; notwithstanding, the average rate of new fibre deployment in the world for 30-count single-mode fibre cable is 80 km/hr or 700,800 km/year [1].

The performance of silica fibre lightwave systems has progressed from the 1970s to the 1990s in a series of five generations [2], whereby each succeeding generation improved upon the performance of the last. A brief description of each generation follows.

First generation lightwave systems (1970s) operated at a wavelength of 830 nm and used multimode fibre because semiconductor devices, such as light emitting diodes (LED), semiconductor laser diodes (SLD) and photodetectors, could be fabricated from GaAs. They operated at a line or bit rate of 45 Mb/s and allowed a non-regenerated link distance of approximately 10 km.

Second generation systems (early 1980s) used LEDs and SLDs fabricated from InGaAsP operating at a wavelength of 1310 nm. Initially, multimode fibre was used, but later, fibre that supported a single transverse mode (single-mode fibre) was introduced. In addition, silica fibre has a local attenuation minimum (0.5 dB/km) and a minimum dispersion (pulse spreading) at 1310 nm. These systems were capable of transmitting data at a rate of 1 Gb/s over 50 km fibre.

Third generation systems (late 1980s) used single longitudinal mode SLD operating at 1550 nm, the attenuation minimum of silica fibre (0.2 dB/km). Fibre attenuation limited the maximum non-regenerated distance to approximately 100 km for gigabit per second transmission rates.

Fourth generation systems also operated at a wavelength of 1550 nm; however, the distance between electronic regenerators was substantially increased by using erbium doped fibre amplifiers (EDFA) to directly amplify the optical signal. Current point-to-point link distances of 140 km operating at 10 Gb/s using standard single-

mode fibre are commercially available [3]. Unless dispersion compensation techniques are used, the dispersion characteristics of standard single-mode fibre now limit the maximum non-regenerated distance, instead of attenuation.

The fifth generation of lightwave systems has not been strictly defined. Some consider optical transmission based on solitons, which are intense non-dispersive optical pulses, to be the fifth generation. Many now believe that dense wavelength division multiplexed (DWDM) transmission is the fifth generation lightwave system. Since the effects of dispersion are proportional to the square of signal bandwidth (or approximately the signal bit rate), increasing the bit rate much beyond 10 Gb/s may be impractical because of fibre dispersion and the requirement for advanced ultra-high-speed electronics, transmitters and receivers. Instead of increasing the bit rate of the time division multiplexed (TDM) signal, multiple wavelengths may be simultaneously transmitted through a single fibre.

A typical WDM point-to-point link is shown in Figure 1.1. Note that a single optical fibre is used to carry multiple signals. WDM transmission has become the leading candidate for increasing transmission capacity for the following reasons: 1) standard EDFAs simultaneously amplify optical signals from 1530 nm to 1565 nm thereby reducing system cost and complexity because individual wavelength channels do not need to be optically demultiplexed and separately amplified; 2) many wavelength channels can be transmitted through a single fibre; 3) WDM/DWDM components are commercially available; 4) the installed fibre plant can be more efficiently utilized. Hence transmission capacity is increased without requiring the installation of new fibre. For instance, 4-channel 10 Gb/s DWDM systems were developed in 1996, and 32-channel 10 Gb/s DWDM systems are commercially available [3], and 64 and 128-channel systems are on the horizon [4].

Applications such as the Internet, multimedia services, local area networks (LANs) and metropolitan area networks (MANs) are beginning to exploit the benefits of inexpensive and large transmission capacity offered by DWDM system providers.

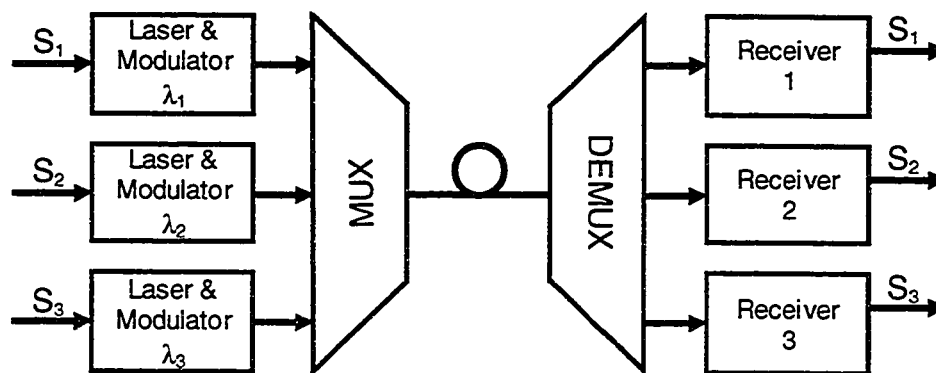


Figure 1.1. Schematic diagram of a three channel WDM system. Electrical signals S_i are converted to optical signals each having a unique wavelength. A WDM MUX combines the three separate wavelengths from three fibres onto a single optical fibre. At the receiving end, a DMUX is used to separate the wavelengths and receivers convert the optical signals to electrical ones.

1.2 Enabling Technologies for WDM Systems

A technology that can increase the capacity of fibre without the need to bury new fibre has obvious cost savings potential. As previously mentioned, fourth generation systems employ EDFAs. Standard EDFAs have an optical gain spectrum extending from approximately 1530 nm to 1560 nm. In this wavelength range, small signal gains of 20-50 dB have been realized, in conjunction with saturation power of ~100 mW (20 dBm). Optical amplifiers overcome fibre attenuation; however, the transmission of a high bit rate (10 Gb/s or greater) TDM signal is limited by dispersion, with 1000 Gb/s-km being a typical bandwidth-distance product (BDP). Incorporating dispersion compensation can increase the BDP, but it is both costly and difficult to manage. Furthermore, TDM signals only use a small fraction of the available fibre bandwidth. For instance, the bandwidth of a typical EDFA is approximately 30 nm or 3.7 THz, hence a 10 Gb/s TDM signal uses only 0.5% (assuming the required bandwidth is 20 GHz), whereas a 10 Gb/s 32-channel DWDM system uses 17% of the available bandwidth. Clearly, the DWDM system better utilizes the inherent bandwidth in fibre systems. Moreover, bandwidth-extended EDFAs have been demonstrated to operate from 1530 nm to 1610 nm [5], doubling the bandwidth available to DWDM systems.

Standard single-mode fibre, which currently represent 95% of the installed fibre base [1], has a dispersion coefficient of 17 ps/(nm·km) at a wavelength of 1550 nm and limits the non-dispersion compensated BDP to 1 Tb/s·km. In 1998 Lucent Technologies announced two new fibres, AllWave™ and TrueWave™ [6]. Standard fibre has an OH hydroxyl ion absorption peak around 1400 nm; however, AllWave™

eliminates this peak, allowing transmission over the 1310 nm to 1550 nm wavelength range. AllWave™ is targeted at the metropolitan area networks (MAN) and cable television (CATV) networks that do not require optical amplifiers, thereby allowing the entire 1310 nm - 1550 nm spectrum to be used. TrueWave™ is specifically designed for long haul DWDM applications. The attenuation spectrum is uniform from 1530 nm to 1620 nm and the dispersion coefficient has been reduced to ~ 4 ps/(nm·km). Hence, systems employing this new fibre will be capable of a larger number of wavelength channels and extend the dispersion limited distance by more than a factor of four.

In addition to advances in EDFAs and optical fibre, optical multiplexer (MUX) and demultiplexer (DMUX) components have made rapid progress in the last few years. MUXs combine wavelengths from N fibres onto a single fibre, whereas DEMUXs split N wavelengths carried on one fibre to N fibres. Various techniques can be used to implement a MUX/DMUX, such as arrayed waveguide gratings (AWG), fibre Bragg gratings and interference filters. Each has its own advantages and disadvantages. The International Telecommunications Union (ITU) standardized on a 100 GHz wavelength channel spacing. Nonetheless, ultra-DWDM laboratory demonstrations have used a 50 GHz channel spacing, which demand extremely high performance MUXs/DMUXs and manufacturers have demonstrated 160-channel WDM demultiplexers [7].

AWGs (Figure 1.2) are photonic integrated circuits fabricated using micro-fabrication techniques and consist of a passive power splitter, a section of parallel waveguides (arrayed waveguides) and a passive power combiner. The length of each successive arrayed waveguide is longer than the previous one by a constant value. Hence the light in each successive waveguide is delayed by a multiple of this constant and the device behaves similar to a diffraction grating. The tolerance of the waveguide delays, the collection efficiency of the arrayed-waveguides and the cross-talk between adjacent waveguides are key parameters that must be simultaneously optimized to achieve high performance devices.

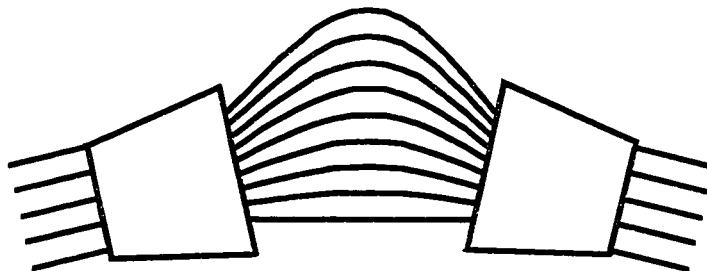


Figure 1.2. Schematic drawing of an arrayed-waveguide grating. Slab waveguide power splitter/combiners are used. Increasing the number of waveguides between the power splitter and combiner reduces the insertion loss and increases resolution of the device.

A fibre Bragg grating (FBG) is effectively a volume diffraction grating created inside an optical fibre. By inducing a periodic sinusoidal variation in the refractive index of the core/cladding of an optical fibre, certain wavelengths will be reflected and others transmitted. Wavelengths near the Bragg wavelength (the Bragg wavelength is equal to twice the period of the refractive index modulation) are reflected. A MUX or DMUX can be constructed by cascading a series of FBGs. Each FBG is tuned to a slightly different wavelength and separated by a directional coupler. One added benefit of FBGs is that they are directly compatible with single-mode fibre, thereby simplifying assembly and coupling.

A third technique used to construct wavelength MUX/DMUXs incorporates thin-film interference filters. An optically transparent film of alternating layers of high and low index materials, each one-quarter wavelength thick, is deposited on a transparent substrate. Light corresponding to the appropriate wavelength(s) will be reflected. A schematic drawing of an interference filter MUX/DMUX is shown in Figure 1.3. The thin-film layers are usually deposited with conventional vacuum deposition techniques. A novel method of fabricating these filters using glancing angle deposition (GLAD) is presented in Chapter 2.

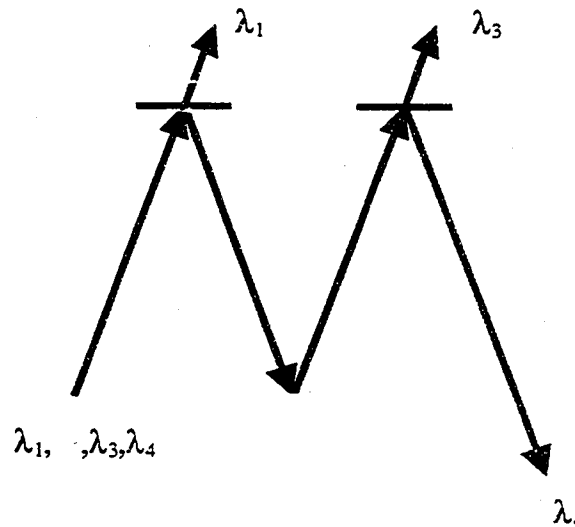


Figure 1.3. Implementation of a four-channel wavelength demultiplexer with thin-film interference filters. Each filter transmits only a single wavelength and reflects the rest.

1.3 Signal Transparent Networks

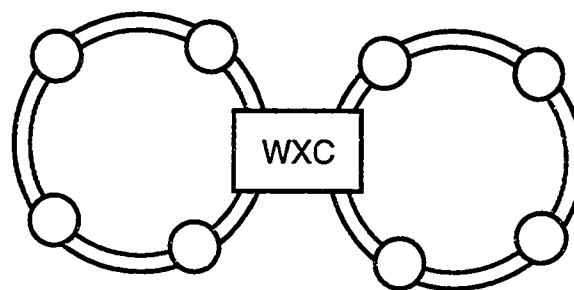
Although WDM point-to-point links are now installed in commercial systems, the technology has not yet been fully exploited. In a typical WDM link, the optical

signals are demultiplexed at each node, converted to electrical signals, switched and retransmitted as optical signals. The disadvantages with this approach are that it limits the bandwidth for future upgrades and requires that all the optical signals be converted, even though some optical signals simply pass through the node. Therefore, the next logical step *may* be an all-optical network, which could potentially eliminate the unnecessary and costly electrical conversion process.

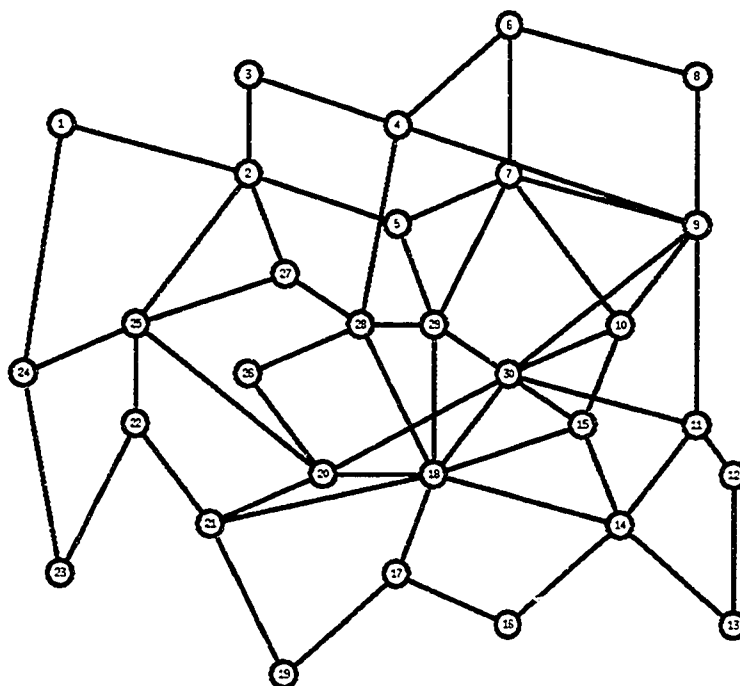
In an all-optical network, the signals remain in the optical domain during the entire transmission process. The signal is only converted to the electrical domain when access to one of the baseband electrical signals is required or when the signal must be regenerated. As a result, an optical switch and optical wavelength converter are required. This is indeed daunting, since optical wavelength converters are not commercially available and suffer from various practical difficulties, such as high cost, high polarization dependence, and high noise figures [67]-[68].

It now is becoming apparent that all-optical networks may only be practical for small or constrained networks. For example, most transport networks are designed with a ring architecture, as shown in Figure 1.4. It is relatively easy to administer and manage optical rings. If the signal were to remain in the optical domain, wavelength contention may occur on adjacent rings. Furthermore, dispersion and attenuation will go unchecked unless these effects are managed on a signal-by-signal basis, greatly complicating administration and operation of a network. Hence, the wavelength cross-connects may need to be signal transparent, not optically transparent. The distinction is subtle and leads to many ramifications. If the optical signals are converted to electrical signals when they traverse from one ring to the next, they may be transmitted using any available wavelength, avoiding wavelength contention or resolution. Furthermore, it is much easier to reamplify, reshape, and retime (3R regeneration) the signal in the electrical domain than in the optical domain. It is because of these and other reasons that all-optical networks, at least in the near term, may be deployed as signal transparent networks rather than optically transparent networks.

A signal transparent network is one in which the signal may be transmitted using wireless, optical or electrical techniques, but does not impose a bit rate or signal format restriction. In effect, a signal transparent network is equivalent to an analogue network. Thus, any signal format, such as quadrature amplitude modulated, binary, duobinary, multilevel, etc., operating at an arbitrary bit rate can be transmitted, with the proviso that it does not exceed the analogue bandwidth of any network component.



(a)



(b)

Figure 1.4. (a) Individual rings may be administered and provisioned as all-optical rings. When two ring intersect, an opaque wavelength cross-connect (WXC) may be used to avoid wavelength contention and perform 3R regeneration. (b) Complex networks with multiple rings will require sophisticated management if the entire network is all-optical.

1.3.1. Wavelength Cross-connects

One component that may be necessary in optical networks is a wavelength cross-connect (WXC), whereby any wavelength channel on an input fibre(s) can be connected to any wavelength channel in the output fibre(s). One major obstacle with all-optical WXC is that an optical wavelength converter is required. Current research devices suffer numerous problems, such as poor signal-to-noise ratio, high power consumption, and poor conversion efficiency [66],[68]. However, electronic or

optoelectronic WXC may be constructed with existing commercially available components, such as wavelength MUX/DMUX and optoelectronic or electronic switch cores. Although it is difficult to construct an analogue electronic switch with the required performance, analogue optoelectronic switches with the required bandwidth and cross-talk isolation have been demonstrated [73]. Analogue switches are required if signal transparency is to be maintained. Digital electronic switches imply that the data stream operate at a particular bit rate and maintain a binary format.

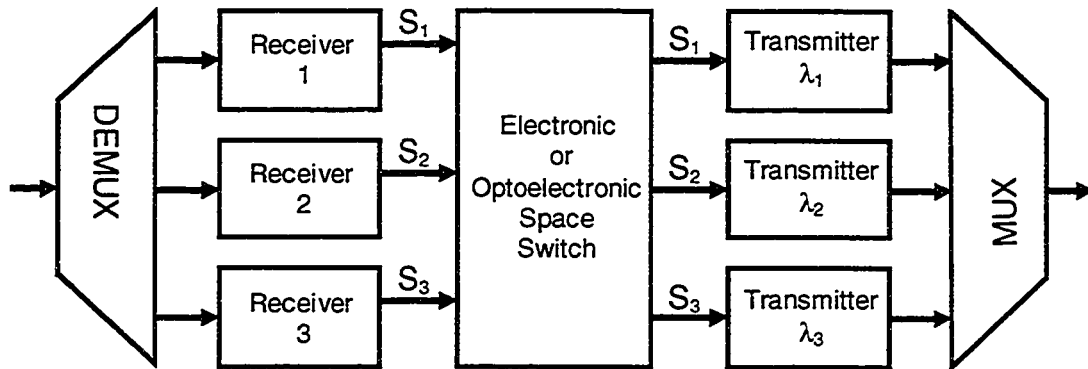


Figure 1.5. A wavelength cross-connect using an electronic or optoelectronic space switch, MUXs/DMUXs, receivers (photodetectors) and transmitters (lasers and modulators). An all-optical WXC may be constructed by replacing the electronic space switch with an optical switch, eliminating the transmitters and replacing the receivers with optical wavelength converters. Note, S_i are the electrical information signals.

A prototype optoelectronic switch that may have the necessary bandwidth, cross-talk suppression, has been developed at TRILabs [62]. Chapter 4 discusses the details of the operation and construction of a 4x4 hybrid integrated optoelectronic switch.

1.4 Thesis Organization

The main body of this thesis is divided into three chapters, each discussing a single topic. Each chapter is self-contained, describing the relevant theory, design, experiments, and applications.

In Chapter 2, thin-film interference filters are discussed. An introduction to the design and fabrication of thin-film interference filters is given. The relevant theory necessary to design interference filters is then developed. A filter synthesis tool incorporating some of the theoretical developments and performance optimization routines written for Windows95/NT platform is introduced. Using the tools developed,

a GLAD thin-film filter was fabricated. The reflection spectrum was measured and compared to the original simulations. A summary is also provided.

In Chapter 3, a multimode polymer based thermo-optic switch is discussed. The primary application is to incorporate the 1x4 optical switch into the optical distribution of a 4x4 hybrid integrated optoelectronic switch. The optical design and simulation is performed with a beam propagation method program. Thermal modeling of the device was performed to predict the required switching power and response time. A number of devices were fabricated at the Communication Research Centre (CRC) in Ottawa. A modified photolithography technique was developed to work with the liquid UV-curable polymers. Switching and passive measurements of the fabricated devices are provided. Comparisons between theory and experiment are made and comments regarding the differences are discussed.

Chapter 4 presents the work on a 4x4 hybrid integrated optoelectronic switch matrix. Introduction to the basic optoelectronic switching principle is presented. Applications of the optoelectronic switch in WDM networks, CATV networks and for broadband signal processing are discussed. A description of the crosspoint and transmitter module construction and testing are then given. Future design issues regarding improved performance and scalability are then addressed

Recommendations for further work and conclusions are given in Chapter 5.

2. Inhomogeneous Thin Film Optical Filters Fabricated Using Glancing Angle Deposition

2.1 Introduction

Optical filters are used extensively in diverse applications, including telecommunications, photography, and spectroscopy. One important type of optical filter is fabricated by depositing thin films of transparent optical materials onto a surface to alter its transmission or reflection spectrum. For example, anti-reflection coatings are used to coat camera lenses, microscope objectives, telescope lenses, and eyeglasses, in order to maximise transmission and minimise reflections. High-reflection coatings are used to create highly reflective surfaces, such as those found on telescope mirrors.

Optical filters capable of very high spectral resolution are based on interference effects. Fabry-Perot filters and interference filters employ resonances inside optical cavities resulting in constructive and destructive interference. The spectral response and theory pertaining to the more common cavity filters such as the Fabry-Perot filter are quite different from those of other types of interference filters, such as rugate filters and quarter wave stacks. Hence, we will not discuss cavity filters.

When light enters an interference filter, a portion is reflected at each discontinuity in the filter. The distributed reflections from the filter then add coherently causing constructive or destructive interference at the output. Consequently, these filters are known as multiple interference filters or simply interference filters.

The most common interference filter configuration is a quarter-wave stack (QWS). A QWS is fabricated by growing alternate high and low index layers, one-quarter wavelength thick, on top of each other. The filter will reflect light whose wavelength is twice the optical thickness of the periodic high-low index structure. In the case of a QWS, the optical thickness (defined as the physical thickness times the refractive index) of one period is equal to

$$OT = n_H t_H + n_L t_L \quad (2.1)$$

where n_H and n_L are the refractive indices of the high and low regions and t_H and t_L are the physical thickness of the high and low index regions, respectively.

A second type of multiple interference filter is a rugate filter. A typical rugate filter has a continuously graded refractive index as a function of depth. Often the refractive index profile is designed with a periodic quasi-sinusoidal refractive index variation, as will be discussed in a later section.

In general, the refractive index profile of a rugate filter may be fabricated from an inhomogeneous film of material (continuously varying index profiles), or from a series of homogeneous thin-film layers (layers of constant refractive index), which simulate a continuous graded film. As a result, either homogeneous or inhomogeneous refractive index profiles can be used to create rugate filters.

It is evident that there are a number of constraints and features that must be concurrently addressed in filter design and fabrication. Table 2.1 summarises some parameters of interest. It will be shown in the following sections that the glancing angle deposition (GLAD) thin-film growth technique can achieve many of the criteria listed.

Table 2.1. Properties and characteristics of optical filters. A filter design must address each issue concurrently, while still allowing for an optimum design.

Optical Property	Mechanical Property	Processing/Fabrication Features
<ul style="list-style-type: none"> • Bandwidth control • Reflection or Transmission efficiency 	<ul style="list-style-type: none"> • Rugged • Hard surface/scratch resistant • Environmentally robust, i.e., insensitive to temperature, humidity, etc. 	<ul style="list-style-type: none"> • Deposition time • Yield • Film uniformity (related to yield) • Intrinsic film stress

2.2 Rugate Filters

Optical interference filters are created by depositing a number of thin-film layers onto a substrate. Often dielectric materials are used because of their hardness, spectral transparency and high refractive index. Metals are also used, but are usually restricted to high-reflectivity mirror coatings. If alternating high and low index layers one-quarter wavelength thick are deposited, incident light will be reflected at the wavelength of interest. This is a result of multiple reflections interfering with each other, producing a symmetric reflection peak of a particular bandwidth about the centre wavelength.

A rugate filter has continuous variations in the refractive index profile as a function of depth. These filters may be made of a number of discrete layers that synthesise a continuous variation, or be a true continuous/graded refractive index

variation [8]. The discrete implementation requires many layers, typically a few tens of nanometres thick, of alternating high and low index materials. This can be thought of as “pulse width modulation” of the refractive index profile. Filters created using discrete layers are classified as homogeneous films, because the index is constant for some given thickness. In contrast, a continuous refractive index variation is usually obtained with an inhomogeneous film whose refractive index changes constantly as a function of depth.

2.2.1. Index Profile of a Rugate Filter

Before a spectral reflection calculation can be performed, it is necessary to describe the refractive index profile mathematically. For a simple rugate filter having a single sinusoidal index modulation, the index profile can be described by

$$n(x) = n_{avg} + \frac{\Delta n}{2} \sin\left(\frac{2\pi x}{\Lambda} + \phi\right) \quad (2.2)$$

where n_{avg} is the average index, Δn is the peak-to-peak index variation, ϕ is a phase term which may be a function of x , $\Lambda = \lambda_o / 2 \cdot n_{avg}$ and λ_o is the vacuum wavelength. Equation (2.2) describes a rugate filter that has a single reflection peak centred about λ_o . The index profile and reflection spectrum are shown in Figure 2.1.

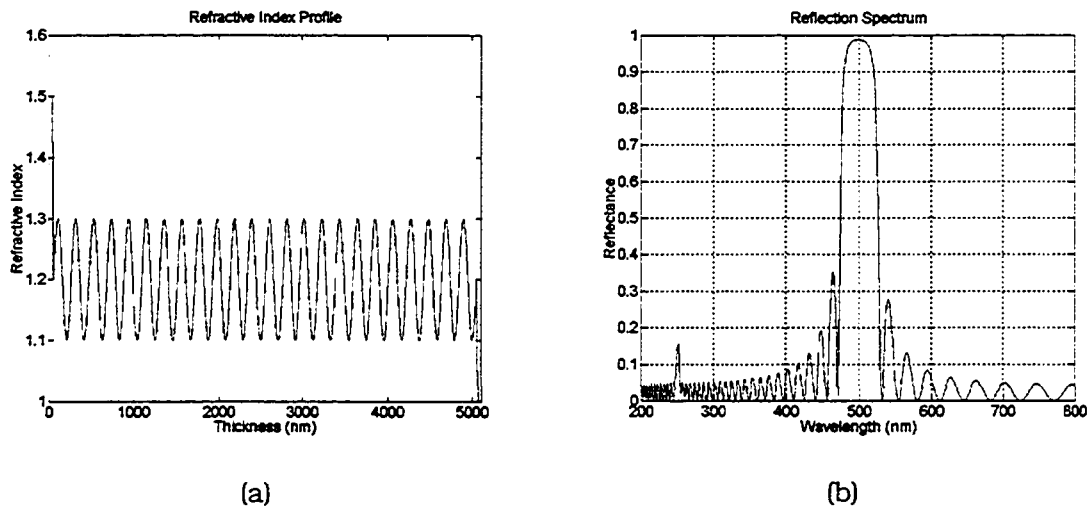


Figure 2.1. Refractive index profile for a rugate filter with a single reflection peak. The refractive index profile is shown in (a) and the corresponding reflection spectrum in (b). Note that the glass ($n=1.5$) and air ($n=1$) interfaces have been included in the refractive index profile in (a).

The index profile of a generalized rugate filter is described by

$$n(x) = n_{avg} + \sum_{j=1}^M \frac{\Delta n_j}{2} \sin\left(\frac{2\pi x}{\Lambda_j} + \phi_j\right) \quad (2.3)$$

where there are now M reflection peaks and $\Lambda_j = \lambda_j / 2 \cdot n_{avg}$. One advantage of rugate filters is their ability to produce reflection peaks at multiple wavelengths as defined by the previous equation. For example, Figure 2.3 and Figure 2.2 illustrate two possible multi-line rugate filters.

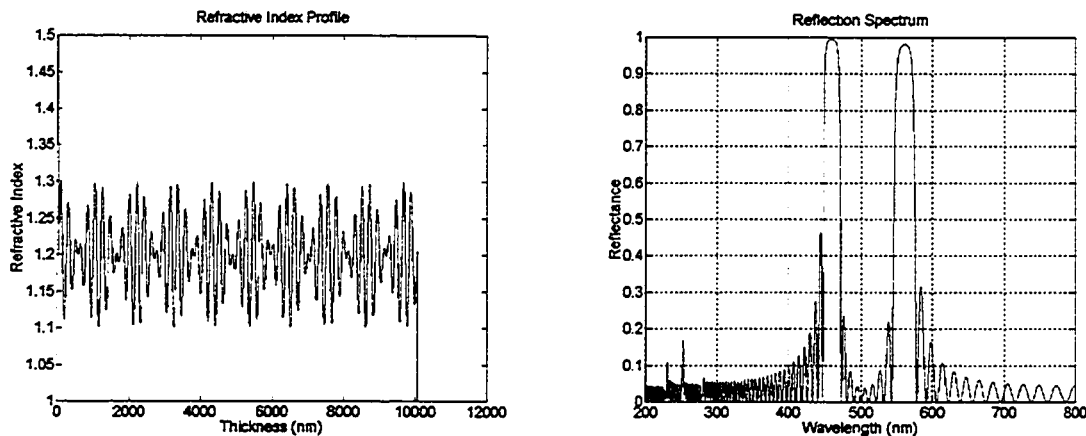
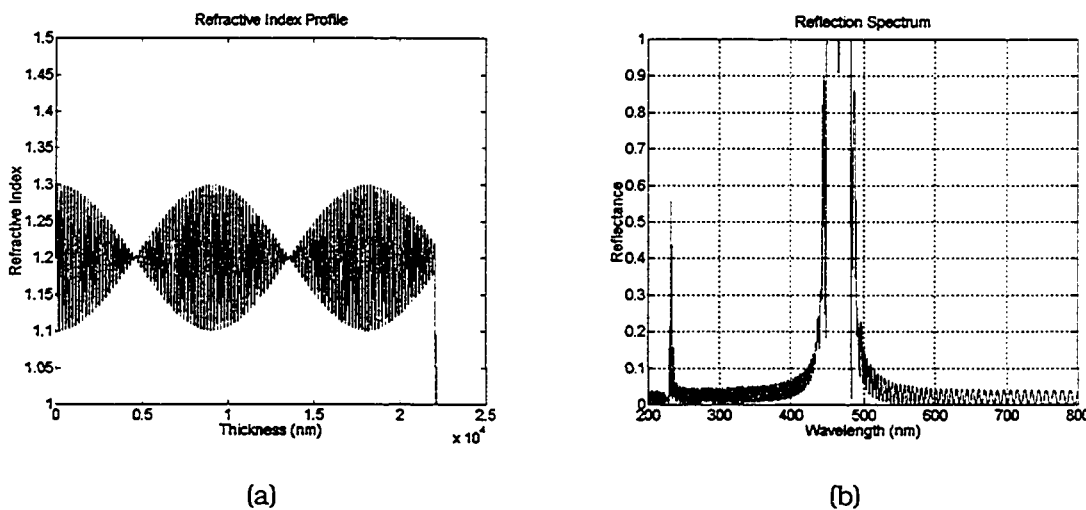


Figure 2.2. Refractive index profile corresponding to a rugate filter with two peaks centred at 460 nm and 560 nm. Shown on the right is the corresponding reflection spectrum.



(a)

(b)

Figure 2.3. Refractive index profile corresponding to a rugate filter with two peaks centred at 460 nm and 470 nm. This configuration may be used to create a reflection peak that is broader than those obtained by using a single line filter for a given filter thickness.

The reflection spectra shown in Figure 2.1 and Figure 2.3 do not include an anti-reflection (AR) coating. AR-coatings provide an intermediate layer that reduces the mismatch between two material interfaces. Without an AR-coating, broadband reflections occur, resulting in a filter with poor spectral characteristics.

2.3 Methods of Calculating a Reflection Spectrum

Accurate and flexible methods of calculating the reflection spectrum of a rugate filter are of paramount importance if high calibre optical filters are to be designed. Important attributes of good numerical models include accurately calculating a reflection spectrum and performing the calculation on arbitrary refractive index profiles. As is often the situation, there are trade-offs among accuracy, flexibility and speed of computation. Hence an overview of the most common methods of calculating reflection spectra will be presented.

2.3.1. Characteristic Matrix Method

The most flexible and accurate method is denoted as the "characteristic matrix method" (CMM). This method is capable of computing the reflection spectrum of an arbitrary index profile, but neglects the effects of chromatic dispersion and attenuation [9]. The basic steps required to implement the method include: discretising the index profile into layers of constant refractive index, calculating the characteristic matrix (CM) of each layer, computing the total CM by sequentially matrix multiplying all the individual CMs, and finally calculating the complex amplitude reflectance from the elements of the CM. Repeating this exercise over a range of wavelengths results in a reflection spectrum.

A differential equation relates the forward and backward travelling electromagnetic wave [10], and is given by

$$\frac{d}{dz} \begin{bmatrix} A(z) \\ B(z) \end{bmatrix} = C(z) \begin{bmatrix} A(z) \\ B(z) \end{bmatrix} \quad (2.4)$$

where $A(z)$ is the forward propagating wave, $B(z)$ is the backward propagating wave, and $C(z)$ is a z -dependent 4-element coupling matrix. The solution to (2.4) for a single pair of layers of period Λ is schematically shown in Figure 2.4 and given by

$$\begin{bmatrix} A(z=0) \\ B(z=0) \end{bmatrix} = M_m(z=0) \begin{bmatrix} A(z=\Lambda) \\ B(z=\Lambda) \end{bmatrix} \quad (2.5)$$

where

$$M_m = P_l R_U P_h$$

and

$$P_l = \begin{bmatrix} e^{j\phi_h} & 0 \\ 0 & e^{-j\phi_h} \end{bmatrix}$$

$$P_h = \begin{bmatrix} e^{j\phi_l} & 0 \\ 0 & e^{-j\phi_l} \end{bmatrix}$$

$$R_U = \frac{1}{\sqrt{n_h n_l}} \begin{bmatrix} n_{avg} & -\frac{1}{2}\Delta n \\ -\frac{1}{2}\Delta n & n_{avg} \end{bmatrix}$$

$$\phi_h = k n_h t_h; \quad \phi_l = k n_l t_l; \quad k = \frac{2\pi}{\lambda_o}.$$

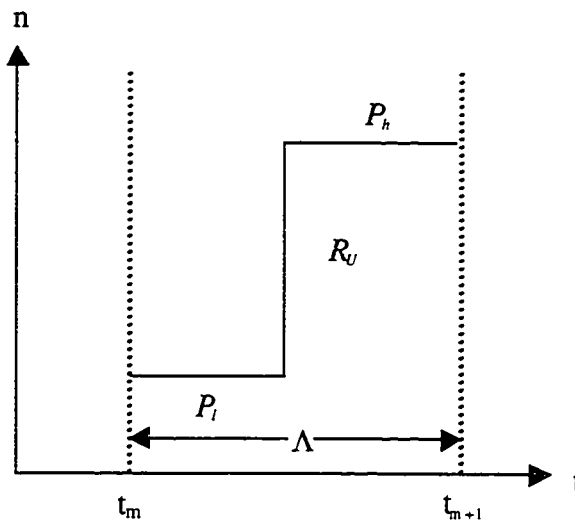


Figure 2.4. The three intermediate matrices, P_l , R_U and P_h are multiplied together to get the characteristic matrix for a single layer. The horizontal axis represents thickness and the vertical axis represents refractive index.

The complete CM for an arbitrary index profile is then

$$M = M_1 M_2 M_3 \dots M_m = \begin{bmatrix} M'_{11} & M'_{12} \\ M'_{21} & M'_{22} \end{bmatrix} \quad (2.6)$$

where M'_m are the CM's for layer m . The complex reflectance r , defined as the ratio of the forward travelling wave to the backward or reflected wave, is equivalent to the following expression

$$r = -\frac{M'_{12}}{M'_{11}} \quad (2.7)$$

and the reflectance R is calculated by

$$R = |r|^2. \quad (2.8)$$

The above equations permit an arbitrary index profile to be discretised and the corresponding reflection spectrum to be calculated. For example, consider the index profile in Figure 2.5. The continuous index profile is discretised into m layers and the characteristic matrix, M_m , for each layer is calculated. The overall characteristic matrix is then given by equation (2.6). The reflection spectra calculated by the CMM and corresponding index profiles for two filters are shown in Figure 2.6 and Figure 2.7.

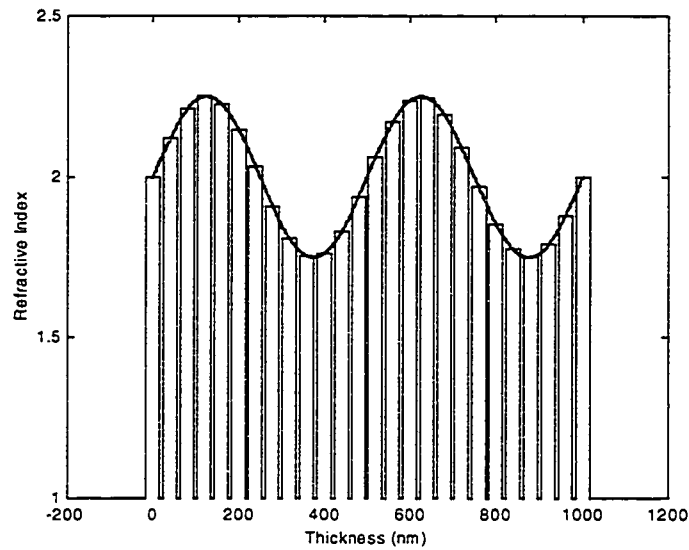


Figure 2.5. Example of how an inhomogeneous (continuously graded) index profile is discretised into many homogeneous layers. The characteristic matrix method can then be used to calculate the reflection spectrum.

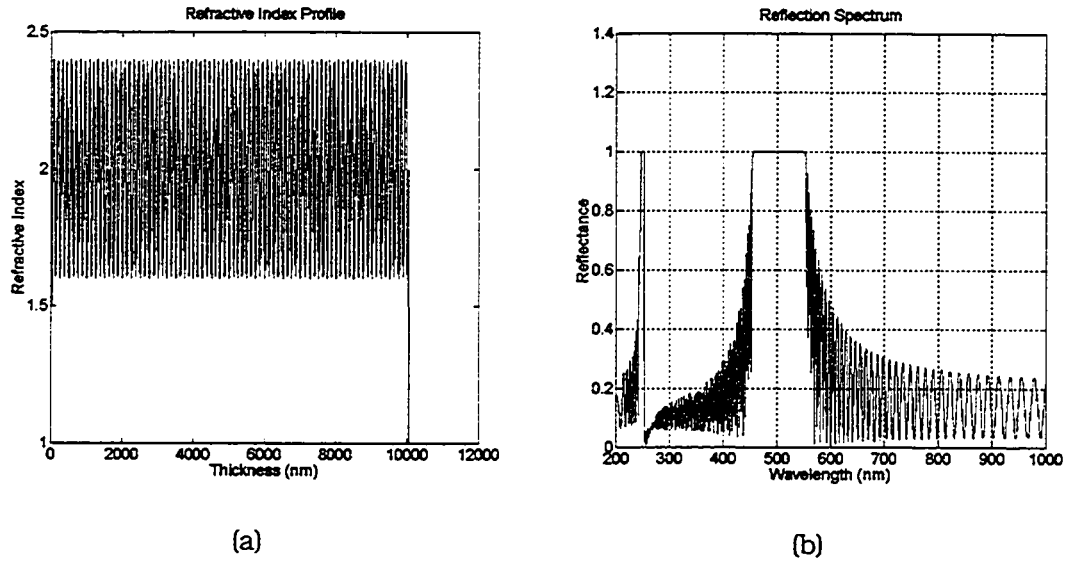


Figure 2.6. The index profile given in (a) was used to calculate the reflection spectrum in (b) using the CMM. The index variation in (a) is $\Delta n=0.8$. The index of the substrate was taken to be $n=1.5$ (glass) and the index of the incident medium was taken to be $n=1.0$ (air). The 3-dB bandwidth and reflectance of (b) are, $BW=103$ nm and $R=100\%$, respectively.

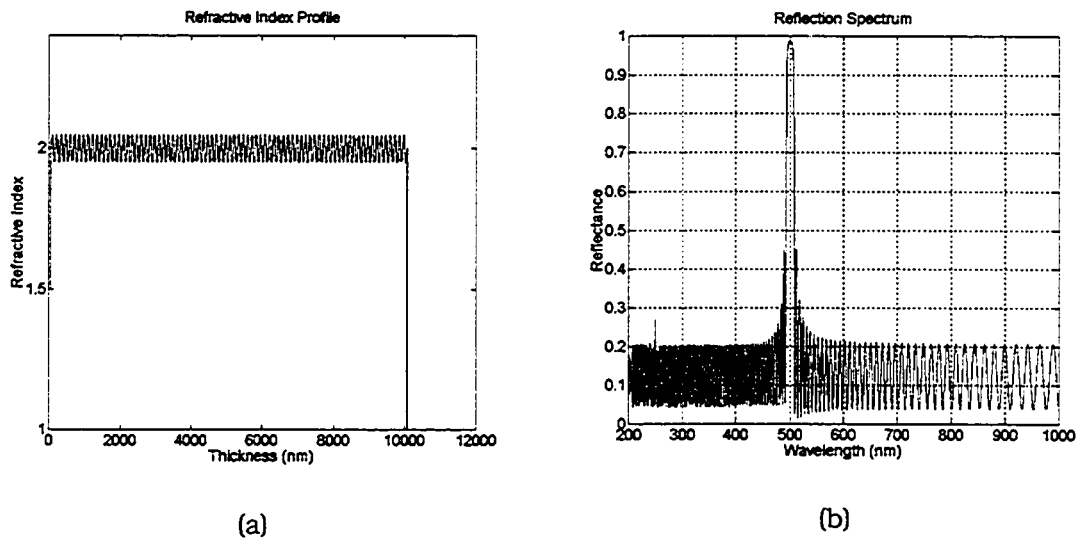


Figure 2.7. The index profile in (a) with $\Delta n=0.1$. Note that the bandwidth of the reflection peak has narrowed as compared with Figure 2.6. The 3-dB bandwidth of the reflection peak in (b) is $BW=16$ nm and a peak reflectance of $R=98.8\%$.

The effect of the substrate and air interfaces on the reflection spectrum was also investigated. The reflection spectra in Figure 2.8 and Figure 2.9 correspond to the

index profiles in Figure 2.6 and Figure 2.7, with the substrate and air interfaces neglected.

The utility of the CM method is quite clear, although computation time is a significant drawback. Using this method to calculate a reflection spectrum for arbitrary index profiles requires a relatively large number of samples, and therefore requires a large number of matrix operations. Furthermore, these operations must be repeated for each wavelength of interest in order to create a reflection spectrum. Notwithstanding, a typical calculation requires approximately 30 seconds on a PentiumPro 200 MHz class personal computer. This may not seem very slow, but the coupled-wave theory approach performs a similar calculation in less than a second at the expense of reduced flexibility and accuracy.

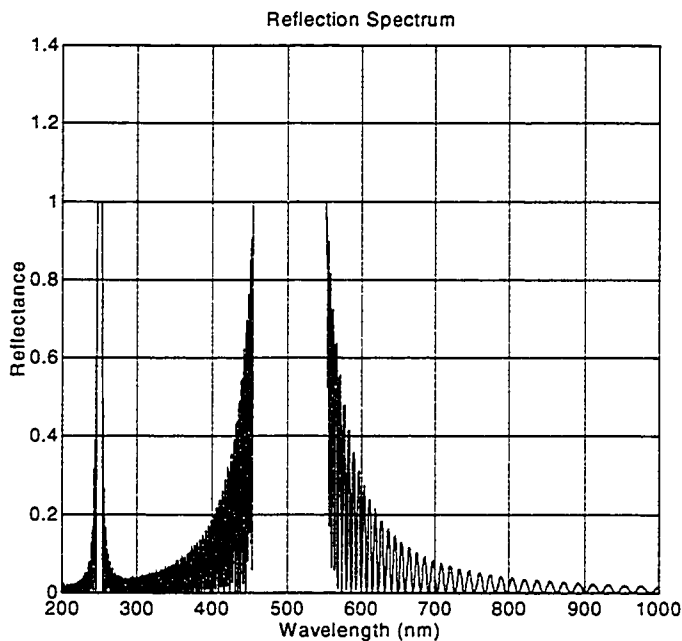


Figure 2.8. Reflection spectrum of a single line rugate neglecting the effect of the substrate and air interfaces, but otherwise identical to the index profile of Figure 2.6.

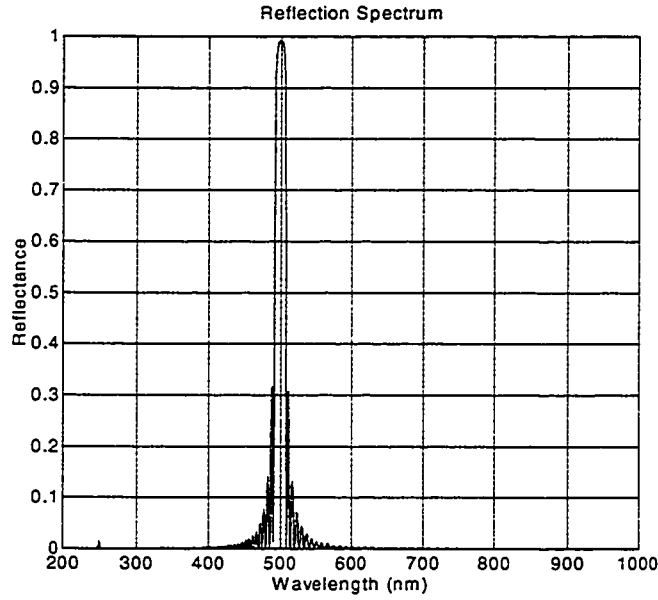


Figure 2.9. Reflection corresponding to the index profile given in Figure 2.7 with the exception that the substrate and air interfaces have been neglected. Note that the broad bandwidth reflections are almost completely eliminated.

2.3.2. Coupled-Wave Theory

Using coupled-wave theory, Southwell [11] was able to derive useful formulae that characterise rugate filters. The complex reflectance for a given wavelength is expressed by a single equation. The most attractive feature of the coupled-wave method is computational speed. Matuschek [10] has refined Southwell's theory to include arbitrarily strong index modulation, although the theory is more complicated and requires some non-intuitive assumptions.

A summary of the results, attributes and disadvantages will be given. The equation that describes the complex reflectance r of a rugate is quite complicated. However, omitting the effects of the substrate and incident medium results in a simplified equation for r , as given by

$$r = \frac{-\kappa \sinh(sL)e^{-\phi}}{s \cosh(sL) + j \frac{\alpha}{2} \sinh(sL)}, \quad (2.9)$$

where

$$\begin{aligned}
s &= \sqrt{\kappa^2 - \left(\frac{\alpha}{2}\right)^2} & \alpha &= 2k_z - K_1 \\
\kappa &= \frac{k_o^2 \Delta n g}{k_z 4n_{avg}} & K_1 &= \frac{4\pi n_{avg}}{\lambda_1} \\
k_o &= \frac{2\pi n_{avg}}{\lambda_o} & k_z &= k_o \cos(\theta) \\
g &= \begin{cases} 1 & s\text{-polarization} \\ -\cos(2\theta) & p\text{-polarization} \end{cases} & \theta & \text{is angle of incidence} \\
L &= \frac{\lambda_1 N}{2n_{avg}} & \phi & \text{is the initial phase angle of the sinusoid}
\end{aligned}$$

N is the number of rugate periods.

Two primary disadvantages of the coupled-wave approach include (a) reduced accuracy when the index variations are large ($\Delta n \gg 0.1n_{avg}$) and (b) restriction to sinusoidal index profiles. The scope of the coupled-wave theory may be extended if the index profile is represented as a Fourier series. For each sinusoid the complex reflectance may be computed and the results summed to compute the complete complex reflectance. Performing such an operation severely offsets the original computational speed advantage. Although these restrictions limit the usefulness of the method, two approximations derived from the coupled-wave theory remain useful estimates. The full-width half-maximum bandwidth (BW) and peak reflectance (R) can be approximated as

$$BW = \frac{\Delta\lambda}{\lambda} = \frac{\Delta n}{2n_{avg}} \quad (2.10)$$

$$\log_{10}(1 - R) = -0.6822 \frac{\Delta n}{n_{avg}} + \log_{10}\left(\frac{4n_o}{n_s}\right) \quad (2.11)$$

where n_o is the index of the incident medium and n_s is the substrate refractive index. The coupled-wave method is generally not well suited for calculating arbitrary index profiles or sinusoidal index profiles with large index changes, although equations (2.10) and (2.11) are useful guidelines when designing simple rugate filters.

The reflection spectra for the index profiles shown in Figure 2.6 and Figure 2.7, calculated using the coupled-wave method, are shown in Figure 2.10. The effect of the large index difference in Figure 2.10(a) is to show that the predicted bandwidth is 158 nm versus the CMM calculation of 103 nm. The bandwidth as calculated by the

coupled-wave approach is nearly the same as determined by the characteristic matrix method for in Figure 2.10(b), were the refractive index variation is small.

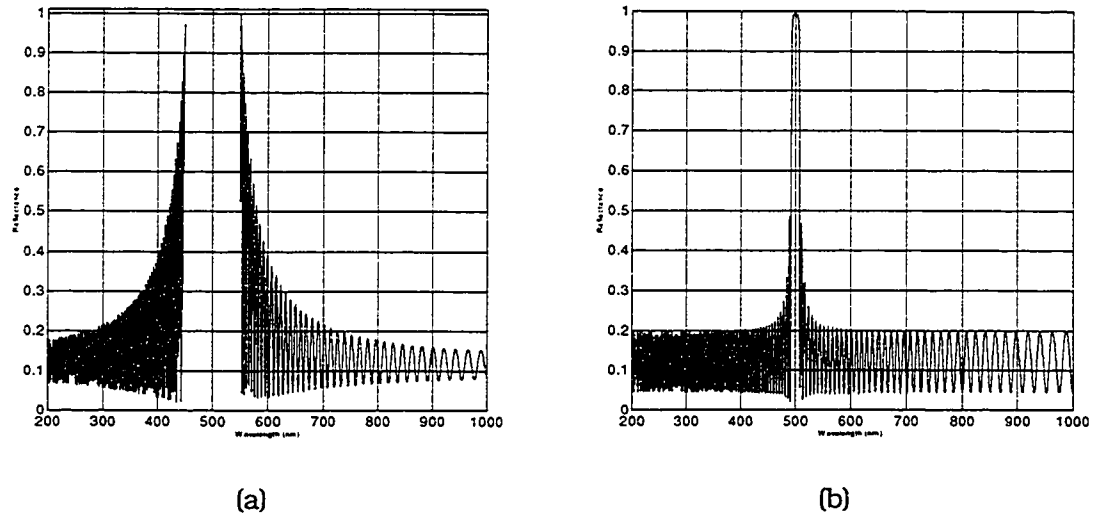


Figure 2.10. Calculated reflection spectra corresponding to the index profiles given in Figure 2.6 and Figure 2.7, respectively. The 3-dB bandwidth for (a) and (b) is 158 nm and 16 nm, respectively. Note that the reflection spectrum of (a) is quite different from Figure 2.6 due to the large index difference. In contrast, the coupled-wave approach gives good results for (b) where the index difference is a factor of eight less.

2.3.3. Derivation of Integral Calculation of Reflectance

A third method of calculating a reflection spectrum is the integration method [12]. Insight into the relationship between the refractive index $n(x)$ and reflectance $R(\lambda)$ can be gained by deriving the theory for this method.

The incremental complex amplitude reflectance of a film at a distance x is $\Delta r = (dr/dx)\Delta x$. The total complex reflectance r equals the sum of all the incremental reflectance from $x=-L/2$ to $L/2$, or

$$r(\lambda) = \int_{-L/2}^{L/2} e^{j2kx\sin(\theta)} \frac{dr}{dx} dx, \quad (2.12)$$

where the wavenumber is given by $k=2\pi/\lambda$ and the phase factor $e^{j2kx\sin(\theta)}$ accounts for the wave passing through the material a total distance of $2x\sin(\theta)$.

A relationship between the incremental reflectance and refractive index can be obtained using Fresnel's equations. For TE (transverse electric) polarisation the

following expression is obtained (using a Taylor series expansion of Δn and neglecting second order terms).

$$\frac{\Delta r}{\Delta n} = \frac{-1}{2n \sin^2(\theta)} \quad (2.13)$$

Since the second order terms have been omitted in (2.13), it is assumed the refractive index changes slowly relative to wavelength of light as a function of x . Using the approximation

$$\frac{dr}{dx} = \frac{dr}{dn} \frac{dn}{dx} \approx \frac{\Delta r}{\Delta n} \frac{dn}{dx} \quad (2.14)$$

the relationship between $n(x)$ and $R(\lambda) = |r(\lambda)|^2$ may be calculated as

$$r(\lambda) = \int_{-L/2}^{L/2} \frac{e^{j4\pi x \sin(\theta)/\lambda}}{2n \sin(\theta)} \frac{dn}{dx} dx. \quad (2.15)$$

Equation (2.15) may be computed numerically to provide the reflection spectrum corresponding to the index profile, $n(x)$. Notice that there is no contribution to the reflectance when $n(x)$ is constant. Therefore, the limits of integration may be extended to infinity without any loss of generality, since the regions outside $-L/2$ to $L/2$ are assumed to be homogeneous. It then becomes apparent that $r(\lambda)$ is related to $n(x)$ through "a" Fourier transform, where the transform variables are x and $4\pi \sin(\theta)/\lambda$, instead of the usual time and frequency variables. This important relationship will be discussed further in the next section

In summary, three methods of calculating the reflection spectrum of an index profile have been described. The most accurate method is the characteristic matrix method. It accurately calculates reflection spectra for arbitrary index profiles in less than a minute using a personal computer. The coupled-wave method offers high computational speed but is restricted to index profiles with sinusoidal index modulations and with low peak-to-peak index variations. Finally, the integration method is not very accurate when large index variations exist and is not computationally efficient. However, this latter method does provide an indication of the relationship between an arbitrary index profile and a reflection spectrum.

2.4 Rugate Filter Synthesis

This section presents two methods that may be used to design rugate filters. One approach utilizes (2.3) and (2.10) in the design process. Since (2.10) is only an approximate relationship an iterative approach is often warranted. A second method of designing rugate filters involves the use of the Fourier transform. The main advantage

of this method is the ability to produce an index profile from a specified reflection spectrum. However, the Fourier transform method produces an index profile that results in an inexact replica of the desired reflection spectrum. Hence, this method requires an iterative approach or an optimisation algorithm to achieve the desired filter specifications.

2.4.1. Fourier Transform Synthesis Method

An approximate analytic expression relating the refractive index profile to the reflection spectrum can be obtained using some of the information in Section 2.3.3. The derivation of this method is lengthy; therefore, only an overview of the theory and results will be presented.

For a normally incident wave, “a” spectral reflection function [13] can be redefined as

$$Q(k) = \int_{-\infty}^{\infty} \frac{1}{2n} \frac{dn}{dx} e^{j2\pi kx} dx \quad (2.16)$$

where $k=2\pi/\lambda$ is the wavenumber in the medium, and x is the optical thickness. Inverting the Fourier transform and integrating over x in (2.16) results in

$$\ln\left(\frac{n(x)}{n_o}\right) = \frac{j}{\pi} \int_{-\infty}^{\infty} \frac{Q(k)}{k} e^{-j2\pi kx} dk \quad (2.17)$$

where n_o is the reference refractive index of the surrounding material.

The $Q(k)$ spectral function is not unique nor is it exactly equal to the complex reflection amplitude. Therefore, a relationship between the Q function and r or R must be obtained. It has been shown in [13] that (2.18) are all valid approximate expressions that relate the magnitude of $Q(k)$ to the transmittance, T ($T=1-R$). Furthermore, only the magnitude of $Q(k)$ is specified while the phase remains arbitrary, and thus the phase may be used to “sculpt” or modify the reflection spectrum.

$$\begin{aligned} |Q_1| &= \sqrt{\frac{1}{2} \left(\frac{1}{T} - T \right)} \\ |Q_2| &= \sqrt{1 - T} \\ |Q_3| &= \sqrt{\frac{1}{T} - 1} \end{aligned} \quad (2.18)$$

The results of (2.18) are a direct consequence of two fourth-order estimates of the transmittance:

$$\begin{aligned}\frac{1}{T} &= 1 + |Q|^2 + O(Q^4) \\ T &= 1 - |Q|^2 + O(Q^4)\end{aligned}\tag{2.19}$$

where $O(Q^4)$ includes terms roughly on the order of Q^4 and higher. It was also shown that there are an infinite number of acceptable Q functions [13], subject to the constraint that Q is roughly fourth order accurate and satisfies

$$F(T) = F(1) + \left. \frac{\partial F}{\partial T} \right|_{T=1} (T-1) + \frac{1}{2} \left. \frac{\partial^2 F}{\partial T^2} \right|_{T=1} (T-1)^2 + \dots\tag{2.20}$$

if

$$\begin{aligned}|Q|^2 &= T - 1 \\ |Q| &= \sqrt{F(T)}.\end{aligned}\tag{2.21}$$

This assumption is valid provided that $F=0$ and the first derivative of F with respect to T equals -1 when $T=1$. Although Q is not uniquely defined, it is important that selecting a particular Q function produces a transmittance spectrum that is nearly the same as the specified spectrum. This ambiguity leads to a number of problems with using this method to design a filter having a particular response. First, the spectral response for a filter should be calculated for each Q function. Once an adequate response is obtained, the design must be numerically optimized.

The dependence of the calculated reflection spectrum versus the *desired* spectrum is best illustrated by two examples. Figure 2.11 illustrates the effect of Q -function selection. Note how the calculated spectra differ when all other parameters have been fixed. The peak reflectance is similar for Q_1 and Q_2 ; however, the bandwidth is more accurately predicted using Q_2 . More importantly, the effect of the Q -functions on bandwidth and reflectance are a function of the bandwidth itself. For example, a prototype filter with the same parameters, but with the bandwidth reduced by an order of magnitude is shown in Figure 2.12. As a result, this method would likely be used to provide the initial design to a program that can then optimize the spectral response.

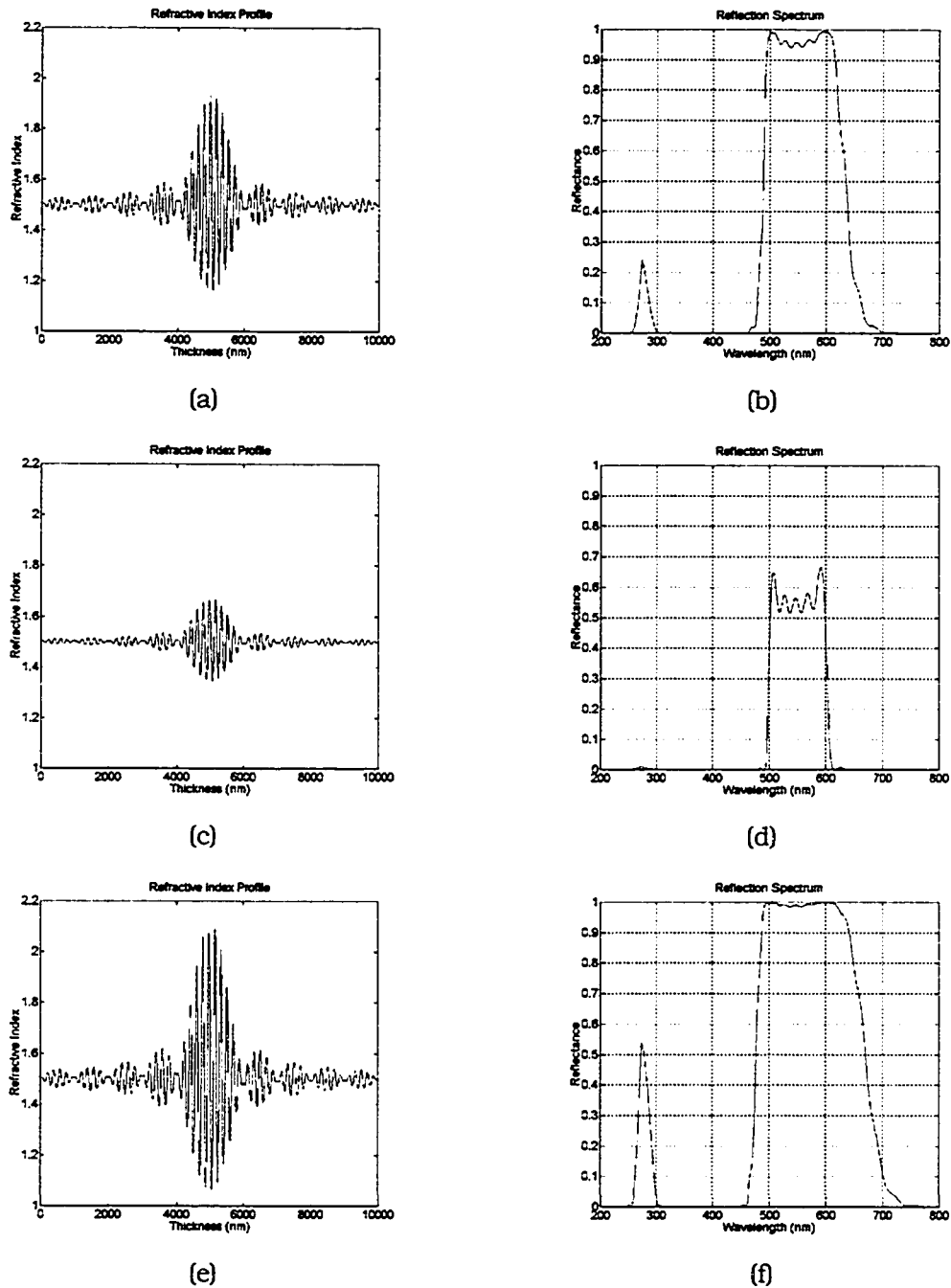
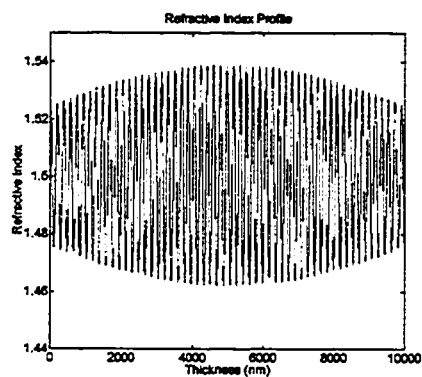
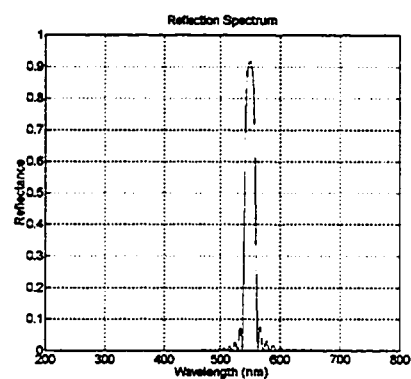


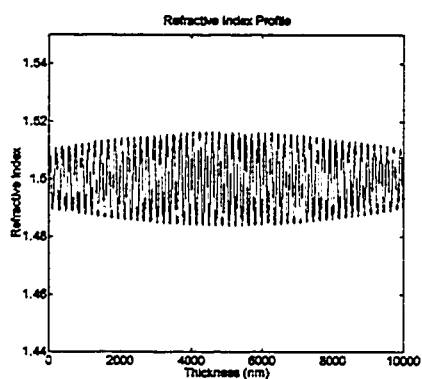
Figure 2.11. Comparison of Q -functions Q_1 through Q_3 , respectively. The left column shows the index profile corresponding to the reflection spectrum on the right. The same filter design parameters were used. The design/prototype filter was a rectangular shaped filter having a bandwidth of 100 nm centred at 550 nm and a peak reflectance of 90%. The 3-dB bandwidth for b), d), and f) are 145 nm, 102 nm, and 193 nm. The reflection peak at 250 nm corresponds to the second harmonic. Note that the three different Q -functions produce different spectral responses, therefore the filter design will need optimized.



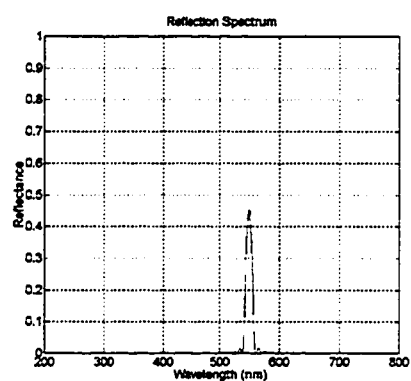
(a)



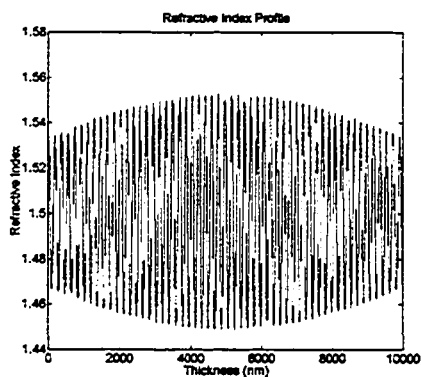
(b)



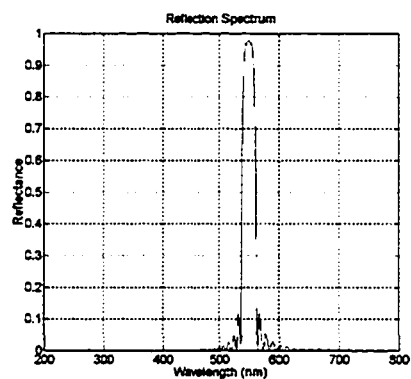
(c)



(d)



(e)



(f)

Figure 2.12. Comparison of Q -functions Q_1 to Q_3 , when the prototype brickwall filter bandwidth is reduced to 10 nm. The 3-dB bandwidth for b), d), and f) are 18.7 nm, 11.7 nm and 23.2 nm, respectively.

2.4.2. Simulated Annealing Optimization Algorithm

Simulated annealing is a simple and powerful global optimizer that has been used to optimize the refractive index profile of thin-film multilayer filters [14]. It is a mathematical model that represents a material cooling from a hot, energetic state, to a cool (orderly), minimum energy state. The term *annealing* refers to how metals are temperature treated to obtain favourable properties. It has been shown that a global solution is guaranteed if a proper temperature annealing schedule is followed [15].

The role of the temperature is twofold. First it controls how the optimization method behaves and second it indicate the number of iterations. For temperatures greater than unity, more emphasis is given to exploration than optimization, i.e., global exploration is sought, while at lower temperatures the method behaves much more like a local optimization algorithm, such as a gradient based method.

Initial parameters must first be entered, such as the temperature and initial point in the solution space. The temperature is set to a sufficiently high value ($\gg 1$) that will allow the SA algorithm enough time to search the solution space. The actual choice of the initial temperature is problem dependent, a value of 10-100 was used in this work. Once the optimization procedure is initiated, the following events take place. A random point some distance from the initial point in the solution space is chosen according to a probabilistic function $g(x)$, known as the generating function. The energy or error of the cost function, E , is calculated and is accepted or rejected according to a probabilistic function $h(x)$, know as the acceptance function. For example, a value of E may be accepted even though it is higher (worse) than the previously calculated value. When the temperature is high, the probability of accepting a new point is roughly one-half, but as the temperature decreases, the probability of accepting a higher energy decreases. Therefore, when the temperature is high, uphill or higher energy values may be accepted, thereby allowing the method to escape from local minima in the solution space. In summary, the basic SA procedure consists of the following steps:

1. Choose a (high) starting temperature T and a random or user specified starting point x . $T \leftarrow T_0$ and $x \leftarrow x_0$.
2. Calculate the value of the cost function at the starting point. $E \leftarrow f(x_0)$.
3. For k iterations and while T is sufficiently large, repeat the following steps.
 - a. Choose a new point x' , using the generating function $g(x)$.
 - b. Calculate the value of the cost function at x' . $E' \leftarrow f(x')$.
 - c. Accept the new x' and E' according to the acceptance probability function, $h(x)$.
 - d. Reduce the temperature T , by annealing, $T(k+1) \leftarrow c \cdot T(k)$, $0 < c < 1$.
4. Return x and E as the optimal solution and optimal cost function value.

The standard SA algorithm (also known as the Boltzmann algorithm) uses a Gaussian probability density function, given by (2.22), where D is the number of dimensions/parameters in the solution space. The acceptance function is given by (2.23), which is known as the Metropolis criterion [17]. A plot of the generating and acceptance functions, $g(x)$ and $h(x)$, are shown in Figure 2.13. It is apparent that the temperature plays a crucial role in how the solution space is sampled. Figure 2.14 graphically illustrates how the temperature affects the exploration of the solution space. The parameter x is a vector that represents both the thickness of a homogeneous thin-film and the refractive index. The values of x are optimized such that the calculated filter response, i.e. reflection or transmission spectrum, closely matches the desired response. The energy represents the mean square error between the desired and calculated response and the temperature is inversely proportional to the number of iterations.

$$g(x) = (2\pi T)^{-D/2} \exp\left(-\frac{\Delta x^2}{2T}\right) \quad (2.22)$$

$$h(x) = \exp\left(-\frac{\Delta E}{T}\right) \quad (2.23)$$

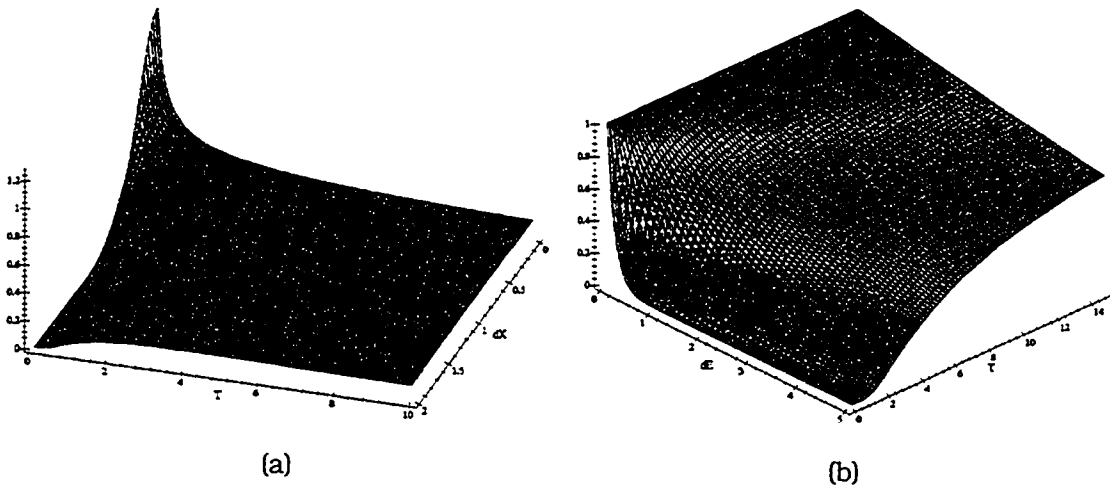


Figure 2.13. Two-dimensional plots of (a) the generating function and (b) the acceptance function. In (a), as the temperature T tends towards zero, the deviation, Δx , of a new value from the previous value decreases. In (b), when the temperature is high, the probability of accepting a worse solution is approximately 0.5. As the temperature is lowered, the probability of selecting a worse solution also decreases.

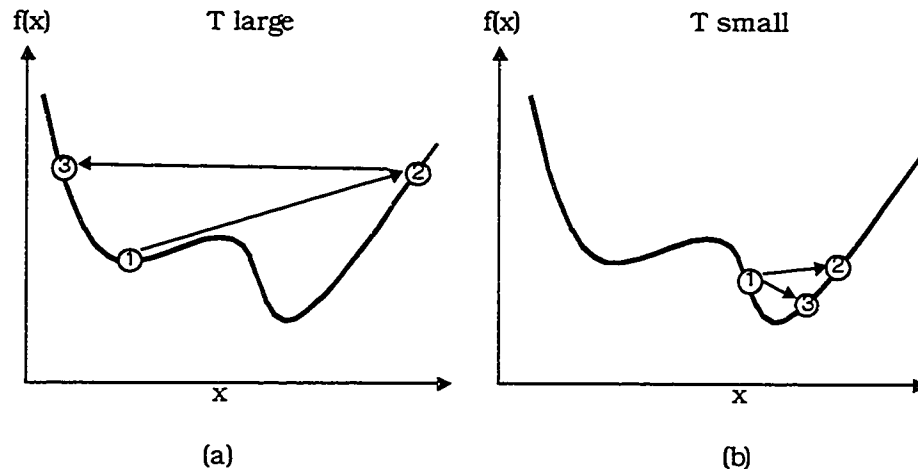


Figure 2.14. Schematic illustration of how the temperature parameter influences how the SA algorithm explores the solution space. The numbers in (a) and (b) represent consecutive iterations. When the temperature is high (a), each new parameter of the solution vector is likely to be fairly distant, i.e. a large dx , from the previous value. Also, the probability of accepting a worse value of the function to be minimized, $f(x)$, is high (~50%). As the temperature is lowered, it is more probable that newly generated points will be close to the previous point. Furthermore, as shown by the transition from iteration 2 to 3 in (b), uphill or worse solutions are less likely to be accepted.

2.4.3. Windows95 Based Filter Synthesis and Optimization Program

Initially, Matlab[®] was used to calculate the reflection spectrum of an index profile using the CM method. Unfortunately, the computation time became excessive as the number of layers increased. To overcome this limitation, a FORTRAN program was written that calculated the reflection spectrum from an index profile that was specified in Matlab. This was a somewhat cumbersome approach, so a custom Windows95[®] based program was written which implemented the characteristic matrix method.

Since this was a custom program being written, an optimization routine(s) was also incorporated. The program allows the user to enter an index profile and a target/desired reflection spectrum. The user then selects either a global or local optimization algorithm, which is used to minimize the mean-square error between the calculated and desired reflection spectrum.

There are two parameters for each layer, namely the refractive index and the thickness. Therefore there are a total of $2N$ parameters that need to be optimized, where N is the number of layers. The cost function or objective function requires that the reflection spectrum be calculated over some wavelength region. As a result, the number

of calculations performed per iteration is quite large. For example, an inhomogeneous or continuous refractive index profile that is 10 μm thick may have 200 to 2000 parameters, depending upon the number of discrete layers used to approximate the continuous index profile. As the index profile is optimized, local minima are frequently encountered. Consequently, the optimization algorithm must be able to overcome these local minima and find the global minima or global minimum. There are a number of different methods and techniques that can be used to optimize an optical filter design [18],[19], but simulated annealing was chosen due to its simplicity and ability to find a global solution.

A publicly available SA algorithm implemented in FORTRAN was obtained from the Internet and incorporated into the thin-film optimization program [20]. Although the program code was developed for economics; it was modified for use in this work. A screen capture is shown in Figure 2.16. The top window illustrates the calculated reflection spectrum and the refractive index profile. These plots are simultaneously and periodically updated every 2, 5, 10, or 30 seconds during the optimization. Parameters such as the initial temperature, maximum and minimum layer thickness, and refractive index range, are entered in the main parameter dialog box. Shown in Figure 2.15 is an example of an index profile that has been modified so that the reflection spectrum could be optimized.

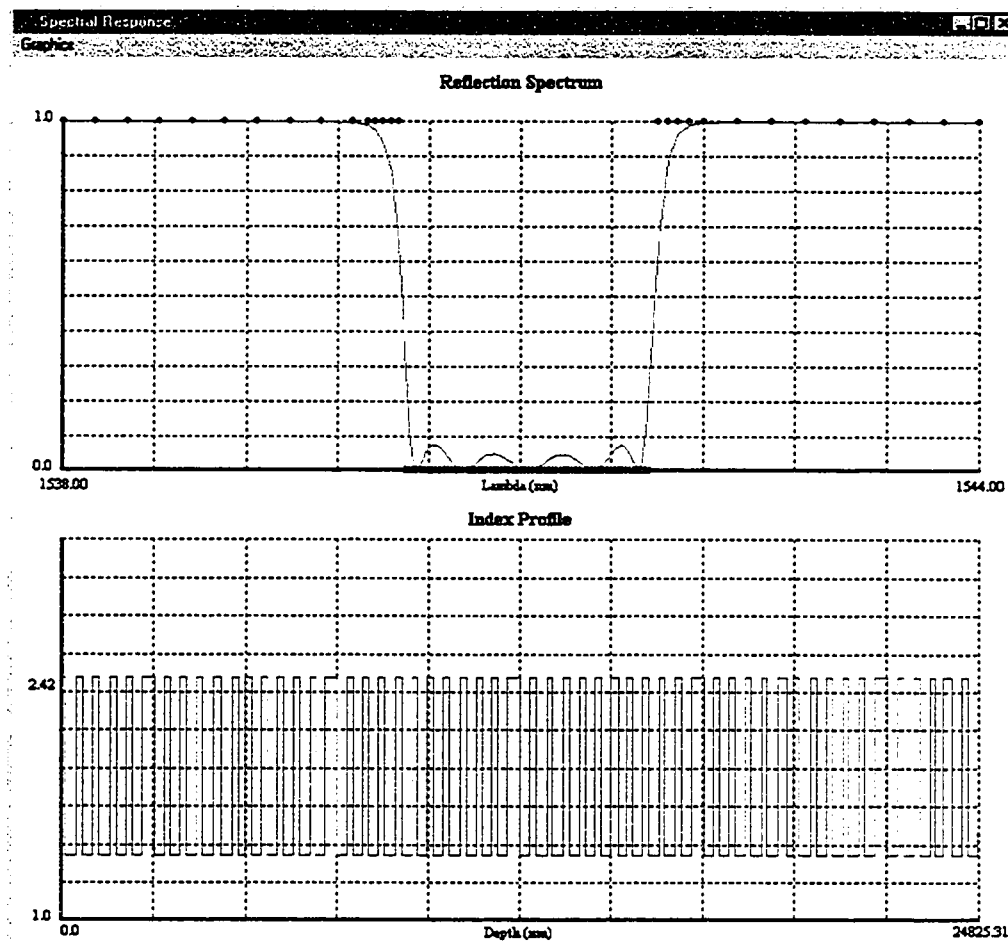


Figure 2.15. The refractive index profile was altered to optimize the reflection spectrum. The circles represent the desired reflection spectrum and the continuous line is the calculated reflection spectrum. The reflection spectrum is calculated as a function of wavelength. The target spectrum is specified as a series of ranges with constant wavelength spacing and reflection coefficient. Therefore, in regions where the spectrum is changing slowly, fewer calculations are performed, thus reducing the computation time.

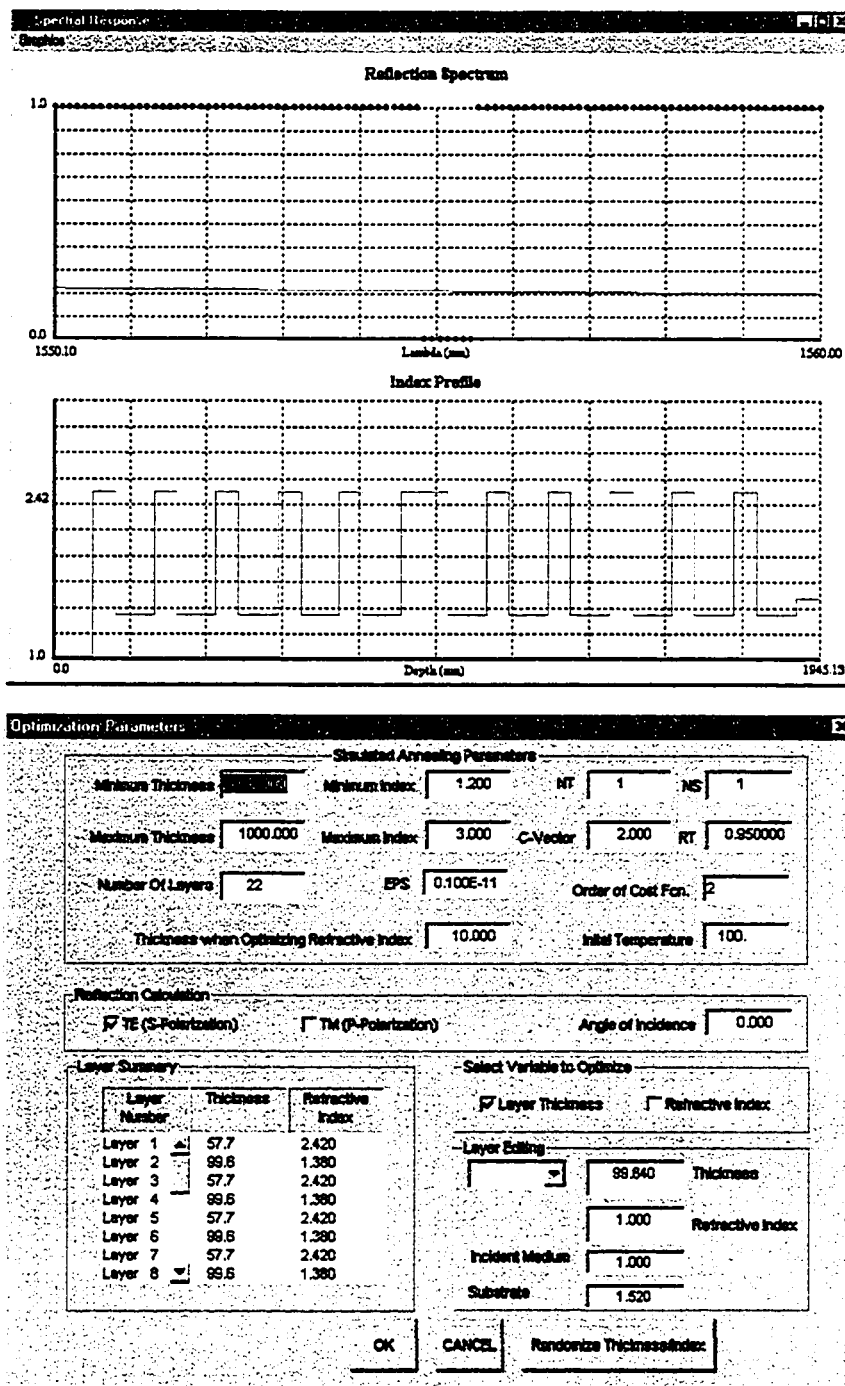


Figure 2.16. Screen capture of the custom written Win95 based filter optimization program. The red circles in the top plot indicate the target reflection spectrum and the solid line represents the calculated reflection spectrum. The second graph illustrates the current refractive index profile as a function of depth. The dialog box shown at the bottom is where most of the program data/parameters are entered.

2.5 Filter Fabrication Methods

There are various thin-film growth techniques that may be used to deposit inhomogeneous thin-films, such as co-deposition [21], various chemical vapour deposition (CVD) methods [22], and ion-beam-assisted [23] methods, to name a few. These techniques achieve a continuous variation in index by altering the material composition as a function of depth. Co-deposition simultaneously deposits two materials onto a common substrate, thereby creating a mixture of the two materials. To a first approximation, the mixture has a refractive index given by the sum of the bulk index of each material weighted by its percent composition. Similarly, CVD achieves a continuous index variation by altering the gas flow rates to effect the material composition. An attribute common to all of these methods is complexity. Sophisticated feedback systems must be employed to ensure the process is repeatable and produces an accurate reproduction of the specified index profile. Furthermore, most of these techniques are restricted to growing thin films since the growth rate is slow (typically many hours per filter) and the intrinsic film stress is high [24]. In contrast, Glancing Angle Deposition (GLAD) can deposit films a few microns thick in minutes while simultaneously producing films with low intrinsic stress [25].

The GLAD technique used for growing continuous graded-index thin films is shown conceptually in Figure 2.17. A *single* material is evaporated onto a substrate that is simultaneously tilted and rotated. Tilting the substrate away from the normal direction leads to glancing angle deposition, which results in a more porous film. If the substrate is periodically tilted, an alternating porous-dense structure results, which has a periodic and continual varying effective refractive index. Finally, the substrate is concurrently rotated to avoid oblique columnar growth. Figure 2.18 illustrates the effect of tilt and rotation on the film's microstructure.

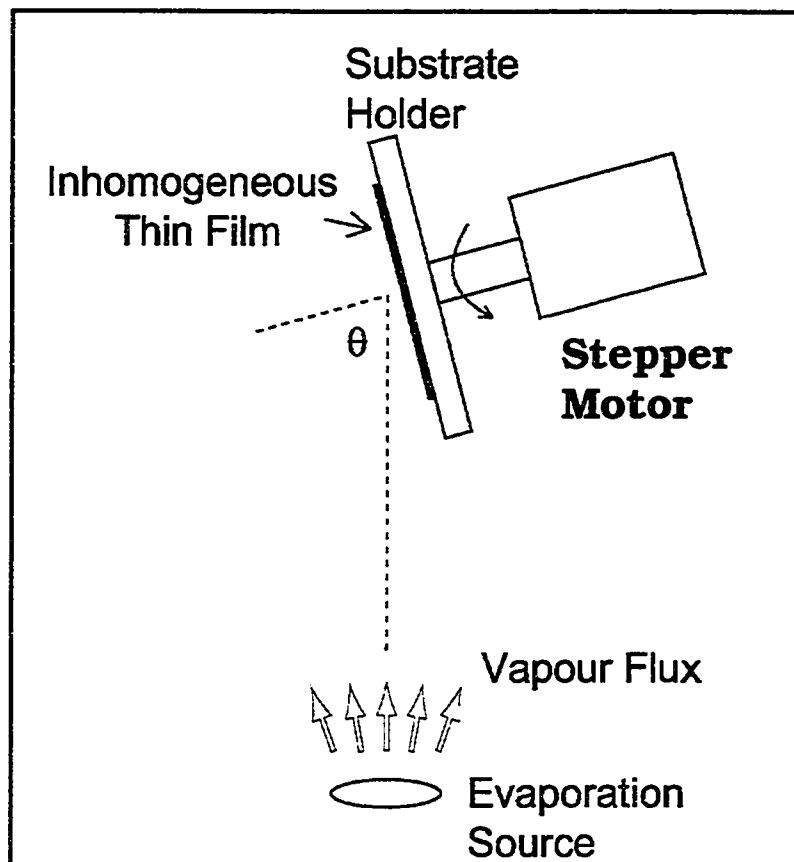


Figure 2.17. Conceptual drawing of a GLAD system. The substrate holder rotates about one axis and tilts about the other. As the vapour flux is deposited onto the substrate, various processes combine to produce sculpted films.

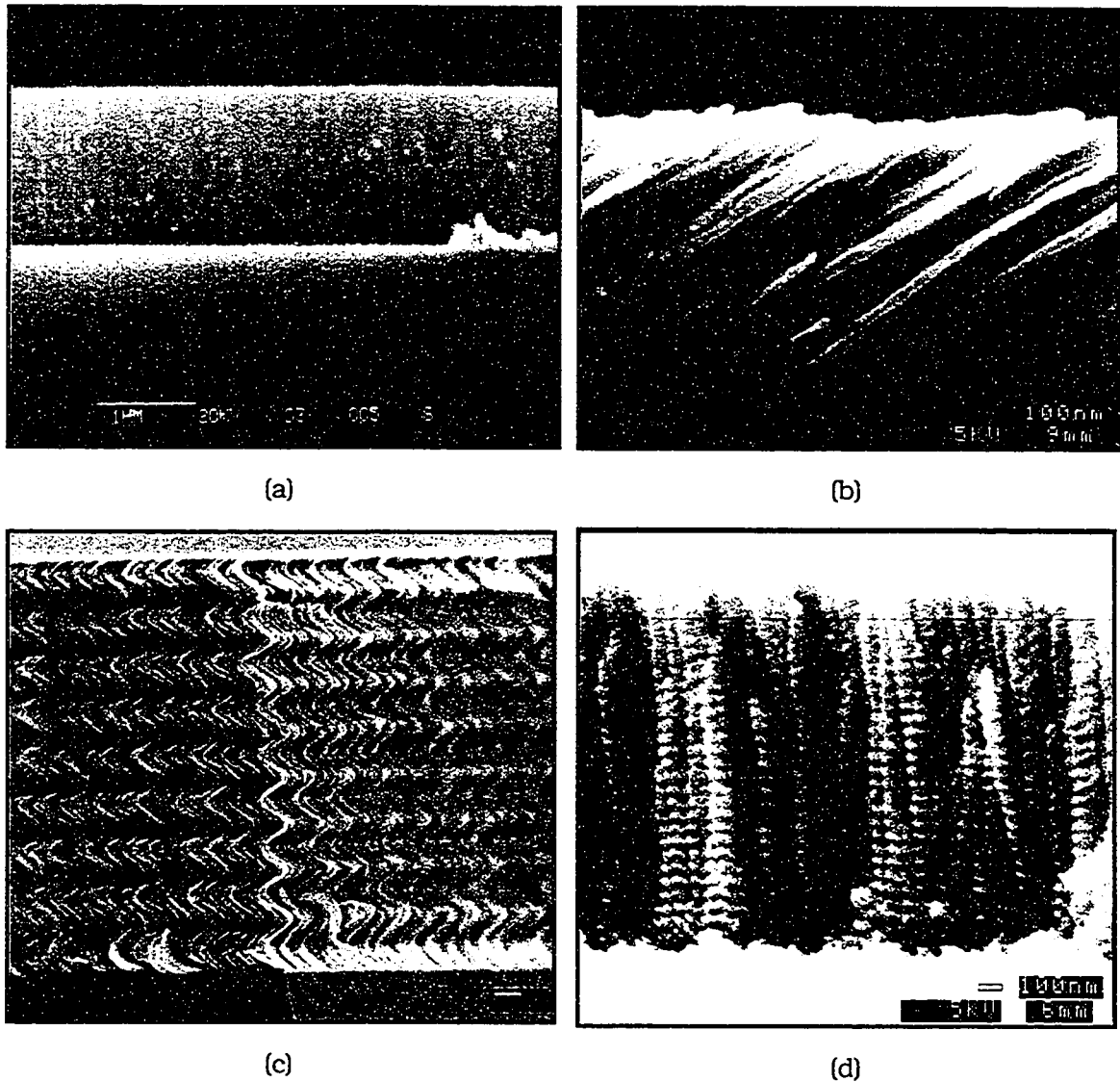


Figure 2.18. Effects of tilt and rotation on film growth. A fully dense MgF_2 (a) results from normal incident film growth, (b) MgF_2 grown with the substrate tilted. (c) SiO grown by rotating the substrate slowly and with a constant tilt (helix pitch $\sim 2 \mu\text{m}$) and (d) MgF_2 grown with fast rotation and constant tilt (helix pitch $\sim 60\text{nm}$) [26].

2.6 Experimental Results

In [25], measurements of density and effective refractive index of films fabricated with GLAD were approximated by a simple density weighted sum of the index of the film material and the index of air. This sum was found to accurately predict the effective refractive index as measured with a prism coupler. Based on similar measurements, it was estimated that the MgF_2 density varied between 90% and 30% of bulk when

deposited at $\theta=51^\circ$ and $\theta=81^\circ$, respectively. From the preceding results, the indices of fully dense MgF_2 and air were used to obtain an estimate of the refractive index of the film to be 1.11 and 1.34 ($n_{\text{avg}}=1.22$, $\Delta n=0.23$). The thickness of the film was measured from the SEM (scanning electron microscope) picture shown in Figure 2.19 was approximately $2.6 \mu\text{m}$ in $N=14.5$ periods of $\Lambda \approx 180\text{nm}$. This thickness value is large for thermally evaporated MgF_2 , which typically fractures from stress when deposited thicker than about $1 \mu\text{m}$, and is an indicator that these films have low stress. Using these thickness measurements, the theoretical reflection spectrum was calculated using the characteristic matrix method (CMM) implemented in FORTRAN. The measured and theoretical reflection spectra are shown in Figure 2.20. The specified accuracy of the spectrometer is 3%. Fitting the CMM model to the measured spectrum using the known film thickness and estimates of the density variation, the index was determined to be between 1.13 to 1.31 ($n_{\text{avg}}=1.22$, $\Delta n=0.18$), a result in good agreement with the estimates from the film density variation. The peak reflectance is $R=82\%$ and the bandwidth is $BW=50 \text{ nm}$ centred at 460 nm . Calculations using (2.10) and (2.11) yield a bandwidth $BW=34 \text{ nm}$ and a reflectance $R=92\%$, which demonstrates the inaccuracy of these formulae for large index variations. Since the effect of stress is low in these films, it is anticipated that very thick filters with a correspondingly narrow passband can be grown.

To obtain a variable refractive index using GLAD, the density or porosity of the film is varied. The response of a filter fabricated from porous films is susceptible to humidity because water may condense inside the film and alter its response. For certain applications this is not desirable; therefore it has been proposed that a thin fully dense "cap" layer could be deposited on the surface. Such a filter would be less affected by humidity and be much more mechanically robust. However, in certain applications the porosity may prove beneficial. For example, chemical sensing applications may exploit the large surface area of these porous films. Hence, one of the design goals may be to maximize the surface area of a particular film.

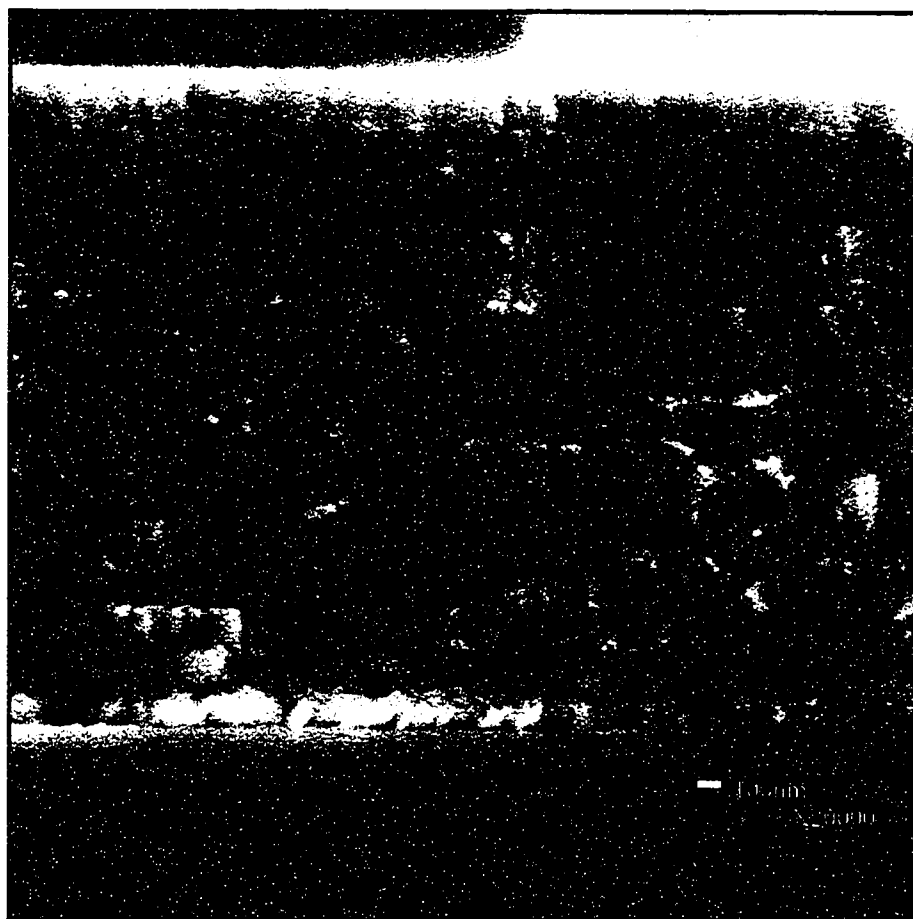


Figure 2.19. SEM micrograph of a rugate filter that has a sinusoidal refractive index profile. The refractive index has been estimated to vary from 1.11 to 1.34. The boundaries between the high and low index layers can just be discerned as dark lines. The film was deposited by rotating the substrate rapidly and by varying the substrate tilt sinusoidally.

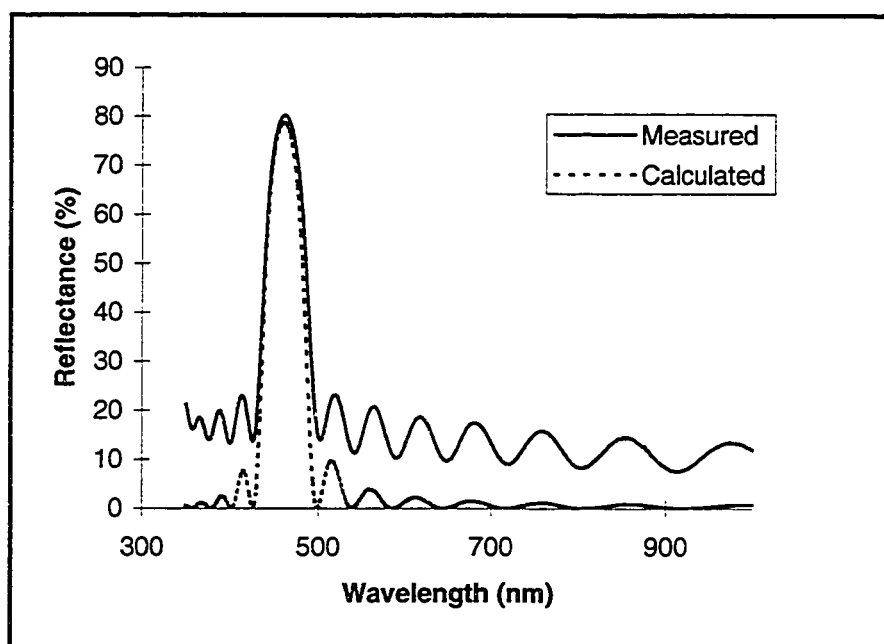


Figure 2.20. Reflection spectrum of a rugate filter fabricated using GLAD. The bandwidth is approximately 50 nm and the peak reflectance is 82%. The characteristic matrix method was used to calculate the reflection spectrum. The vertical offset between the two curves is believed to be the result of scattering within the film. The spectrometer has an accuracy of 3%.

2.7 Applications

2.7.1. Telecommunications Applications

Thin-film filters are used to construct WDM multiplexers and demultiplexers. These passive optical components are crucial in the design of present and next generation ultra-dense WDM systems (system with >100 channels spaced 50 GHz apart). There are a number of passive optical devices capable of meeting the needs for low density WDM (<8 channels); however, only a few devices can meet the specifications required by dense and ultra-dense WDM systems. For example, a typical dense WDM specification may require the following parameters for a filter:

1. Passband ripple less than 1 dB.
2. Filter bandwidth 50% of the channel separation.
3. Stopband suppression greater than 20 dB.
4. Filter roll-off greater than 100 dB/nm.
5. Total optical loss through the device must be less than 3 dB.
6. Channel uniformity better than 3 dB.
7. Temperature and humidity stability.

Hence, a high-performance optical component is required.

One method of fabricating a wavelength de-multiplexer involves the use of optical filters. Each filter may be designed to allow only one wavelength channel to be transmitted, while simultaneously reflecting all other wavelengths. A rugate filter may be designed in such a manner. In order for a rugate filter to meet the specifications previously described, a film approximately 100 μm thick with suitable index modulations would be required. Films grown using GLAD may have an advantage, because of the lower intrinsic stress and simple fabrication procedure.

2.7.2. Other Areas

Recent research efforts in WDM systems have spawned a large amount of development in related test and measurement equipment. Of particular interest are narrow line-width tunable 1550 nm lasers. One method of creating a tunable 1550 nm laser is by using a length of erbium doped optical fibre optically pumped by 980 nm laser light. Semi-transparent mirrors and a 980/1550 nm demultiplexer are also required components. The mirrors define a resonant cavity and the pumped erbium fibre provides a gain medium, while the demultiplexer is used to filter the residual 980 nm pump light from the desired 1550 nm light. A rugate filter with appropriate spectral response may replace these two components, thus achieving a significant cost savings and simplifying product assembly. Tuning the laser is accomplished by slightly rotating one of the rugate filters, thereby altering or shifting the reflection peak slightly as described by equation (2.15).

Another research area requiring high performance optical filters is spectroscopy. In spectroscopic applications, a filter enhances the signal-to-noise ratio by allowing only the wavelengths of interest to be transmitted. The filter is necessary since all photodetectors are responsive to a broad range of wavelengths.

The design and fabrication of anti-reflection coatings may also be simplified using GLAD. The reflectance of a glass-air interface is approximately 4%, assuming that the refractive index of glass is $n=1.5$. AR-coatings are used to prevent back-reflections off various WDM components such as erbium doped fibre amplifiers, optical isolators and optical circulators. The reflection spectrum of a fully dense MgF_2 AR-coating on glass is shown in Figure 2.21(a), calculated using the characteristic matrix method. In contrast, AR-coatings that could be grown using GLAD are shown in Figure 2.21(b) and Figure 2.21(c). AR-coatings that reduce the reflectivity of a material below 0.01 percent over a broad range of wavelengths may require the refractive index to vary gradually [27] or require a number of discrete layers to be grown under stringent control.

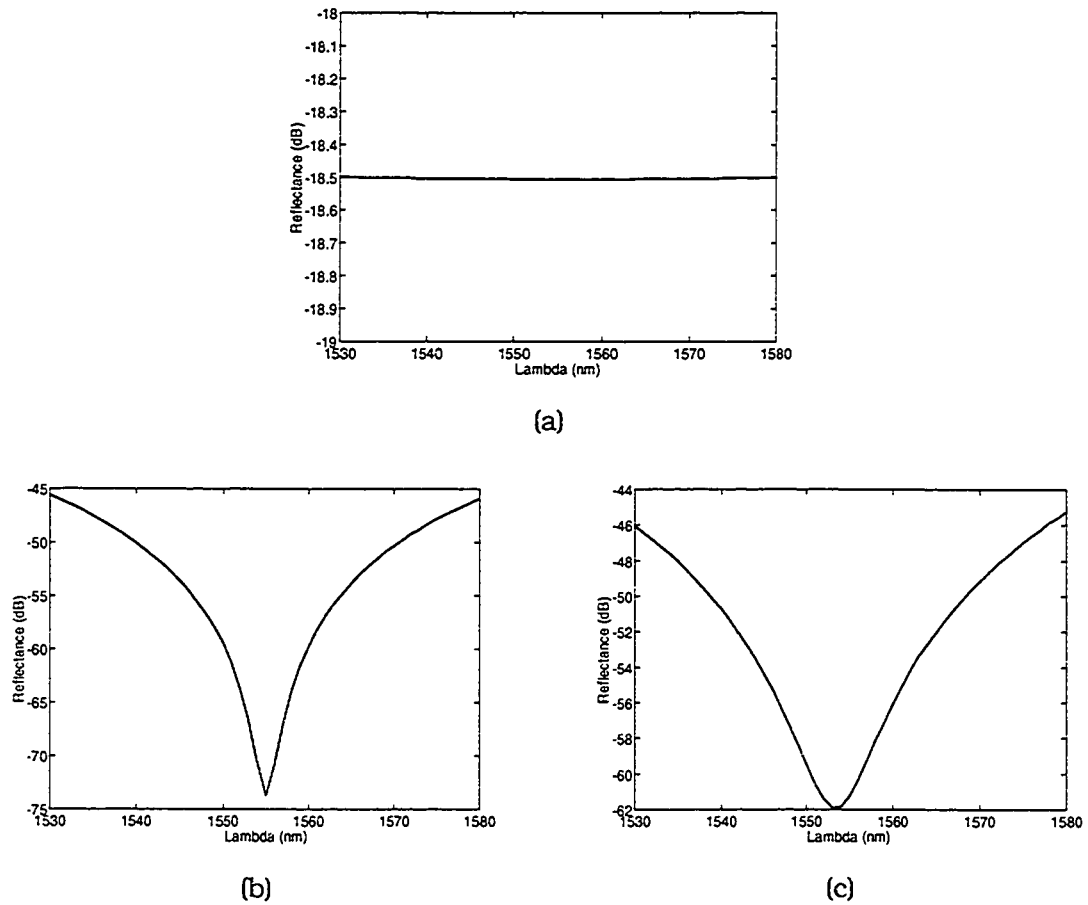


Figure 2.21. Calculated reflection spectra for a glass-air interface that has been treated with different AR-coatings. The reflection coefficient from an air-glass interface is typically 4%. The spectrum when a fully dense layer of MgF_2 ($n=1.38$) is used as an AR-coating on glass is shown in (a). In (b) the effect of GLAD deposited MgF_2 film ($n=1.225$) with no capping layer is shown. In (c), a GLAD MgF_2 film ($n=1.225$) and a 10 nm MgF_2 ($n=1.38$) cap layer is used.

Figure 2.21b includes the effect of adding a 10 nm fully dense layer of MgF_2 film, often referred to as a capping layer, which improves the environmental stability and robustness of the coating. The effect on the optical performance of the GLAD anti-reflection coating with the capping layer is inconsequential.

2.8 Summary

Fabrication of rugate filters using glancing angle deposition is an inexpensive, simple and flexible process. The GLAD process is versatile enough to create complex

refractive index profiles that allow high performance filters to be designed and fabricated. Furthermore, using GLAD, a true inhomogeneous thin-film structure may be grown, which is of importance for AR-coatings.

A program that used the characteristic matrix method to compute the reflection spectrum was combined with a global optimization algorithm, called simulated annealing, to calculate the reflection spectrum of arbitrary index profiles. The program adjusts the thickness and refractive index of a thin-film filter subject to a number of specified constraints, until the mean-square-error between the desired and calculated reflection spectrum is minimized.

Using GLAD, a multilayer thin-film filter was fabricated and tested. The measured reflection spectrum closely matched the reflection spectrum calculated using the characteristic matrix method. GLAD thin-film filters may be used in WDM systems, chemical sensing applications, to develop anti-reflection coatings, and for various laboratory purposes.

3. Multimode Thermo-optic Polymer Switch

3.1 Background

Optical switches are useful for the routing or switching of light signals. Some advantages of optical switching, where the signal remains in the optical domain throughout the switching process, are manifested in reduced system complexity, greater reliability, and signal transparency. Since the input optical signal is not converted to the electrical domain, optical-to-electrical and electrical-to-optical conversion is not required, therefore system complexity and cost are reduced. Optical switches are used in a variety of different applications, such as in optical networks and instrumentation, some of which will be discussed in further detail.

Optical switches can be broadly classified as possessing an electrical or optical control signal. Electrically-controlled optical switches, such as thermo-optic, electro-optic, acousto-optic, opto-mechanical and micro-mechanical switches, are the most common [28],[29],[30]. Optically-controlled switches, often referred to as all-optical switches, usually make use of some non-linear material or process to perform the switching function. Examples of all-optical switches include semiconductor or erbium doped fibre amplifiers used in Mach-Zehnder interferometers, employing cross-phase modulation, cross-gain modulation, or four-wave mixing [31],[32],[33]. The switch discussed in this work is an electrically controlled thermo-optic device.

Most switches, optical or electrical, are designed to be compatible with standard single-mode optical fibre, as dictated by the needs of commercial long-haul optical fibre networks. Furthermore, important switch parameters or characteristics, such as polarization dependent loss (PDL), insertion loss, switching time, reliability, physical size, number of input/output ports and cost, must be carefully balanced. Opto-mechanical switches are the most successful because they offer low loss, use proven technology and are commercially available. Characteristics of modern opto-mechanical switches are generally acceptable or favourable when discussed in this context. Notwithstanding, opto-mechanical switches rely on stepper motors and bulk optics to couple light from an input fibre to an output fibre. The main disadvantages of the opto-mechanical process are:

1. A slow switching time (>1 ms),
2. large physical size,
3. low level of component integration, and
4. high cost, resulting mainly from the use of manual component assembly.

Clearly, a new switching technology is required to circumvent the limitations imposed by the use of discrete mechanical components.

A different technology that has achieved significant commercial success uses polymer waveguides and the thermo-optic effect to produce an integrated optical switch. Such switches are produced commercially by JDS Fitel Inc. An advanced polymer (uses deuterium and fluorine), which exhibits low loss at 1550 nm, is patterned on a substrate using a photolithographic process. A second layer of polymer is used to clad the guiding layer and provide optical isolation from the two metal heaters that exist on either side of the Y-splitter (see Figure 3.1). A 1x2 switch is formed from a single-mode waveguide input, a Y-splitter and two single-mode outputs. When an electrical current is passed through one of the heaters, the temperature of the polymer below the heater rises, thereby causing the refractive index of the polymer to decrease slightly (most polymers have a negative thermo-optic coefficient on the order of $10^{-4} \text{ }^\circ\text{C}^{-1}$). Since the refractive index decreases with the application of heat, the waveguide mode or optical field shifts to the opposite side of the Y-splitter. Although the concept is straightforward, great care must be taken in designing the waveguides, cladding thickness and heaters so that power consumption and cross-talk are minimized. Larger switch dimensions are obtained by cascading multiple 1x2 switches. Table 3.1 summarizes a number of switches available from JDS Fitel.

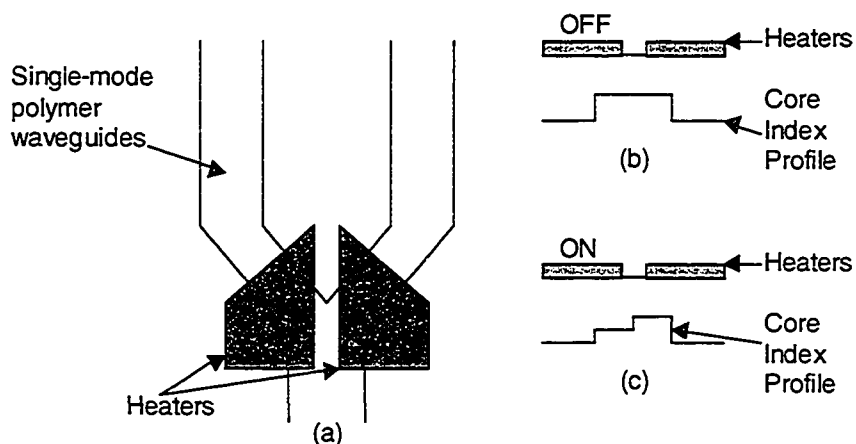


Figure 3.1. Top view (a) and cross-section view (b) of a Y-junction 1x2 thermo-optic polymer switch. Switching is achieved by applying current to one heater. The refractive index of the polymer is lowered due to the thermo-optic effect inherent in the polymer. The result is that an optical signal travelling through the polymer waveguide will experience a shift to the opposite side of the splitter (c) (effect is exaggerated and simplified for clarity).

Table 3.1. Performance summary of JDS Fitel's commercially available polymer thermo-optic switches. Specifications are valid in the optical bandwidth range from 1530-1565 nm [78].

Switch Size	Insertion Loss (dB)	Crosstalk (dB)	Switching Time (ms)
1x2	< 2.5	<-25	<2
1x4	<4.0	<-25	<2
1x8	<5.0	<-25	<2
2x2	<3.5	<-30	<2

The thermo-optic switch that was designed, fabricated and tested here utilizes polymer multimode waveguides and a Mach-Zehnder interferometer. Switching is achieved by applying electrical current to heaters located under phase shifters. The increased temperature lowers the refractive index of the phase shifting waveguides, and causes the light to be directed to a specific output port. The details of the operation, design, fabrication and testing are presented in the following sections, but some of the applications of optical switches will be discussed first.

3.2 Optical Switching Applications

Most optical switching applications require single-mode operation. Single-mode operation is a requirement for protection switching of SONET rings and wavelength cross-connects since standard single-mode optical fibre is used at the inputs and outputs of the switch. An application that does not necessarily require single-mode operation is the use of optical distribution in an optoelectronic switch. Three examples will be discussed, where each application highlights a different aspect of optical switching.

3.2.1. SONET Ring Protection Switching

SONET is an acronym for Synchronous Optical *NET*work. It is an international standard that specifies the electrical and optical interfaces, and the software protocols used in optical networks. The SONET standard also specifies the allowable bit rates or line rates for a fibre link as shown in Table 3.2. The OC-n designation signifies an optical interface data rate and standard. Similarly, STS-n is used to designate an electrical SONET signal standard. Unlike the older plesiochronous digital hierarchy in which the bit rates at different levels are not strictly correlated, each hierarchical level in SONET is an integer multiple of the basic OC-1 bit rate and is therefore correlated.

This results in a number of advantages such as simpler terminal equipment and lower equipment cost. Also the SONET data overhead increases in the same proportion due to the constant, bit-rate independent frame size.

Table 3.2. Commonly used SONET bit (line) rates for optical fibre networks. The bit rate or line rate is the total number of bits transmitted per second, while the data rate is the bit rate minus the amount of SONET overhead information.

SONET Designation	Bit Rate (Mb/s)	Data Rate (Mb/s)
OC-1	51.84	50.112
OC-3	155.52	150.336
OC-12	622.08	601.344
OC-48	2488.32	2405.376
OC-192	9953.28	9621.504

An important characteristic of a SONET network is that it is synchronous; the information signal is synchronised to a single clock. Hence, the location of a SONET frame within a data stream is precisely known. Therefore a tributary signal may be added or dropped without demultiplexing the signal to the basic OC-1 rate. Furthermore, if the OC-1 signal is transporting older DS-0 or DS-1 data streams, they too can be added or dropped without demultiplexing due to the synchronous payload enveloped in the frame. Complex and costly (de)multiplexers used in the older pleisochronous digital networks may be replaced by a much simpler add/drop multiplexer (ADM).

SONET networks are most often topologically organized and provisioned as rings. Figure 3.2 illustrates a typical four-node SONET ring, where one fibre pair carries the working capacity (solid line), and the other pair is used for spare capacity (dashed line), ring protection, and survivability. This ring illustrates the simplest scheme for fault tolerant operation: one-for-one protection. One fibre is used for data transport and the other is used as an alternative route.

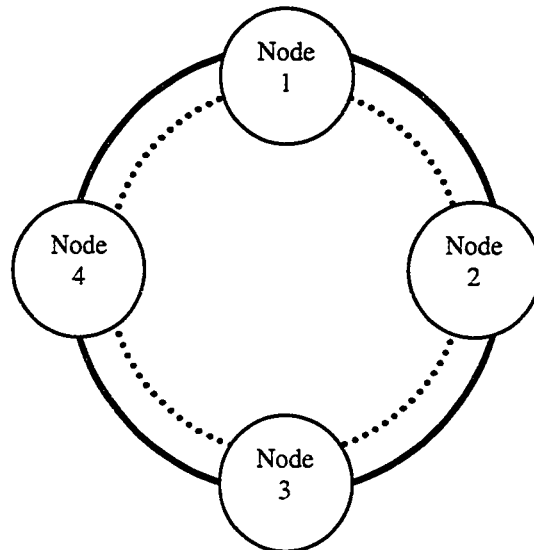


Figure 3.2. An example of a four node SONET ring with one-for-one fibre protection. Each heavy line represents a pair of fibres. For BLSRs, data can flow in both directions around the ring, while for UPSRs, data is always routed either clockwise or counter clockwise around the ring.

When a SONET receiver detects a string of zeros for more than $10\ \mu\text{s}$ a "loss of signal" alarm is triggered [34]. The terminal equipment communicates the alarm condition upstream and downstream. A series of steps are initiated to restore the working capacity via the spare link. The restoration time of a ring depends on its implementation. Bellcore standards specify that for a bi-directional line switched ring (BLSR) containing 16 nodes and less than 1200 km in length, the end-to-end switching time must be less than 50 ms [35]. For larger BLSRs, the end-to-end switching time must be no greater than 100 ms. A unidirectional path switched ring (UPSR) must restore all working capacity within 60 ms [36]. Only a fraction of the total switching time can be allotted to the actual switch because there must be allowance for software and status communication overhead. As a rule, the switching time of a piece of hardware, whether it is an ADM or switch, should be less than 10 ms.

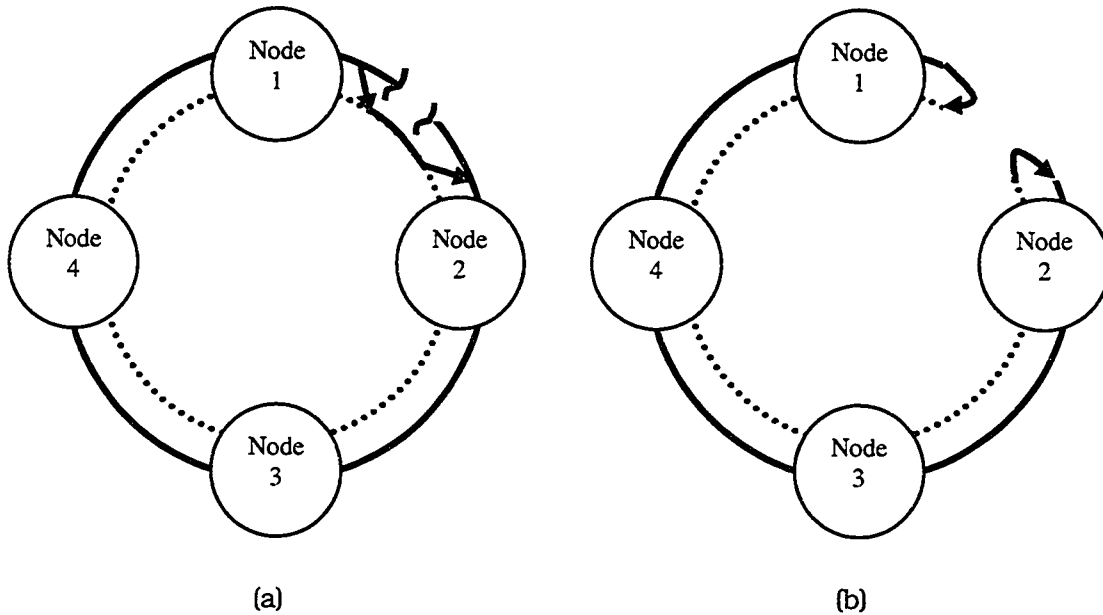


Figure 3.3. When a fibre cut occurs between nodes 1 and 2, the working capacity (heavy line) of the ring can be restored by using the spare link (dotted line). (a) represents the shortest path restoration route and (b) is the longest route. Both routes can be used to restore the working capacity, although the shortest one is preferred. Note, the actual switching function takes place inside nodes 1 and 2, but is illustrated outside the nodes for clarity.

The restoration examples illustrated in Figure 3.3 require different switch configurations as shown in Figure 3.5. Note that Figure 3.5(b) can alternatively be drawn in the cross-state if the spare spans for nodes 4-1 and 1-2 are swapped. This is called the unidirectional line switched ring configuration.

Commercially deployed SONET networks presently use electrical switches, i.e., optical-to-electrical followed by an electrical-to-optical conversion, for restoration. However, with the advent of wavelength division multiplexing (WDM), it may be advantageous to use optical switches to switch multiple data streams that may exist on one physical fibre. As a result, the span will be restored at the photonic layer rather than at the electrical layer, resulting in a reduction of the SONET terminal equipment complexity since the WDM signal does not have to be demultiplexed.

When optical switches and optical add/drop multiplexers are introduced into a SONET network, then "optical rings" may be possible. Present SONET systems employ "electrical rings" and simply use fibre as a point-to-point transmission medium. With WDM technology, a new photonic layer may be introduced, which will operate below the SONET layer, as shown in Figure 3.4. In such networks, there will be a need for

protection at the optical level as well as at the SONET level. At first this may seem like overhead, but one reason that protection at the optical level may be necessary is that SONET may be replaced by a different transport system. For instance, the protocol used for internets, TCP/IP, has been discussed as one possibility [37]. Current systems transport TCP/IP in SONET frames or even TCP/IP over asynchronous transfer mode (ATM) cells in SONET frames, lowering transmission efficiency and increasing costs. The transmission of TCP/IP directly over the photonics layer may be a paradigm shift in how Internet data is transported from source to destination.

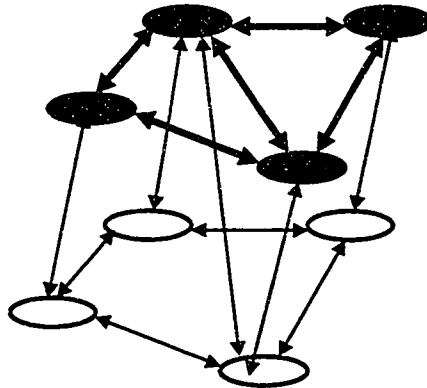


Figure 3.4. Example of how an optical layer (top) may be used in conjunction with the SONET layer (bottom). With such an architecture, the optical layer may be used for link protection and to more efficiently route traffic.

Various switch configurations could be used, as shown in Figure 3.5. For example, the operation shown in Figure 3.5(a) could be implemented with two 1x2 switches or one 2x4 switch. Other possibilities include using a "one-sided switch", where there is no distinction between inputs and outputs [38].

As the number of fibre pairs in a ring increase, so too must the switch dimension. Since the largest commercially available optical switch matrix dimension is 32x32, more research must be conducted in the areas of optical switching and integrated optics or micro-mechanical devices, to produce larger matrix sizes.

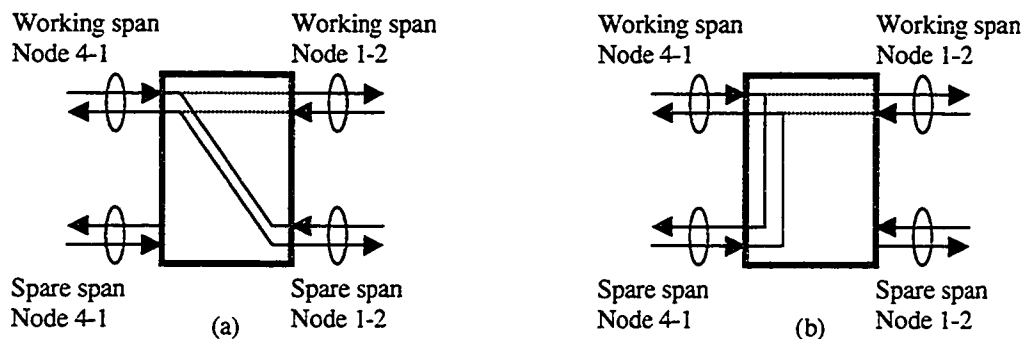


Figure 3.5. (a) In a path switched ring, the protection switch is normally configured in the bar-state (dotted lines) and is switched to the cross-state (solid lines) for protection. (b) In a bi-directional line switched ring, the protection switch is normally configured in the bar-state (dashed lines) and is switched to the cross-state (solid line) for protection.

3.2.2. Local Area Networks

The requirement for large bandwidth communications between computers has stimulated the development of faster local area networks (LAN). It is common to find desktop computers in an office environment connected via coaxial or Category-5 copper cable running an Ethernet protocol. Ethernet is a standard IEEE protocol that runs on the data link layer of the OSI model and specifies both software and hardware requirements for LANs. Until recently, Ethernet networks have operated at either 10 Mb/s (10 Base-T) or 100 Mb/s (100 Base-T or fast Ethernet). The IEEE standard also specifies an optical standard for Ethernet that uses graded-index multimode optical fibre. However, due to the increasing number of computers and the client-server architecture most prevalent today, the bandwidth provided by fast Ethernet is insufficient. As a result, Ethernet has been extended to include Gigabit Ethernet.

Gigabit Ethernet operates at a line rate of 1.25 Gb/s [1]. The transmission medium can be glass graded-index multimode fibre (62.5 μm core/125 μm outer diameter), glass step-index multimode fibre (50 μm core/125 μm outer diameter), glass single-mode fibre, or multimode plastic optical fibre. Similarly, a variety of transmission sources operating at various wavelengths can be used, such as 780 nm or 1300 nm LEDs or laser diodes, or 980 nm vertical cavity surface emitting lasers (VCSEL). Gigabit Ethernet may be used for future inter-office links and campus backbones. An opportunity exists to use multimode optical switches to provide protection for such an Ethernet network, much in the same way that optical switches can be used in long-haul WDM-SONET telecommunications systems.

3.2.3. Incorporation of an Optical Switch in an Optoelectronic Switch Matrix

The previous two applications discuss how an optical switch may be used as a component in a system. In contrast, this application highlights some of the reasons why it may be beneficial to incorporate a multimode polymer switch into a much more complicated device, an optoelectronic switch matrix.

The original application for the thermo-optic switch was to replace the passive optical waveguide distribution used in a 4x4 optoelectronic switch (OES). In an OES, the optical distribution is used to split an input optical signal into four, and then distribute each signal to a photodetector. The main disadvantage with this approach is that the signal power is reduced by a factor of four or 6 dB. This limits scalability and requires lasers with higher optical power. One solution is to replace the passive waveguide Y-splitters with an integrated polymer switch. The switch could then route all the power to the appropriate photodetector thereby circumventing the 6 dB power penalty. Details of the optoelectronic switch will be presented in Chapter 4.

Since there currently is no commercially available integrated multimode switch, an integrated thermo-optic polymer switch concept was investigated. In addition to the aforementioned requirements, a thermo-optic switch must exhibit low excess loss. By replacing the passive splitters with an active switching element, the inherent power penalty may be overcome. An added benefit is the switch occupies less physical space than the Y-splitters, mostly due to the use of space-efficient multimode interference (MMI) couplers.

3.3 Theory of Operation

The multimode thermo-optic polymer switch (MTOPS) is based on the design concept of a generalized Mach-Zehnder interferometer (MZI), with the use of multimode interference (MMI) couplers in place of Y-splitters [52]. A unique aspect of the switch described here is that all optical waveguides support multiple spatial modes, hence the use of modally insensitive splitters was a requirement. MMI couplers are planar integrated devices that operate on the principle of self-imaging. Since self-imaging is inherently modally insensitive, MMI couplers were used [52]. A conceptual diagram illustrating the device structure is shown in Figure 3.6. Light is coupled to the input guide on the left and is split into four equal intensity signals by the first MMI coupler. By applying current to electrical heaters to cause refractive index changes, phase shifts are introduced in each of the MZI waveguide arms. The relative phase shifts may be adjusted so that the second MMI coupler produces the signal in any one of its four output guides.

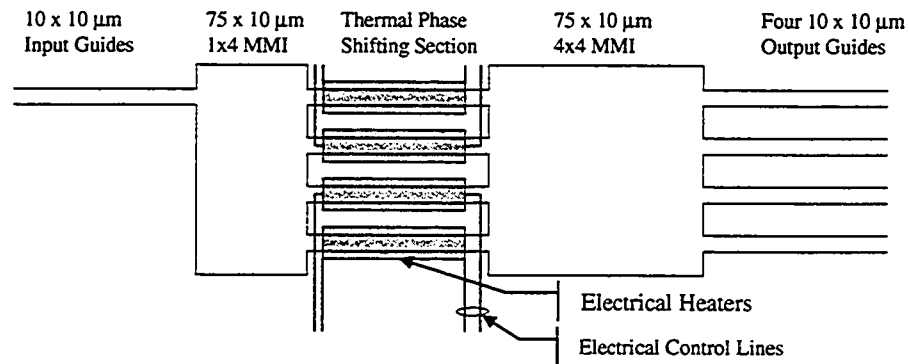
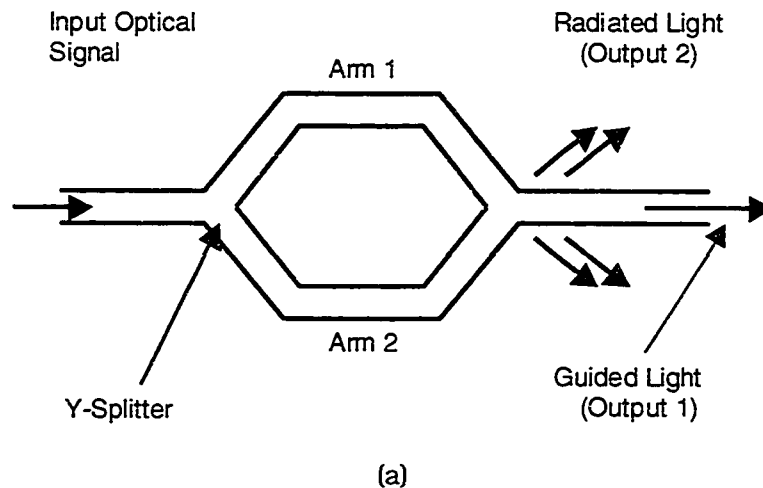


Figure 3.6. Conceptual drawing of a 1x4 thermo-optic switch. Multimode polymer waveguides and multimode interference couplers are used to construct a four-arm generalized Mach-Zehnder interferometer. Phase shifters are used to switch the input optical signal to any output.

The functionality of a 4-arm generalized MZI can be derived by first describing the operation of a traditional 2-arm MZI. A 2-arm MZI may be designed as a single-input single-output device using Y-splitters. A two-port 2-arm MZI may be designed using directional couplers. Figure 3.7 illustrates two examples of integrated MZIs.



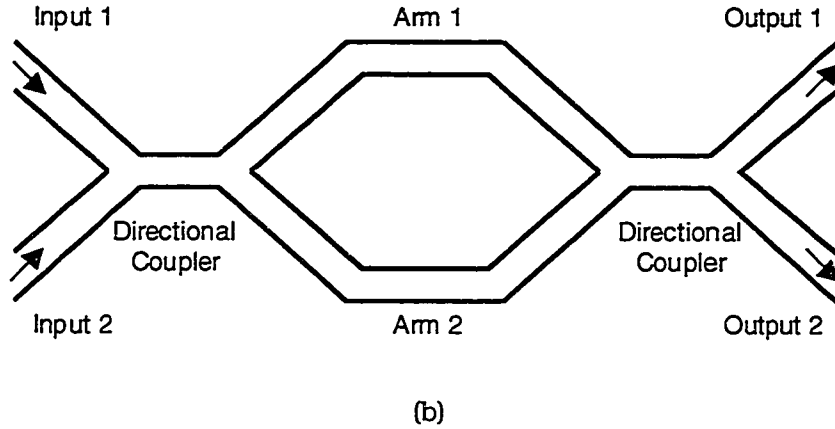


Figure 3.7. A single-port integrated optic Mach-Zehnder (a) actually has two outputs: a guided port and a radiation (lossy) port. A true integrated two-port Mach-Zehnder (b) can be designed using directional couplers, where both outputs are guided.

The analysis that follows applies to both single and dual-output MZIs. If it is assumed that the signal intensity in both arms are equal, then the intensity at the output(s) of a MZI device can be described by (3.1), where I_0 is the input intensity and $\Delta\phi$ is the phase difference. Equation (3.1) can easily be derived using phasors. If U_1 and U_2 represent the complex amplitude of two monochromatic signals in arms 1 and 2, then the output intensity I is equal to the sum of magnitudes squared, as given by (3.2), where * indicates the complex conjugate. If the intensity of the light in each arm is equal, i.e., $I_0 = |U_1|^2 = |U_2|^2$, and the phases are given by ϕ_1 and ϕ_2 , respectively, then (3.2) can be more succinctly expressed by (3.3). Shown in Figure 3.8 is a graph of (3.3).

$$I = 2I_0 [1 + \cos(\Delta\phi)] \quad (3.1)$$

$$I = |U_1 + U_2|^2 = |U_1|^2 + |U_2|^2 + U_1 U_2^* + U_1^* U_2 \quad (3.2)$$

$$I = 2I_0 + 2I_0 \cos(\phi_1 - \phi_2) = 2I_0 [1 + \cos(\Delta\phi)] \quad (3.3)$$

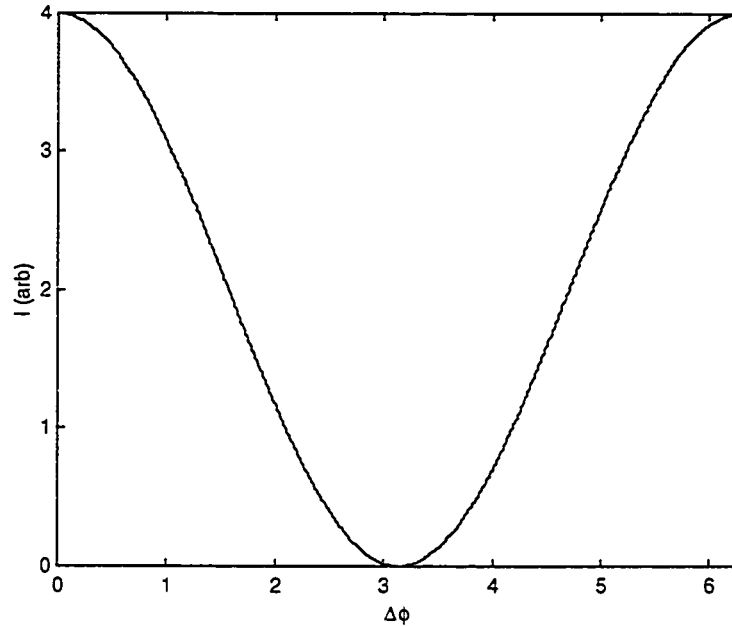


Figure 3.8. Dependence of the output intensity on the phase difference for a Mach-Zehnder interferometer. When the signals are completely out-of-phase, $\Delta\phi=\pi$, destructive interference results in zero light intensity at that particular output.

The expression that describes the output intensity of a four-arm generalized MZI is given by (3.4), where the notation $\Delta\phi_{ij}$ signifies the phase difference between the light in arms i and j . Unlike a two-arm MZI that requires a phase difference of 180° to switch, a four-arm MZI requires a phase difference of 90° between signals. Since the waveguide supports multiple modes, the intensity given by (3.4) is only for one mode and therefore needs to be applied to each of the guided modes. The output intensity is given by the sum of the intensity of each of the modes. Unfortunately, a plot of (3.4) is impossible because it is a function of three independent variables. The phase differences are interrelated, and the expression can be reduced to three independent variables.

$$I = |U_1 + U_2 + U_3 + U_4|^2$$

$$I = 4I_0 + 2I_0 \left[\cos(\Delta\phi_{12}) + \cos(\Delta\phi_{13}) + \cos(\Delta\phi_{14}) + \cos(\Delta\phi_{23}) \right. \\ \left. + \cos(\Delta\phi_{24}) + \cos(\Delta\phi_{34}) \right] \quad (3.4)$$

Although (3.4) is exact, there are some assumptions made in the derivation. First, as mentioned, the signals are assumed to be of equal intensity. Practically, the output intensities from fabricated splitters are likely to be unequal. The degree of mismatch between the two outputs is specified as the splitter imbalance, which is given by (3.5). Equation (3.6) represents the extinction ratio of a two arm MZI, and is defined as the ratio of the minimum to maximum power (with $P_{\text{imbalance}}$ expressed as a fractional number). Table 3.3 illustrates the effect of splitter imbalance on the extinction ratio. Lastly, the contrast ratio is defined as the ratio of power detected at the output ports in the off-state to power in the output port in the on-state, and is given by (3.7). It is desirable for optical switches to achieve a high extinction ratio and a high contrast ratio, since signal crosstalk will degrade the signal-to-noise ratio.

Table 3.3. Effect of splitter imbalance on a 1x2 or 2x2 Mach-Zehnder optical switch. Control of the splitter imbalance is crucial in achieving good switching performance.

Power Imbalance (dB)	Extinction Ratio (dB)
0.5	-30.8
1.0	-24.8
3.0	-15.3

$$P_{\text{imbalance}} = \left| 10 \log \left(\frac{P_1}{P_2} \right) \right| \quad (3.5)$$

$$ER = \frac{1 + P_{\text{imbalance}} - 2\sqrt{P_{\text{imbalance}}}}{1 + P_{\text{imbalance}} + 2\sqrt{P_{\text{imbalance}}}} = \frac{P_{\text{off}}}{P_{\text{on}}} \quad (3.6)$$

$$P_{i,\text{contrast}} = \frac{P_i}{\sum_j P_j} = \frac{P_i}{P_{\text{total}}} \quad (3.7)$$

Unlike a conventional two-arm MZI where only two signals interfere with one another, in a generalized MZI, multiple signals (four in the case of the MTOPS) interfere with one another, which greatly complicates the expression describing its behaviour as

shown in (3.4). Furthermore, as will be discussed later, the MMIs contribute additional phase delays to each of the four signals, thereby making the task of deriving an analytical expression difficult. As a result, most of the design and theoretical modeling was performed using standard numerical analysis.

3.4 Material Selection

Material selection is vital in the design of any device. Although a number of materials are suitable for the thermo-optic switch, this discussion will be limited to glasses, semiconductors, and polymers.

The first and most commonly used material for integrated optics is high purity silica (SiO_2) glass. This material can be deposited using chemical vapour deposition, flame hydrolysis or a sol-gel process [39]-[40]. For the purposes of this discussion, it is sufficient that the material be of high quality, i.e. low loss and free of stress, which causes birefringence. High purity silica glass waveguides have been fabricated with a propagation loss 0.01 dB/cm at 1550 nm and commercial foundries are capable of producing waveguides with losses typically less than 0.5-0.1 dB/cm [41]. Nevertheless, in the context of thermo-optic switches, glass has some disadvantages, namely:

1. low thermo-optic coefficient (10^{-5} to 10^{-6} $^{\circ}\text{C}^{-1}$),
2. moderately low thermal conductivity, and
3. moderately high processing costs.

As a result, even though glass is widely available, it is not the best choice.

Semiconductors are widely used in the integrated optics for active devices, such as lasers, modulators, amplifiers, and photodetectors. It is therefore desirable to use these materials for switches due to the ease of integration. Materials such as silicon, gallium arsenide, and indium phosphide are well characterized, and highly refined processes have been developed for their deposition. Two difficulties encountered with the use of semiconductors in thermo-optic switches are the need for thick high purity epitaxy and the high expense of both processing and acquiring the material. The refractive index of a semiconductor can be altered by heat via the temperature dependence of the free carrier concentration [42]. However, to achieve low loss waveguides required for optical distribution, high purity epitaxy must be used. Furthermore, the choice of substrate material is also restricted due to crystal lattice compatibility issues. Thus, semiconductors are not the best candidates for thermo-optic switches.

Polymers are organic materials made primarily from a combination of hydrogen, carbon, oxygen, nitrogen and other elements. Polymers exhibits the largest thermo-

optic coefficient, typically between $-1 \cdot 10^{-4}$ to $-5 \cdot 10^{-4} \text{ } ^\circ\text{C}^{-1}$. Favourable characteristics include:

1. relatively simple processing,
2. ability to planarize a surface,
3. compatibility with many different materials, i.e. glass, silicon or ceramic substrates,
4. variable in film thickness over a large range, typically from 0.5-50 μm ,
5. variable refractive index during polymer synthesis, and
6. low material costs.

However, polymers also have the following disadvantages:

1. relatively high propagation loss at longer wavelengths ($\sim 2 \text{ dB/cm}$ at 1550 nm),
2. uncertain environmental stability, i.e. temperature, vibration, humidity and
3. properties change with age.

Many of the undesirable properties have been mitigated, to some extent, by newly developed advanced polymers. For instance, the high loss at 1550 nm, on the order of 2-3 dB/cm, has been attributed to the carbon-hydrogen bond absorption peak. New polymers are either fluorinated (i.e. fluorine added) or deuterated (i.e. hydrogen replaced by deuterium) and have been reported to have losses $< 0.2 \text{ dB/cm}$ at 1550 nm [43]-[46]. Unfortunately, most of these new polymers are not commercially available. The manufacturers of these polymers tend to grant access to the materials via licensing or through collaborative research ventures. Table 3.4 summarizes the advantages and disadvantages when using glass, semiconductors, or polymers in thermo-optic switches.

Table 3.4 Summary of the properties and characteristics of glass, semiconductors, and polymers for use in thermo-optic switches

	Glass	Semiconductors	Polymers
Material Cost	moderate	high	low
Processing Cost	moderate	high	low to moderate
Thermo-optic Coeff.	low	moderate	high
Environmental Stability	high	moderate	moderate
Propagation Loss	low	low to moderate	moderate to high

In addition to the technical merits of polymers, TRILabs already had a polymer device research program which focused on passive optical components such as passive optical waveguides and microlenses [47]-[48]. Therefore, a natural extension of that research program was to investigate the performance of active devices based on polymers. This gave further support for using polymers rather than glass or semiconductors.

It is crucial that polymers be compatible with a number of substrate materials. This is an important issue for the intended applications, such as in the hybrid integrated optic switch, whereby a number of materials are integrated. After weighing the merits of all the materials, polymer was chosen for the thermo-optic switch.

The MTOPS was fabricated with UV-curable Norland optical adhesives (NOA). NOA 65 has a low refractive index, approximately 1.5145 at 1550 nm (STP), and was used as the cladding layer. NOA 63 has a refractive index of 1.5367 at 1550 nm (STP) and was used for the core layer. The refractive index values were measured using a prism coupler and are accurate to $\pm 1 \cdot 10^{-4}$ according to the instrument manufacturer. The thermo-optic coefficient specified by the manufacturer is $-1.8 \cdot 10^{-4} \text{ } ^\circ\text{C}^{-1}$ for the Norland polymers.

3.5 Design and Simulation

The design and simulation of the MTOPS comprise three parts: waveguides, MMI couplers, and heaters. The waveguides and MMI couplers are passive optical components and were designed and simulated using a combination of analytical and numerical methods. However, the analytical formulae were typically only used for the initial design and final design was refined using numerical simulations.

The design and simulation of the heaters included choosing a metal with the appropriate resistivity such that the thickness of the metal film would not adversely affect the uniformity of the polymer films. Detailed 2D thermal modeling was performed using PDEase, a commercial finite element software package. The results from the thermal analysis were then used to calculate the required refractive index change to alter the state of the switch for a given input current/power.

3.5.1. Waveguide Structure

The basic waveguide structure used throughout the switch is shown in Figure 3.9. The thickness and width of the core were chosen to be nominally 10 μm . This is approximately the mode field diameter of a single-mode fibre, and should provide efficient coupling. The thickness of the cladding layer was minimized such that the

speed of the device and the optical isolation between the core and substrate were maximized.

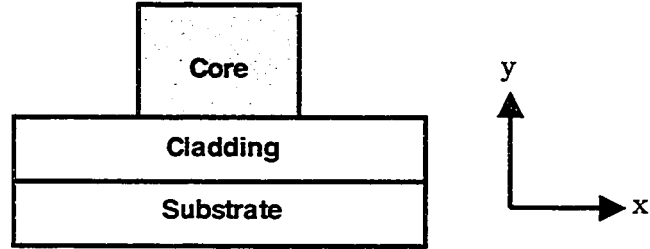


Figure 3.9. Geometry of the polymer waveguide used in the MTOPS. The refractive indices of the core and cladding layers are 1.5367 and 1.5145, respectively. Both glass and silicon substrates were used. The heating elements are made by depositing a very thin layer of chromium between the cladding and substrate.

Most of the development was done on silicon substrates rather than glass, due to logistics and a higher thermal conductivity for silicon. The cladding layer was thick enough to prevent the propagating modes from leaking or tunnelling into the substrate and causing high loss. To accurately predict the isolation between waveguides, the modes of the waveguide were calculated.

The various modes of a waveguide are represented by different spatial field distributions, as specified in Maxwell's equations or equivalently Helmholtz's equation. A closed form solution is available for slab waveguides, but is not available for two-dimensional structures. Equation (3.8) is a scalar approximation that can be used to find the modes, Φ_i , for an asymmetrical slab waveguide of width a , where the amplitude coefficients A , B and C are found by imposing the condition that the field and derivatives are continuous at the boundaries. The modes inside a waveguide are not necessarily separable, so the problem cannot be reduced to a two-dimensional one using the so-called "effective index method" without the loss of some information [49]. Therefore, a two-dimensional mode-solver program was written using MATLAB[®].

$$\Phi_i(x) = \begin{cases} A_i \exp(-P_i x) & x > a \\ B_i \cos(Q_i x) & 0 < x < a \\ C_i \exp(R_i x) & x < 0 \end{cases} \quad (3.8)$$

The modes of a waveguide were obtained by solving for the eigenvalues and eigenvectors of (3.9). The v^{th} eigenvalue is equal to the propagation constant, β_v , and the field distribution or mode profile is given by the v^{th} eigenvector. The numerical solution of (3.9) was accomplished by replacing the derivatives with second order

accurate central finite differences on a uniform grid, as shown in (3.10). Equation (3.10) was cast into matrix form and solved numerically using MATLAB. Illustrated in Figure 3.10 are the twelve largest eigenvalues (actually the effective index is shown, which is related to the propagation constant by the relation $\beta_v = n_{\text{eff},v} \cdot k_0$) and their associated eigenvectors. The solution method imposes a hard boundary, i.e. zero field at the four outer edges of the solution domain, therefore some numerical artifacts (solutions of the equation that are not physically meaningful) resulted.

The thickness of the cladding was increased until the intensity of the fundamental mode at the substrate interface was 30 dB lower than the peak intensity. Figure 3.11 shows a plot of the cross-sectional intensity for the fundamental mode for a 5 μm thick cladding. Notice that the intensity plot is asymmetrical, as would be expected for a waveguide that is bound by two different materials (air and polymer).

$$\nabla^2 \mathbf{E} = (\beta_v^2 - n^2 k_0^2) \mathbf{E} \quad (3.9)$$

$$\frac{E_{i+1,j} - 2E_{i,j} + E_{i-1,j}}{\Delta x^2} + \frac{E_{i,j+1} - 2E_{i,j} + E_{i,j-1}}{\Delta y^2} = (\beta_v^2 - n_{i,j}^2 k_0^2) E_{i,j} \quad (3.10)$$

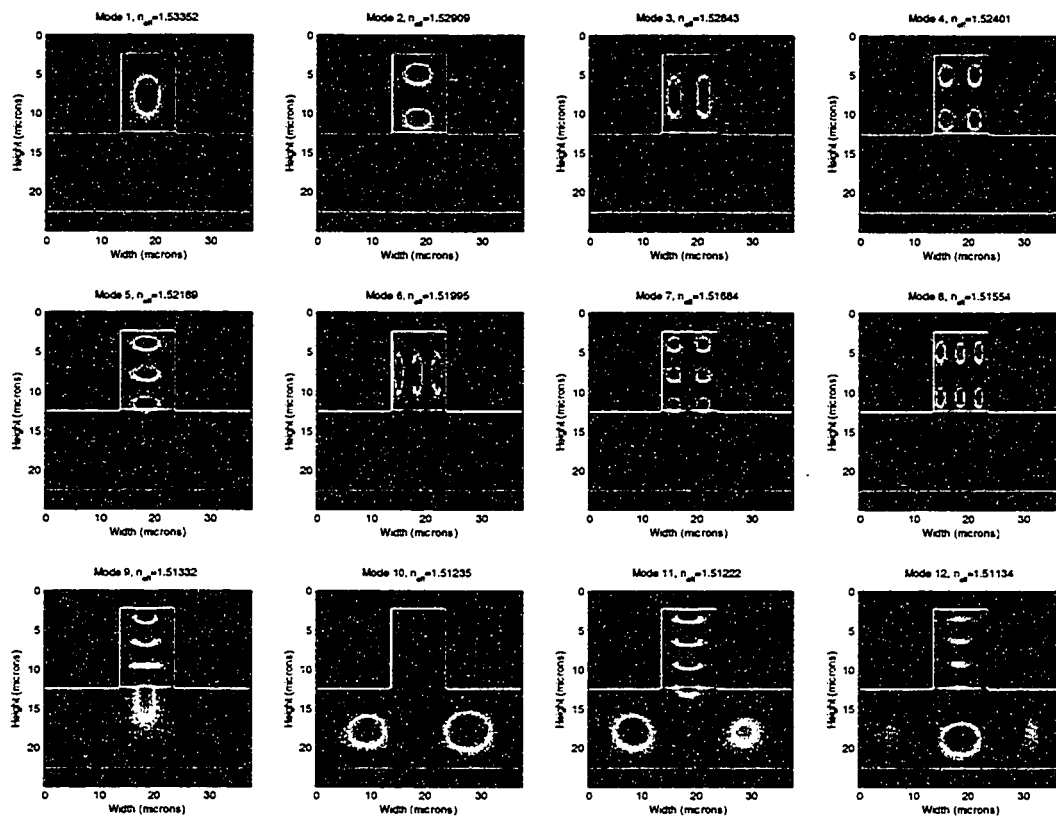


Figure 3.10. The twelve largest eigenvalues and eigenvectors for the waveguide structure shown in Figure 3.9. The effective refractive index for each mode, which is equal to the propagation constant divided by the free space wavenumber, is indicated at the top of each figure. Due to the limited size of the solution space, i.e. finite computer memory, modes 10-12 are numerical artifacts and are not guided. It can also be seen that mode 9 is probably not a guided mode since the effective index is lower than the cladding index.

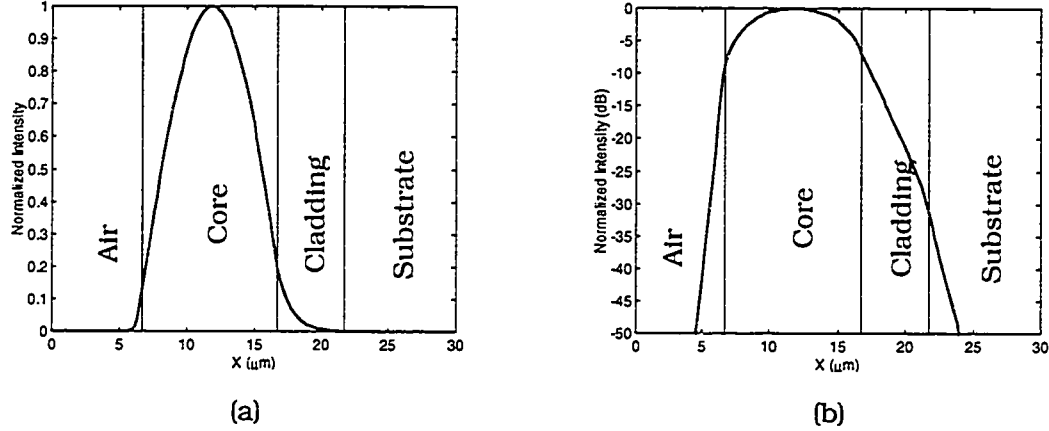


Figure 3.11. Cross-sectional intensity plots of the fundamental waveguide mode. The vertical lines indicate the boundaries between the core, cladding, and substrate regions. The ratio of the field intensity at the cladding-substrate interface to the peak intensity was -30 dB.

The modal power distribution in the input waveguide was analyzed with a single-mode fibre excitation to investigate the modal sensitivity of the splitters and generalized MZI. The analysis was performed using the first nine modes of the waveguide calculated by a 2D mode solver. The overlap integral (3.11), was then used to calculate the coupling factor between the single-mode input ϕ and each guided mode Φ_v as a function of the offset of the input fibre. The fractional power coupled to each mode is given by the square of the coupling parameter and the total coupling efficiency is equal to the sum of the squares of c_v . Shown in Figure 3.12 are power distribution plots for the first nine modes of a 10 μm by 10 μm waveguide when excited by a single-mode fibre. Hence the maximum coupling efficiency does not occur at the geometric centre because the modes are skewed by the presence of the cladding layer. Also, it can be seen that most of the power is contained in the fundamental or first waveguide mode when the input fibre is properly aligned to the waveguide. As the fibre position moves away from the optimal position, more power is coupled to the higher order modes.

$$c_v = \int_{-\infty}^{\infty} \int_{-\infty}^{\infty} \Phi_v \cdot \phi dx dy, \quad v = 1, \dots, 9 \quad (3.11)$$

3D BPM simulations were performed to investigate the effect of offsets of the input fibre on the coupling loss and contrast ratio for the MTOPS. The results are shown in Figure 3.13. The coupling loss and contrast ratio increases as the input offset is increased. From this data the alignment tolerance of the input fibre is less than $\pm 2 \mu\text{m}$.

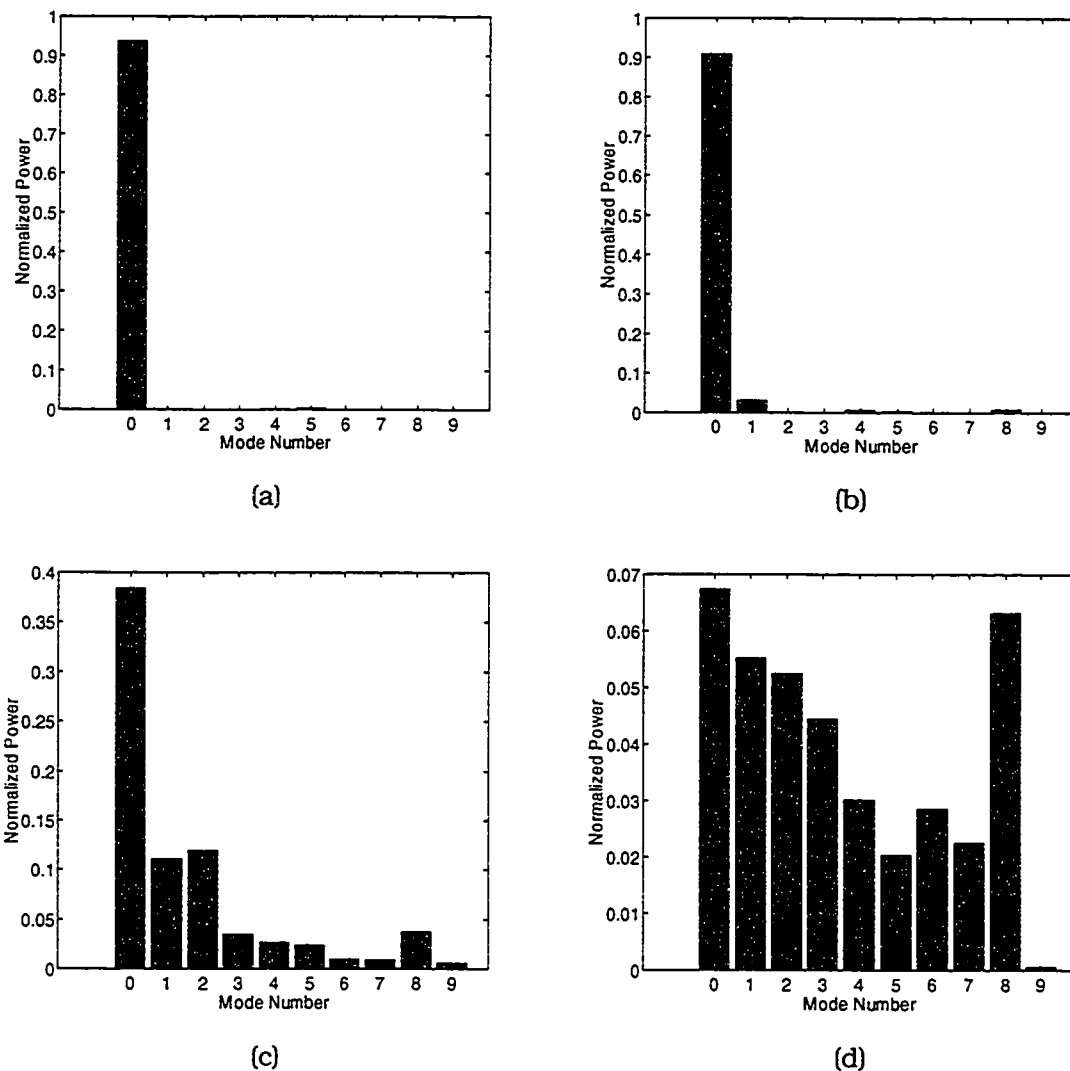


Figure 3.12. Calculations of the normalized power distribution for the first nine modes supported in a $10\ \mu\text{m} \times 10\ \mu\text{m}$ polymer waveguide. The coupling efficiency and offset of the input fibre were: (a) 94.7 % (-0.24 dB) for the geometric centre of the waveguide, (b) 95.6 % (-0.2 dB) for a vertical offset of $1.2\ \mu\text{m}$, (c) 76.1 % (-1.2 dB) for $3\ \mu\text{m}$ offset in both directions, and (d) 38.5 % (-4.1 dB) for a $5\ \mu\text{m}$ offset in both directions.

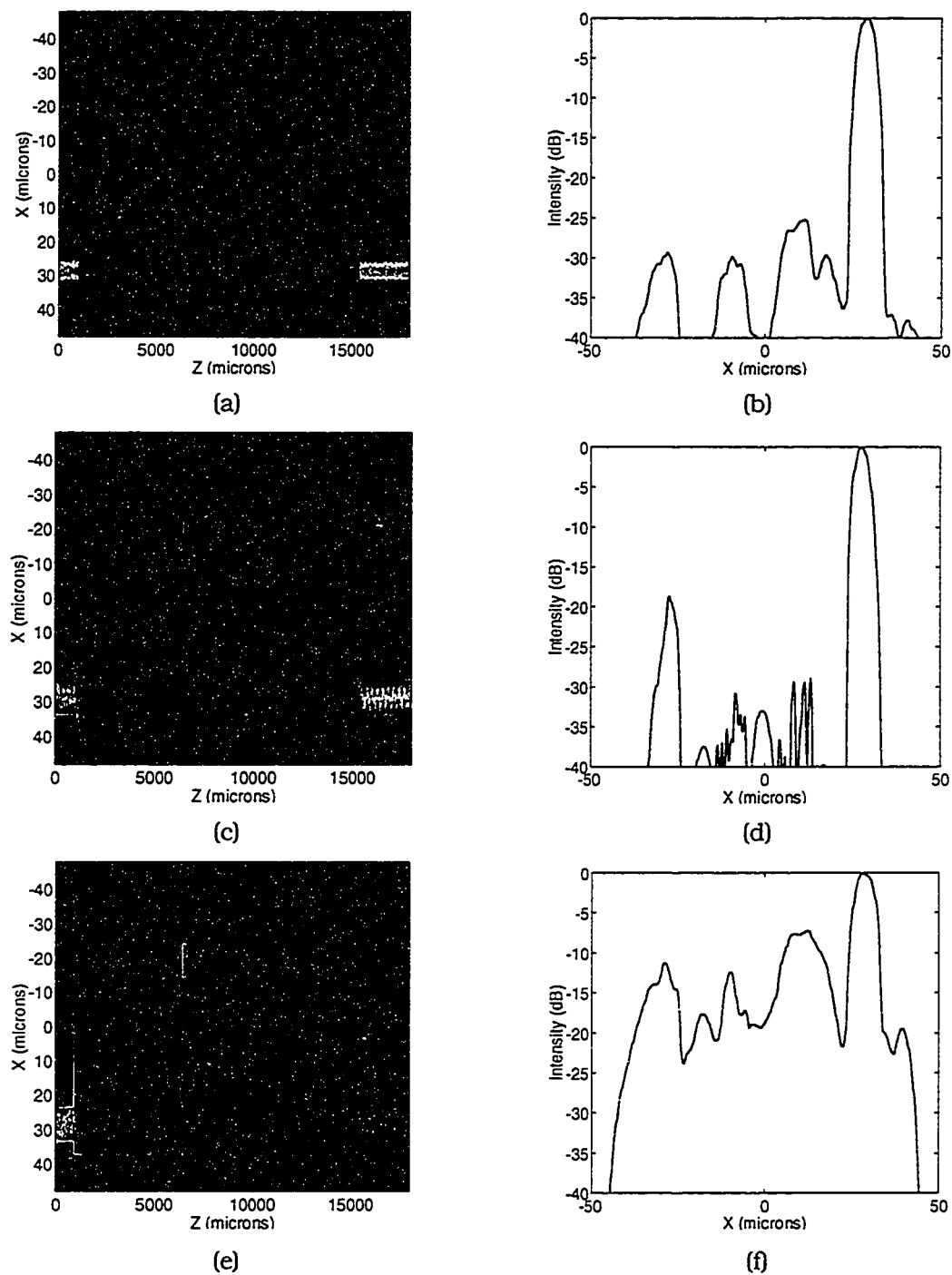


Figure 3.13. 3D BPM simulations illustrating the effect of input offset on coupling loss and switch contrast ratio. In (a), the input field was located at the geometric centre, and resulted in a total loss of 0.5 dB and a contrast ratio of 23.4 dB. In (c), the input was located at $\Delta y = -3 \mu\text{m}$, $\Delta x = 3 \mu\text{m}$, and resulted in 1 dB of loss and a contrast ratio of 20 dB. For a $-5 \mu\text{m}$ offset in y and $5 \mu\text{m}$ offset in x (e), the loss and the contrast ratio were 6.7 dB and 5.4 dB, respectively. Figures (b), (d) and (f) are cross-sectional plots of the intensity profile at the output of the switch.

3.5.2. Multimode Interference Couplers

A basic MMI structure is illustrated in Figure 3.14. The theory describing the operation of a MMI is quite lengthy and well documented [50]; hence only a brief summary is presented here.

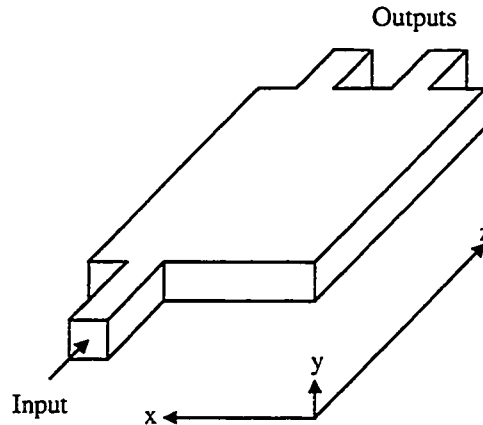


Figure 3.14. Perspective drawing of a 1x2 multimode interference coupler. The input field excites multiple modes in the MMI. The propagating modes have a phase relationship that results in multiple images along the z-direction. The length and width of a MMI are critical design parameters and have a direct bearing on the relative intensities at the output ports.

A MMI is a wide multimode section of waveguide, with the input excitation at specific transverse locations giving rise to the self-imaging effect. Self-imaging occurs when the input field or multiples of the field are periodically reproduced along the direction of propagation. The phenomenon of self-imaging results because the phases of the propagating modes are interrelated [51].

3.5.2.1. Theory of Operation

To comprehend the basic operation of a MMI, consider a multimode waveguide with hard boundary conditions (the field equals zero at the boundary). A metal walled or air-clad dielectric waveguide approximates the ideal situation where the field(s) fall to zero at the walls. The electric field inside a waveguide is given by (3.12), where the transverse wavenumber, k_t , and effective width, W_{eff} , are given by (3.13) [52]. The width of the waveguide, W , and the effective refractive index of the cladding (or film), N_f , and core, N_c , are known parameters. The transverse locations of the access guides for a 4x4 MMI coupler are illustrated in Figure 3.15, with the first four modes described by (3.12) plotted in Figure 3.16. Typically, MMI couplers have more modes to improve imaging resolution [53], such as those used in the MTOPS (75 μm wide and ~ 380 lateral modes and four vertical modes).

$$\Phi_i(x) \equiv A_i \sin(k_i x), \quad 0 < x < W \tag{3.12}$$

$$k_i = \frac{\pi(i+1)}{W_{eff}} \tag{3.13}$$

$$W_{eff} = W + \frac{\lambda_o}{\pi\sqrt{N_f^2 - N_c^2}}$$

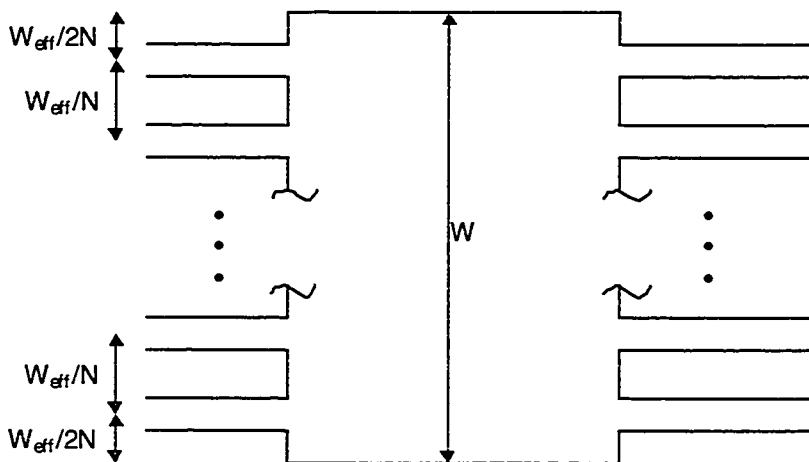


Figure 3.15. The input and output waveguides must be located at specific transverse locations as indicated in the drawing. N is the number of input/output waveguides.

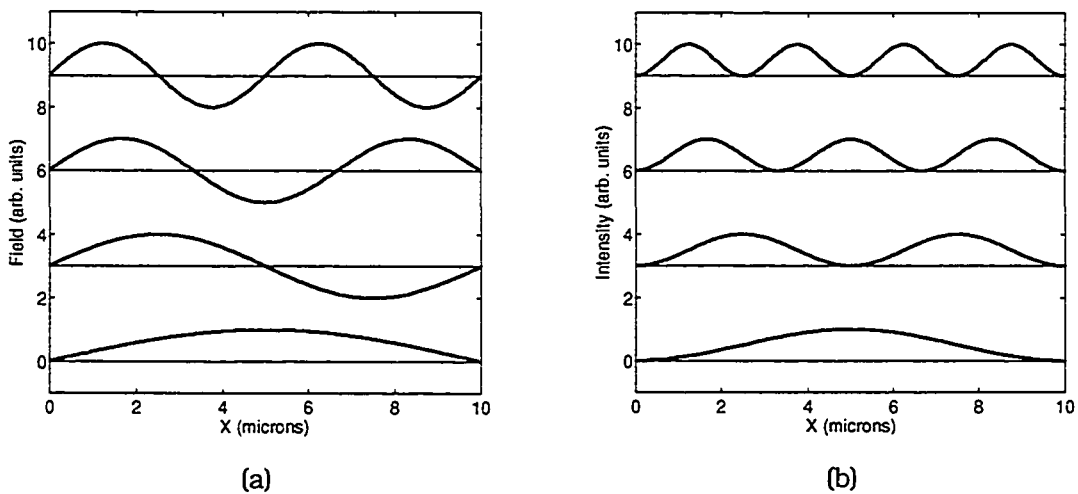


Figure 3.16. The field (a) and intensity (b) of the first four modes in a metal walled waveguide. The plots for each mode are offset for clarity and the thin horizontal lines represents zero.

By solving for the propagation constant in the dispersion relation [12] and using a binomial expansion, one obtains [52],

$$\beta_i \approx \beta_0 - \frac{(i+1)^2 \pi \lambda_0}{4N_c W_{eff}^2} = \beta_0 - \frac{i(i+2)\pi}{3L_\pi} \quad (3.14)$$

where L_π is the beat length and is defined by (3.15). The quadratic dependency of the propagation constant on the mode number i gives rise to the self-imaging effect in MMI couplers [52].

$$L_\pi = \frac{\pi}{\beta_0 - \beta_1} = \frac{4N_c W_{eff}^2}{3\lambda_0} \quad (3.15)$$

There are three main coupler configurations: the 1 to N equal intensity state which splits the input signal equally among the outputs, the cross-state and the bar-state. The cross- and bar-state configuration lose their meaning somewhat for switches larger than 2x2. For switches larger than 2x2, the state of a coupler must be explicitly specified. Figure 3.17 graphically illustrates the three configurations.

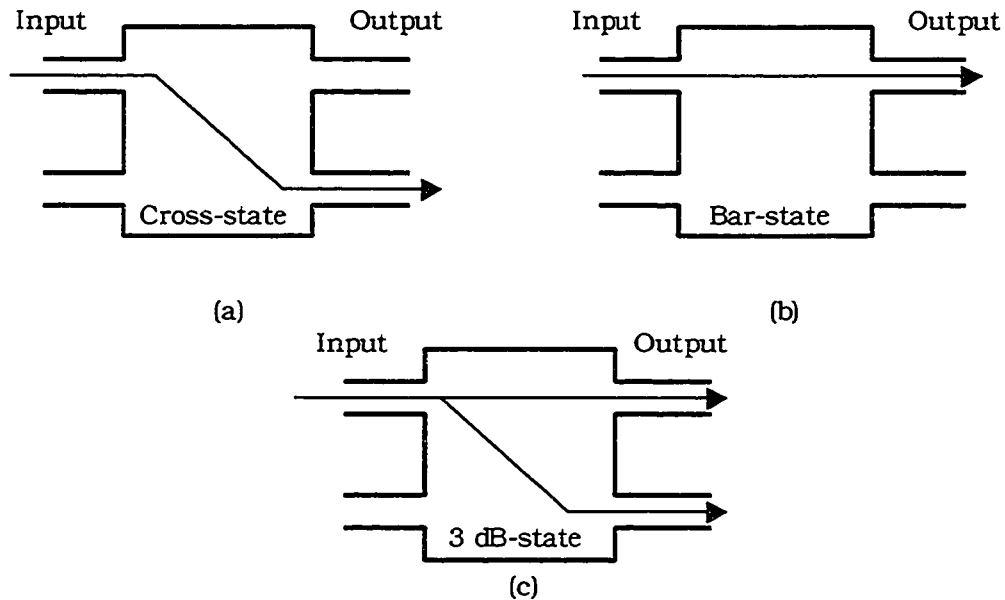


Figure 3.17. The cross-state occurs when the input signal is cross-connected to an output (a). The bar-state occurs when the input signal appears at the same lateral output (b). The equal-split or 3 dB state results when the input signal is split equally among the outputs. The definition of cross and bar states is not well suited for switches larger than 2x2, because there are many cross-states and only one bar-state. Therefore, when stating a switch is in the cross-state, extra information must be provided for switches larger than 2x2 to eliminate ambiguity.

Unlike conventional Y-splitters or directional couplers, a MMI coupler may operate in two different resonance conditions: restricted resonance and general resonance. In many situations, restricted interference can be used to reduce the length of an MMI coupler by a factor of four, with certain trade-offs. Restricted interference, including symmetric and paired interference, results when only certain modes in the MMI structure are excited [54]. When the input is located at the centre of an MMI, symmetric interference occurs due to the excitation of the even modes [52]. In a similar manner, paired interference occurs when an even number of inputs are located at symmetric transverse locations such that modes 2,5,8, ..., are not excited [52].

3.5.2.2. Simulation Results

In general resonance interference, no modal excitation restrictions are imposed. The MMI couplers used in the MTOPS split the power equally to all four outputs and are nominally 75 μm wide. Initial calculations used (3.15) and (3.16) to predict the 6 dB length, and were later refined using 2D and 3D BPM simulations. These formulae were used for initial calculations after the design problem was reduced from two dimensions to one using the effective index method. Furthermore, the accuracy of these formulae decreases with increasing number of modes. The calculated 6 dB length, $L_{6\text{-dB}}$, was 5570 μm . Shown in Figure 3.19 is the result from a 2D BPM simulation of a 75 μm wide MMI coupler. The coupling length determined from the BPM simulation was 5461 μm , 109 μm shorter than predicted by the analytical equations. A plot of a MMI coupler connected to output waveguides is shown in Figure 3.20. The locations of the input/output guides, relative to the centre of the MMI, were optimized and it was found that $\pm 9 \mu\text{m}$ and ± 28.75 gave the best results.

$$L_{6\text{-dB}} \equiv \frac{3L_{\pi}}{4} \quad (3.16)$$

One limitation of MMI couplers is their sensitivity to fabrication tolerances. Figure 3.18 illustrates the effect of length and width variations (ΔL and ΔW respectively) on the excess loss of a 1x4 MMI coupler. Clearly, stringent process control is required to optimize the performance of a MMI coupler.

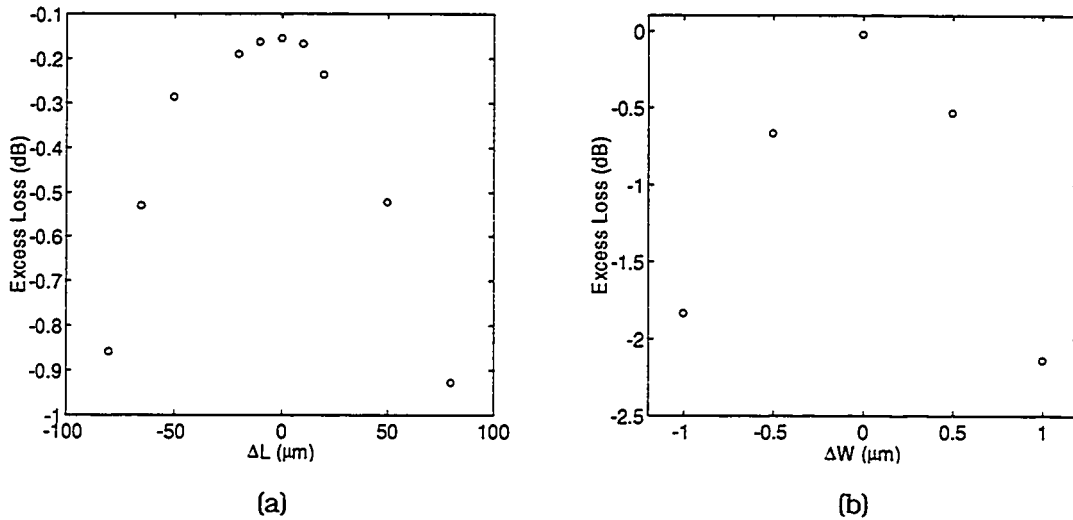


Figure 3.18. Excess loss of a 1x4 MMI as a function of the sensitivity to length and width variations calculated using 2D BPM simulations. Notice that the MMI coupler is extremely sensitive to width variations, ΔW , resulting in stringent device fabrication tolerances.

3.5.2.3. Phase Properties of MMI Couplers

The phase relationship between any input and output signal in a general resonance MMI coupler is given by (3.17) [50], where the numbering convention used is shown in Figure 3.21. The relative phase of each output signal is important when cascading two MMI couplers because the output intensity of a MZI as described by (3.4) depends on the phase difference between the signal in each arm. Table 3.5 summarizes the input to output phase relationship for a 4x4 MMI coupler based Mach-Zehnder switch [55].

$$\phi_{i,j} = \phi_0 - \frac{\pi}{2}(-1)^{i+j+N} + \frac{\pi}{4N} \left[i + j - i^2 - j^2 + (-1)^{i+j+N} \left(2ij - i - j + \frac{1}{2} \right) \right] \quad (3.17)$$

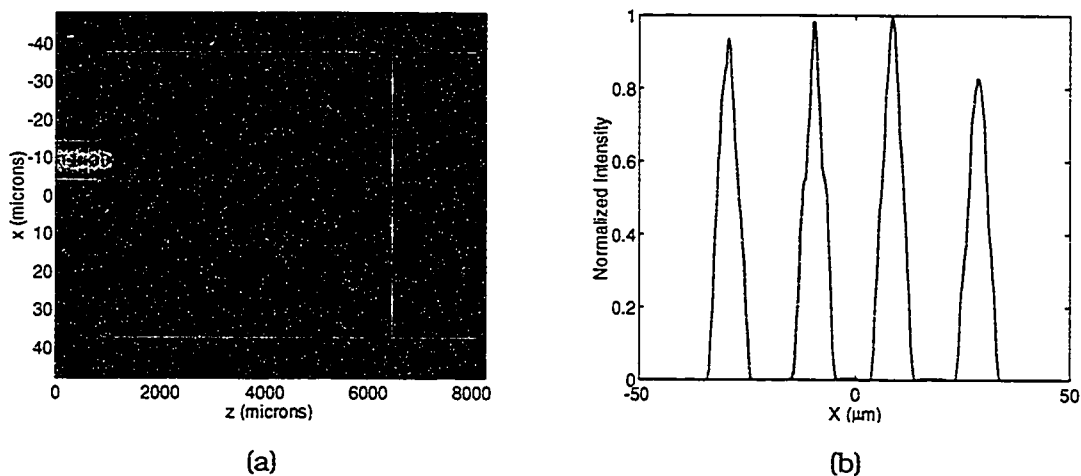


Figure 3.19. (a) Intensity plot of a $75\ \mu\text{m}$ wide MMI obtained from a 2D BPM simulation. The vertical line indicates where the input signal splits into four, which corresponds to a 6 dB MMI coupler length of $\sim 5480\ \mu\text{m}$. (b) A plot of the intensity at the 6 dB length.

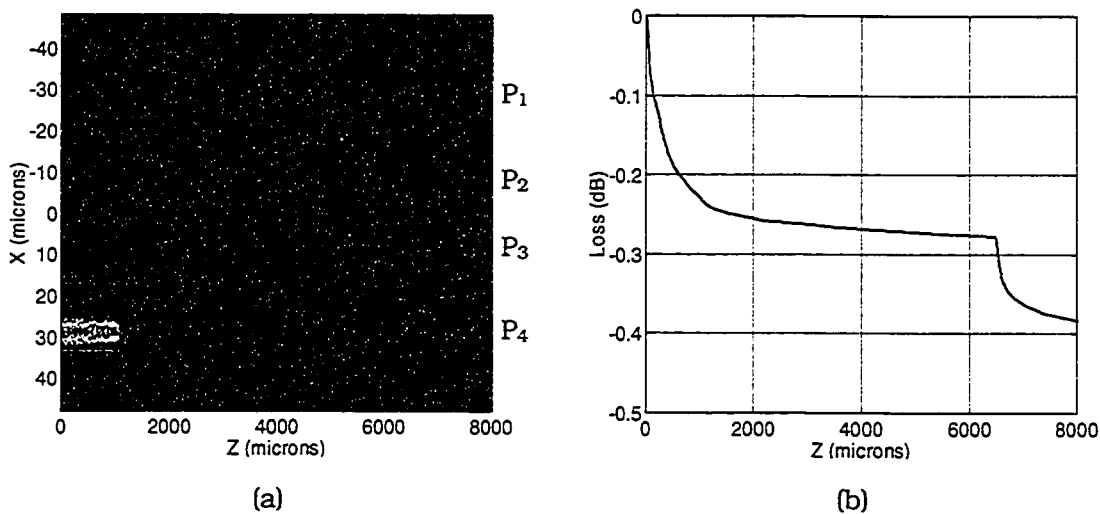


Figure 3.20. (a) Intensity plot from a 3D BPM simulation of a $75\ \mu\text{m}$ wide MMI coupler. (b) The coupling and insertion losses were 0.27 dB and 0.1 dB, respectively. The relative power in each of the outputs, labelled from top to bottom, were approximately $P_1 = -6.35\ \text{dB}$, $P_2 = -6.40\ \text{dB}$, $P_3 = -6.48\ \text{dB}$, and $P_4 = -6.44\ \text{dB}$.

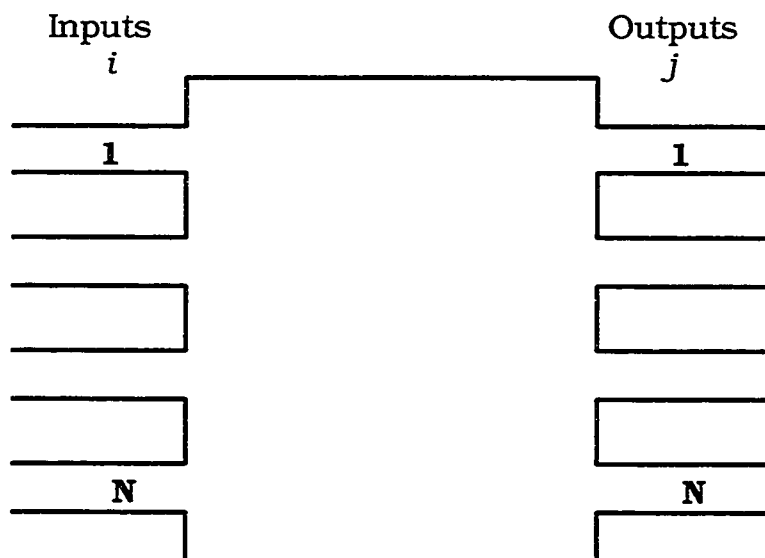


Figure 3.21. Numbering convention used to describe the phase relationship between inputs and outputs given by equation (3.17).

Table 3.5. Summary of the phase relationship between any input and output of a 4x4 MMI coupler. A constant phase factor of $47/32 \pi$ was added so that the phase factors were multiples of $1/4 \pi$.

	j=1	j=2	j=3	j=4
i=1	π	$7/4 \pi$	$3/4 \pi$	π
i=2	$7/4 \pi$	π	π	$3/4 \pi$
i=3	$3/4 \pi$	π	π	$7/4 \pi$
i=4	π	$3/4 \pi$	$7/4 \pi$	π

3.5.3. Effects of Multiple Modes on the Performance of a Generalized Mach-Zehnder Interferometer

Multimode waveguides were used in the MTOPS. Predictably, performance was adversely affected since the behaviour of multiple spatial mode interference is much more complicated than single-mode or plane-wave interference. The output intensity of the MTOPS is governed by the phase difference between the four signals from the phase shifters. If single-mode waveguides were used, a simple analysis would consist of calculating the interference of the four signals as represented by four phasors. However, when using multimode waveguides, the light from each arm is distributed

across many modes, with each mode having a different propagation constant. Furthermore, the modal power distribution in each arm may be different. As a result, complete constructive and destructive interference may not be achievable, thereby reducing the contrast and extinction ratios.

The effects of multiple modes were clearly demonstrated when 2D BPM simulations were compared to 3D BPM simulations. The contrast ratios predicted by the 3D simulations were lower than those predicted by the 2D simulations. Shown in Figure 3.23 and Figure 3.13 are the results from the 2D and 3D BPM simulations, respectively. Note that the contrast ratio is altered when the input field was offset by $1\ \mu\text{m}$ in the x and y directions, a result of coupling more power into more modes. When the output from a single-mode fibre is perfectly aligned with the fundamental mode of the waveguide only even modes are excited, but when the single-mode fibre is offset slightly, power is also coupled into the odd modes. Fundamentally, it becomes more difficult to achieve complete constructive/destructive interference with an increasing number of modes due to the mode dependent propagation constant. This is a result of the propagation constants differing for various modes. Hence the phase shift required to cause complete destructive interference are also slightly different, thereby reducing the contrast ratio.

The effect of a mode dependent propagation constant was investigated by calculating the propagation constants for the first four modes of a $10\times 10\ \mu\text{m}$ polymer waveguide using a 2D mode solver. First, the propagation constants β_1 to β_4 were calculated for an unpowered switch. Next, the refractive index of the waveguide was lowered by $1.1\cdot 10^{-4}$ and the propagation constants were recalculated. The phase shift of each mode was calculated for a $3518\ \mu\text{m}$ long waveguide and are summarized in Table 3.6. The phase change degrades with increasing mode number as illustrated in Figure 3.22, but the deviation from the nominal value is small for the first few modes. As a result, the effect will not be too great since most of the power is carried by the lower order modes. Note, these numbers were chosen because they are the same as those used in the BPM simulations.

Table 3.6. Calculated propagation constants normalized to the free-space wavenumber k_0 for the first four modes of a $10 \times 10 \times 3518 \mu\text{m}$ waveguide. The phase change, $\Delta\phi$, should be $\pi/2$ or 1.5708.

β/k_0 ($n_{\text{core}}=1.5367$)	β'/k_0 ($n_{\text{core}}=1.5365$)	$\Delta\phi=\Delta\beta L$
1.5332942	1.5331837	1.5758
1.528519	1.528411	1.5402
1.527881	1.527772	1.5544
1.523108	1.523000	1.5402

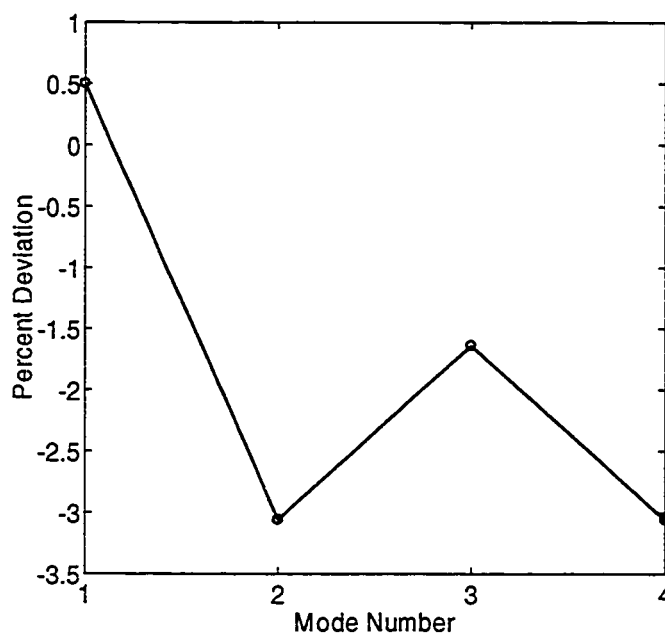


Figure 3.22. Calculated percent deviation of the phase change from the ideal value of 1.5708 for the first four modes of a $10 \times 10 \times 3518 \mu\text{m}$ polymer waveguide.

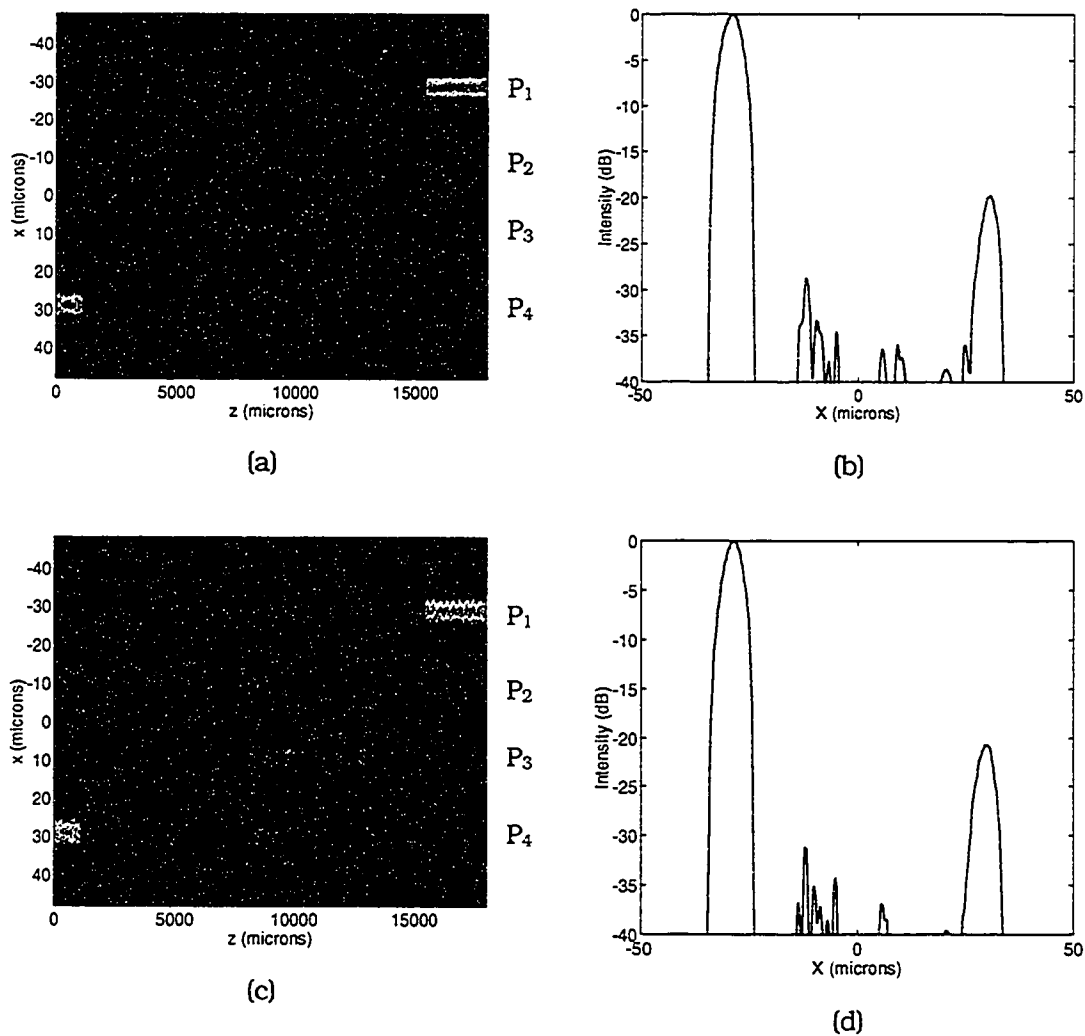


Figure 3.23. 2D BPM simulations illustrating the effects of input coupling misalignment. Intensity plots in the x - z plane are shown on the left side, while plots of the output intensity are shown on the right. The input excitation is located at the centre of the input guide in (a) and (b) and was offset by $1\ \mu\text{m}$ in (c) and (d). The relative power in each of the output waveguides for (b) and (d) are: $P_1 = -0.29\ \text{dB}$, $P_2 = -27.1\ \text{dB}$, $P_3 = -32.6\ \text{dB}$, $P_4 = -20.3\ \text{dB}$, and $P_1 = -0.22\ \text{dB}$, $P_2 = -31.3\ \text{dB}$, $P_3 = -37.3\ \text{dB}$, $P_4 = -21.1\ \text{dB}$, respectively.

3.5.4. Thermal Design Considerations and Modeling Results

By incorporating thermally controlled phase shifters, the state of the MTOPS can be altered. This was accomplished by depositing a thin layer of chromium beneath the MZI arms. When electrical current passes through the chromium heaters, Joule

heating causes a local temperature increase, resulting in a lowering of the refractive index. The change in refractive index per degree temperature change is approximated by the thermo-optic coefficient, and is

$$\frac{\Delta n}{\Delta T} = -2 \cdot 10^{-4} \text{ } ^\circ\text{C}^{-1} \quad (3.18)$$

for the Norland optical adhesives used in the MTOPS [56].

A 2D thermal model of the waveguide structure was established to better predict the heat dynamics and thermally induced refractive index changes. Since some thermal-physical properties and parameters were not precisely known, approximate values were used. An important assumption was that the thermo-optic coefficient and thermal conductivity of the polymer were independent of temperature, which should be a good approximation since the simulated temperature change was no greater than 40 °C.

Equation (3.19), also known as the heat equation, was used to model the temperature profile in the waveguide. The equation relates temperature T to the heat source \dot{q} (units of W/m^3), the thermal conductivity k (units of $\text{W}/\text{m}\cdot^\circ\text{C}$), and thermal diffusivity α (units of m^2/s). Steady-state thermal analysis can be performed by setting the time derivative in (3.19) to zero.

$$\nabla^2 T + \frac{\dot{q}}{k} = \frac{1}{\alpha} \frac{\partial T}{\partial t} \quad (3.19)$$

In addition, appropriate boundary conditions must be applied at all interfaces. Since the temperature change was rather small, radiative heat transport was neglected. Although conductive heat transfer was assumed to be dominant mechanism within the polymer material, free convection occurs at the air-polymer interfaces and must also be taken into account. Convective boundary conditions were applied at air-polymer and air-substrate interfaces using (3.20), where h is the interfacial heat-transfer coefficient and T_A is the ambient temperature.

$$\left. \frac{\partial T}{\partial x} \right]_{x=B} = \frac{h}{k} (T - T_A) \quad (3.20)$$

A commercial program, called PDEase, employs finite element approximations to solve equations (3.19) and (3.20). The source scripts for the steady-state and transient analysis can be found in Appendix I. The geometry used in the thermal models is shown in Figure 3.24. Other important parameters used in the simulation are summarized in Table 3.7. The results from the steady-state analysis are shown in Figure 3.25. The power per unit length required to raise the temperature of the waveguide core by 10 °C was predicted to be 80 W/m, hence a heater length of 5 mm required 400 mW of power.

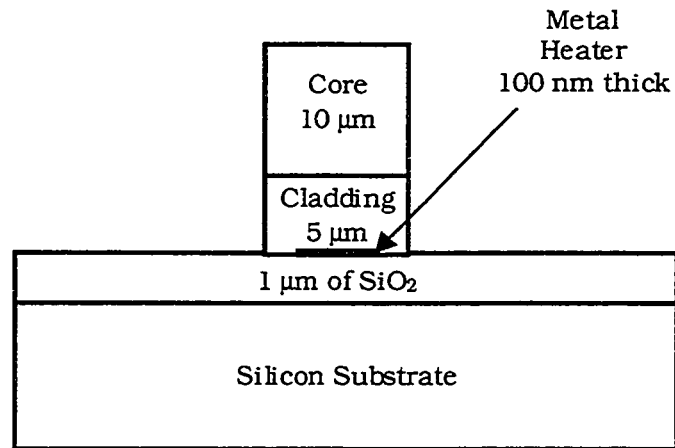


Figure 3.24. Waveguide structure used in thermal analysis. The core and cladding polymer layers were combined since their thermal properties were nearly identical.

Table 3.7. Summary of the constants used in the thermal models (source [57]-[58]).

	Polymer Core/Cladding	Glass Buffer	Chromium Heater	Silicon Substrate
Thermal conductivity (W/m·°C)	0.2	1	70	124
Specific heat (J/kg·°C)	1420	700	460	1045
Density (kg/m ³)	1100	2500	7800	2328

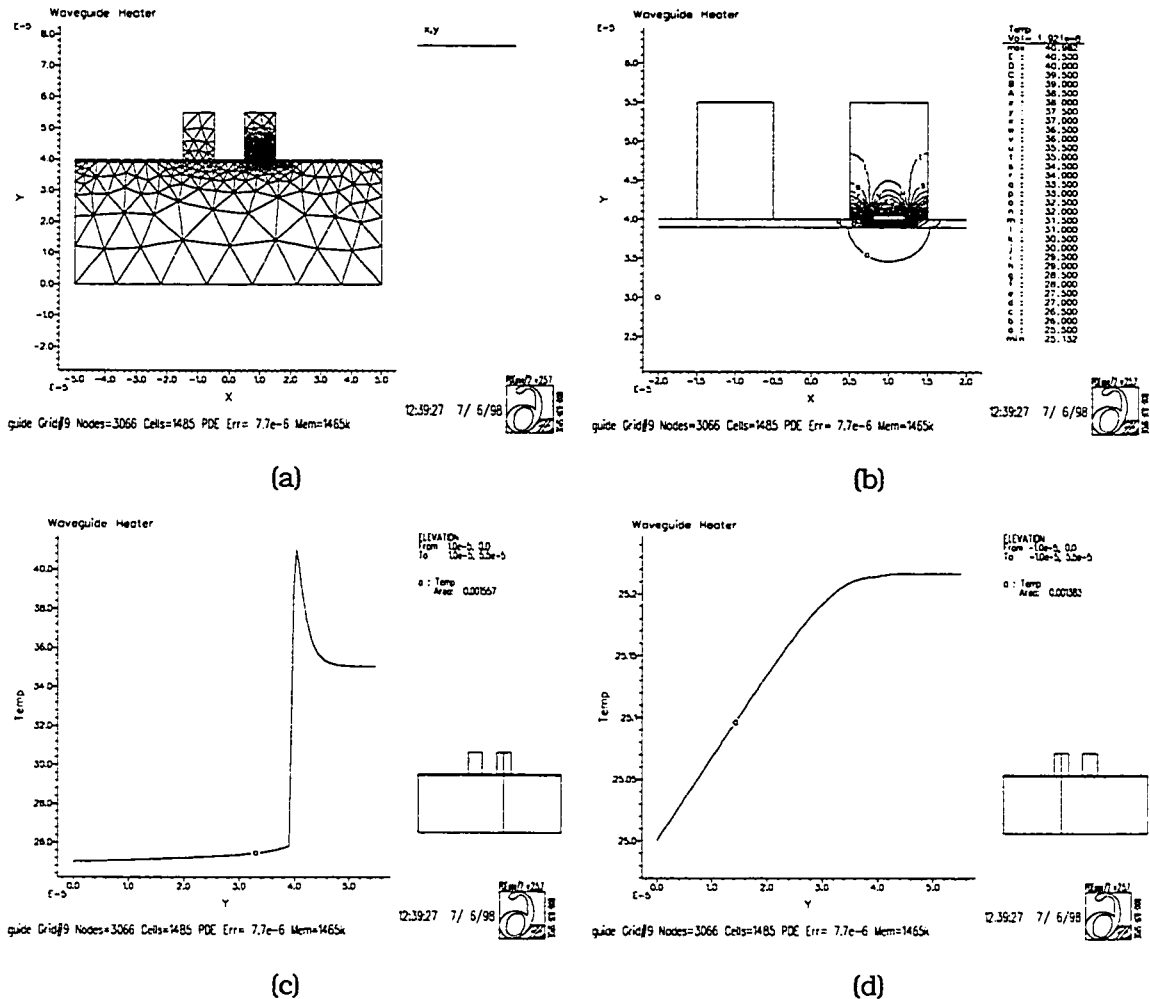


Figure 3.25. Steady-state thermal modeling results obtained from PDEase. (a) The geometry and refined finite element mesh used to solve the problem. (b) Contour plot of the temperature profile. (c) Cross-sectional temperature profile of a waveguide with the heater turned on. Note the temperature is nearly constant in the waveguide. (d) Temperature profile of a waveguide approximately 20 μm from the heater representing the thermal cross-talk or equivalently the thermal isolation. The vertical line shown in the thumbnail plots located in the lower right corner of plots (c) and (d) represent the path used to calculate the cross-sectional temperature plots.

A transient or time-dependent thermal analysis was also performed to arrive at an estimate of the switching time. The results are illustrated in Figure 3.26. From the plots, the switching time was estimated to be ~ 6 ms (3 ms for both rise and fall times), and is primarily limited by the thickness and thermal conductivity of the polymer waveguide and cladding layers.

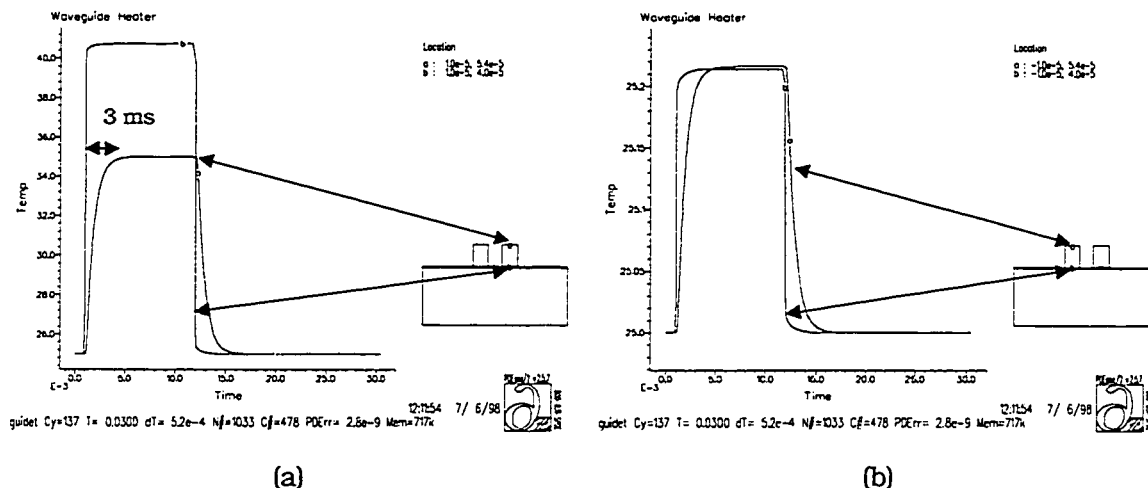


Figure 3.26. Transient thermal modeling results. Temperature profiles were generated as a function of time at four specific points. The arrows indicate the locations on the thumbnail plots where the temperature was monitored. (a) The temperature was measured on the top surface of the heater and waveguide. The switching time estimated from (a) is ~ 3 ms. (b) The temperature was measured at the SiO₂-polymer interface and at the top of the waveguide.

3.5.5. Beam Propagation Simulations of the Overall Device

A number of BPM simulations were performed on the overall device to determine the contrast ratio and insertion loss. Comparative simulations were performed to observe the agreement of 2D and 3D simulations. The 2D simulations produced more optimistic results, (lower losses and better contrast ratios) but otherwise agreed well with the 3D simulations.

Shown in Figure 3.27 are the results from a 2D BPM simulation of the entire device in the absence of current applied to the heaters, (or the unbiased state). The phase delay imparted by the cascaded MMI couplers causes complete destructive interference at two outputs. The length of the phase shifters or arms was shortened, to reduce computation time and memory usage, without any loss of generality or accuracy. Shown in Figure 3.28 is a result from a 2D BPM simulation when the refractive index of arms two and three were lowered to achieve complete switching of input four to input one. A 3D BPM simulation of the entire device was shown previously in Figure 3.13(a).

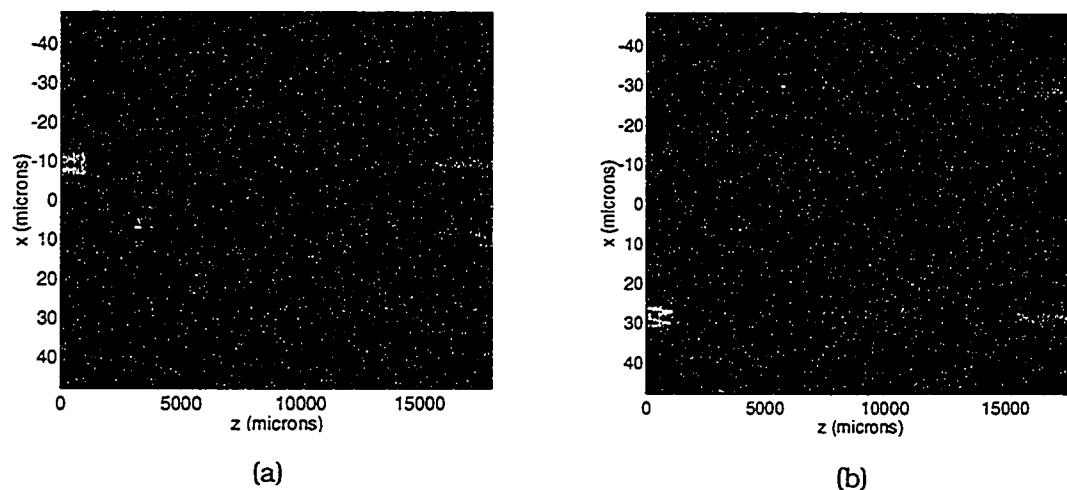


Figure 3.27. 2D BPM simulations of the overall device operating in the unbiased state. Each MMI imparts a phase delay to each signal, and when cascaded results in the intensity plots shown. (a) When the signal is applied to input two, two equal signals are produced at outputs two and three. (b) When the signal is applied to input four, two equal signals are produced at outputs one and four. The remaining two combinations can be obtained by making use of symmetry. The total loss, not including propagation loss, was <0.2 dB.

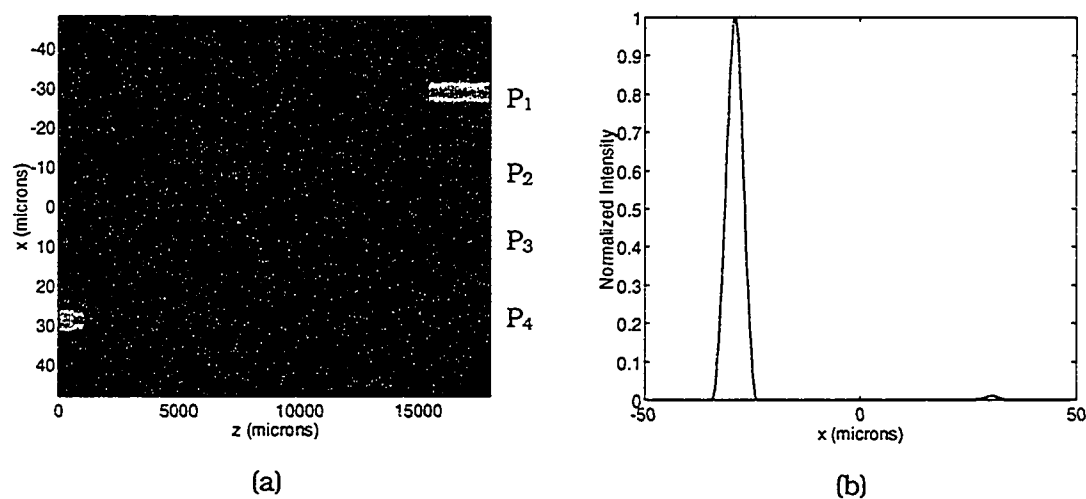


Figure 3.28. 2D BPM simulations showing the MTOPS connecting input-four to output-one. (a) Intensity plot. (b) Cross-sectional intensity plot at $z=18$ mm. The output power relative to the launched power for each output is: $P_1=-0.22$ dB, $P_2=-31.3$ dB, $P_3=-37.3$ dB, and $P_4=-21.1$ dB.

3.6 Device Fabrication

The MTOP was fabricated using a photolithographic process. Shown in Figure 3.29 is a composite of the four level mask set used to fabricate the device. Figure 3.30 illustrates each of the separate mask layers used in the photolithography process.

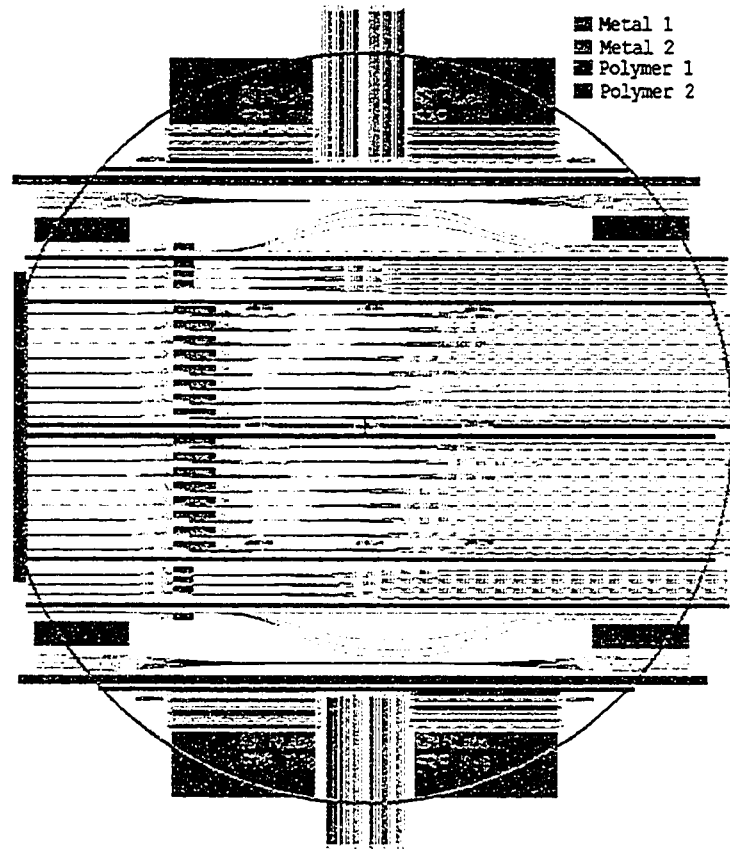


Figure 3.29. Composite plot of the four layer mask set used in the photolithography fabrication process. Mask layers Metal 1 and Metal 2 were used to pattern the chromium heaters and gold interconnect metal. Mask layers Polymer 1 and Polymer 2 were used to pattern the cladding and core polymer layers.

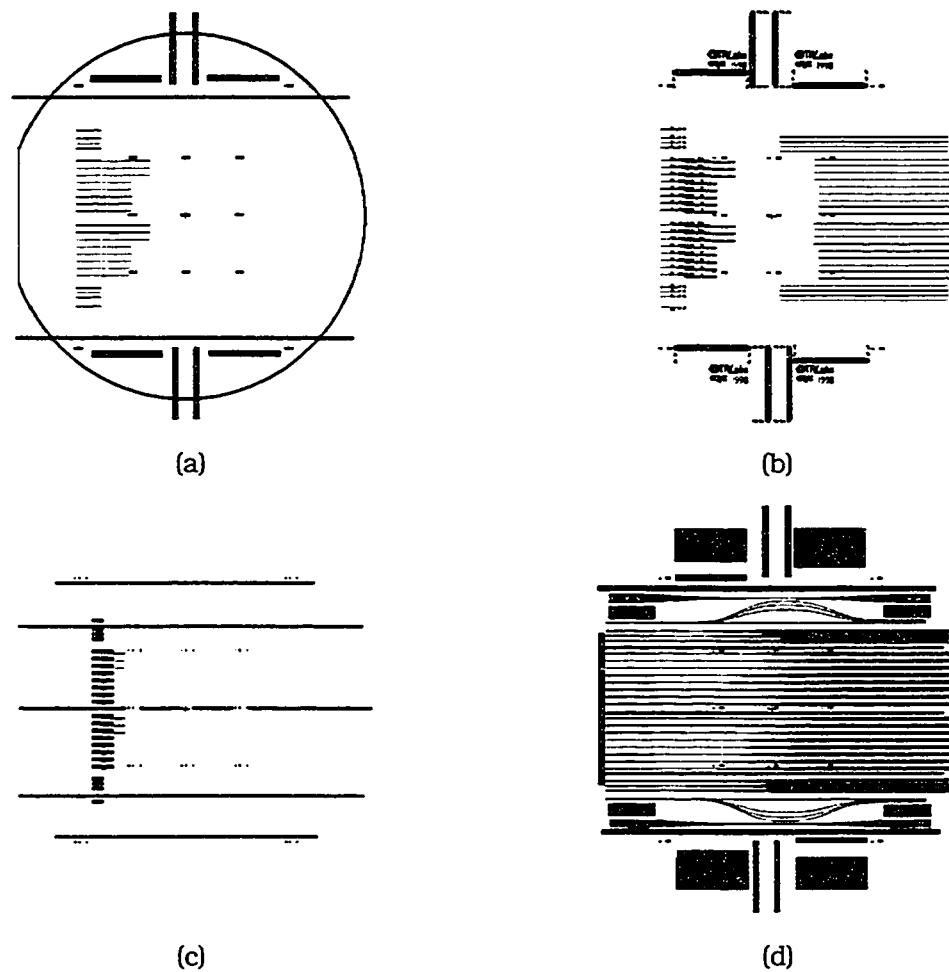


Figure 3.30. Plots of the individual mask layers. The chromium heaters are patterned with mask layer Metal 1 (a). The electrical interconnections were made using mask layer Metal 2 (b) to pattern gold. Mask layers Polymer 1 (c) and Polymer 2 (d) were used to pattern the cladding and core polymer layers, respectively. Note that during the mask fabrication process, negative images of layers one, two and three were generated. This was due to the use of positive photoresist in the lift-off process and simplified the layout of the cladding mask.

3.6.1. Metal Deposition

Two metal layers were used to control the phase shifters of the MTOPS. The first layer was fabricated by depositing a 100 nm thick layer of evaporated chromium metal. The resistance of a metal layer is a function of its thickness, area and resistivity. The resistance of a 1mm long by 8 μm wide by 100 nm thick deposition was calculated to be 160 Ω , assuming a resistivity of $12.9 \cdot 10^{-8} \Omega \cdot \text{m}$ [57]. The actual measured resistance of the heaters varied from 725-727 Ω , most likely due to variances in the resistivity and film thickness. A 1 μm thick layer of gold layer used to interconnect the heaters was then evaporated on top of the chrome layer.

The metal layers were patterned using a lift-off photolithography process. Since the process used is proprietary to the Communication Research Centre (CRC), only a general overview will be given. A substrate coated with a thin photoresist layer was placed in a mask-aligner and exposed, through the appropriate mask, to UV light. The substrate was developed so that the exposed photoresist was removed. After evaporating metal onto the substrate, the remaining photoresist was "lifted-off" leaving a patterned metal substrate.

Shown in Figure 3.31 are photographs taken through an optical microscope of wafers that had the metal layers processed. A frequent problem (during processing) occurred when the second mask would move prior to exposure, causing a misalignment between the two layers. This could lead, as shown in Figure 3.30(c)-(d), to the shorting of one of the four heaters to an adjacent control line.

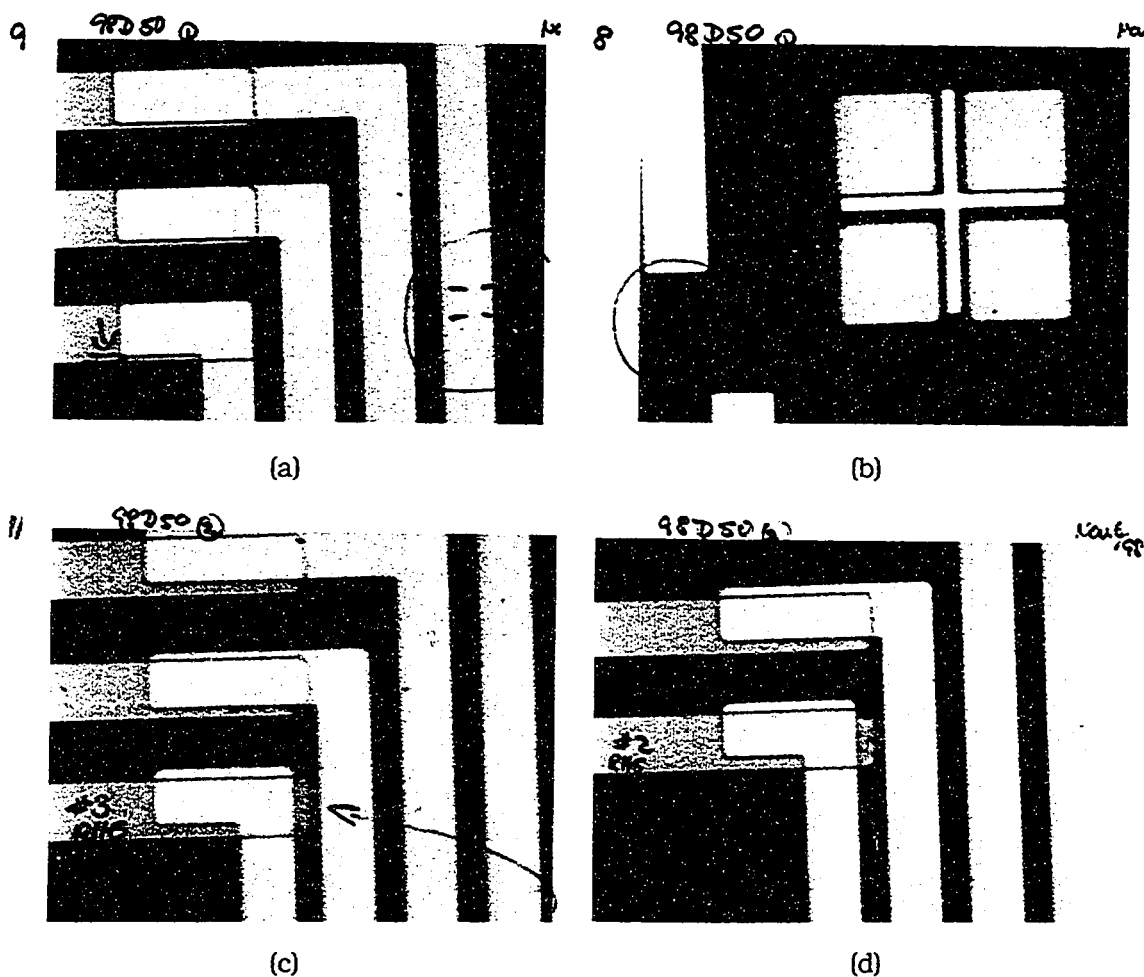


Figure 3.31. Photographs of the processed metal layers taken through an optical microscope. The vertical gold traces in (a), (c) and (d) are nominally $8\ \mu\text{m}$ wide. Photos (a) and (b) clearly illustrate the two layers misaligned by approximately $1\text{-}2\ \mu\text{m}$. Photos (c) and (d) illustrate adjacent heater control lines may become shorted out due to misalignment.

3.6.2. Polymer Waveguide Fabrication

The waveguide sections were designed to be $10\ \mu\text{m}$ wide and the MMI couplers were $75\ \mu\text{m}$ wide. The required tolerances of the waveguides were not very strict, but as discussed in Section 3.5.2, the MMI couplers are very sensitive to width variations. Therefore, a photolithography process was used in an attempt to meet the required tolerances.

Although photolithography offers excellent dimensional control, there was one unique problem that arose in the fabrication process. The polymers used in the MTOPS

are liquids and must be processed in the liquid state since exposure to UV light causes them to solidify. This posed a problem for photolithography since the photo-mask usually makes physical contact with the photoresist, or in this scenario the polymer. Contact between the mask and the liquid polymer would not be practical because exposure to UV light would cement the mask to the substrate.

The solution to this problem was the placement of thin metal shims on the polymer-coated substrate to prevent the mask from making physical contact with the polymer. It was determined empirically that five 0.003" thick tantalum foil shims prevented the mask from adhering to the substrate. The position of the five shims on the substrate is shown in Figure 3.32. The shims were manually placed on each wafer using tweezers.

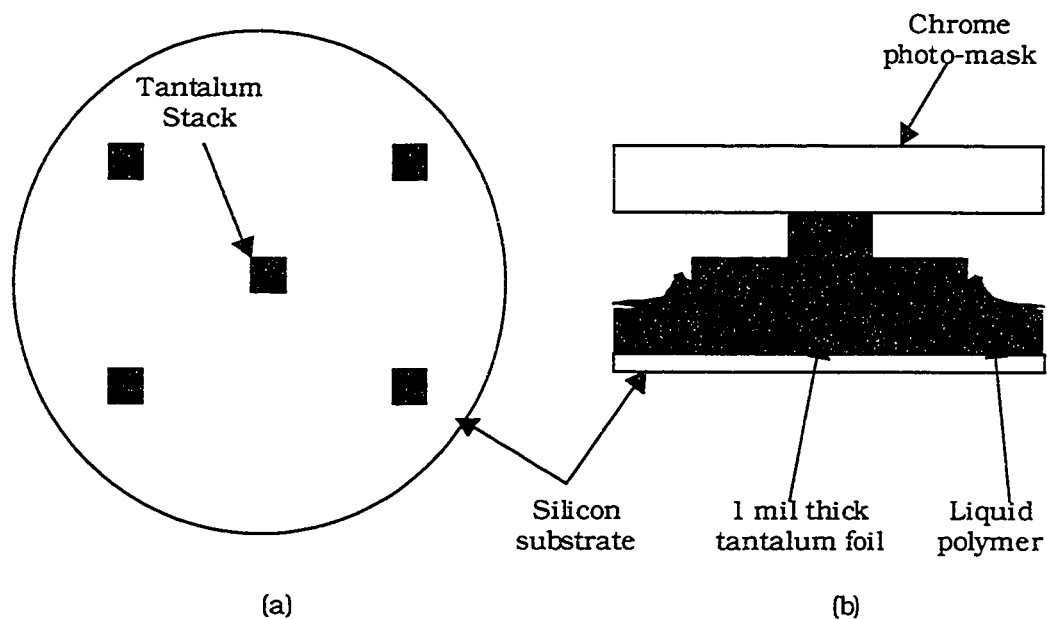


Figure 3.32. The locations of the five shims are shown in (a). Cross-sectional view of three 1 mil tantalum foil pieces stacked vertically (b). Note the width and length of the shims were different for each layer. Since the lower shim would displace the liquid polymer, the polymer would tend to coat the sides and even the top surface of the middle shim. To prevent the liquid polymer from adhering to the mask the top-most shim was made as narrow as possible. The middle shim was typically 3-5 mm square and the top and bottom shims were approximately 1 mm square.

Once the problem of keeping the mask from adhering to the substrate was solved, an attempt was made to optimize the UV exposure time. Initial estimates for the exposure time were 20 minutes for the core and cladding as indicated by the manufacturer of the polymer. Practically, optimal exposure time was determined to be

2 hours for the cladding layer and 10 minutes for the core layer. Using these exposure times resulted in durable polymer layers that withstood the rinsing process.

Figure 3.33 illustrates the progress that was made during the process development. Initial attempts produced poorly defined features, but by reducing the shim thickness and refining the process, feature definition improved. Shown in Figure 3.34 are electron microscope photographs illustrating the waveguide roughness and cross-section. The waveguide sidewall roughness is believed to be partly related to both the process and inherent properties of the polymer. Shown in Figure 3.35 is a fully processed silicon wafer. The white lines are optical waveguides.

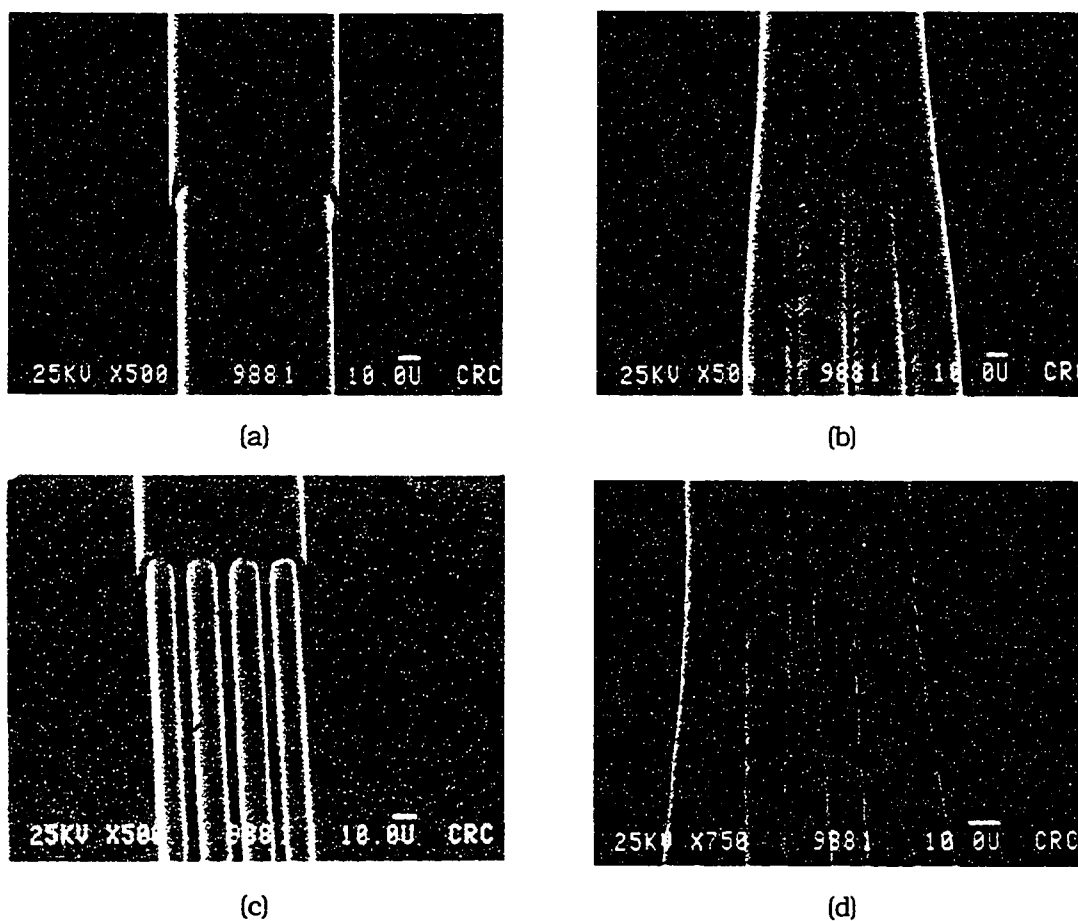


Figure 3.33. Electron microscope photographs illustrating the results from the first attempt at processing the polymer (a)-(b) and using a more refined process (c)-(d). The initial process used 4 mil thick shims and because of diffraction, produced poorly defined features (a)-(b). Further process refinements and 3 mil thick shims, resulted in better delineated features.

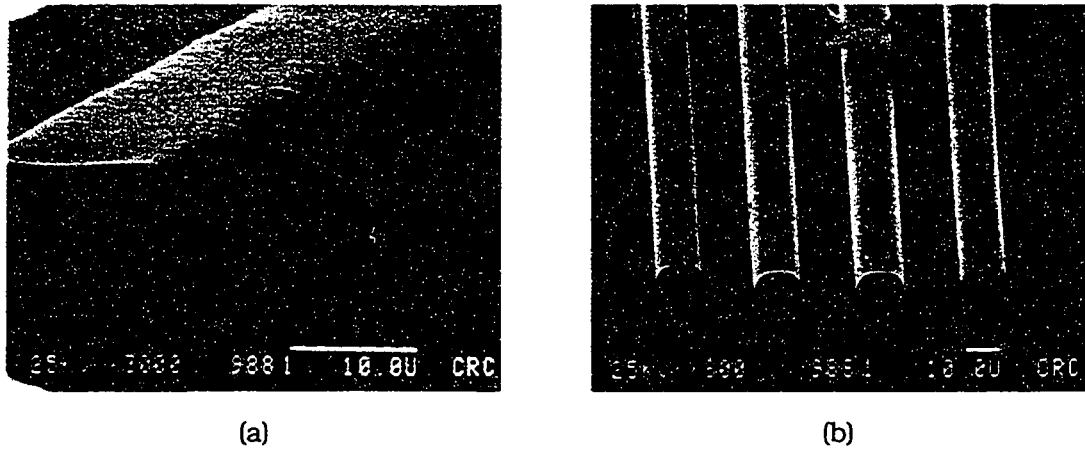


Figure 3.34. Electron microscope photographs showing waveguide sidewall roughness (a) and waveguide cross-section (b).



Figure 3.35. Photograph of a processed silicon wafer. The white lines are optical waveguides.

A second method of patterning polymer was also investigated. The method used a patterned transparent substrate to pattern the polymer without using a mask and is schematically shown in Figure 3.36. Specifically, a glass substrate was patterned with a $1\ \mu\text{m}$ thick gold layer using photolithography. Polymer was then spun on top of the

metal. The glass substrate was exposed to UV light from the side that was not metalized. The metal layer acted as a mask that was in direct contact with the polymer, thereby eliminating the need to use shims. However, since the substrate had to be patterned with metal, heaters and interconnect metal could not be incorporated. Hence, the use of this method was limited to fabricating passive polymer devices.

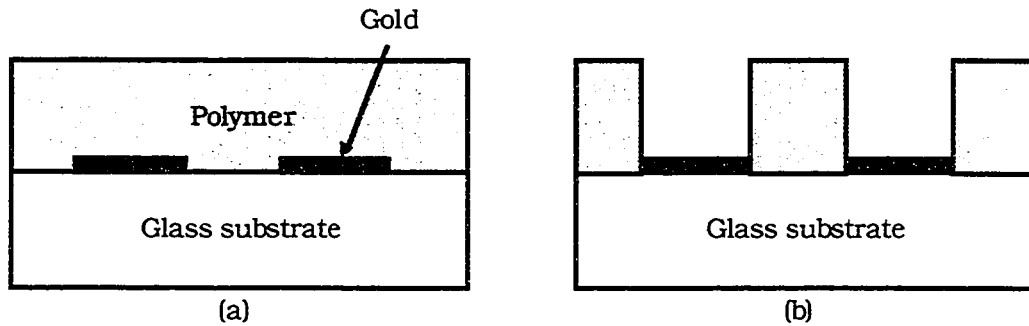


Figure 3.36. Liquid polymer was spun on top of a patterned glass substrate (a). A patterned polymer layer results after exposure to UV light and removal of the unexposed polymer (b).

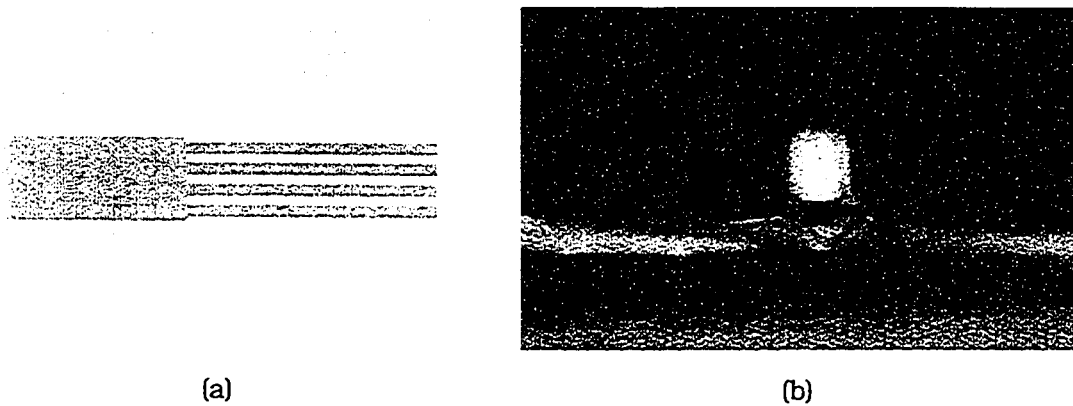


Figure 3.37. Photograph of a gold patterned glass substrate (a). Resulting polymer waveguides (b) after exposure to UV light and rinsed with acetone.

3.7 Experimental Results

A total of three samples were successfully fabricated on metalized silicon substrates. Sample number 12-11-98 had both the Polymer 1 and Polymer 2 layers patterned, while samples 8-11-98 and 9-11-98 only had the Polymer 2 layer patterned (waveguide core layer). Experiments were conducted to determine the propagation loss of a $10\ \mu\text{m}$ wide by $10\ \mu\text{m}$ high waveguide, the on-off contrast ratio and the switching time.

3.7.1. Passive Optical Performance

The attenuation of light travelling along a straight waveguide was determined using the cut-back method. The cut-back method consists of taking a series of optical power measurements for different waveguide lengths and fitting a linear curve to the data. The slope of the line yields the propagation loss. The procedure is as follows:

1. Couple light into the input side of the waveguide.
2. Monitor the output power and maximize the total throughput power.
3. Record the output power and waveguide length.
4. Cleave the output waveguide and measure the maximum output power for the shortened waveguide.
5. Repeat steps three and four.
6. Plot the output power vs. waveguide length.
7. The slope of a linear curve fit gives the loss in dB/cm.

One assumption is that the output coupling efficiency is constant for each cleave, i.e. the waveguide end facets are similarly smooth/rough for each cleave. It is further assumed that the same optical power can be coupled to the waveguide for each measurement. By optimizing the total throughput power, the input coupled power may be almost equal for all measurements. Hence, the final calculation indicates the propagation loss.

The measurement setup to determine the propagation loss is shown in Figure 3.38. The positions of the input and output microscope objectives were optimized using three-axis XYZ micropositioners to maximize throughput optical power.

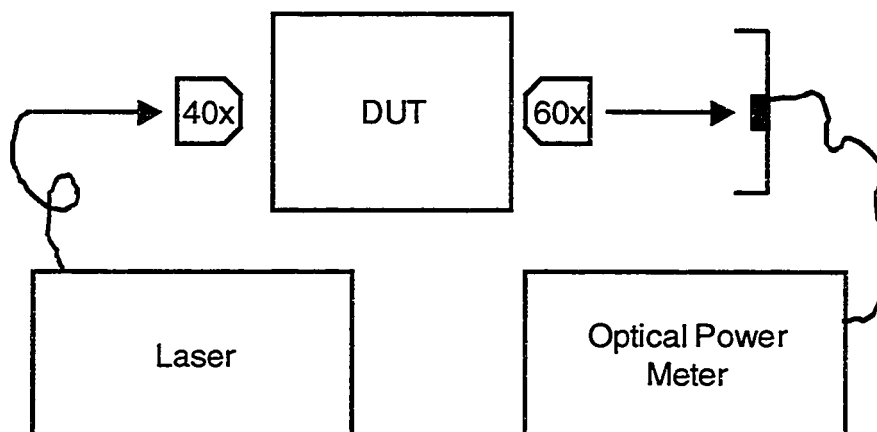


Figure 3.38. Light from an optical fibre on the left, is focussed by a 40x microscope objective onto the waveguide under test (or device under test, DUT). The light from the output of the waveguide is collected, collimated by a 60x objective, and focussed onto a long wavelength (germanium) photodetector approximately 50 cm from the sample. A calibrated optical power meter displays the optical power incident on the photodetector.

Shown in Figure 3.39 are the loss measurements for four different straight waveguides from sample 8-11-98. The average propagation loss was approximately 1.6 dB/cm at a wavelength of 1550 nm. The measured optical power from the first 40x objective was 0.5 mW. Subtracting the propagation loss from the input power indicated that the coupling loss was approximately 13 dB. The 40x objective was replaced with a 20x objective having a numerical aperture that better matches the waveguides. The coupling loss was reduced to approximately 8 dB.

Knowledge of the coupling and propagation loss allowed the excess loss of the switches to be estimated. Using the same measurement setup, the total output power from a switch was measured to be 11.1 μ W, when the input optical power was 670 μ W. The excess loss was estimated to be 6 dB, after coupling and propagation losses were subtracted, compared to 0.5 dB obtained from the BPM simulations

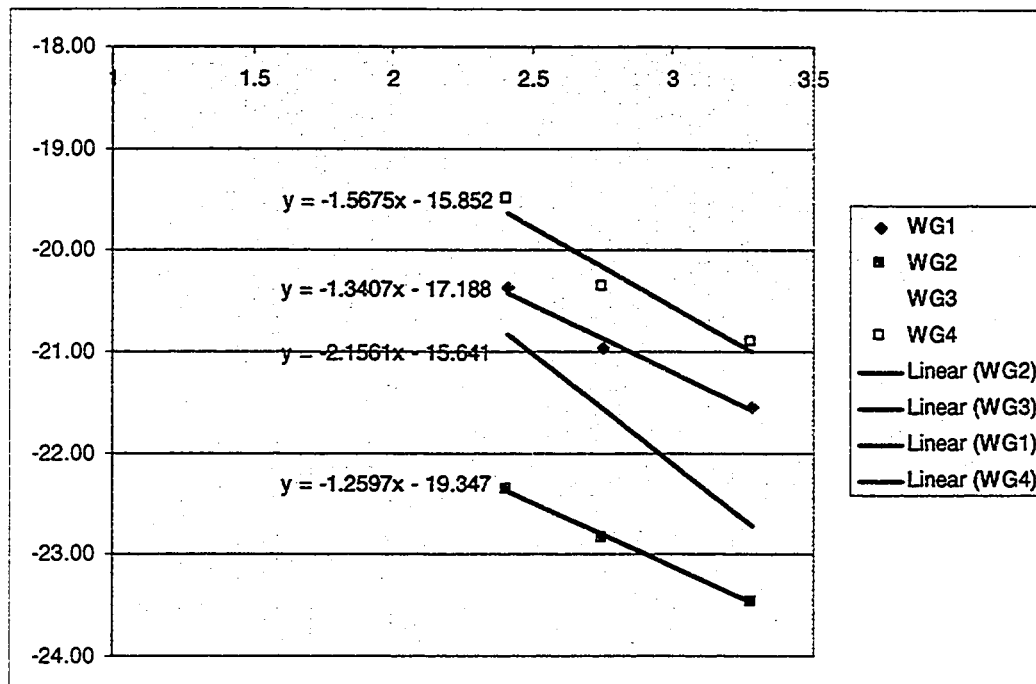


Figure 3.39. Cut-back measurements to determine propagation loss. The trend-lines are linear curve fits to the data. The slope of the line equals the propagation loss in dB/cm. The average propagation loss is approximately 1.6 dB/cm.

3.7.2. Switching Action

After the passive measurements were completed, power was applied to the heaters beneath the phase-shifters. The temperature and thus refractive index of the MZI arm waveguides were altered by varying the current applied to each of the four heaters. With the appropriate currents applied to the four heaters, the light could be made to partially switch from one output to another. Shown in Figure 3.40 are photographs of the test setup used to measure loss and the switching action. A long wavelength camera replaced the photodetector in Figure 3.38 and imaged the output waveguide(s) of a switch (see Figure 3.42). The largest measured on-off contrast was 5.3 dB, significantly better than the 2.2 dB reported by [59] for a silicon based 1x2 multimode MZI.

To confirm light was being switched rather than selectively attenuated, the power for all four outputs was measured for different electrical currents. The results are summarized in Figure 3.41. The graph clearly indicates that the switch was directing light from the input to different outputs.

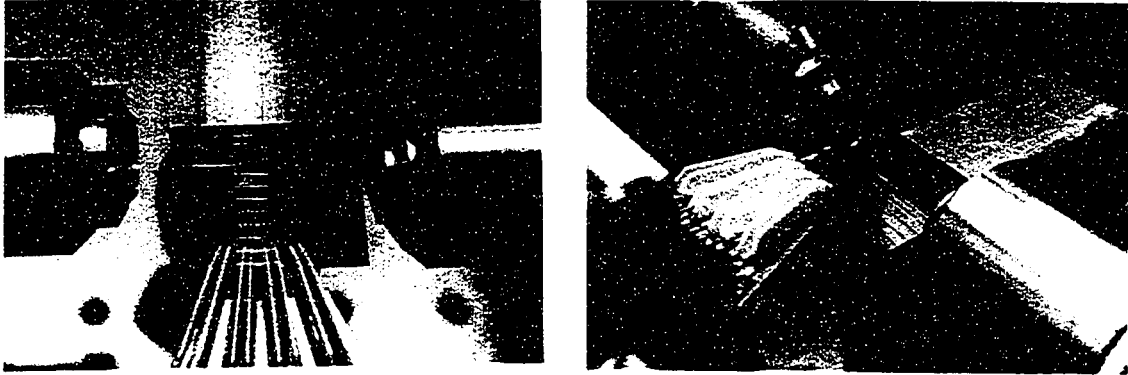


Figure 3.40. Photographs of the test setup used to couple light to and from the switches. A multiple lead probe is used to supply current to the heaters. Light is focused by the left microscope objective into an input waveguide. Light from the output waveguide(s) is collected by a high numerical aperture (NA) microscope objective on the right. This objective also is used to image the output light onto a camera or photodetector.

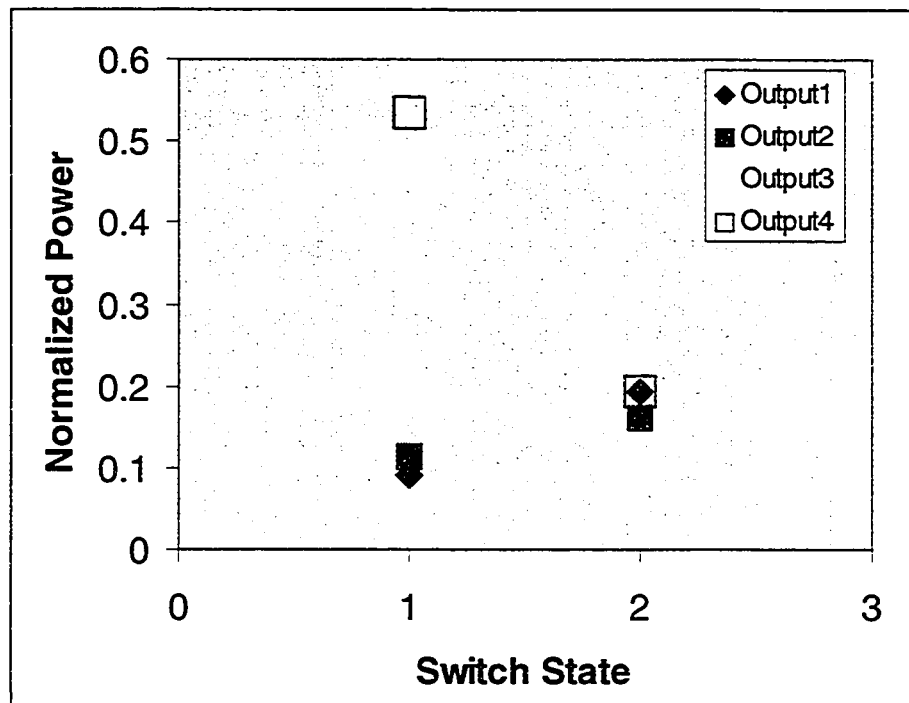


Figure 3.41. The optical power from each output was normalized to the total optical power from all outputs for each of three switch states. State 1 is for the following heater currents, $I_1=27$ mA, $I_2=0$, $I_3=14.1$ mA and $I_4=0$. Switch state 2 is for the following currents, $I_1=25$ mA, $I_2=24$, $I_3=12.6$ mA and $I_4=0$. Notice the power is switched from Output 4 to Output 3, indicating that switching has occurred. The accuracy of the data is approximately $\pm 5\%$.

Also, light from output three was imaged onto the long wavelength camera as shown in Figure 3.42, while the phase-shifters were adjusted to give minimum and maximum intensity. The modes of the waveguide are clearly visible. The low order modes are interfering properly; however, the extinction ratio of the higher order modes are not as good. This is a result of the mode-dependent propagation constant that was discussed previously.

More spatial optical modes will be supported by a waveguide as the wavelength of light is reduced. Instead of operating at 1550 nm, a laser source operating at 670 nm was used. Shown in Figure 3.43 are images of the same output waveguide when stimulated by 670 nm and 1550 nm light. As expected, the number of modes increased for the shorter wavelength.

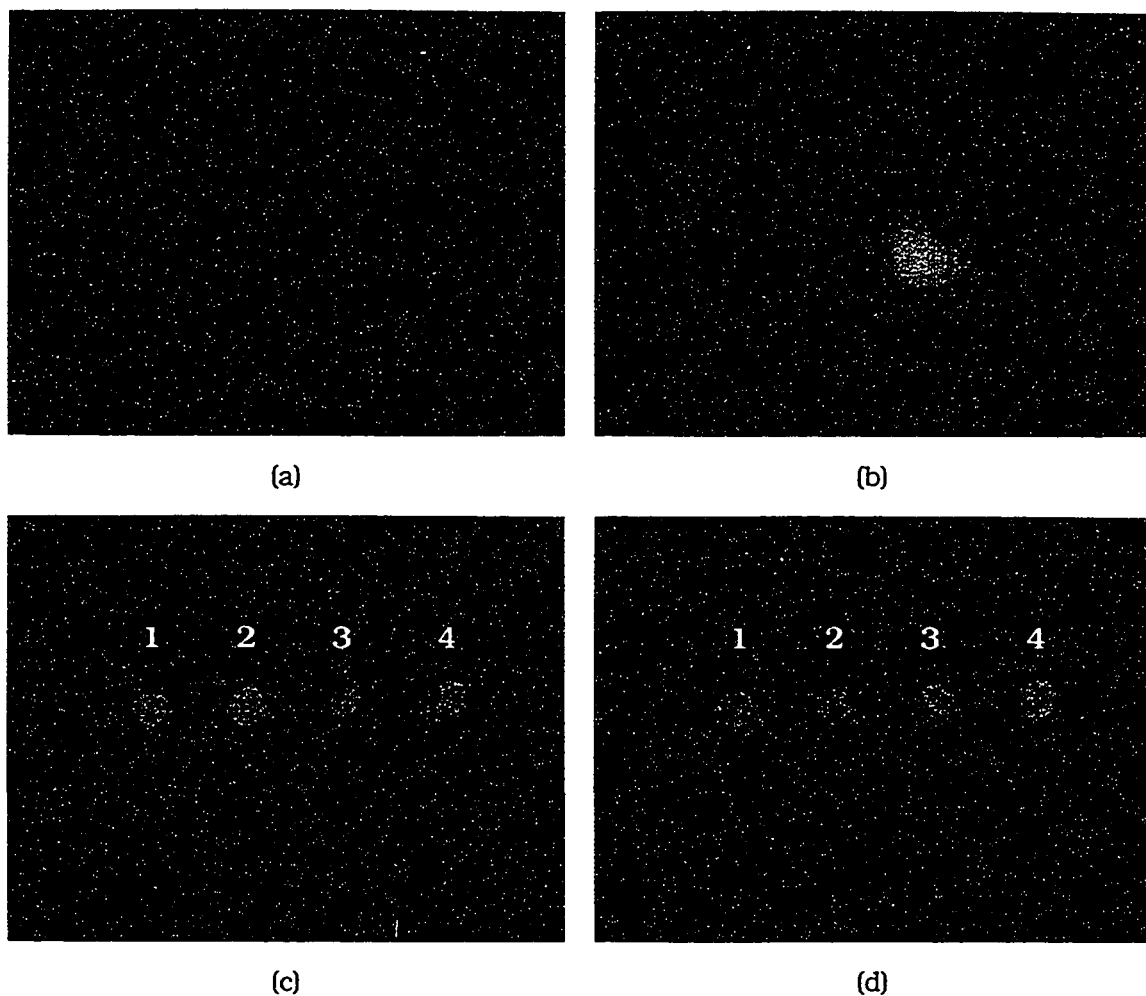


Figure 3.42. Pictures of the output waveguides imaged using a long-wavelength camera. The off- and on-state of a single channel are shown in (a) and (b), respectively. The intensity in (a) and (b) was reduced to prevent the camera from saturating. Images of all four output waveguides when channel three is in (c) the off-state and (d) in the on-state.

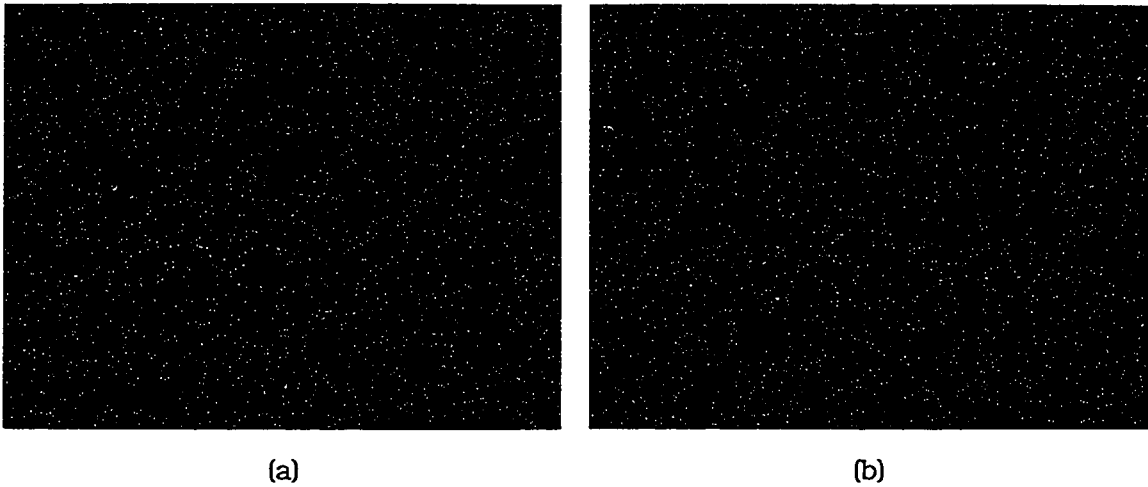


Figure 3.43. Comparison of the mode structure for (a) 670 nm and (b) 1550 nm light. Predictably, more modes are supported at the shorter wavelength.

3.7.3. Transient Response

The switching time was determined by applying a periodic square wave signal to heaters two and three. Shown in Figure 3.44 are photographs of the oscilloscope screen illustrating the input and measured signals. The power from output three was focused onto a photodetector that was directly connected to the oscilloscope. The bandwidth of the photodetectors was greater than 20 kHz; hence its affect on signal distortion was insignificant. The lowest measured rise- and fall-times were 1 ms and 2 ms, respectively.

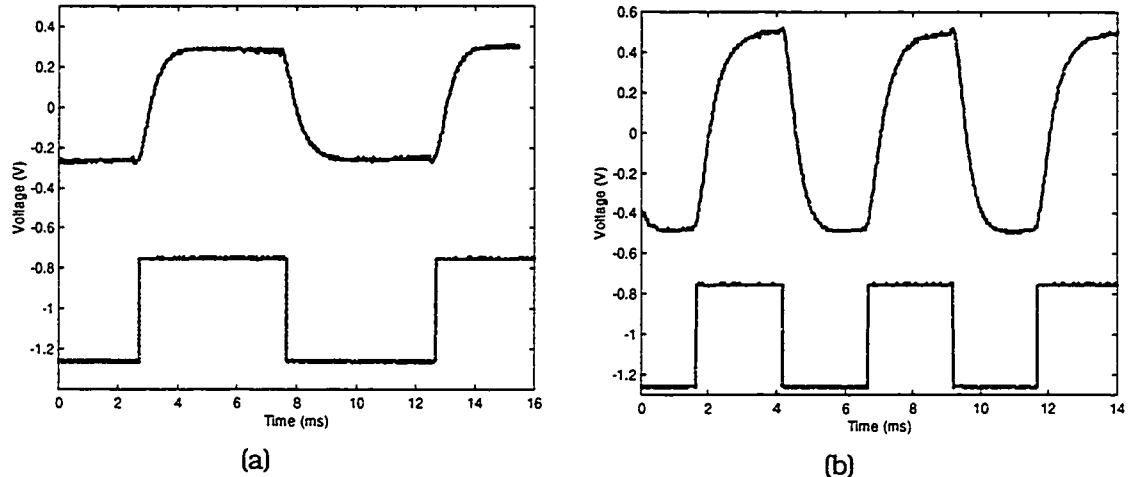


Figure 3.44. Switching time measurements of a MTOPS. (a) A 10 V_{pp} 100 Hz square wave signal applied to arms two and three resulted in a rise time of 1.3 ms and a fall time of 1.4 ms. (b) A 10 V_{pp} 200 Hz square wave signal applied to arms one and four resulted in a rise time of 1.3 ms and fall time of 1.3 ms. Note, a 0.5 V_{pp} square is shown for reference instead of the 10 V_{pp} drive signal.

3.7.4. Comparison of Simulated and Experimental Results

The modeled optical performance did not agree well with measured results for two main reasons. First, the BPM simulations used the optimal coupler length and width. However, due to fabrication tolerances, the width varied by as much as 2 μm . The excess loss increased as described in Section 3.5.2.2. The contrast ratio degraded due to poor imaging of the MMI couplers because the input optical field was not properly reproduced at the MMI coupler outputs. Second, the modal power distribution varied across the four phase-shifting waveguides thereby preventing complete constructive and destructive interference. Shown in Figure 3.45 are 3D BPM simulations of MMI couplers that are 1 μm and 2 μm wider than the optimal width of 75 μm . These BPM simulations indicate that the MMI couplers are severely affecting the performance of the device. An improved fabrication process may produce devices more closely matching the optimum device configuration.

The thermal model accurately predicted the switching time or transient response of the switch. The thermal analysis indicated that a rise and fall time of approximately 2-3 ms should be obtainable. The best experimentally measured rise and fall times were approximately 1 ms and 2 ms, respectively. The discrepancy is likely due to inaccuracies of some of the thermal physical properties used in the model.

When the free parameters were eliminated, both the optical and thermal models better agreed with experimental results. Some model limitations remain. For instance,

it would be difficult to incorporate waveguide sidewall roughness into the BPM models. Certainly the effect of waveguide sidewall roughness on signal attenuation can be estimated, but it is much more difficult to consider how sidewall roughness effects the phase or propagation constant of a propagating mode. Finally, the thermal model is two-dimensional; therefore the effect of longitudinal heat transfer was neglected. The metal layer conducts heat away faster than the polymer; therefore, the experimental results were better than the simulated results.

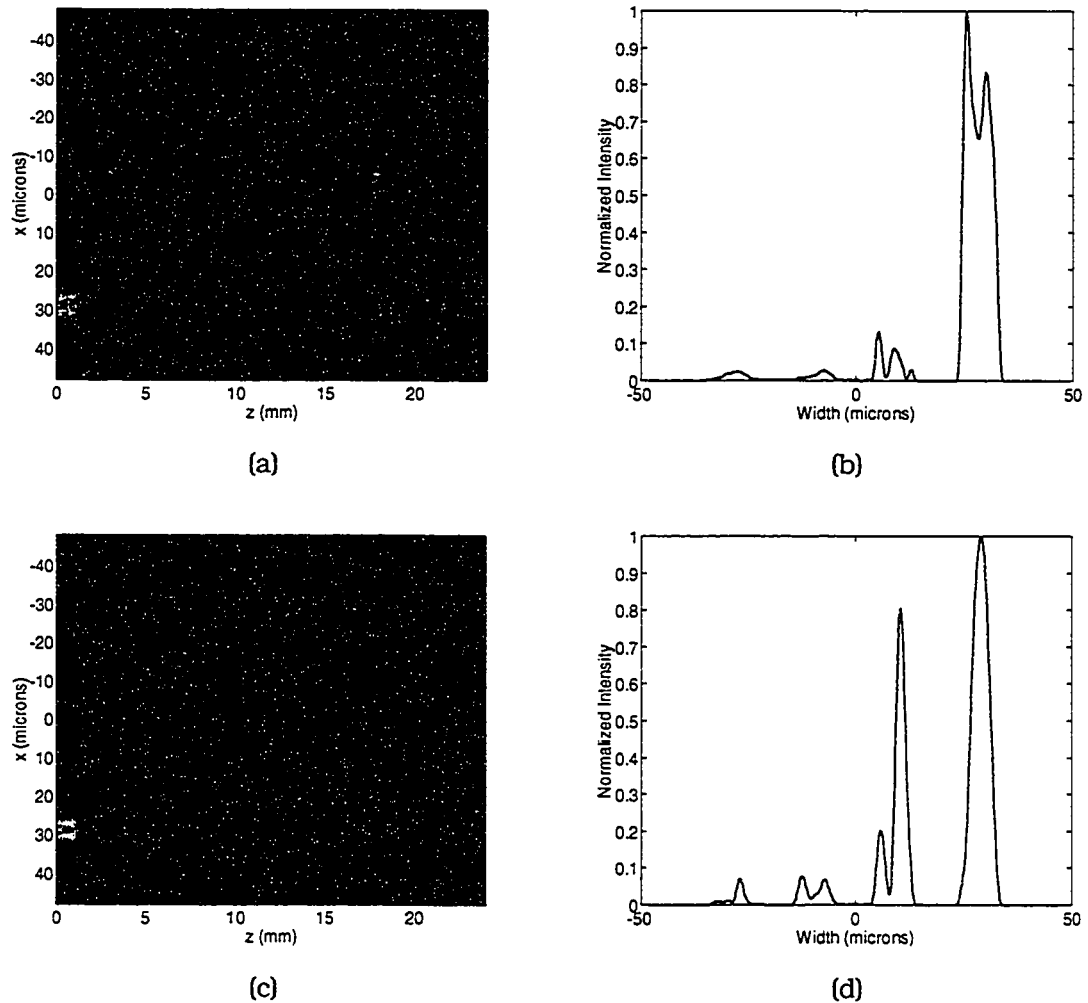


Figure 3.45. 3D BPM simulations of the MTOPSs that have non-optimal coupler length and width. In (a) the width was increased to $76 \mu\text{m}$. The worst contrast ratio and excess loss were 11.0 dB and 4.4 dB, respectively. In (c) the width was increased to $77 \mu\text{m}$, and the worst contrast ratio and excess loss were 1.7 dB and 5.5 dB, respectively. Plots (b) and (d) illustrate intensity at the output of the device as a function of x at the output of the switch.

3.8 Summary

Presently, the main obstacle is the fabrication process for polymer waveguides. Although a photolithography process was developed for the liquid UV-curable polymers, other techniques may be used. For instance, a mask projection technique may be used to form an image of the mask on the surface of the substrate. Another process uses an UV laser to selectively cure the polymer. However, it is difficult to produce large rectangular waveguides with square corners when the laser beam is circular. Hence, this effect would have to be investigated to determine its impact on the switch performance.

Finally, the insertion loss of the device may be substantially reduced if the Norland polymers were replaced with advanced low loss polymers. Many of these polymers have achieved commercial acceptance. Furthermore, though the advanced polymers have a lower propagation loss, they retain the key features of all polymers, such as a high thermo-optic coefficient, ease of fabrication, varying refractive indices and low cost. These polymers may allow future polymer based switches to be more practical and flexible.

Experiments on the multimode thermal-optic polymer switch have verified the feasibility of the original design. Even though some performance parameters were not achieved, key characteristics such as switching light from one output to another and millisecond response time were demonstrated in this first prototype. Subsequent efforts may be able to obtain improved performance.

4. Hybrid Integrated Optoelectronic Matrix Switch

4.1 Introduction

Switching information is a vital function in modern communication networks due to the inherent need to route data dynamically from one user to another. Located at network nodes, switches in conjunction with sophisticated routing algorithms are able to direct multiple incoming signals to outputs, thereby providing continuous and reconfigurable communication channels.

At present the majority of switching activity in modern communication networks is accomplished with electronic switches. Information routed from input to output remains an electrical signal throughout the switch. Electronic switches have certain innate advantages due to their construction via standard microfabrication facilities. For example, an electronic switch core may include an integrated clock recovery unit, pulse shaping, re-timing circuitry, and signal amplifiers, all of which can be integrated onto a single gallium arsenide or silicon die. However, two significant disadvantages of electronic switches are their inability to both handle high data rates and maintain low channel cross-talk.

The electrical data rate of present state-of-the-art commercial systems is approximately 10 Gb/s. At these rates, only the most advanced semiconductor materials are practical. Fundamental properties of the semiconductor material, such as the electron and hole mobility, limit the speed at which signals can be switched. Furthermore, as the data rate increases the problems of channel cross-talk and interference becomes greater, thus a new technology will likely be required to accommodate these ultra-fast signal rates.

As mentioned in Chapter 3, optical switches are practical in fibre networks, but their use also comes with some disadvantages. The very properties that make lightwave particles or photons ideal for transmission also make them poor candidates for logic operations. This is because photons, which are bosons (integer spin particles), do not like to interact with one-another, unlike electrons which are fermions (spin one-half particle), and which are greatly affected by one-another. This is the main reason why optical computers are only research devices of limited capability. Similarly, it is difficult to perform complex logic operations, such as clock recovery, signal re-timing, and pulse shaping, on optical signals in fibre networks.

An optoelectronic switch (OES) is a hybrid device that exploits the merits of both optical and electrical switches. Optical distribution is used to provide high inter-channel isolation, while electrical control is used to perform channel selection. The

architecture of the optoelectronic switch investigated at TRLabs makes use of an optical 'broadcast' and electronic 'select' to form a high quality switch matrix, as shown in Figure 4.1 and Figure 4.2.

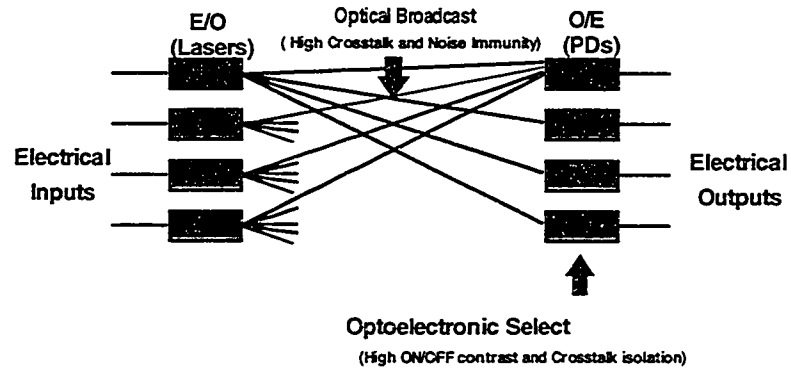


Figure 4.1. Architecture of an optoelectronic switch matrix. The output from each laser on the left is split into N optical signals and broadcast to each photodetector array on the right. At the photodetector (PD) array, one of N optical signals is selected by biasing 'on' one of N photodetectors in the array.

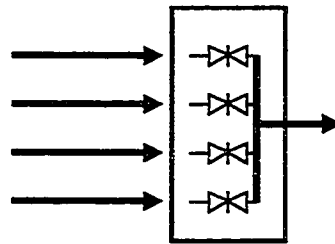


Figure 4.2. A detailed view of an O/E photodetector element. Light from four optical fibres or waveguides (left) illuminates each photodetector. Selection is achieved by biasing on one of the four photodetectors. The photocurrent is then delivered to a common output (right).

4.2 Applications

The design of the OES results in a high performance analogue switch matrix that can be used in applications containing purely digital, analogue, or a combination of digital and analogue signals. Furthermore, the switch is both bit rate and signal-format insensitive. Therefore, one channel may carry analogue video, another channel may carry a SONET OC-3 data stream and a third channel may carry a multilevel signal, such as a 4-level amplitude shift-keyed or quadrature-modulated signal. In this section three applications of optoelectronic switching are discussed.

4.2.1. Wavelength Cross-connect and Reassignment in Optical Networks

There is a general consensus that wavelengths in a wavelength division multiplex (WDM) network need to be reused, otherwise wavelength blocking will result at the physical layer [65]-[72]. Wavelength blocking occurs when two or more signals having the same wavelength are transmitted in the same direction on a single optical fibre. By incorporating wavelength converters, wavelengths in an optical network may be reused and/or reassigned. Figure 4.3 illustrates an example of how wavelength reassignment can be used to avoid wavelength blocking in an optical network that employs wavelength cross-connect (WXC) switches.

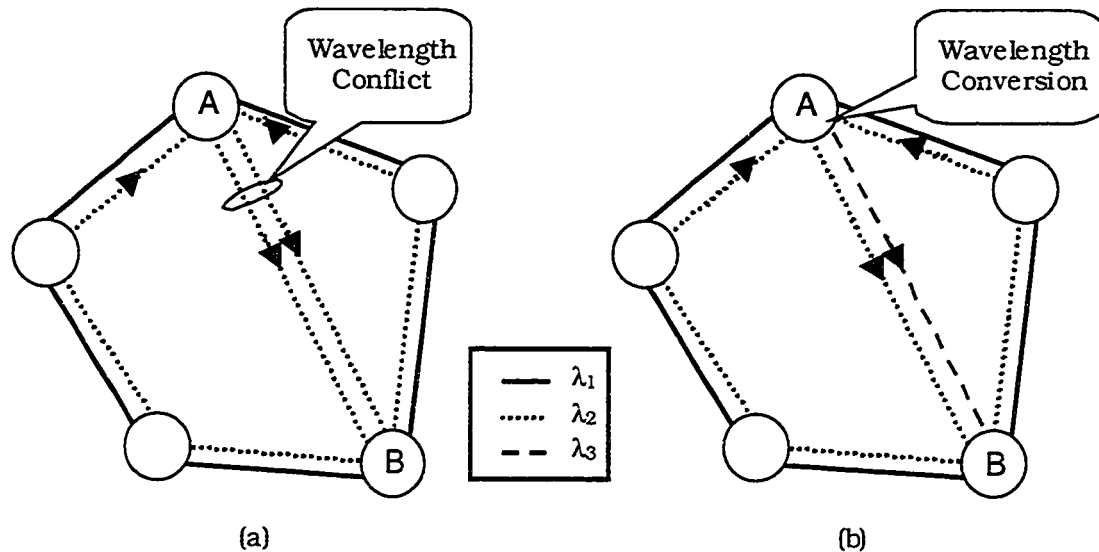


Figure 4.3. Comparison of an optical network which does not contain wavelength conversion (a) and one that can reassign wavelengths (b). All spans contain a single fibre. In (a) two rings require the same wavelength in span A-B and therefore conflict with one another, whereas in (b) wavelength reassignment circumvents wavelength blocking.

The operation required at a node in Figure 4.3 is both a switching and a wavelength conversion operation. These functions may be accomplished entirely in the optical domain or in the electrical domain. For the operation to be done entirely in the optical domain, an optical switch and an optical wavelength converter are required. There has been rapid progress in the development and commercialization of optical switches [66]; however wavelength converters are still very much in the research stage [67],[68],[69].

One method of wavelength conversion is to detect the optical signal and then retransmit it at a different wavelength. Furthermore, the conversion process may incorporate an electronic or optoelectronic switch [70],[71] and thereby perform both wavelength conversion and switching.

Owing to their superior performance and data rate and format independence, optoelectronic switches are very good candidates for the switch core of a WXC. Figure 4.4 compares an all-optical and an optoelectronic WXC switch. An OES requires extra optical-to-electrical and electrical-to-optical conversions compared to an optical WXC. The basic trade-off between the two approaches has led to the debate of all-optical or signal transparent networks, versus opaque networks, where optical-to-electrical conversions take place [72]. There are indeed advantages and disadvantages to both approaches, but the performance of all-optical networks is less favourable than a comparable opaque network primarily because of optical amplifier noise accumulation (amplified spontaneous emission), poor quality optical wavelength conversion, fibre non-linearity and accumulation of dispersion (chromatic and polarization mode dispersion).

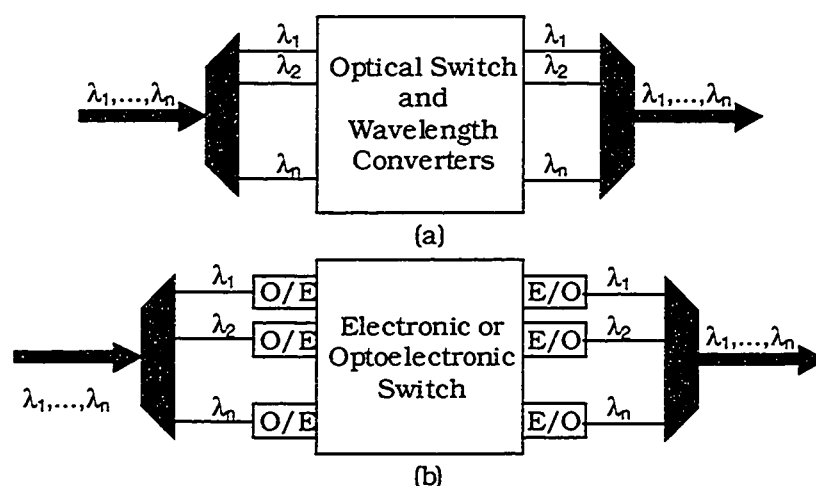


Figure 4.4. A wavelength cross-connect node in an optical network can be designed using only optical components or a mixture of optical and electronic devices. The all-optical approach shown in (a) requires a WDM demultiplexer/multiplexer, an optical switch and a number of wavelength converters. The second approach (b) uses an optical demultiplexer/multiplexer but replaces the optical switch with an OES and wavelength converters with optical-to-electrical electrical-to-optical transducers.

Although a WXC switch that incorporates an OES is generally more complex than a switch with an all-optical design, the opaque design offers a number of advantages. First, the OES can accommodate any data rate and signal format permitted by the channel bandwidth. Thus, even though the network is opaque to optical signals, i.e. there are O/E and E/O conversions, signal transparency is maintained [73]. Second, when the optical signals are converted to electrical signals, re-timing, pulse re-shaping, and re-amplification (3R regeneration), can be easily performed on the bit stream. The result is an improvement in the signal-to-noise ratio, and limits the effects of noise, dispersion and other system impairments. Last, the

technology and components used in the hybrid integrated OES are mature and may be developed into a commercial product quickly and inexpensively.

4.2.2. Broadband Analogue Switch for CATV Networks

Many cable television networks now distribute both analogue NTSC signals and Internet data on the same physical medium. Shown in Figure 4.5 is an example of a CATV network that uses a hybrid fibre-coax architecture. As can be seen, any device inserted into such a network must be capable of transmitting and receiving both analogue and digital signals. Furthermore, this architecture lends itself to the use of an optoelectronic switch with the use of both optical and electrical signals in the network. Therefore, the optical-to-electrical conversion provided by the OES may be beneficial since it is an inherent requirement of such a system.

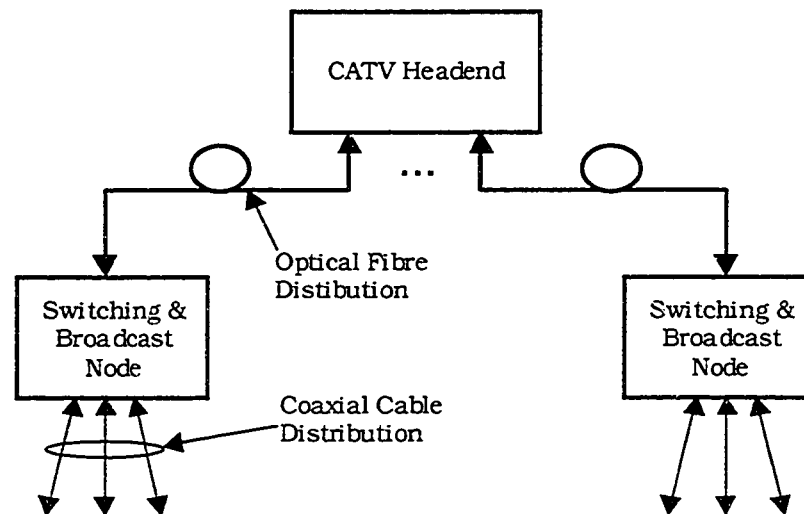


Figure 4.5. In modern CATV networks, analogue and digital information signals are bi-directionally routed on a combination of optical fibre and coaxial cable.

The superior analogue switching characteristics of the OES are an additional advantage since a video signal is very sensitive to channel distortion. Most electronic switches that have a channel bandwidth of 1 GHz are designed for digital signals to satisfy reduced cross-talk and distortion requirements. As a result, the architecture of CATV networks are ideal candidates for using optoelectronic switches with their superior bandwidth, isolation, cross-talk and low-distortion properties.

4.2.3. High Speed Broadband Signal Processor

In contrast to the previous two examples, which illustrated switching applications, this example describes how an OES can be configured to perform signal processing.

There are three basic operations that an optoelectronic signal processor can perform: summation, delay and multiplication. These three operations, which are schematically illustrated in Figure 4.6, are implemented using fibres/waveguides and photodetector arrays. The discrete-time impulse response of a system, given by (4.1), can be realized by combining these three operations. Equation (4.1) can be implemented using a finite impulse response (FIR) filter architecture or more generally a transversal filter (Figure 4.7). For example, the impulse response of a moving average or low-pass filter would have $V_n=0.25$ for $n=1..4$. A number of experiments have previously been conducted with the 10x10 OES to verify its ability to perform signal processing functions [60],[63]. Furthermore, a broadband neural network has also been experimentally demonstrated using similar operations [63].

$$h(t) = \sum_{n=-\infty}^{\infty} V_n \delta(t - nT) \quad (4.1)$$

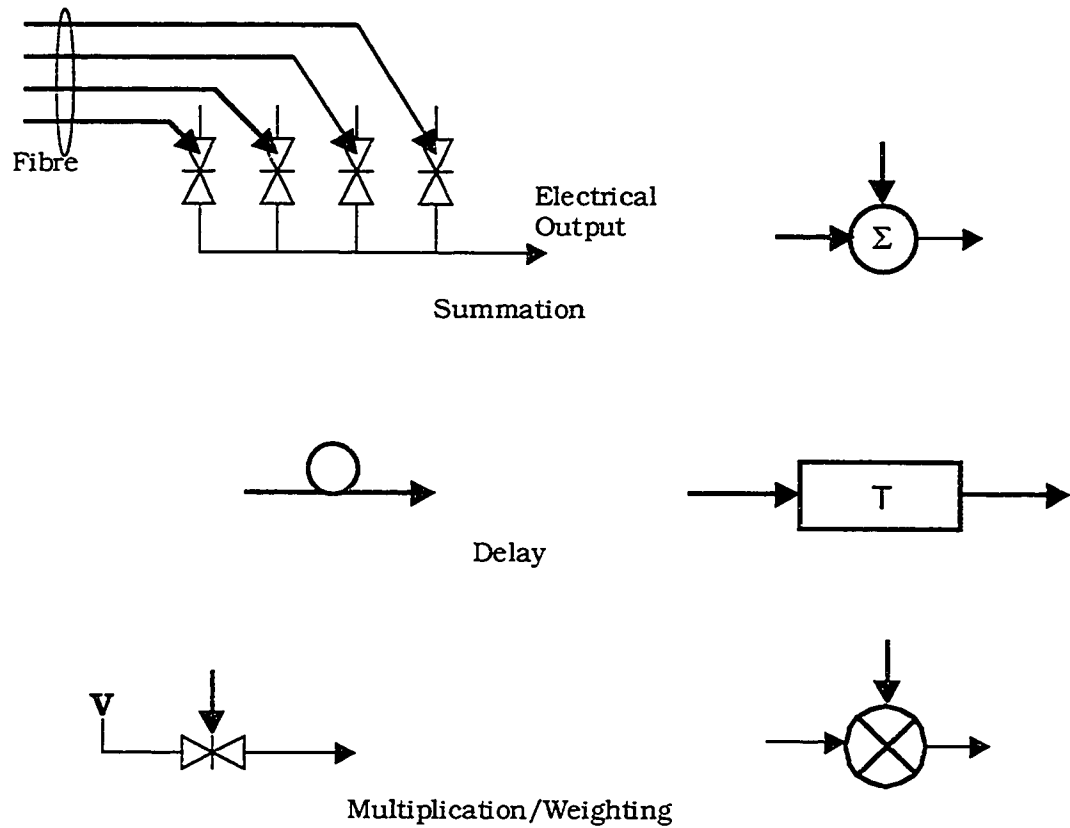


Figure 4.6. The three basic operations that can be performed by an optoelectronic switch are: summation, delay, and multiplication. The summation operation illustrates how a 1x4 MSM photodetector array is used to add four optical signals and convert the result to an equivalent electrical signal. Note that the multiplication and summation operations may be combined into a single parallel operation. The red (thick) and black (thin) lines correspond to optical and electrical signals, respectively. Delay is achieved by inserting a specific length of fibre having a known propagation delay time between each detector in an array and the splitter.

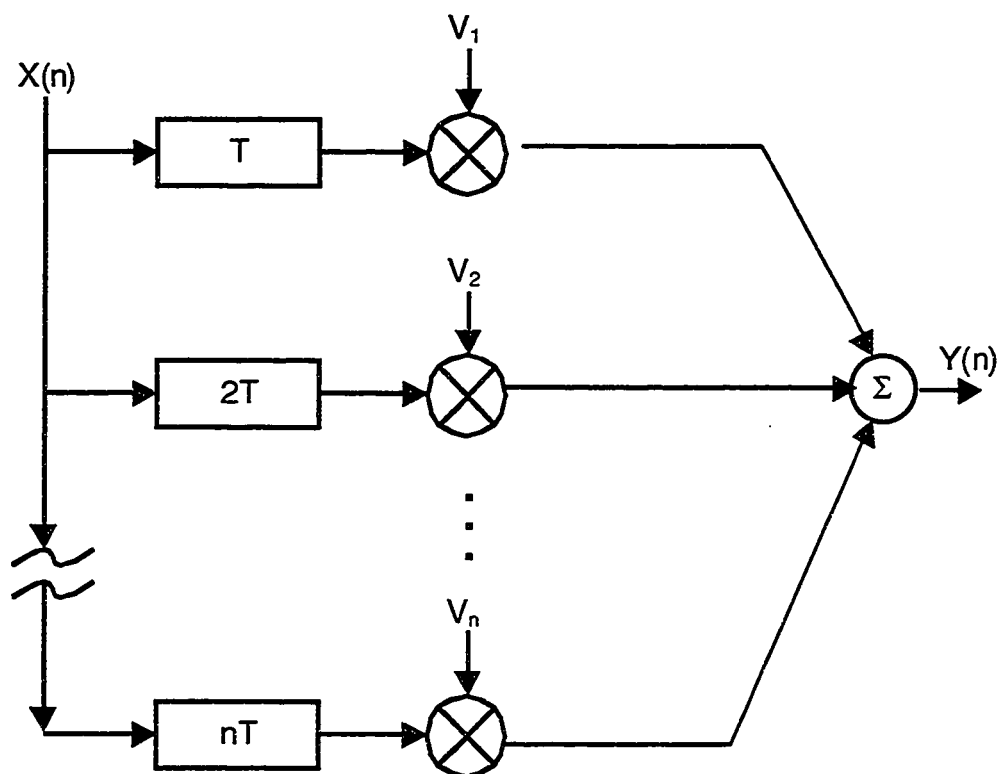


Figure 4.7. Transversal filter implemented using operations that can be performed by an optoelectronic switch. The weights, V_n , are produced by altering the bias voltage of individual MSM detector. To be most practical, the frequency response of the detectors should be independent of responsivity, i.e. the bias voltage should not significantly reduce the bandwidth of the MSM.

4.3 Implementation

The first OES prototype, shown in Figure 4.8, was a 10x10 matrix switch constructed using discretely packaged components and optical fibre splitters for the signal distribution [60]. The performance specifications are summarized in Table 4.1. While the 10x10 switch has excellent performance specifications, its size, cost, lack of integration and reliance on manual assembly limits its commercial potential. As a result, a 4x4 switch project, using hybrid integration, was initiated. The initial specifications required the 4x4 switch to meet or exceed those of the 10x10 switch. This goal was achieved by the first hybrid integrated OES prototype [61]. Subsequently, an enhanced requirement of accommodating 10 Gb/s signals was added, a design goal that was fulfilled by the second hybrid integrated OES prototype [62].

These design goals were achieved in two stages. First, a prototype hybrid switch with a bandwidth of approximately 2 GHz was demonstrated. This device was not packaged, nor were all of its channels operable. A second prototype hybrid switch

achieved a minimum channel bandwidth of 6 GHz using higher performance components and was partially packaged. Ongoing efforts to further improve the performance and packaging of the switch are underway at TRILabs.

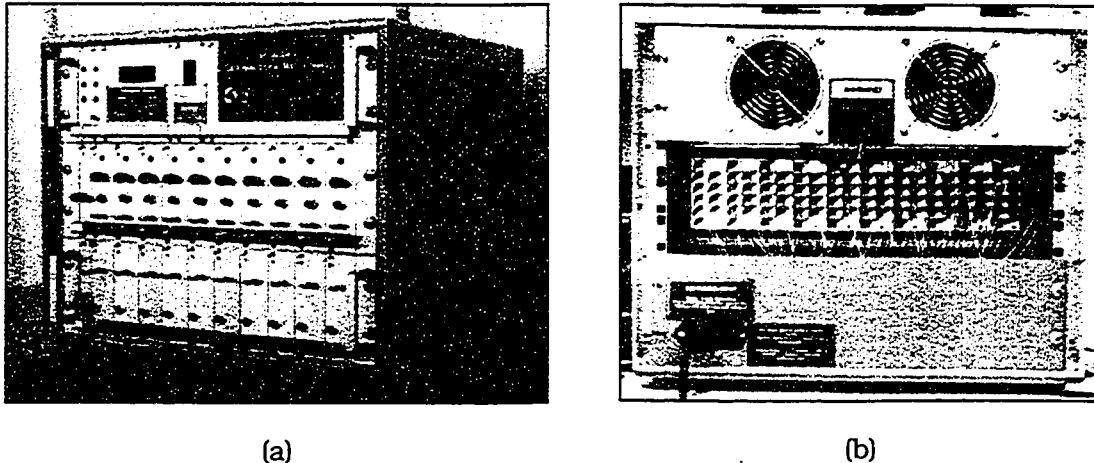


Figure 4.8. The discretely packaged 10x10 OES was a fully assembled non-blocking switch matrix. The front panel (a) illustrates the 10 electrical inputs and outputs that connect to the transmitters and crosspoints, respectively. In (b), the back of the enclosure was removed to reveal the 100 optical fibres used for the optical distribution. The dimension of the switch is 0.53 m x 0.43 m x 0.50 m.

Table 4.1. Performance summary of the 10x10 optoelectronic matrix switch. Cross-talk and contrast measurements were made at 1 GHz [63].

On/Off Contrast	>60 dB
Cross-talk Suppression	>60 dB
Analogue Bandwidth	1.2 GHz
Switching Time	5 ns (controller limited to 10 μ s)

4.3.1. Overview of the 4x4 Hybrid Integrated Optoelectronic Switch

The hybrid integrated optoelectronic switch was designed with performance, manufacturing and flexibility in mind. This resulted in an architecture shown in Figure 4.10. The switch was separated into two primary modules. First, a transmitter module converts electrical input signals to optical signals. The optical signals are transmitted via graded index (GRIN) multimode fibre to a crosspoint module. This second module performs the switching function by routing the signals to one of four electrical output

ports. This configuration is known as an electrical-in electrical-out configuration. Similarly, by rearranging the design to place the crosspoint module first, an optical-in optical-out configuration can be realized.

The transmitter module consists of four distributed feedback (DFB) semiconductor lasers operating at a wavelength of approximately 1550 nm, wirebonded to an aluminum nitride (AlN) ceramic substrate patterned with 50 Ω coplanar transmission lines (Figure 4.9). These coplanar transmission lines carry the RF signals that directly modulate the lasers. Since the AlN substrate has a high thermal conductivity, (>160 W/m \cdot K), it acts as a passive thermal heat sink and eliminates the need for active thermoelectric cooling. The lasers are placed on a 5 mm pitch to reduce electrical coupling between adjacent channels. The laser light is coupled into 62.5 μ m core graded index fibres, forming the output channels of the module.

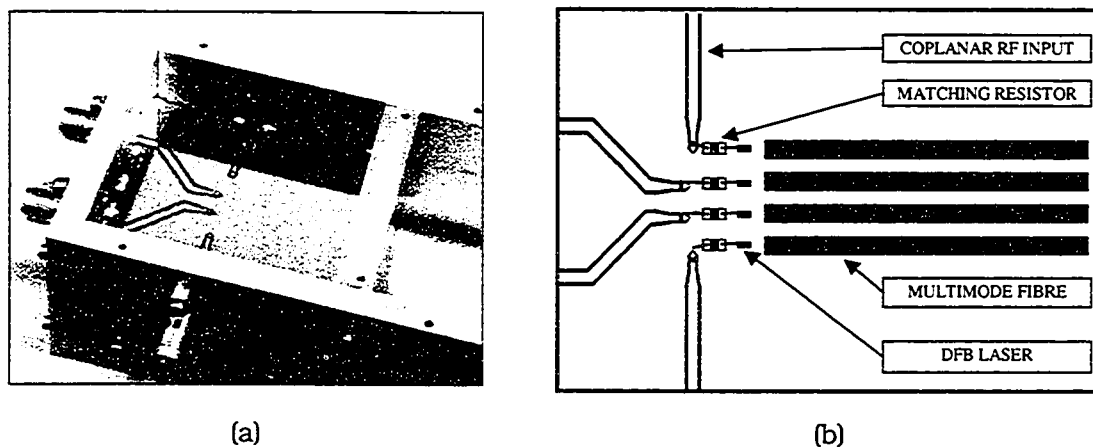


Figure 4.9. Photograph of the transmitter module package in a RF enclosure (a). Schematic of the patterned aluminium nitride substrate (b) illustrating 50 Ω coplanar transmission lines, semiconductor lasers and butt-coupled graded index multimode fibre.

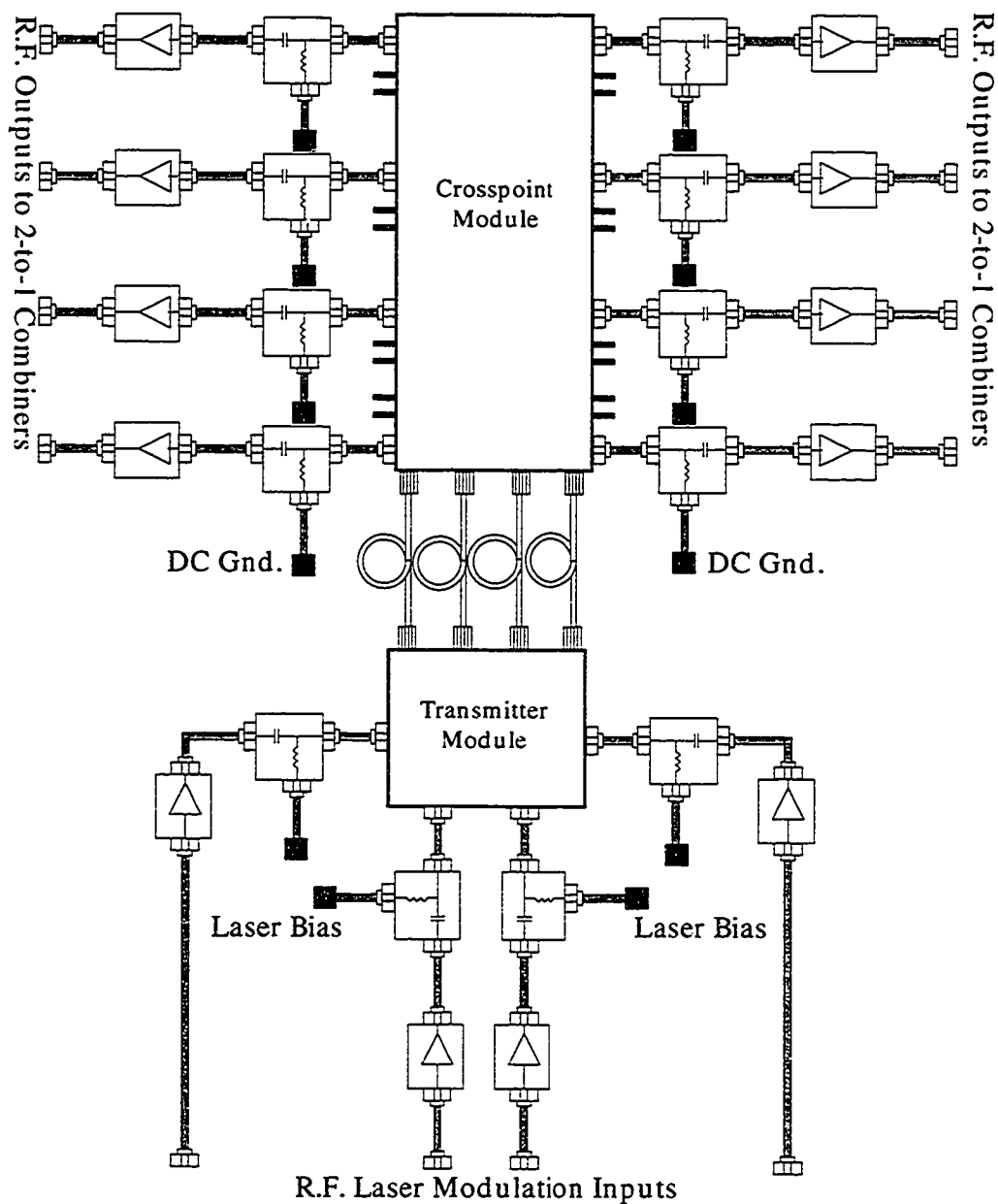


Figure 4.10. Schematic drawing of the 4x4 hybrid integrated optoelectronic switch matrix. Electrical signals applied to the inputs of the transmitter module at the bottom directly modulate semiconductor lasers. The resulting optical signals are transported by graded index multimode fibre to the crosspoint module. Each incoming optical signal is split into four by polymer waveguide splitters and distributed to one of four 1x4 metal-semiconductor-metal photodetector arrays. The desired optical signal selected by biasing 'on' the appropriate photodetector in the array. The resulting electrical signal is amplified and directed to one of four electrical (RF) output ports.

The crosspoint module (Figure 4.11) contains two sub-modules: the RF electrical substrate and the optical distribution submount. The RF substrate provides the physical and electrical connections to the metal-semiconductor-metal (MSM) photodetector arrays. The optical distribution submount is a separate substrate patterned with laser-written or photographically defined polymer waveguides.

The linear array of MSM photodetectors are mounted on a high-purity (99.6%) RF alumina substrate (Figure 4.12) patterned with gold bias control lines and coplanar RF outputs. Each MSM array contains eight MSM photodetectors, connected to a common electrical bus on 0.5 mm pitch. Only four of the eight elements were used in this prototype. To obtain broadband arrays with a uniform frequency response from each detector, an artificial transmission line bus concept was used [64]. The ends of the bus are connected to two 50 Ω coplanar transmission lines, each of which has an external SMA connector. The two signals from each bus can then be electrically combined using a broadband RF combiner and amplified with commercially available broadband amplifiers.

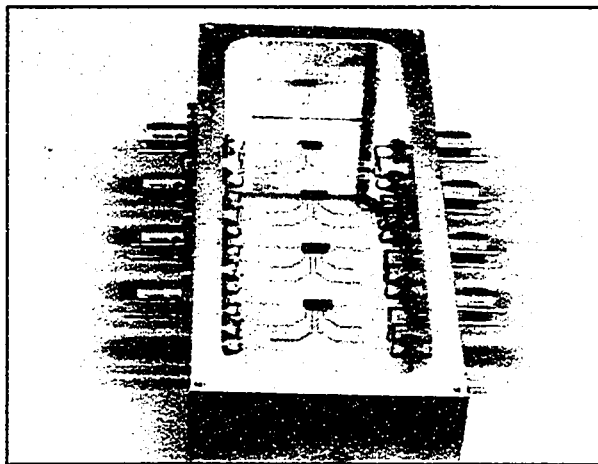


Figure 4.11. Photograph of the packaged crosspoint module. The four rectangular devices in the centre of the substrate are the MSM photodetector arrays. Protruding through the left and right sides of the enclosure are the RF outputs (threaded SMA connectors), and electrical control lines (thin wires). The coplanar transmission lines can be seen leading away from the MSM photodetector arrays.

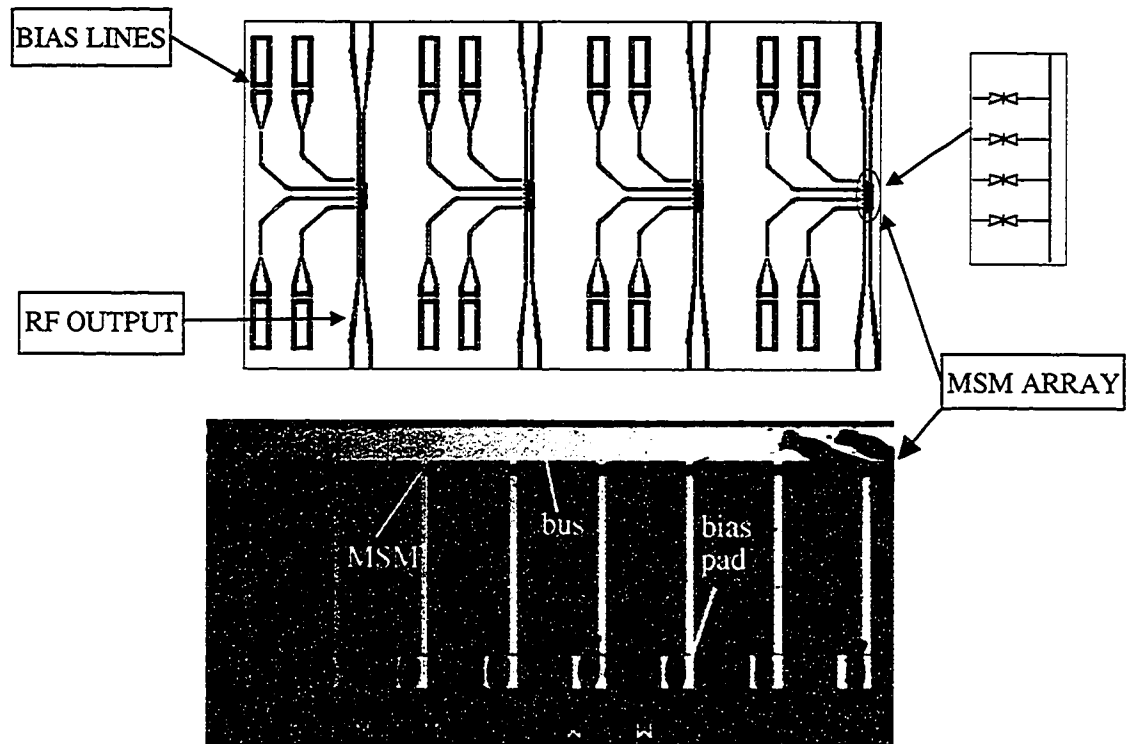
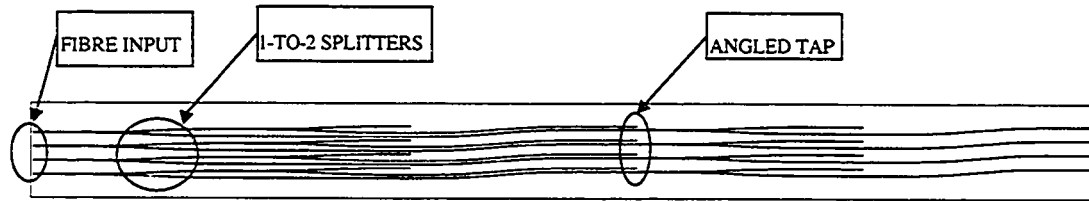
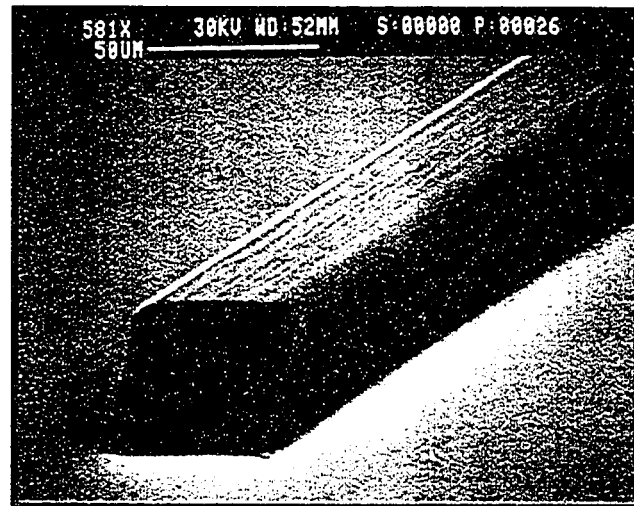


Figure 4.12. The gold pattern alumina substrate (top) provides physical support and electrical connections to the metal-semiconductor-metal photodetector arrays (bottom).

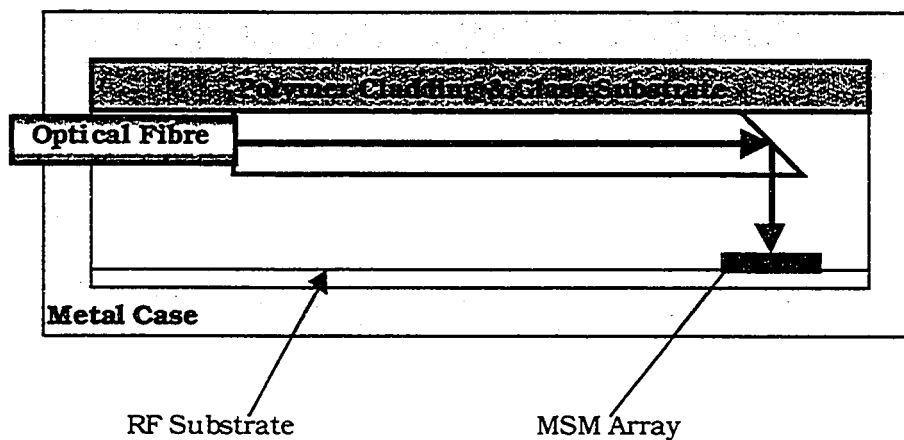
The input optical signals enter the module through connectorized GRIN multimode fibres butt-coupled to laser-written polymer waveguides. Each waveguide splits into four waveguides, one for each output channel, using a series of symmetric 1-to-2 laser-written splitters as shown in Figure 4.13(a). The optical signals are directed out-of-plane to the MSM arrays by angled-end taps. These taps are fabricated by undercutting the polymer waveguide at 45° angle with a microtome. Shown in Figure 4.13(b) is a SEM of a 50 μm square polymer waveguide with a 45° tap. When assembled, the glass submount, shown in Figure 4.13(c), is actively aligned to the RF substrate by maximizing the output power from the MSM arrays.



(a)



(b)



(c)

Figure 4.13. Scale drawing of the optical distribution submount (a) illustrating the locations of the 1x2 polymer splitters. The positional information in (a) was used for defining both laser written and photolithographic polymer waveguides. A scanning electron microscope photograph of a laser written polymer waveguide with a 45° cut is shown in (b). A cross-section of the polymer waveguide (c) reveals how light travelling from left to right is redirected vertically out-of-plane by a 45° angle-cut in the polymer via total internal reflection at the polymer-air interface.

4.4 Metal-Semiconductor-Metal Photodetectors and Photodetector Arrays

A metal-semiconductor-metal (MSM) photodetector is a planar device patterned with metal interdigitated fingers on a photosensitive semiconductor material. The MSM photodetector arrays in the hybrid OES are a fundamental component of the device. First, the detectors serve as transducers that convert optical signals to electrical signals. Second, they perform the optoelectronic selection operation, where 1 of N optical signals is selectively converted to an electrical signal. Third, owing to their low capacitance, relatively large area MSM detectors may be fabricated with >10 GHz bandwidth, allowing for data rate and signal format transparency. Last, the MSM fabrication process is relatively simple due to its planar construction, therefore costs and defects are relatively low. Thus MSM photodetectors were chosen for the hybrid integrated OES. Consequently, this section will review the basic operation of an MSM detector and highlight some of the developments that have led to the design of MSM photodetector arrays with a broadband uniform frequency response.

4.4.1. Theory of Operation

The structure of a typical MSM photodetector is shown in Figure 4.14 and Figure 4.15. Although the isolation, barrier enhancement and passivation layers may be omitted, they become a requirement if high responsivity and uniform broadband frequency response are desired. A brief description of each layer follows. Details of the device physics will not be given but may be found in the literature [74].

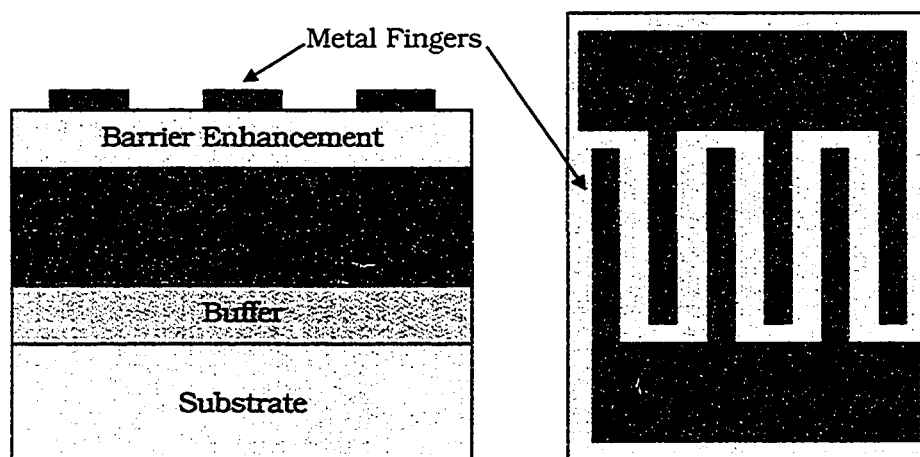


Figure 4.14. Cross-sectional view (left) and top view (right) of a typical MSM photodetector. Not shown is a cap or passivation layer that has the dual purpose of reducing surface charge traps and operating as a narrow-band anti-reflection coating.

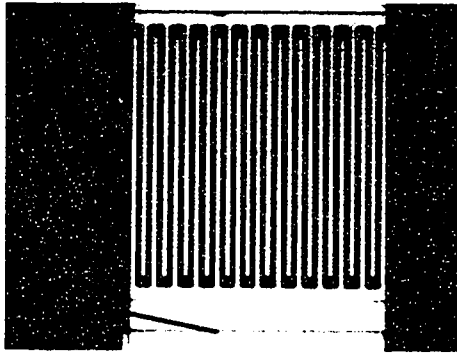


Figure 4.15. Photograph of a single MSM photodetector. The light coloured area represent the metal fingers and metal interconnect, while the darker areas are semiconductor material. Also visible is the mesa edge used to isolate adjacent devices and reduce surface leakage current.

The choice of the substrate material determines the sensitivity of the device as a function of wavelength. Generally, GaAs substrates are used for short wavelength operation (780-850 nm) and InP substrates are used for longer wavelengths (1310 nm and 1550 nm) used in optical telecommunication networks. Even though high quality substrates are employed, the surface quality is normally less than optimal and a buffer layer is usually deposited.

The buffer layer is a thin (50-200 nm) layer of high quality epitaxy that is lattice-matched to the substrate. Since the buffer layer is produced under a vacuum, its surface is free of oxidation and contaminants. Other high quality lattice-matched epitaxial layers may then be grown free (or with a greatly reduced number) of defects.

The isolation layer is used to prevent charge carriers (electrons and holes) that have been generated deep inside the device from being collected by the metal electrodes. This greatly improves the speed of the device. Often the buffer and isolation layers are combined into a single layer that incorporates the properties of both layers.

The most important layer is the absorption region. It is in this layer where incident photons are converted into the electron-hole pairs responsible for producing the photo-current. This layer is critical in determining the device responsivity and bandwidth. Increasing the layer thickness increases the probability of absorbing an incident photon. However, as the layer thickness is increased, the transit time limited bandwidth of the device is reduced [74]. Therefore, a careful trade-off between light collection efficiency and speed must be struck during design.

The metal fingers form back-to-back Schottky contacts that are separated by an exposed semiconductor material. Hence, the DC response (Figure 4.16) resembles an optically controlled diode. Although the planar design simplifies fabrication and

reduces cost, the metal fingers shadow the underlying photosensitive semiconductor and thus reduce the device's responsivity.

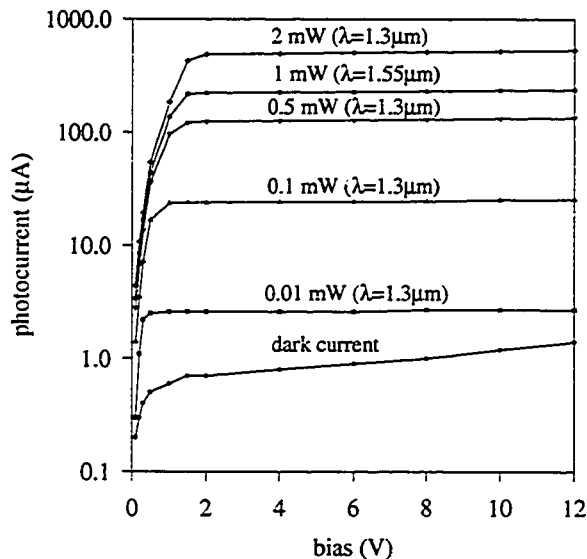


Figure 4.16. Measured DC I-V characteristic for a long wavelength MSM photodetector. (source [74]). Note that higher bias voltages are required to saturate the device.

The barrier enhancement layer increases the bandgap between the metal and the semiconductor material. This is especially important in InGaAs since the Schottky barrier height is quite low (~ 0.2 eV). The low energy bandgap results in carrier re-injection, photoconductive gain and excessive dark current. Excessive dark current may limit the signal-to-noise ratio and the photoconductive gain may result in low frequency gain and therefore poor broadband frequency response [74]. Also, the layer reduces surface charge states, which may contribute to the dark current and act as recombination sites that reduce the device responsivity.

A passivation/anti-reflection (AR) coating layer may also be incorporated. Si_3N_4 is often used to treat the surface of the barrier enhancement layer (protecting it from oxidation, etc.). A narrow optical bandwidth optical AR-coating can be achieved by choosing this layer to be one-quarter optical wavelength thick.

To explain the operation of MSM photodetectors, consider the scenario where a photon is incident on the semiconductor material. An electron-hole pair will be generated if the photon energy is greater than the bandgap energy of the semiconductor (Figure 4.17). When a MSM in the "on" state, the alternate metal fingers are positively and negatively biased. The photo-generated electrons and holes are swept to the nearest cathode and anode by a static electric field resulting from the applied bias voltage. If the electric field is strong enough, the carriers will quickly reach their

respective saturation velocities, and the detector has maximum bandwidth. Therefore, there is little to be gained by raising the bias voltage much above this field saturation value. A modest increase can be noticed when higher optical power levels are used (see Figure 4.16).

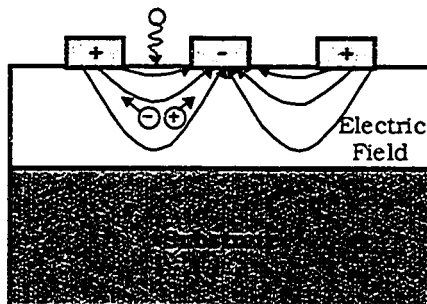


Figure 4.17. An electron (-) and hole (+) pair generated by an incident photon, that has an energy greater than the bandgap of the semiconductor, are swept to the cathode (+) and anode (-), respectively, due to the internal electrical field created by the bias voltage. If the field is strong enough, the electrons and holes will reach their saturation velocities in a very short distance.

4.4.2. Linear Arrays of MSM Photodetectors

When individual MSM photodetectors are connected to one-another, a linear photodetector array is formed. Figure 4.18 is a schematic illustration of a linear array of MSM photodetector, where one terminal of each MSM is connected to a common output bus and the other is attached to a bias control line. Shown in Figure 4.19 is a photograph of a 1x8 linear photodetector array. Previous work has resulted in MSM arrays with moderately uniform frequency response and 2-3 GHz of bandwidth [63],[74]. These photodetector arrays were used in both the original 10x10 OES and the first hybrid integrated OES prototype. A plot of the frequency response for a typical detector in the array is shown in Figure 4.20 [61].

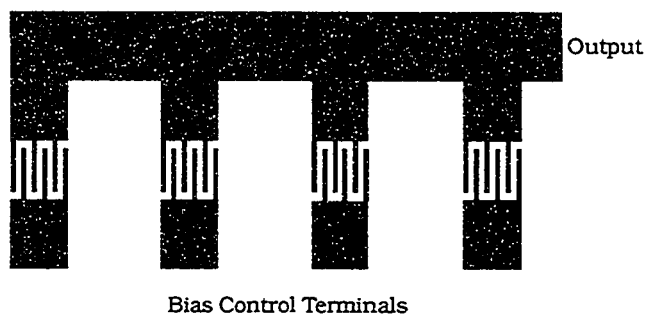


Figure 4.18. Schematic drawing of a 1x4 linear array of independently bias controlled MSM photodetectors connected to a common RF bus.

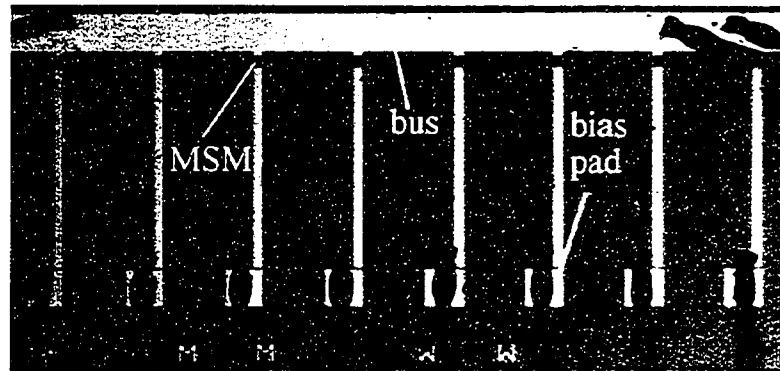


Figure 4.19. Photograph of a 1x8 linear MSM array. Also shown on the left, right and bottom side of the die are the wire bonds used to provide electrical connections to the RF substrate. For a perspective of size, the bias bond-pads (bias pads) are 100 μm on each side.

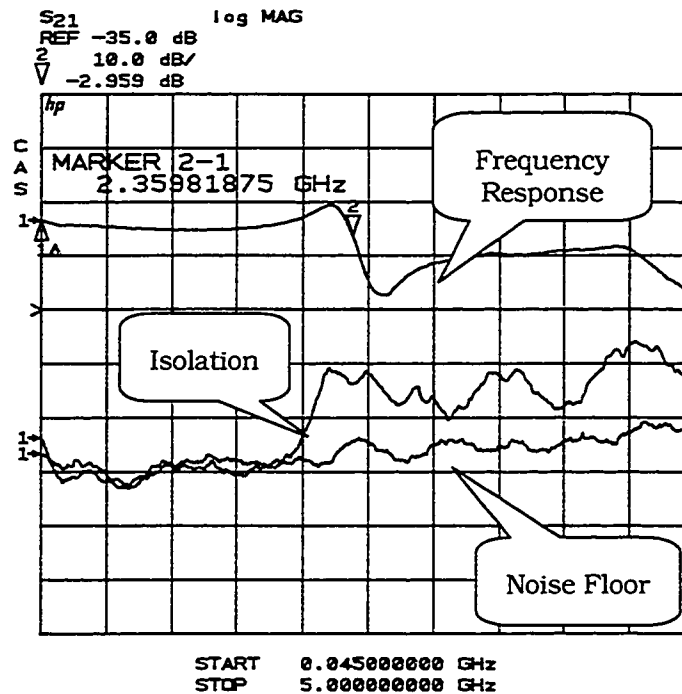


Figure 4.20. Frequency response from a first generation 1x4 linear MSM photodetector array. Note that although the 3-dB bandwidth of the device was limited to 2.35 GHz, the detector was still responsive up to >5 GHz, indicating that a better design could substantially improve the operational bandwidth. The lower two curves indicate the isolation when the bias was set to zero under illumination and the noise floor of the test setup.

The frequency response of each MSM in a linear array depends on its position relative to the output of the common bus. This can be better understood with the assistance of a simplified lumped element model of a MSM array as shown in Figure

4.21. MSM detectors that are farther from the output encounter higher parasitic capacitance, inductance and resistance (the resistive component results in a position-dependent attenuation factor) and hence have a degraded frequency response compared to MSM detectors near the output.

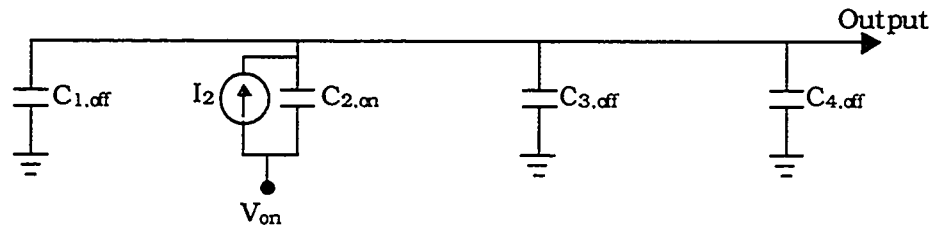


Figure 4.21. A approximate lumped element model of a linear array of MSM photodetectors attached to a common bus. $C_{i,off}$ is the total capacitance of the i^{th} MSM plus the wirebond pad in the "off" or unbiased state. Similarly, $C_{i,on}$ is the total capacitance of an MSM and its bondpad, in the "on" or biased state. V_{on} indicates a bias voltage present on detector two.

The difficulty of designing a broadband position independent MSM photodetector array was addressed and solved by DeCorby, *et al.* by noting that the common bus, if properly designed, may be used to compensate for the capacitance of the MSM detectors [74]. The impedance matched bus concept was experimentally verified [75]. As a result, a new photolithography mask set (Figure 4.22) was designed to incorporate this impedance matching concept. Also incorporated were coplanar microwave transmission lines (Figure 4.23), which improved the electrical isolation between adjacent MSM detectors and allowed direct on-chip electrical probing and testing.

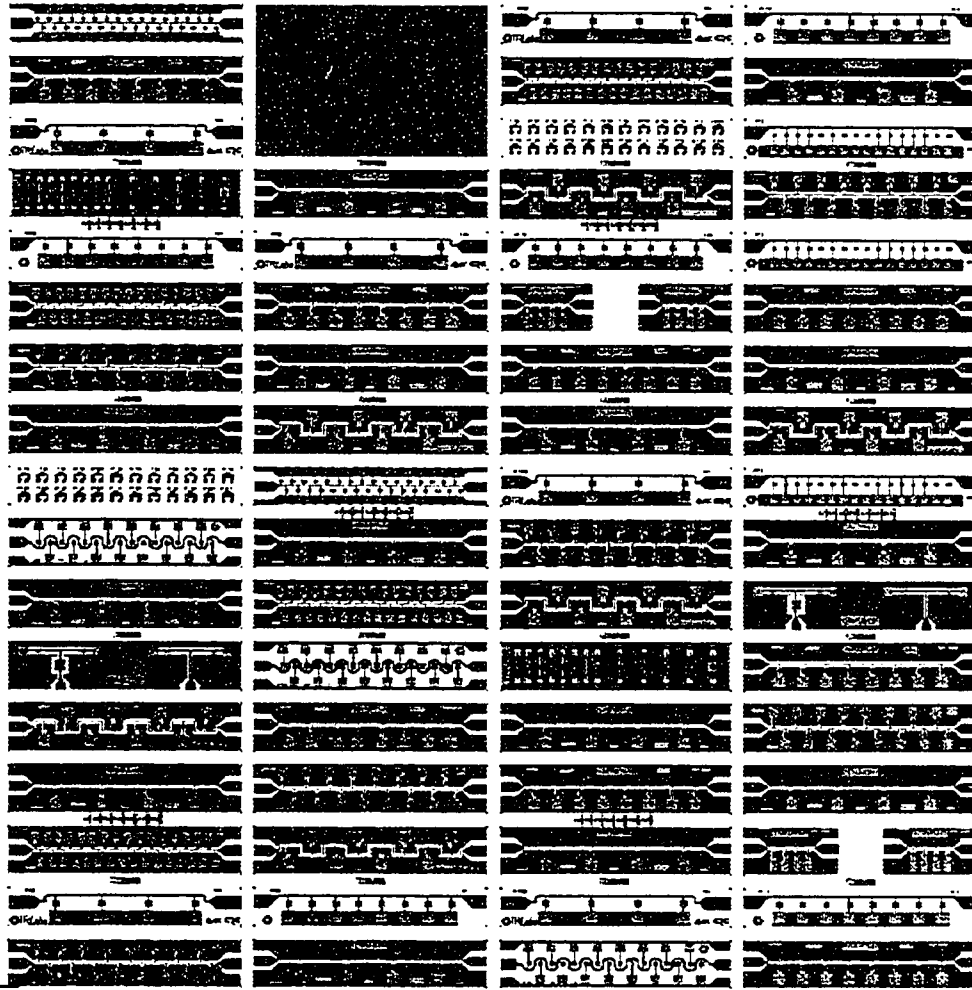


Figure 4.22. Unit cell for the new mask set designed by DeCorby [74]. The unit cell, measuring approximately 21 mm square, is repeated nine times on the mask. A total of 5 masks, one for each layer, are used when fabricating the MSM photodetectors. In addition to the photodetector arrays, there are individual detectors used for comparison testing, and a differential photodetector element. The large red rectangle is an opening in the mask that aids in the alignment process and is used for process calibration and monitoring purposes.

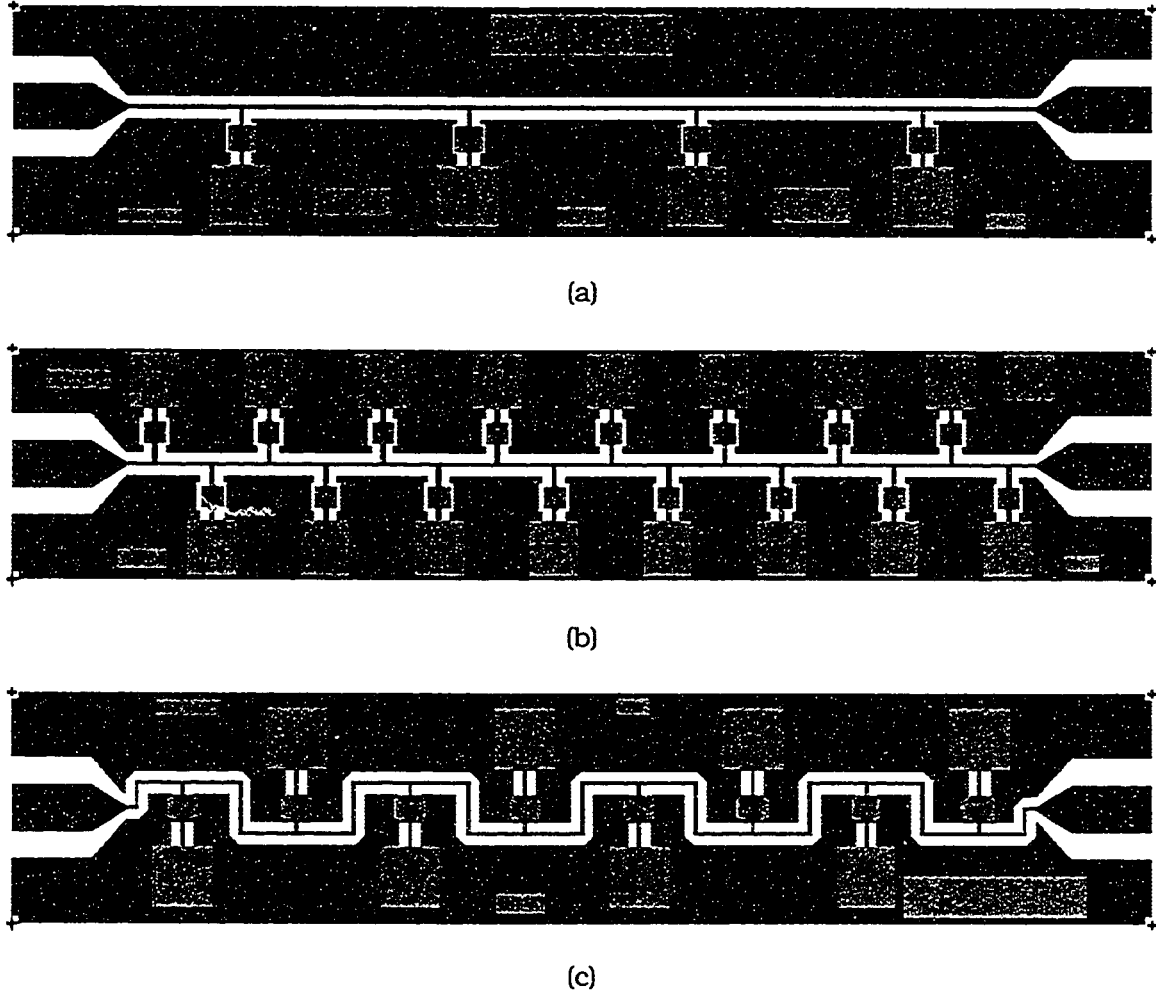


Figure 4.23. Layout for three different second generation MSM photodetector arrays that incorporate the impedance matched bus concept and coplanar transmission lines. (a) Shows a 1x4 array with detectors on 1 mm pitch designed for the 1x4 hybrid integrated OES. In (b) the MSM detectors were attached to both sides of the array to facilitate the larger 1x16 array while maintaining isolation. In (c) a serpentine bus was used so that the detectors are co-linear. MSM detectors are the red squares, the common bus is turquoise, the ground plane metal is purple and green represents where windows will be opened.

This new mask is designed for long wavelength photodetectors fabricated on InP substrates. Processing difficulties have delayed the arrival of the new devices, and as a result, they have not yet been incorporated into the hybrid integrated OES or this thesis. However, ongoing projects will assemble and test the switch with the new detector arrays.

4.5 Crosspoint Module

The crosspoint module is the core of the hybrid integrated OES, containing both the optical distribution and the MSM photodetector arrays. This section will present detail of the fabrication both hybrid integrated OES prototypes.

4.5.1. Optical Distribution

The optical broadcast function of the OES architecture was accomplished using polymer waveguide splitters. A laser writing process and photolithography were investigated in parallel as different waveguide fabrication techniques.

The photolithographic technique and process details used for patterning UV curable polymers is discussed in Chapter 3, Section 3.6.2. Shown in Figure 4.24 is the layout for the optical distribution for the second prototype switch. The waveguide losses of photographically defined waveguides are slightly higher (~ 2 dB/cm at 1550 nm) than comparable laser written waveguides.

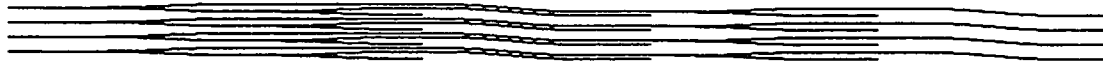


Figure 4.24. Scale view of the mask layout designed by the author and used to create the optical distribution in the hybrid integrated OES. On the mask, the dark lines are 50 μm wide and correspond to the absence of chrome. Thus, when UV light is exposed through a mask placed overtop a polymer coated substrate, the exposed polymer cures and forms optical waveguides. The longest waveguide is 78 mm long.

Laser writing is an inexpensive and flexible process that uses a focused UV laser beam to selectively cure the liquid polymer [76]. Custom written LabView[®] software (Figure 4.25) written by the author was used to control a Newport MotionMaster[®] motor controller board and motorized translation stages. Shown in Figure 4.26 is a photograph of the laser writing station. Two linear 6" translation stages are attached at 90° to each other. A vertical stage is used to adjust the height of the substrate and control the beam width. By writing away from the focal point of the beam, waveguides of arbitrary width may be fabricated, as long as the power and translation speed are adjusted to ensure that the polymer is being fully cured. Typical values used to write a 50 μm square waveguide are a translation speed of 0.5 mm/s and an optical power of 0.5 mW.

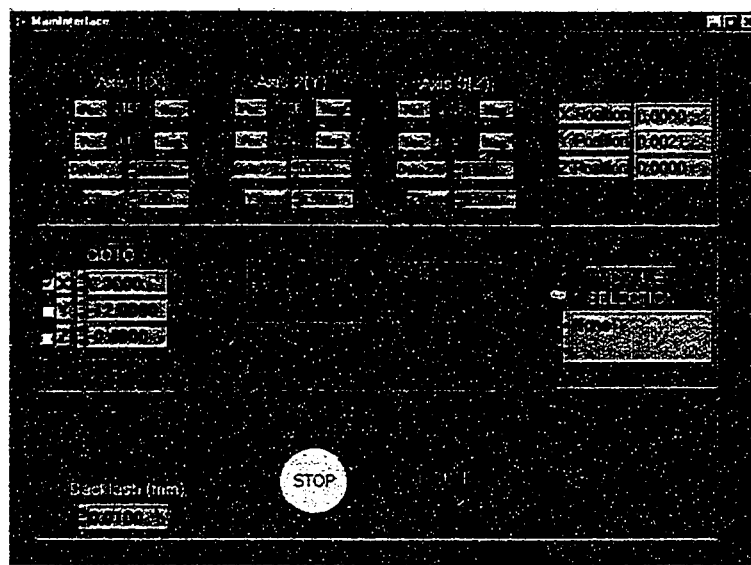


Figure 4.25. Main interface window of the LabView control program, called PC-XYZ. Real-time control and monitoring of three axes can be done from this window. The Module Selection box (located right middle) is used to select pre-written routines, such as S-bends, splitters, calibration routines, etc. The program is highly modularized, and is currently being expanded to allow users to load a CAD layout file into the program.

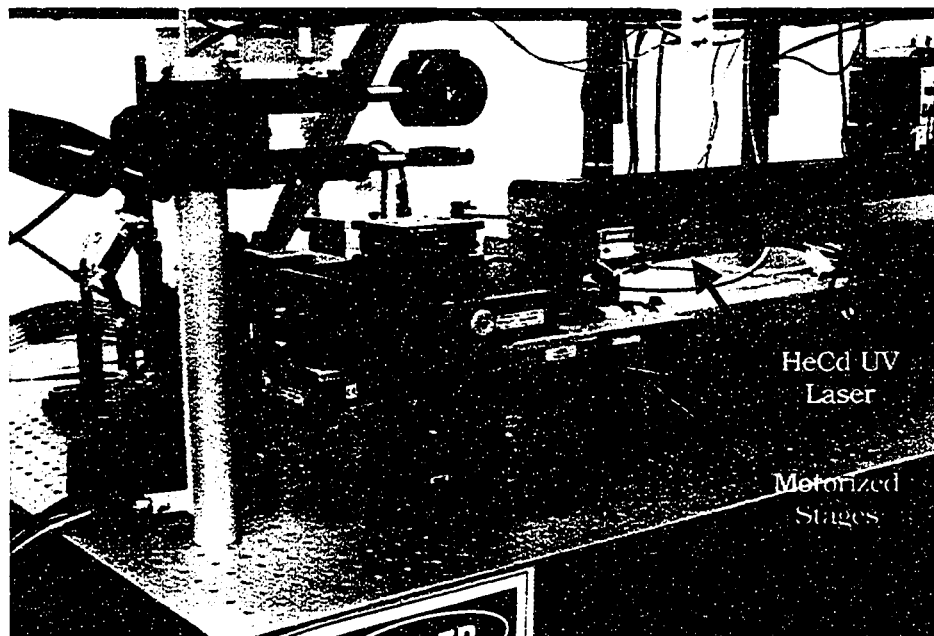


Figure 4.26. Photograph showing the laser writing station. The two crossed linear translation stages are indicated as the upper and lower stage. Some of the optics used for beam expansion and collimation can also be seen in the background.

4.5.2. Power and Dispersion Budget

The power budget is used to determine the required signal power present at the output of the transmitter to maintain a target signal-to-noise ratio (SNR) at the output of the receiver/crosspoint module. Another important design rule, the dispersion budget, is used to determine the amount of signal distortion imparted by the multimode waveguides.

The receiver sensitivity, defined as the optical power required to obtain a target bit-error-rate (typically 10^{-9}) or SNR, must be determined before a power budget can be deduced. To begin, a simplified noise analysis is used to determine the receiver sensitivity of an MSM photodetector.

There are three main sources of noise in photodetectors: shot noise, thermal noise and amplifier noise. The photon shot-noise results from the random generation of electron-hole pairs. The noise variance or mean square noise current is given by (4.2), where I_p is the photocurrent, equal to the responsivity times the optical power, I_d is the device dark current, q is the charge of an electron and Δf is the noise equivalent bandwidth of the receiver.

$$\sigma_s^2 = \langle i_s^2 \rangle = 2q(I_p + I_d)\Delta f \quad (4.2)$$

Thermal noise results from the random generation of current in the load resistor. The amplifier noise is often specified by the manufacturer as the noise figure, and is equal to the ratio of the input SNR to the output SNR. Amplifier noise is attributed to internally generated thermal noise from bias resistors and the noise associated with the transistors. The thermal and amplifier noise can be combined into a single expression given by

$$\sigma_T^2 = \langle i_T^2 \rangle = \frac{4k_B T \Delta f F_n}{R_L} \quad (4.3)$$

where F_n is the amplifier noise figure, k_B is Boltzman's constant [J/K], T is the operational temperature in [K], and R_L is the equivalent load resistance. A typical noise figure for a broadband amplifier with a bandwidth from the kilohertz range to five to ten gigahertz is 6 to 10 dB [77].

Since the variances are assumed to be Gaussian and statistically independent, the total mean square noise current is equal to the sum of the variances. The SNR, which is defined as the ratio of average signal power to noise power, is given by (4.4). For a MSM photodetector, the photocurrent is equal to the product of the responsivity

and the incident optical power. If the receiver is thermal noise limited, then (4.4) can be simplified to (4.5).

$$SNR = \frac{I_p^2}{2q(I_p + I_d)\Delta f + 4k_B T \Delta f F_n / R_L} \quad (4.4)$$

$$SNR = \frac{R_L (R P_{in})^2}{4k_B T \Delta f F_n} \quad (4.5)$$

To maintain a bit-error-rate of less than 10^{-9} , the SNR must be greater than 144 (21.6 dB) when the receiver is thermal noise limited [2]. Substituting $R_L=50 \Omega$, $T=300 \text{ K}$, $F_n=10$, $\Delta f=6 \text{ GHz}$ and $R=0.5 \text{ A/W}$ into (4.5), reveals that optical power incident on the photodetector should be at least $86 \mu\text{W}$ or -10.7 dBm .

The power budget can now be used to calculate the required laser launch power. Table 4.2 summarizes the major system losses. The best and worst case power required from the laser to achieve the desired receiver sensitivity are 5 dBm (3.2 mW) and 16 dBm (40 mW), respectively. The waveguide loss changes due to the varying length of waveguide between the input and MSM arrays. The range of waveguide loss may be reduced if asymmetric splitters were employed, although it is difficult to accurately control the tap or split ratio.

Table 4.2. Summary of the loss budget for the hybrid integrated OES.

Item	Loss (dB)
Laser Coupling to GRIN Fibre	1-2
Fibre-waveguide Coupling	1
Waveguide Loss (3-8 cm, 2 dB/cm @1550 nm)	6-16
Excess Loss of Two Splitters	0.5
Inherent Split Loss	6
Angled End-Tap	1

Either high power laser diodes or optical amplification would be required to meet the required receiver sensitivity. Another possibility is the use of lower loss polymer. Polymers that have a propagation loss of $0.2\text{-}0.5 \text{ dB/cm}$ at 1550 nm [43] are currently used in commercial products [78]; however, the polymer itself is not commercially available. Using a polymer with a propagation loss of 0.5 dB/cm would result in a

worst case waveguide loss of only 4 dB and would allow relatively low power DFB lasers to be used without external optical amplification. The second option is to replace the polymer waveguides with an optical switch. Instead of transmitting one quarter of the power to each MSM photodetector, an optical switch could divert all of the optical power to the appropriate photodetector. Chapter 3 discussed in detail a polymer switch that is compatible with the OES architecture and occupies less space than the existing passive waveguide optical distribution.

The polymer waveguides used are roughly 50 μm square and contain many modes. Using (4.6), the response time σ_{MOD} per unit length of a multimode fibre [12] is 0.4 ps/cm, when the nominal refractive index of the core, n_{co} and n_{cl} are 1.5367 (Norland polymer NOA 63) and 1.5145 (NOA 65), respectively. The refractive indices for the core and cladding polymers were obtained using a high precision prism coupler. For an 8 cm long waveguide, the response time would be 3.2 ps, which is a small fraction of a 10 Gb/s binary signal. Therefore, the effects of waveguide dispersion can be safely ignored.

$$\sigma_{MOD} = \frac{(n_{co} - n_{cl})L}{2c} \quad (4.6)$$

4.5.3. Substrate Design and Layout

The design and layout of the RF substrates for both prototypes were verified using Hewlett Packard's Microwave Device Simulator (HP-MDS). Two major design differences between the two prototypes are noteworthy. First, the spacing between the DC bias lines and the spacing between RF outputs on the second prototype were increased to allow for DC feed-throughs and SMA connectors, respectively. Second, two RF outputs per array are present on the second prototype substrate as opposed to one per array on the first prototype. This dual RF output design allowed both ends of each MSM photodetector array to be terminated into a 50 Ω load. As a result, the substrate for the second prototype was considerably larger than the first substrate, which initially caused one problem. The original motorized stages used for laser writing were capable of a maximum 50.8 mm (2 inches) of travel. The optical distribution for the second prototype required ~80 mm long waveguides, therefore the aspect ratio (defined as the ratio of the length to width) of the Y-splitters was correspondingly decreased. By decreasing the length of the straight input waveguide section, the optical distribution was written using the 50 mm stages, at the expense of increasing the excess loss of the

splitters. A photograph of the substrate used in the first prototype is shown in Figure 4.27. A drawing of the substrate used in the second prototype is shown in Figure 4.28.

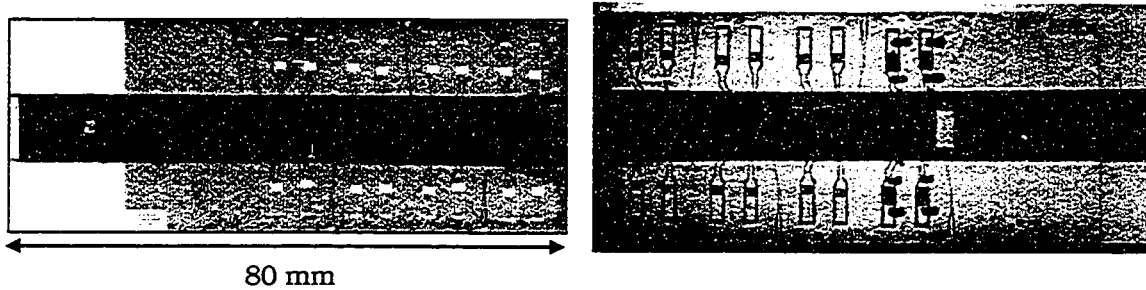


Figure 4.27. Photographs of the crosspoint substrate use in the first prototype OES. The photo on the left illustrates the bare substrate and the polymer waveguides. The red material is a thin layer of photoresist that was used as a buffer and UV light absorber. Without this layer, the reflected laser light from the rough gold film was diffuse and resulted in distorted waveguide profiles (a lower grade 96% unpolished alumina substrate was used). On the right, one output channel was populated and tested. The horizontal lines barely visible are the laser written polymer waveguides.

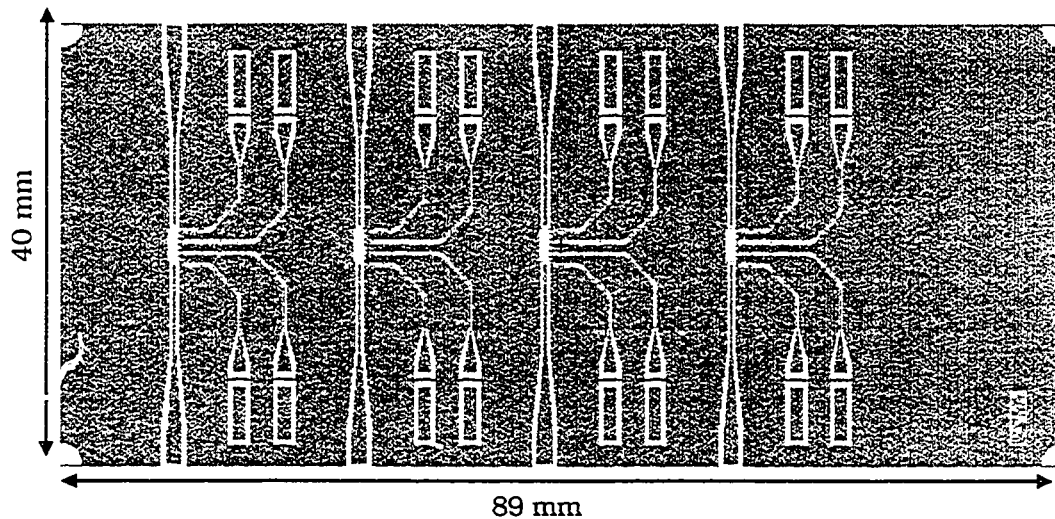


Figure 4.28. Scale view of the RF substrate used in the crosspoint module for the second prototype designed by the author. The yellow areas are evaporated gold. Also, the gold are is a ground plane, with the exception of the centre conductors of the coplanar transmission lines. The coplanar transmission lines were used to minimize cross-talk and only require one side of the substrate to be metalized. Furthermore, vias were not required to connect components, i.e. resistors, capacitor and inductors, because the ground plane is on the same surface.

Most of the bias decoupling circuitry was incorporated onto the substrate, with the exception of the bias-TEE on the RF outputs, which are required for DC return path

to ground continuity. The bias decoupling circuit used is shown in Figure 4.29. Additional decoupling was provided by DC feed-throughs, but limit the switching time to approximately 100 μ s.

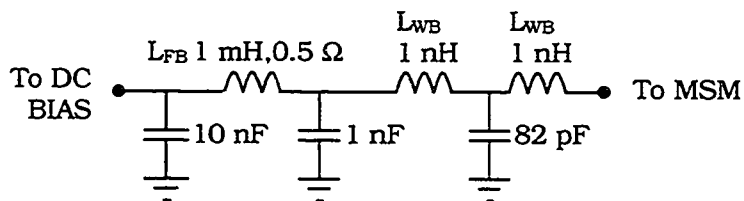


Figure 4.29. Circuit schematic for bias decoupling. L_{WB} is the inductance from each wire-bond and L_{FB} is the inductance of the ferrite bead (lossy inductor). The proximity of the first capacitor to the MSM is crucial in achieving high frequency decoupling (the 82 pF capacitor is a parallel plate capacitor measuring $\sim 400 \mu$ m on each side). A π -circuit is constructed from the 1 nF and 10 nF capacitors and the ferrite bead.

4.5.4. Experimental Results

The crosspoint module for prototypes I and II were characterized with a high speed vector network analyzer (Figure 4.30) and a 780 nm lightwave test-set. Frequency response plots for prototypes I and II are shown in Figure 4.20 and Figure 4.31. Owing to the unavailability of longer wavelength MSM photodetector arrays, short wavelength detectors were used in the second prototype OES even though the transmitter module used long wavelength (1550 nm) lasers. It was determined in the course of the work that some older MSM detector arrays could be modified to have similar performance characteristics to the impedance matched bus arrays. Direct measurement of the digital performance was not possible since the 780 nm lightwave test set did not have sufficient output power. However, using a software program written in Matlab, called the Fibre Optics Communications System Simulator (FOCSS) [79], the system eye-diagrams could be derived from the measured frequency response data. The measured frequency response plots were observed to be noisy due to the low optical power available from the lightwave test-set. When the frequency data were used in FOCSS, the eye-diagrams were almost completely corrupted by this noise. This problem was counteracted by filtering the measured frequency response data in Matlab. As a result, the eye-diagrams for the MSM were not directly calculated. Instead, the frequency response data was used in conjunction with the captured digital time sequences from the transmitter module to produce a series of computed system eye-diagrams (see Section 4.6).

The switching time of the packaged crosspoint module was limited to $\sim 100 \mu\text{s}$ by the low frequency cut-off ($\sim 10 \text{ kHz}$) of the feed-throughs. Previous measurements have shown that the switching time of the MSM detectors arrays is $\sim 5 \text{ ns}$ [63].

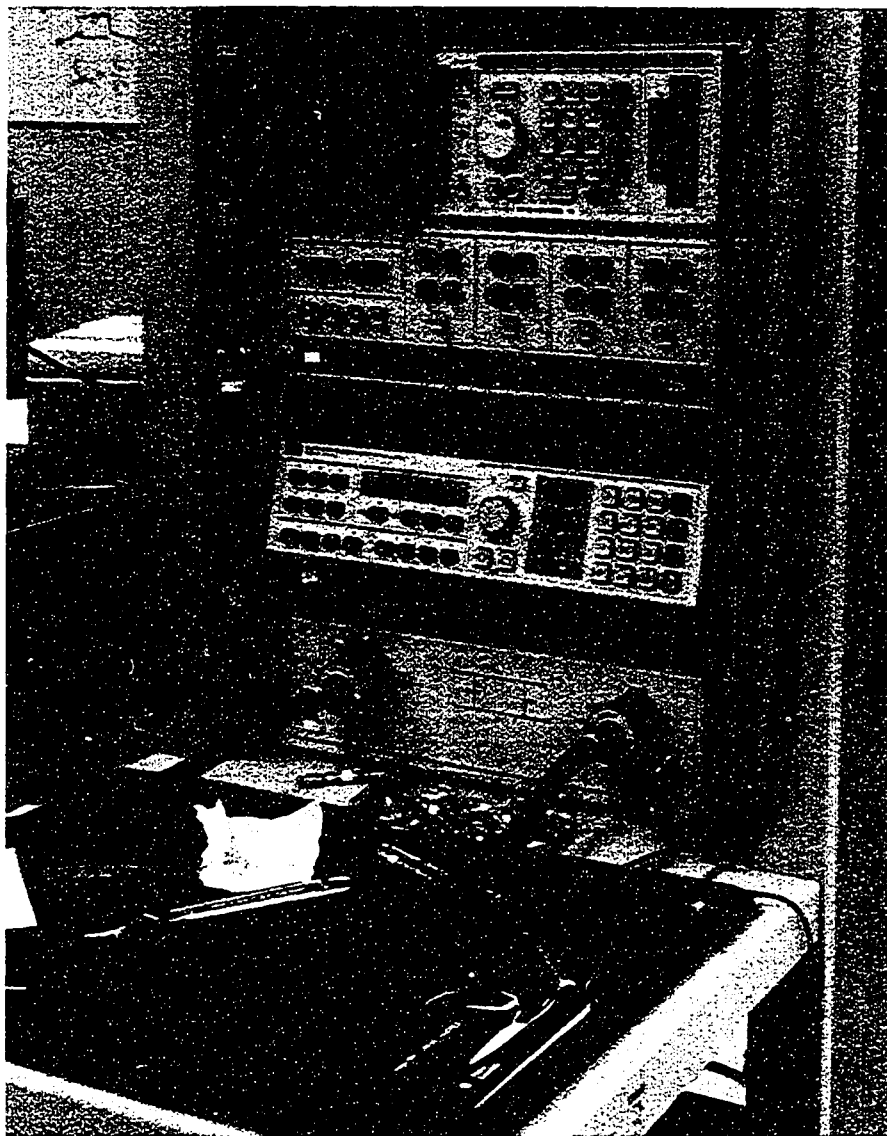


Figure 4.30. Photograph of a vector network analyzer. The two coaxial cables at the bottom are used to measure the frequency characteristics of an RF device.

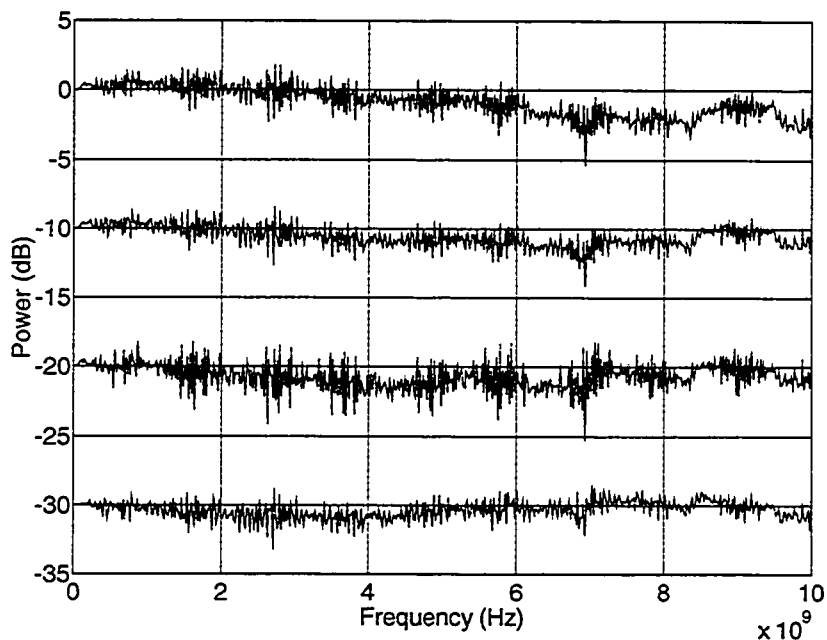


Figure 4.31. Frequency response from one MSM detector array in the second switch prototype. The responses for each of the four channels are offset for clarity.

4.6 Transmitter Module

A photograph and frequency response plot of the first prototype transmitter module is shown in Figure 4.32 and Figure 4.33. The 3 dB bandwidth of the transmitter module was >2 GHz, which exceeded the design target of 1.25 GHz. The module was packaged as shown in Figure 4.32.

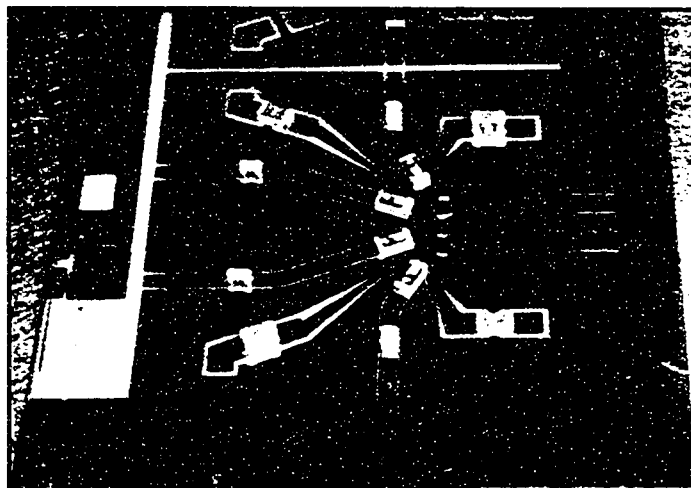


Figure 4.32. Photograph of the laser transmitter used in the first prototype. All the passive and active components were secured to the RF substrate using silver epoxy.

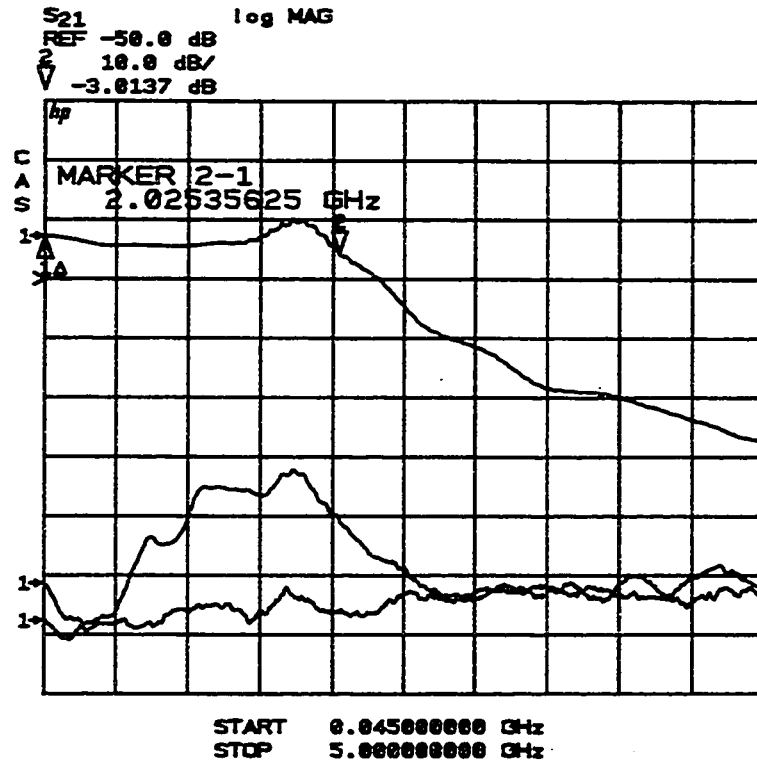


Figure 4.33. Frequency response of the first prototype transmitter module. The 3 dB bandwidth is approximately 2 GHz, which surpassed the targeted 1.2 GHz bandwidth of the 10x10 discretely packed OES.

A scale drawing of the second prototype transmitter substrate was shown previously in Figure 4.9. Coplanar transmission lines were employed for improved cross-talk performance and ease of fabrication. Thin-film ceramic resistors (rated at 1/8 W at 70 °C) measuring 762 μm (0.03") wide by 1.14 mm (0.045") long and having a resistance of 43 Ω were used to match the impedance of the laser to the 50 Ω transmission line. Shown in Figure 4.35 and Figure 4.34 are typical frequency response plots of the laser transmitters used in prototypes I and II. Note the mid-frequency dip in the response. The non-uniform response was adequately corrected with the high-pass equalizer circuit shown in Figure 4.36.

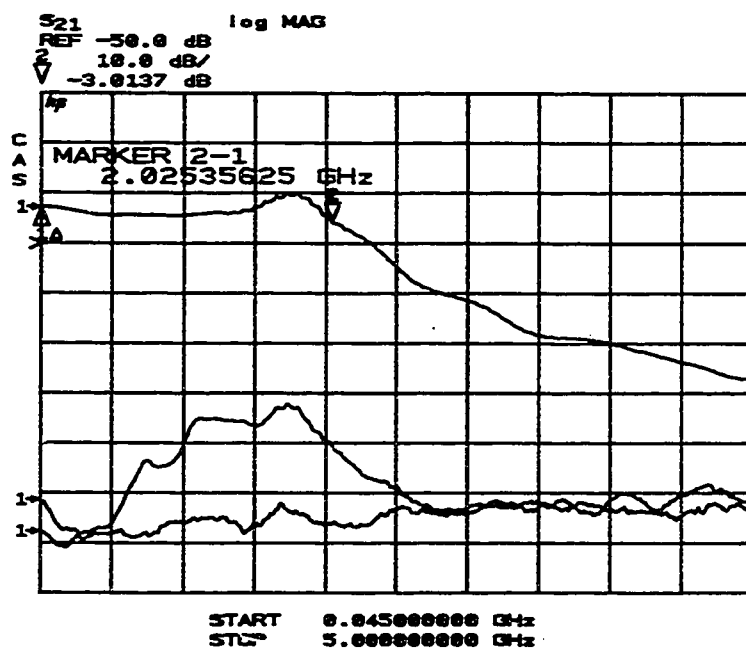


Figure 4.34. Frequency response plot of one laser transmitter channel from first prototype OES

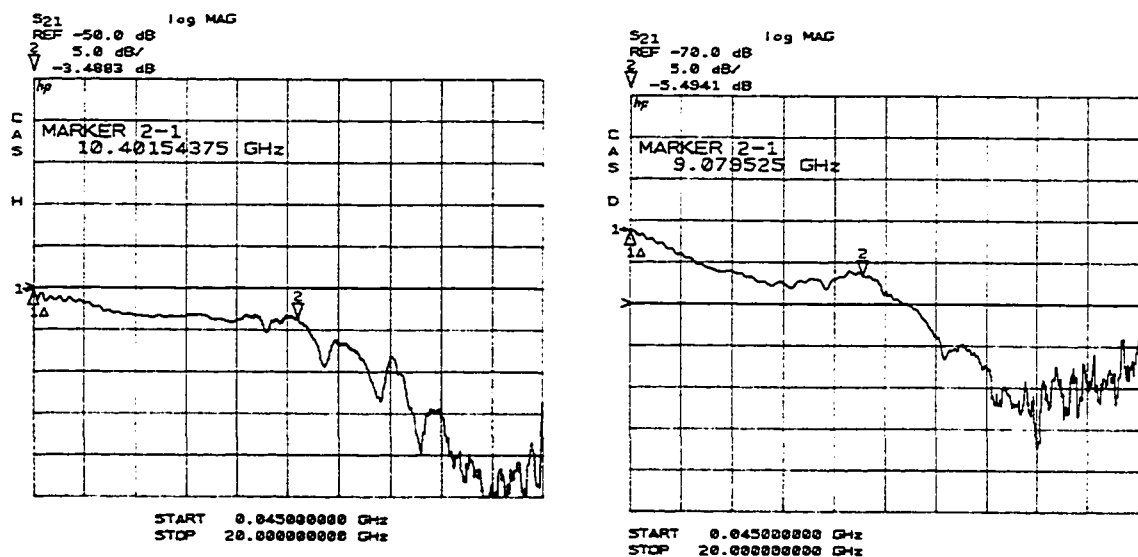


Figure 4.35. Frequency response plots for two different lasers. Note that both transmitters exhibited a low frequency gain, or mid-frequency loss.

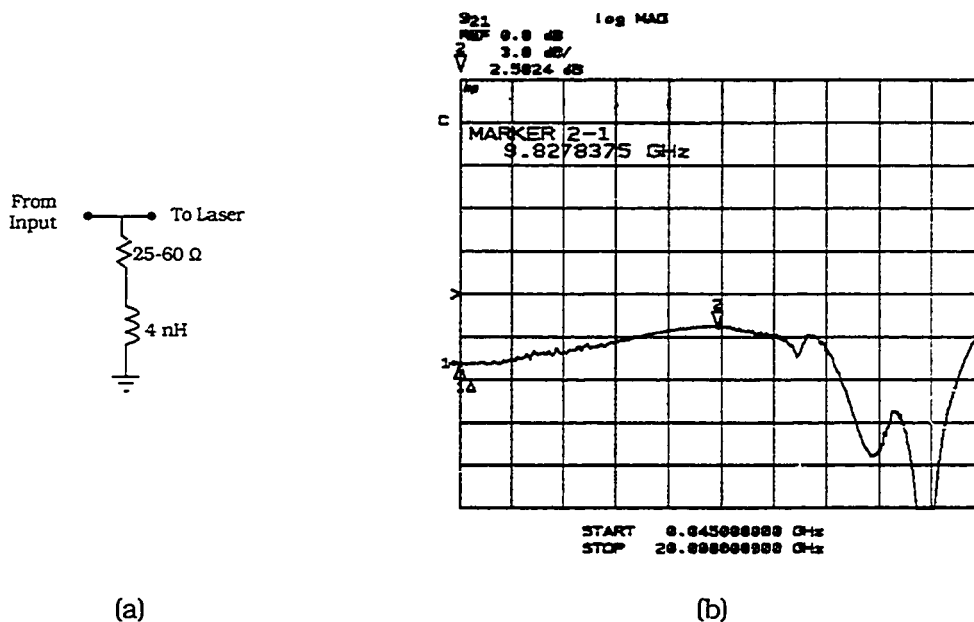


Figure 4.36. Electrical schematic (a) of the high-pass equalizer circuit used for the lasers in the second prototype OES. The frequency response of the equalizer is shown in (b). The insertion loss of this device was 2.5 dB.

The DC light-current ($L-I$) curves for six lasers are shown in Figure 4.37. It was found that the lasers could be categorized into two groups: those that exhibited a slope efficiency of ~ 0.04 mW/mA, and those that had a slope efficiency of ~ 0.017 mW/mA. These lasers were obtained in die form and only tested by the manufacturer for output power, not efficiency. As a result, each laser was tested before used in the transmitter module.

Multimode GRIN fibre was butt-coupled to the laser for maximum collection efficiency and simplicity. However, the reflected laser light from the cleaved fibre facet resulted in an increased relative intensity noise (RIN) [80] and enhanced relaxation oscillation peak (ROP), as shown in Figure 4.38. The fibre location was optimized to minimize the ROP and maximize the coupled power in the fibre using an electrostrictive three-axis positioner to control the fibre position.

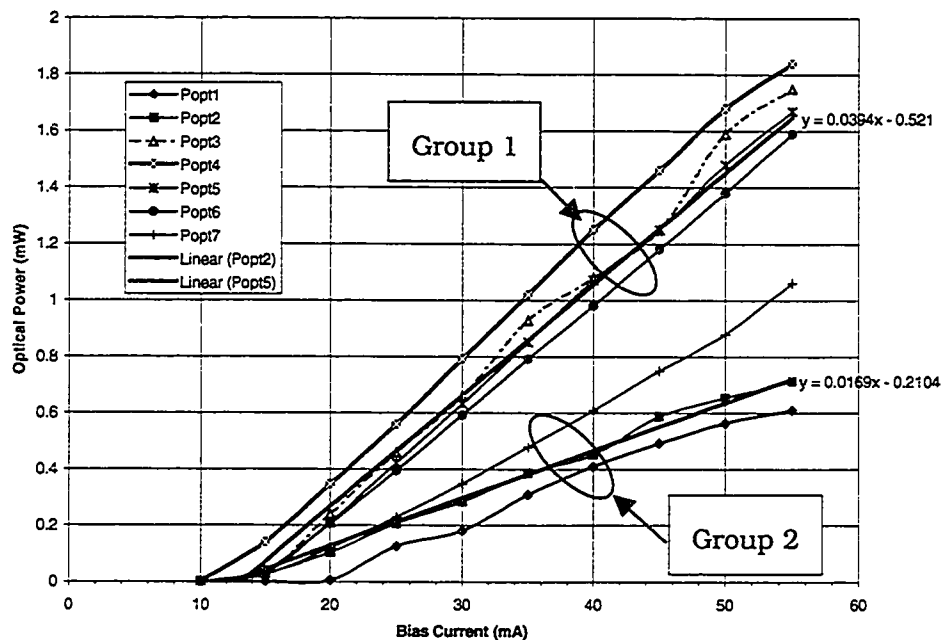


Figure 4.37. Light-current plots for seven lasers tested for use in the second prototype transmitter module. The lasers were classified into two groups: Group 1 has a slope efficiency of 0.04 mW/mA and Group 2 has a slope efficiency of 0.017 mW/mA. Only those with the higher slope efficiency were used in the second prototype transmitter module.

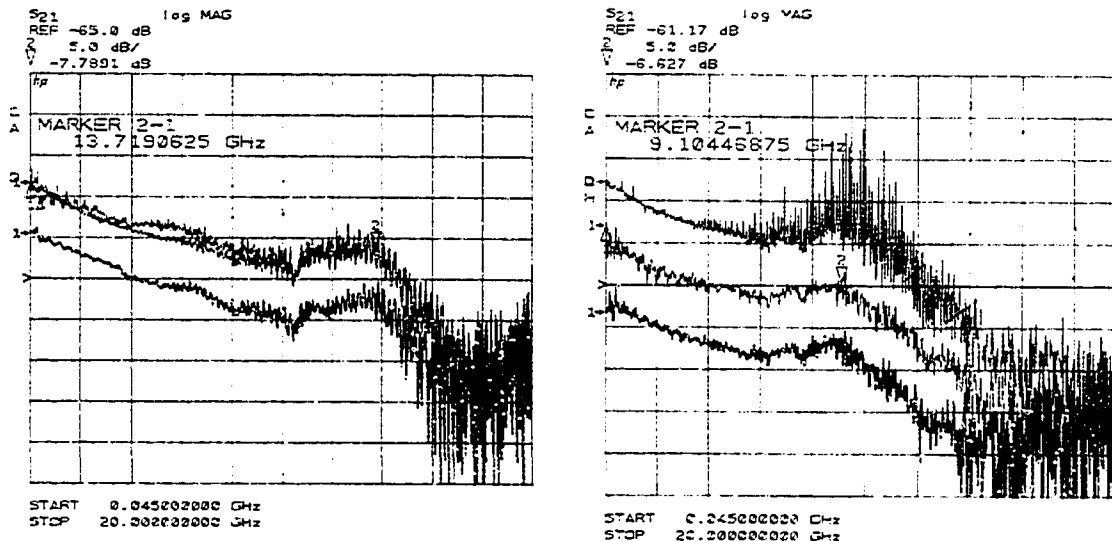


Figure 4.38. Frequency response plots for two different lasers. The plots were obtained for three different fibre positions: blue was very close to the laser facet ($<10\ \mu\text{m}$), green was about $25\text{-}50\ \mu\text{m}$ from the facet and black was about one fibre width or $125\ \mu\text{m}$ from the facet. Note that as the fibre gets closer to the laser facet the amount of light collected increase, i.e. more signal power, however, the relative intensity noise also increases. Also, it can be seen that the effect of back-reflected light affects the two lasers differently.

Bias decoupling was accomplished using external bias-TEEs. Commercially available external bias-TEEs are relatively inexpensive (US \$ 350) and have a bandwidth of 25 GHz. Therefore, it was decided not to include bias decoupling circuitry on the substrate because a simple bias decoupling circuit could limit performance.

Digital data was sent only through the second prototype transmitter module. Shown in Figure 4.40 are eye-diagrams generated by FOCSS from time domain digital sequences captured by a bit-error-rate tester (BERT) and a high speed digitizing oscilloscope at various bit rates (see). As the data rate approaches 10 Gb/s the eye begins to close, however, some of the eye closure was attributed to the test setup. Shown in Figure 4.41 is an electrical back-to-back measurement of the test setup, i.e., the transmitter was not inserted into the signal path. Clearly there is significant signal distortion caused by the actual test set. This only occurs when the data rate is greater than 3 Gb/s because external devices are used to increase the data rate by a factor of four by time division multiplexing the basic signal from the BERT [79].

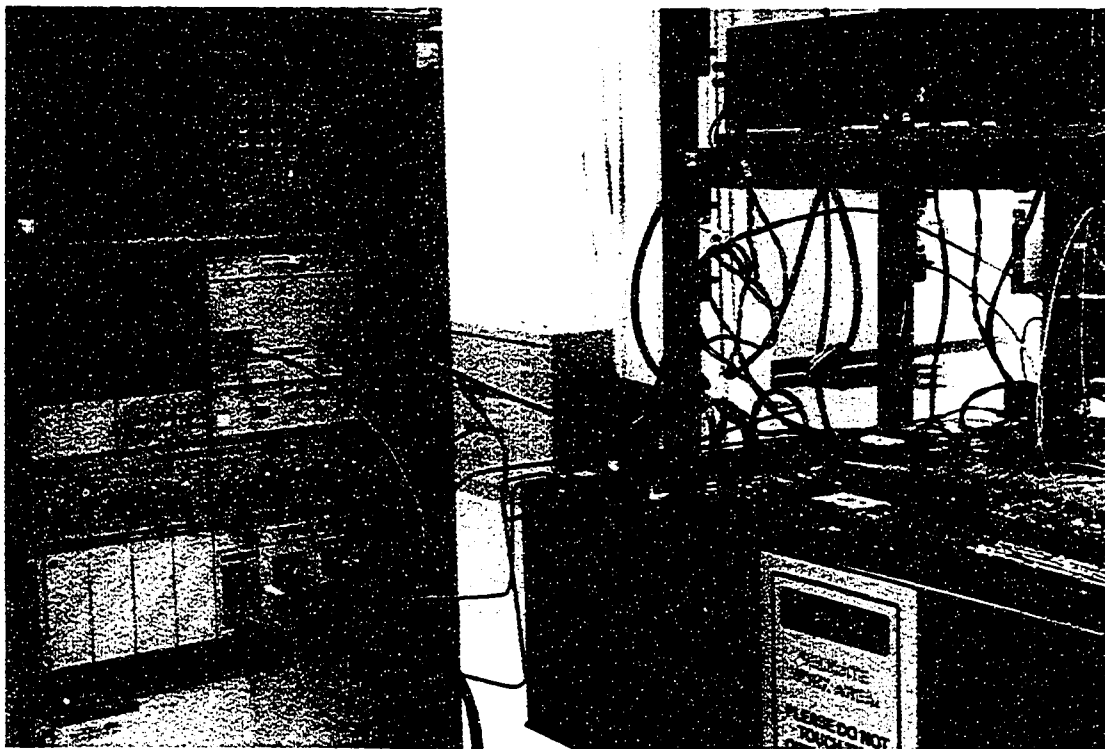


Figure 4.39. Photograph illustrating the BERT and high speed digital oscilloscope (left). Some of the RF components used to increase the data rate beyond the BERT's 3 Gb/s limit are visible on the right.

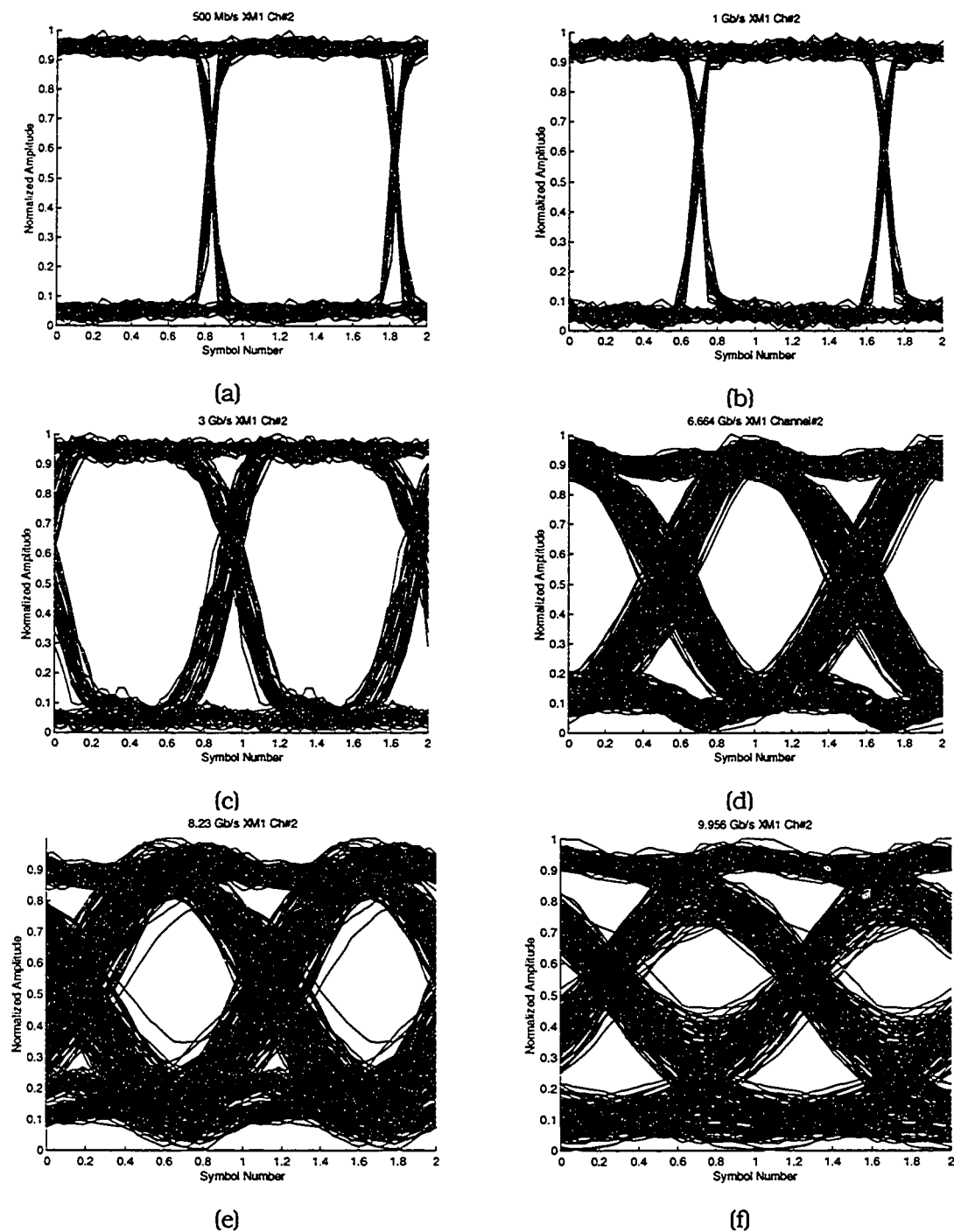


Figure 4.40. Measured transmitter eye-diagrams for the second prototype at the following bit rates: (a) 0.5 Gb/s, (b) 1 Gb/s, (c) 3 Gb/s, (d) 6.7 Gb/s, (e) 8.2 Gb/s and (f) 9.95 Gb/s. Clearly the transmitter module is capable of transmitting data at various rates. The eye closure for data rates greater than 3 Gb/s was partly due to the test setup.

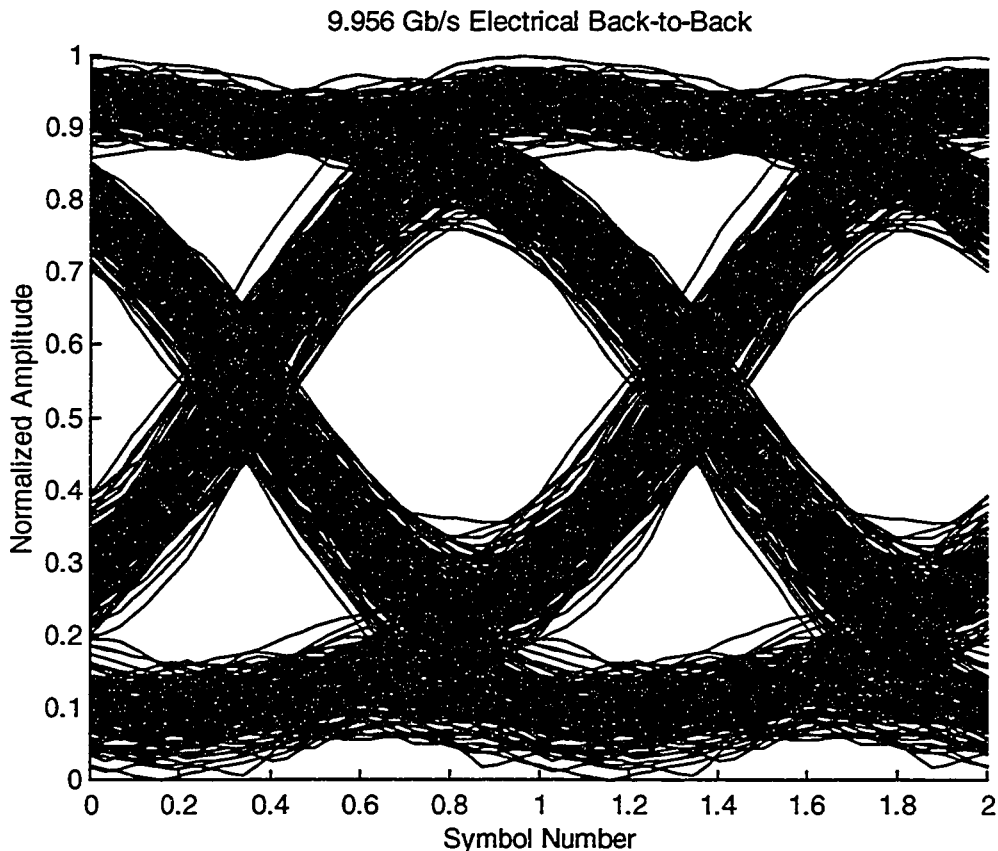


Figure 4.41. Eye-diagram for a 9.95 Gb/s binary signal when the test setup is connected electrically back-to-back. Significant signal distortion is imparted by the test setup.

4.7 Performance of the Entire Switch (Prototype II only)

Frequency response data captured by a network analyser and pulse train data obtain from the BERT were used to predict the performance of the entire switch using FOCSS. The eye-diagrams for 6 Gb/s and 9.95 Gb/s binary data are shown in Figure 4.42. At 9.95 Gb/s the eye has significant closure because the limited channel bandwidth.

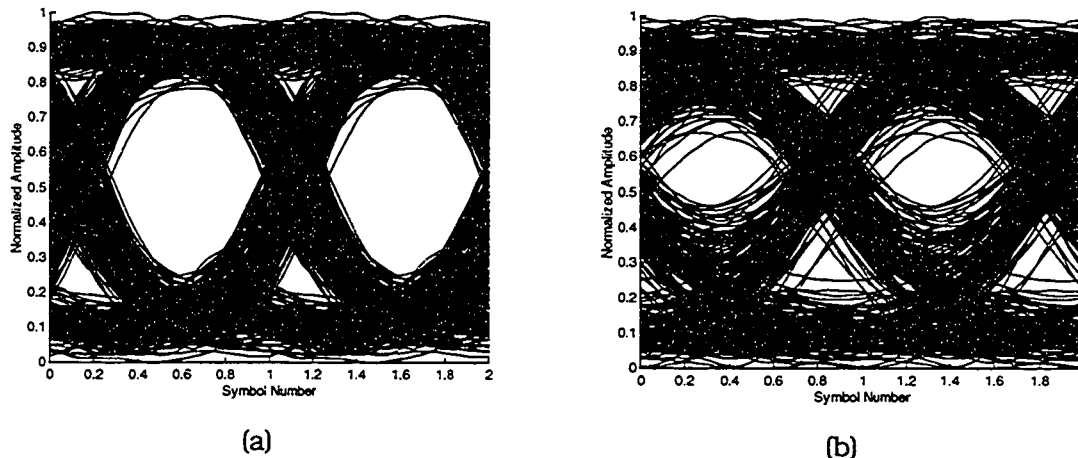


Figure 4.42. System (transmitter and crosspoint modules) eye-diagrams for (a) 6 Gb/s and (b) 9.95 Gb/s binary data. Some of the eye closure was attributed to the test setup (see Figure 4.41)

4.8 Future Design Recommendations and Conclusions

It is possible to scale the current design of the switch to a dimension of 8x8, although propagation loss due to the polymer waveguides would impose a severe limit. Even if advanced polymers were used for the passive optical distribution (propagation loss <0.5 dB/cm) the waveguide loss would still be approximately 10 dB, (assuming that the device could be constructed using 20 cm long optical waveguides). In addition, the inherent splitter loss would be 15 dB, resulting in a minimum loss budget of 25 dB.

The responsivity of a resonant cavity MSM photodetector with narrow fingers ($0.3 \mu\text{m}$ wide fingers with a $1\text{-}2 \mu\text{m}$ gap), may be as high as 1.0 A/W . If such a device was used in conjunction with a low-noise transimpedance amplifier, the receiver sensitivity could be better than -20 dBm. If coupling losses and other excess losses were included, the required output power of the laser would need to be >10 dBm. Such high powered lasers would not be practical due to their restricted bandwidth, and hence lower power lasers may have to be used in conjunction with optical amplifiers. This would result in a complicated system, which is neither cost effective nor highly integrated.

As discussed in Chapter 3, Section 3.2.3, the passive optical distribution could be replaced with an integrated active optical distribution, or more precisely an optical switch. Using such a device would eliminate a large portion of the 15 dB inherent split loss (7-10 dB) and allow conventional low power high bandwidth lasers to be used.

Presently, half of the photocurrent is dissipated into a 50Ω termination resistor at one end of the photodetector array bus. This results in a 6 dB loss of power,

although a broadband microwave power combiner may be used to coherently sum the electrical signals from each end of the photodetector bus. These devices are commercially available, with typical pass-bands from 100 MHz to 10 GHz. As a general rule, SONET systems require a low frequency cut-off of about one ten thousandth of the line rate [81], which for OC-192 (9.95 Gb/s) is approximately 1 MHz and is considerably lower than the 100 MHz attainable from microwave combiners.

Laboratory experiments revealed that a channel bandwidth of 6-7 GHz was obtained for the overall hybrid integrated OES. With some improvements, the bandwidth of the 4x4 OES could be extended to >10 GHz. Lasers with higher output power that are suitable for direct modulation would also help to reduce the loss incurred by the polymer waveguides.

5. Conclusions

This thesis has been primarily concerned with the design, fabrication, and testing of optical filters and switches for use in wavelength division multiplexed optical networks. A summary of the major parts of each project and the corresponding results are presented in this section.

An essential component in a WDM link is a wavelength demultiplexer. A wavelength demultiplexer (DMUX) is used to separate the wavelengths contained in a single fibre/waveguide into N physical paths, where N is the number of wavelengths. A DMUX can be made using arrayed waveguide gratings, diffraction gratings, fibre Bragg-gratings or thin-film interference filters. Each DMUX type has particular advantages and disadvantages, depending upon cost, fabrication tolerances and numerous other performance criteria. Thin-film interference filters offer some compelling advantages, especially in terms of cost, since a single substrate with a thin-film filter (typically many centimetres in diameter) can be sawn into hundreds or thousands of devices. However, the main disadvantage is that they are extremely intolerant to fabrication errors.

The basic structure of a thin-film interference filter consists of alternating layers of high index material followed by a low refractive index material, each one-quarter of a wavelength thick. Multiple reflections from each of the high-low and low-high index interfaces constructively add at particular wavelengths and destructively add at other wavelengths, thereby producing a wavelength dependent reflection/transmission spectrum.

A novel method of creating thin-film filters is to use glancing angle deposition rather than conventional evaporation or sputtering methods. Glancing angle deposition is an evaporation process, whereby the film substrate is simultaneously rotated and tilted with respect to the evaporation source. By controlling the rotation and tilt of the substrate, a film with an arbitrary density as a function of film depth can be produced. The density variation accordingly produces an effective refractive index variation, which if properly deposited, acts as a thin-film interference filter.

Since a film of arbitrary density or index can be deposited, a more general class of filter called rugate filters may be fabricated. Much like the quarter wavelength stack in a thin-film filter, multiple reflections add constructively or destructively depending on the wavelength. However, the refractive index profile of a rugate filter is continuous as a function of film depth. For example, the refractive index profile may be described by a sinusoidal function. To investigate the possible merits of rugate filters, a Windows 95/NT graphical thin-film synthesis program that incorporates a simulated annealing global optimization algorithm was written. The program allows the user to specify an

arbitrary refractive index profile as a function of film depth and calculates the reflection spectrum using the characteristic matrix method. Furthermore, the user may specify a desired reflection spectrum, maximum film thickness, and refractive index range and the program will optimize the refractive index profile. When the simulated annealing parameters are properly specified, the algorithm insures convergence to the global minimum unlike other methods that may become trapped in local minima.

To verify the design of a GLAD interference filter, a band-pass optical filter was fabricated. A full-width at half-maximum bandwidth of 50 nm centred about 460 nm was obtained. Using thickness data obtained from a scanning electron micrograph, the reflection spectrum was calculated with the characteristic matrix method. The theoretical and experimental data agreed very well with one another.

The second project that was undertaken was to design and fabricate a 1x4 multimode thermo-optic polymer switch. The primary application of the optical switch was to replace the passive optical distribution in a 4x4 hybrid integrated optoelectronic switch matrix. In order for the active optical distribution (1x4 polymer switch) to be adopted, it had to be compatible with the existing optoelectronic switch architecture and have low excess loss (<1 dB). Consequently, the 1x4 optical switch was designed with multimode waveguides and multimode interference couplers.

The 1x4 optical switch is configured as a generalized Mach-Zehnder interferometer. The most common form of the Mach-Zehnder interferometer contains two inputs, two phase shifting arms and two outputs. In the current optical switch design, the number of arms has been increased to four thereby allowing the input signal to be switched to any of the four output waveguides. Beam propagation simulations of the 1x4 polymer optical switch indicate that a total loss of less than 1 dB and worst case crosstalk of less than -20 dB should be achievable.

The polymer optical switch was fabricated using a modified photolithography process. Since liquid ultraviolet-curable polymer was used, the photolithography mask could not make physical contact with the polymer. If the mask were to make contact during exposure to UV light, the polymer would fasten the mask to the substrate. The solution was to insert a stack of three 25.4 μm thick tantalum shims between the mask and the substrate. During the exposure process the mask aligner applies pressure to force the mask to make contact with the substrate; however, with the shims in place, the mask was prevented from coming into contact with the substrate.

Three polymer-patterned silicon substrates were successfully processed, each having multiple devices. The best measured contrast ratio and switching time were approximately 5 dB and 3 ms, respectively. Due to fabrication difficulties, the

multimode interference coupler performed poorly. It was estimated that the width of the MMI couplers was between 2 μm to 4 μm wider than the optimal value of 75 μm . Numerical results from 3D beam propagation simulations confirmed this assumption.

The last project involved the development and testing of a 4-channel hybrid integrated optoelectronic switch. Unlike conventional digital cross-connect switches, the optoelectronic switch is an analogue switch. It can therefore switch digital signals of any format or bit rate, and analogue signals simultaneously.

The hybrid integrated optoelectronic switch combines polymer waveguides with metal-semiconductor-metal (MSM) photodetector arrays to create a high performance optoelectronic switch matrix. Furthermore, through integration, the component cost and the amount of manual assembly required were simultaneously reduced as compared to a previously built optoelectronic switch assembled from discretely packaged components. To ease fabrication and yield difficulties, the switch was separated into two modules: the transmitter module and the cross-point module. The transmitter module contains four distributed feedback lasers soldered onto an aluminum nitride microwave substrate patterned with coplanar transmission lines. Furthermore, the AlN substrate acts as a heat sink because of its favourable thermal properties. The completed cross-point module houses the 1x4 photodetector arrays, which are attached to an alumina microwave substrate, and the polymer waveguide optical distribution, which are patterned on a glass or silicon substrate.

Two prototype 4x4 switches were tested, one targeted for a channel bit rate of 2.5 Gb/s and the second targeted for 10 Gb/s per channel. The first prototype was not completely packaged, but the microwave substrates were populated with lasers and photodetector arrays operating at a wavelength of 800 nm. This prototype operated at 2.5 Gb/s per channel.

The second prototype has been partially packaged and tested. Also, the switch was designed to operate at a wavelength of 1550 nm, but the fabrication of the MSM photodetector arrays responsive to 1550 nm light has been delayed due to fabrication difficulties. Therefore, the testing was done with MSM photodetector arrays responsive to 800 nm light. The characterizations of the transmitter (operating at a wavelength of 1550 nm) and cross-point modules (responsive to 800 nm light) were done independently. Later the frequency response data were assembled using software to obtain a complete result. The measured modulation bandwidth of the lasers was greater than 7 GHz and the measured electrical bandwidth of the photodetector arrays was greater than 10 GHz. Using the measured data, the predicted aggregate bandwidth of a

complete 4x4 switch was greater than 6 GHz, sufficient for OC-192 (9.95 Gb/s) binary signals.

In summary, three main projects have been pursued: GLAD thin-film interference filters, the 1x4 polymer optical switch, and the hybrid integrated optoelectronic switch. These three projects have a common theme, namely the use of new technology to enhance the information capacity of fibre optic networks using wavelength division multiplexing.

5.1 Future Work

To further refine the work presented in this thesis, suggestions for future modifications and directions for each of the three main projects will be discussed.

In Chapter 2, thin-film interference filters deposited using glancing angle deposition were presented. In order to make practical devices, the environmental robustness of these films, specifically pertaining to humidity, should be investigated. Also, a clearer understanding of the effective refractive index as a function of porosity should be developed. This would allow better control and *a priori* prediction of the centre wavelength of optical filters and anti-reflection coatings, which are of paramount importance for successful commercialization.

The work performed to date on the 1x4 multimode polymer optical switch illustrated that the concept was sound and that the fabrication is possible. Future endeavours should concentrate on improving the fabrication process, specifically the photolithography process used to define polymer waveguides. Alternatively, new polymeric materials could be used. Since most of the newly developed low-loss polymers are processed in the solid-state rather than the liquid-state, such materials lend themselves better to photolithography. Therefore, the photolithography process would be simplified and the quality of fabricated devices would improve considerably.

The 4x4 hybrid integrated optoelectronic switch matrix project is awaiting the successful fabrication of long wavelength (1550 nm) metal-semiconductor-metal broadband photodetector arrays. When these devices become available, a complete system measurement will be possible. If the 1x4 polymer switch is incorporated into the 4x4 optoelectronic switch, the optical power could potentially be enhanced by 6 dB. Furthermore, if the 1x4 polymer switch can be successfully integrated into the 4x4 optoelectronic switch, then scaling the switch dimension to 32x32 or larger may ultimately be practical.

6. References

- [1] R. C. Bray and D. M. Baney, "Optical Networks: Backbones for Universal Connectivity", *Hewlett-Packard Journal*, Vol. 48, No. 5, December 1997.
- [2] G. P. Agrawal, *Fiber-Optic Communication Systems*, John Wiley & Sons, N.Y. 1997.
- [3] Nortel S/DMS OC-192 TransportNode,
http://www1.nortelnetworks.com/broadband/transport/52k1100_1.html.
- [4] B. P. Keyworth, "WDM Components", Invited Talk, *International Conference on Applications of Photonics Technology*, 1998.
- [5] M. Yamada, A. Mori, K Kobayashi, H. Ono, T. Kanamori, K. Oikawa, Y. Nishida, and Y. Ohishi, "Gain-Flattened Tellurite-Based EDFA with a Flat Amplification Bandwidth of 76 nm", *IEEE Photonics Technology Letters*, Vol. 10, No. 9, pp.1244-1246, September 1998.
- [6] Allwave and Truwave Fibre Developed by Lucent,
http://www.lucent.com/ideas2/perspectives/trends/trends_v5/05.html.
- [7] B. P. Keyworth, JDS Fitel Inc. recruiting presentation, University of Alberta, March 15, 1999.
- [8] R. Bertram, M. F. Ouellette, and P. Y. Tse, "Inhomogeneous Optical Coatings: an Experimental Study of a New Approach", *Applied Optics*, Vol. 28, No. 14, 2935-2939, 1989.
- [9] M. Born and E. Wolf, *Principles of Optics*, Section 1.6.2., Pergamon, N. Y., 1980.
- [10] N. Matuschek, F. X. Kartner, and U. Keller, "Exact Coupled-Mode Theories for Multilayer Interference Coatings with Arbitrary Strong Index Modulations", *IEEE Journal of Quantum Electronics*, Vol. 33, No. 3, 295-302, 1997.
- [11] W. H. Southwell, "Spectral Response Calculations of Rugate Filters Using Coupled-Wave Theory", *Journal Optics Society America A*, Vol. 5, 1558-1564, 1988.
- [12] B. E. A. Saleh and M. C. Teich, *Fundamentals of Photonics*, John Wiley & Sons, N.Y., 1991.
- [13] P. G. Verly, J. A. Dobrowolski, W. J. Wild, and R. L. Burton, "Synthesis of High Rejection Filters with the Fourier Transform Method", *Applied Optics*, Vol. 28, No. 14, 2864-2875, 1989.
- [14] C. P. Chang, Y. H. Lee, and S. Y. Wu, "Optimization of a Thin-Film Multilayer Design by Use of the Generalized Simulated-Annealing Method", *Optics Letters*, Vol. 15, No. 11, pp. 595-597, 1990.
- [15] L. Ingber, "Very Fast Simulated Re-annealing", *Journal Mathematical Computer Modelling*, pp. 967-973, 1989.

- [16] L. Ingber, "Simulated Annealing: Practice Versus Theory", *Journal Mathematical Computer Modelling*, pp. 29-57, 1993.
- [17] C. R. Reeves, *Modern Heuristic Techniques for Combinatorial Problems*, Chapter 2, John Wiley & Sons, N. Y., 1993.
- [18] P. G. Verly, A. V. Tilhonravov, and M. K. Trubetskov, "Efficient Refinement Algorithm for the Synthesis of Inhomogeneous Optical Coatings", *Applied Optics*, Vol. 36, No. 7, pp. 1487-1495, 1997.
- [19] J. A. Dobrowolski and R. A. Kemp, "Refinement of Optical Multilayer Systems with Different Optimization Procedures", *Applied Optics*, Vol. 29, No. 19, pp. 2876-2893, 1990.
- [20] W. Goffe, FORTRAN source code for the simulated annealing algorithm, <http://lib.stat.cmu.edu/general/>.
- [21] W. J. Gunning, R. L. Hall, F. J. Woodberry, W. H. Southwell, and N. S. Gluck, "Codeposition of Continuous Composition Rugate Filters", *Applied Optics*, Vol. 28, No. 14, 2945-2948, 1989.
- [22] P. L. Swart, P. V. Bulkin, and B. M. Lacquet, "Rugate Filter Manufacturing by Electron Cyclotron Resonance Plasma-Enhanced Chemical Vapour Deposition of SiN_x ", *Optical Engineering*, Vol. 36 No. 4, 1214-1219, 1997.
- [23] E. P. Donovan, D. Van Vechten, A. D. F. Kahn, C. A. Carosella, and G. K. Hubler, "Near Infrared Rugate Filter Fabrication by Ion Beam Assisted Deposition of $\text{Si}_{(1-x)}\text{N}_x$ Films", *Applied Optics* Vol. 28, No. 14, 2940-2944, 1989.
- [24] H. Sankur, W. J. Gunning, and J. F. DeNatale, "Intrinsic Stress and Structural Properties of Mixed Composition Thin Films", *Applied Optics*, Vol. 27, No 28, 1564-1567, 1988.
- [25] K. Robbie, and M. J. Brett, "Sculptured Thin Tilms and GLAD: Growth Mechanics and Applications", *Journal of Vacuum Science Technology A*, 15(3), 1997.
- [26] SEM photographs courtesy of K. Robbie.
- [27] W. H. Southwell, "Gradient-index antireflection coatings", *Optics Letters*, Vol. 8, No. 11, 584-586, 1983.
- [28] S. Reinhorn, Y. Amitai, A. A. Friesem, A. W. Lohmann, and S. Gorodeisky, "Compact Optical Crossbar Switch", *Applied Optics*, Vol. 36, No. 5, pp. 1039-1043, February 1997.
- [29] T. Fukushima and T. Sakamoto, "A 7x6 Optical Fibre Grating Demultiplexer-Multiposition Switch for 0.64-0.88 μm Band", *IEEE Journal of Lightwave Technology*, Vol. 14, No. 5, pp. 867-872, May 1996.
- [30] D. O. Culverhouse, T. A. Birks, S. G. Farwell, J. Ward, P. St. J. Russell, "40 MHz All-Fibre Acoustoptic Frequency Shifter", *IEEE Photonics Technology Letters*, Vol. 8, No. 12, pp. 1636-1637, December 1996.

- [31] D. X. Zhu, S. Dubobitsky, W. H. Steier, K. Uppal, D. Tishinin, J. Burger, and P. D. Dapkus. "A Novel All-Optical Switch: The Wavelength Recognizing Switch", *IEEE Photonics Technology Letters*, Vol. 9, No. 8, pp. 1110-1112, August 1997.
- [32] D. Marcemac and A. Mecozzi, "Switches and Frequency Converters Based on Cross-Gain Modulation in Semiconductor Optical Amplifiers", *IEEE Photonics Technology Letters*, Vol. 9, No. 6, pp. 749-751, June 1997.
- [33] C. P. Larsen, and M. Gustavsson, "Linear Crosstalk in 4x4 Semiconductor Optical Amplifier Gate Switch Matrix", *IEEE Journal of Lightwave Technology*, Vol. 15, No. 10, pp. 1865-1870, October 1997.
- [34] W. J. Goralski, *SONET: A Guide to Synchronous Optical Network*, McGraw-Hill, N.Y., 1997
- [35] Bell Communications Research, "General Requirements GR-1230-CORE: SONET Bidirectional Line-Switched Ring Equipment Criteria", November 1995.
- [36] Bell Communications Research, "General Requirements GR-1400-CORE: SONET Dual-Fed Unidirectional Path Switched Ring Equipment Criteria", October 1995.
- [37] P. Jaggi and L Steinhorst, "IP Over Photonics: Making it Work", *Lightwave*, pp. 52-55, January 1999.
- [38] R. I. MacDonald, "Bidirectional Optical Crossconnection", *Proceedings of Canadian Conference on Broadband Research*, pp. 238-243, June 1998.
- [39] S. I. Najafi, T. Touam, R. Sara, M. P. Andrews, and M. A. Fardad, "Sol-Gel Glass Waveguides and Gratings on Silicon", *IEEE Journal of Lightwave Technology*, Vol. 16, No. 9, pp. 1640-1646, September 1998.
- [40] T. Kominato, Y. Ohmori, H. Okazaki, and M. Yasu, "Very Low-Loss GeO₂-Doped Silica Waveguides Fabricated by Flame Hydrolysis Deposition Method", *Electronics Letters*, Vol. 26, No. 5, pp. 327-329, March 1990.
- [41] Photonic Integration Research Inc.,
http://www.piri.com/photonic_integration_research.htm.
- [42] B. Schüppert, J Schmidtchen, A. Splett, U. Fischer, T. Zinke, R. Moosburger, and K. Petermann, "Integrated Optics in Silicon and SiGe-Hetrostructures", *IEEE Journal of Lightwave Technology*, Vol. 14, No. 10, pp. 2311-2322, October 1996.
- [43] J. Kobayashi, T. Matsuura, Y. Hida, S. Sasaki, and T. Maruno, "Fluorinated Polyimide Waveguides with Low Polarization-Dependent Loss and Their Applications to Thermo-optic Switches", *IEEE Journal of Lightwave Technology*, Vol. 16, No. 6, pp. 1024-1029, June 1998.
- [44] Y. Hida, H. Onose, and S. Imamura, "Polymer Waveguide Thermo-optic Switch with Low Electric Power Consumption at 1.3 μm ", *IEEE Photonics Technology Letters*, Vol. 5, No. 7, pp. 782-784, July 1993.
- [45] B. L. Booth, "Low Loss Channel Waveguides in Polymers", *IEEE Journal of Lightwave Technology*, Vol. 7, No. 10, pp. 1445-1453, June 1989.

- [46] R. Yoshimura, M. Hikita, S. Tomaru, and S. Imamura, "Low-Loss Polymeric Optical Waveguides Fabricated with Deuterated Polyfluoromethacrylate", *IEEE Journal of Lightwave Technology*, Vol. 16, No. 6, pp. 1030-1037, June 1989
- [47] B. P. Keyworth, D. Corazza, W. Fuchs, and J. N. McMullin, "Low-Cost Direct-Write Multimode Polymer Waveguides", Post-deadline paper presented at LEOS 1994 Summer Topical Meeting on Integrated Optoelectronics, Lake Tahoe, NV, July 6-8, 1994.
- [48] B. P. Keyworth, J. N. McMullin, D. Corazza, L. Mabbott, T. Neufeld, and T. Rosadiuk, "Dispensed Polymer Microlenses", *Technical Digest Optical Society of America Annual Meeting*, WVV52, September 10-15, 1995.
- [49] R. März, *Integrated Optics: Design and Modeling*, Artech House, Boston, 1995.
- [50] M. R. Piam, *Applications of Multimode Interference Couplers in Wavelength-Division Multiplexing*, Ph.D. Thesis, University of Alberta, 1997.
- [51] L. B. Soldano, F. B. Veerman, M. K. Smit, B. H. Verbeek, A. H. Dubost, and E. C. M. Pennings, "Planar Monomode Optical Couplers Based on Multimode Interference Effects", *IEEE Journal of Lightwave Technology*, Vol. 10, No. 12, pp. 1843-1850, December 1992.
- [52] L. B. Soldano, E. C. M. Penning, "Optical Multi-mode Interference Devices Based on Self-Imaging: Principles and Applications", *IEEE Journal of Lightwave Technology*, Vol. 13, No. 4, pp. 615-627, April 1995.
- [53] P. A. Besse, M. Bachmann, H. Melchior, L. B. Soldano, and M. K. Smit, "Optical Bandwidth and Fabrication Tolerances of Multimode Interference Couplers", *IEEE Journal of Lightwave Technology*, Vol. 12, No. 6, pp. 1004-1009, June 1994.
- [54] M. Bachmann, P. A. Besse, and H. Melchior, "Overlapping-image Multimode Interference Couplers with a Reduced Number of Self-images for Uniform and Non-Uniform Power Splitting", *Applied Optics*, Vol. 34, No. 30, pp. 6898-6910, October 1995.
- [55] P. A. Besse, M. Bachmann, H. Melchior, "Phase Relations in Multi-mode Interference Couplers and Their Application to Generalized Integrated Mach-Zehnder Switches", *Proc. European Conf. Integrated Optics*, pp. 2.22-2.23, April 1993.
- [56] Norland Products Inc., Thermo-optic Coefficient data obtained for NOA 60.
- [57] R. C. Weast, *Handbook of Chemistry and Physics*, 70th Edition, CRC Press, Boca Raton, Florida, 1990.
- [58] J. Bandrup and E. H. Immergut, *Polymer Handbook*, 3rd Edition, John Wiley & Sons, 1989.
- [59] G. V. Treyz, "Silicon Mach-Zehnder Waveguide Interferometers Operating at 1.3 μm ", *Electronics Letters*, Vol. 27, No. 3, pp. 118-120, 1991.

- [60] R. Sharma, R. I. MacDonald, D. Lam, D. Clegg, R. Tholl, "Broadband Optoelectronic Switch for Digital and Analog Signals", *Proceedings of the SPIE*, Vol. 2692, pp. 190-193, 1996.
- [61] D. J. Corazza, A. J. P. Hnatiw, L. M. Mabbott, B. P. Keyworth, R. I. MacDonald, J. N. McMullin, "Four-Channel Hybrid Integrated Optoelectronic Switch", *Canadian Conference on Broadband Research*, 1997.
- [62] A. J. P. Hnatiw, D. W. Boertjes, R. G. DeCorby, J. N. McMullin, R. I. MacDonald, D. J. Corazza, and E. Johnson, "A Four-channel Optoelectronic Switch for use in WDM Networks", *International Conference on Applications of Photonic Technology*, pp.33-38, July 1998.
- [63] R. Sharma, *Broadband Optoelectronic Switching and Signal Processing*, Ph.D. Thesis, University of Alberta, 1996.
- [64] C. L. Goldsmith, G. A. Mangel, and R. J. Baca, "Principles and Performance of Travelling-Wave Photodetector Arrays", *IEEE Trans. On Microwave Theory and Techniques*, Vol. 45, No. 8, 1997.
- [65] A. McGuire and P. Bonenfant, "Standards: The Blueprints for Optical Networking", *IEEE Communications Magazine*, pp. 68-78, February 1998
- [66] S. Carter and N. Chinone, "Optical Crossconnects: Toward a Photonic Network", *Lightwave*, pp. 96-99, February 1998.
- [67] K. Obermann, S. Kindt, D. Breuer, and K. Petermann, "Performance Analysis of Wavelength Converters Based on Cross-Gain Modulation in Semiconductor-Optical Amplifiers", *IEEE Journal of Lightwave Technology*, Vol. 16, No. 1, pp. 78-85, January 1998.
- [68] S. L. Danielsen, P. B. Hansen, K. E. Stubkjaer, M Schilling, K. Wünnstiel, W. Idler, P. Doussiere, and F. Pommerau, "All Optical Wavelength Conversion Schemes for Increased Input Power Dynamic Range", *IEEE Photonics Technology Letters*, Vol. 10, No. 1, pp. 60-62, January 1998.
- [69] R. B. Lee, D. F. Geraghty, M. Verdiell, M. Ziari, A. Mathur, and K. J. Vahala, "Cascaded Wavelength Conversion by Four-Wave Mixing in a Strained Semiconductor Optical Amplifier at 10 Gb/s", *IEEE Photonics Technology Letters*, Vol. 9, No. 6, pp. 752-754, June 1997.
- [70] R. I. MacDonald, "Optoelectronic Hybrid Switching", *Photonics in Switching I*, J. E. Midwinter, Ed., Vol. 1, Academic Press, 1994.
- [71] K. S. Lowe, "A GaAs HBT 16x16 10-Gb/s/Channel Crosspoint Switch", *IEEE Solid-State Circuits*, Vol. 32, No. 8, pp. 1263-1268, August 1997.
- [72] E. L. Goldstein, J. A. Nagel, J. L. Strand, and R. W. Tkach, "National-scale Networks Likely to be Opaque", *Lightwave*, pp. 92-95, February 1998.
- [73] R. I. MacDonald, D. J Corazza, R. Sharma, and D. C. Clegg, "Optoelectronic Switching for Virtual Wavelength Paths", *Photonics in Switching*, Stockholm, Sweden 1997.

- [74] R. G. DeCorby, *Optimization of Metal-Semiconductor-Metal Photodetectors and Advanced Photodetector Structures*, Ph.D. Thesis, University of Alberta, 1998.
- [75] R. G. DeCorby, R. I. MacDonald, A. J. P. Hnatiw, D. W. Boertjes, J. N. McMullin, F. Gouin, J. Noad, "Packaged Array of 8 MSM Photodetectors with Uniform 12 GHz Bandwidth", *Electronics Letters*, Vol. 34, No. 4, pp. 400-401, 1998.
- [76] R. R. Krchnavek, G. R. Lalk, and D. H. Hartman, "Direct Writing of Channel Waveguides Using Spin-on Polymers", *Journal of Applied Physics*, Vol. 66, No. 11, pp. 5156-5160, December 1989.
- [77] Picosecond Pulse Labs, Broadband Electrical Amplifiers ,
<http://www.picosecond.com/coaxcomp/amplifiers.htm>
- [78] JDS Fitel Inc., Beambox Polymer Waveguide Switches,
<http://www.jdsfitel.com/catalog/solidst.html>.
- [79] S. Walklin, *Multilevel Signaling for Increasing the Capacity of High-speed Optical Communication Systems*, Ph.D. Thesis, University of Alberta, 1997.
- [80] K. Petermann, *Laser Diode Modulation and Noise*, Kluwer Academic Publishers, Dordrecht, Netherlands, 1988.
- [81] D. Weymouth, JDS Fitel, Nepean, Canada, *Private Communication*, November 1998.

7. Appendix I: Thermal Modeling Source Code

7.1 Steady State Solution

```
{guide.pde}

{This Pdease script will find the steady-state temperature profile of a
polymer waveguide that is heated by a chromium heater.}

title
  "Waveguide Heater"

select
  errlim=1E-5
  gridlimit=20

variables
  Temp(range=0,100)      { Variable is "Temp" }

definitions
  tmax      = 0.02      {maximum time in sec}
  ts        = 0.001
  tend      = 0.009    {pulse duration is tend-ts}
  um        = 1E-6
  K
  cp
  rho              { kg/m^3}
  Ksilicon = 124      {Phys./Chem. E-104 Thermal Conductivity W/(m C)}
  Kpolymer = 0.2
  Kmetal     = 70
  Kglass     = 1
  cpsil      = 0.25*4.18E3    {heat capacity , J/(kg C) }
  cpglass    = 700
  cppol      = 1.42E3
  cpmetal    = 460
  rhosil     = 2.3283E3    {density in kg/m^3}
  rhoglass   = 2.5E3
  rhopol     = 1.1E3
  rhometal   = 7800

  A = 0      {Source Switch, A = 1 in Region 3}
  source = 4E13
  B1 = 0.5   {Free Space Coupling Coefficient}
  B2 = 0.1
  B3 = 0.1
  Ta = 25    {Ambient Temperature}
  HI = 15*um {Height of Waveguide, cladding + core}

{Define the coordinates of the waveguide structure}

Ax = -50E-6
Ay = 39E-6
Bx = -Ax
```

```

BBy = Ay
Cx = Bx
Cy = 40E-6
DDx = 15E-6
DDy = Cy
Ex = DDx
Ey = DDy {42E-6}
Fx = 5E-6
Fy = Ey
Gx = Fx
Gy = DDy
Hx = -Gx
Hy = DDy
Ix = -Fx
Iy = Ey
Jx = -Ex
Jy = Iy
Kx = -DDx
Ky = DDy
Lx = Ax
Ly = Cy
Mx = Ex
My = Ey+HI
Nx = Fx
Ny = My
Ox = Jx
Oy = My
Px = Ix
Py = Oy

Metxa = 12E-6
Metya = Ey
Metxb = 8E-6
Metyb = Metya+0.5E-6

initial value
Temp=Ta

{This is the steady-state heat equation that will be solved}
{A is used as a switch and determines whether a particular }
{region generates heat}

equations
dx(K*dx(Temp)) + dy(K*dy(Temp)) + A*source =0

{Create the waveguide structure}
boundaries
region 1      {Defines the maximum extent of the system}
  A=0
  K=Kglass
  cp=cpglass
  rho=rhoglass

start(Ax,Ay)

```

```

line to (Bx,BBy)
line to (Cx,Cy) to (DDx,DDy) to (Ex,Ey)
line to (Fx,Fy) to (Gx,Gy) to (Hx,Hy) to (Ix,Iy)
line to (Jx,Jy) to (Kx,Ky) to (Lx,Ly) to finish

```

```

region 2

```

```

A=0
K=Kpolymer
cp=cppol
rho=rhopol

start (Ex,Ey)
natural(Temp)=5*(Ta-Temp)
line to (Mx,My) to (Nx,Ny) to (Fx,Fy) to finish

```

```

region 3

```

```

A=0
K=Kpolymer
cp=cppol
rho=rhopol

start (Jx,Jy)
natural(Temp)=5*(Ta-Temp)
line to (Ix,Iy) to (Px,Py) to (Ox,Oy) to finish

```

```

region 4

```

```

A=0
K=Ksilicon
cp=cpsil
rho=rhosil
value(temp)=Ta
start(Ax,0)
line to (Bx,0)
natural(Temp)=5*(Ta-Temp)
line to (Bx,BBy) to (Ax,Ay) to finish

```

```

region 5

```

```

A=1
K=Kmetal
cp=cpmetal
rho=rhometal
natural(Temp)=5*(Ta-Temp)
start (Metxa,Metya)
line to (Metxa,Metyb)
natural(Temp)=5*(Ta-Temp)
line to (Metxb,Metyb)
natural(Temp)=5*(Ta-Temp)
line to (Metxb,Metya) to finish

```

```

monitors

```

```

contour(Temp) zoom(Kx-5*um,Ky-10*um,DDx-Kx+10*um,My-Ky+15*um) delay=5
elevation(Temp) from ( (Metxa+Metxb)/2,0) to ((Metxa+Metxb)/2,My)
elevation(Temp) from ( (Kx+Hx)/2,0) to ((Kx+Hx)/2,My)

```

```

plots

```

```

grid(x,y)
contour(Temp) zoom(Kx-5*um,Ky-10*um,DDx-Kx+10*um,My-Ky+15*um) pause
elevation(Temp) from ((Metxa+Metxb)/2,0) to ((Metxa+Metxb)/2,My)
pause
elevation(Temp) from ((Kx+Hx)/2,0) to ((Kx+Hx)/2,My) pause
end

```

7.2 Time-Dependent Solution

```

{guidet.pde}

{This Pdease script will find the transient temperature response of a
polymer waveguide that is heated by a chromium heater.}

title
  "Waveguide Heater"

select
  errlim=5E-4

variables
  Temp(range=0,100)      { Variable is "Temp" }

definitions
  um      = 1E-6
  tmax    = 0.03          {maximum time in sec}
  ts      = 0.001
  tend    = 0.011        {pulse duration is equal to: tend-ts}
  K
  cp
  rho     { kg/m^3}
  Ksilicon = 124          {Thermal Conductivity W/(m C)}
  Kpolymer = 0.2
  Kmetal   = 70
  Kglass   = 1
  cpsil    = 0.25*4.18E3  { heat capacity , J/(kg C) }
  cpglass  = 700
  cppol    = 1.42E3
  cpmetal  = 460
  rhosil   = 2.3283E3     {density in kg/m^3}
  rhoglass = 2.5E3
  rhopol   = 1.1E3
  rhometal = 7800

  A = 0                      {Source Switch, A = 1 in Region 3}
  source = 6E14
  B1 = 0.5                   {Free Space Coupling Coefficient}
  B2 = 0.1
  B3 = 0.1
  Ta = 25                    {Ambient Temperature}

```

```

HI = 15*um                {Height of core + cladding}

{Define structure coordinates}

Ax = -50E-6
Ay = 39E-6
Bx = -Ax
BBy = Ay
Cx = Bx
Cy = 40E-6
DDx = 15E-6
DDy = Cy
Ex = DDx
Ey = DDy {42E-6}
Fx = 5E-6
Fy = Ey
Gx = Fx
Gy = DDy
Hx = -Gx
Hy = DDy
Ix = -Fx
Iy = Ey
Jx = -Ex
Jy = Iy
Kx = -DDx
Ky = DDy
Lx = Ax
Ly = Cy
Mx = Ex
My = Ey+HI
Nx = Fx
Ny = My
Ox = Jx
Oy = My
Px = Ix
Py = Oy

Metxa = 12E-6
Metya = Ey
Metxb = 8E-6
Metyb = Metya+0.5E-6

initial value
Temp=Ta

{This is the time-dependent heat equation and will be solved to
determine the transient temperature response of a polymer waveguide to
a heat pulse generated by a chromium heater.}

equations
dx(K*dx(Temp)) + dy(K*dy(Temp)) + A*source = cp*rho*dt(Temp)

```

{Define the waveguide structure.}

boundaries

region 1 {Defines the maximum extent of the system}

A=0

K=Kglass

cp=cpglass

rho=rhoglass

start(Ax,Ay)

line to (Bx,BBy)

line to (Cx,Cy) to (DDx,DDy) to (Ex,Ey)

line to (Fx,Fy) to (Gx,Gy) to (Hx,Hy) to (Ix,Iy)

line to (Jx,Jy) to (Kx,Ky) to (Lx,Ly) to finish

region 2

A=0

K=Kpolymer

cp=cppol

rho=rhopol

start (Ex,Ey)

natural(Temp)=5*(Ta-Temp)

line to (Mx,My) to (Nx,Ny) to (Fx,Fy) to finish

region 3

A=0

K=Kpolymer

cp=cppol

rho=rhopol

start (Jx,Jy)

natural(Temp)=5*(Ta-Temp)

line to (Ix,Iy) to (Px,Py) to (Ox,Oy) to finish

region 4

A=upulse(t-ts,t-ts-tend)-0.2

K=Kmetal

cp=cpmetal

rho=rhometal

start (Metxa,Metya)

line to (Metxa,Metyb) to (Metxb,Metyb) to (Metxb,Metya) to finish

region 5

A=0

K=Ksilicon

cp=cpsil

rho=rhosil

value(temp)=Ta

start(Ax,0)

line to (Bx,0)

```
natural(Temp)=5*(Ta-Temp)
line to (Bx,BBy) to (Ax,Ay) to finish

time 0 to tmax

monitors
for t=0 by 0.001 to 0.003 by 0.002 to tmax
  elevation(Temp) from ( (Metxa+Metxb)/2,0) to ((Metxa+Metxb)/2,My)
  elevation(Temp) from ( (Kx+Hx)/2,0) to ((Kx+Hx)/2,My)

plots
for t=0 by 0.0002 to 0.003 by 0.0005 to tmax

{This generates a temperature vs. time graph.}
histories
  history(Temp) at ((Kx+Hx)/2,My-1*um) ((Kx+Hx)/2,Ey) pause
  history(Temp) at ((Metxa+Metxb)/2,My-1*um) ((Metxa+Metxb)/2,Ey) pause
end
```